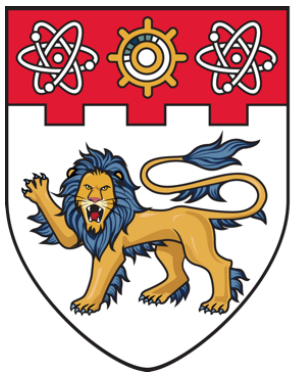

NANYANG TECHNOLOGICAL UNIVERSITY
SINGAPORE

Engineering Cathode and Anode for Rechargeable Aluminum-Ion Aqueous Battery

SONAL KUMAR

SCHOOL OF MATERIALS SCIENCE AND ENGINEERING

2021

Engineering Cathode and Anode for Rechargeable Aluminum-Ion Aqueous Battery

SONAL KUMAR

SCHOOL OF MATERIALS SCIENCE AND ENGINEERING

A thesis submitted to the Nanyang Technological University
in partial fulfilment of the requirement for the degree of
Doctor of Philosophy

2021

Statement of Originality

I hereby certify that the work embodied in this thesis is the result of original research, is free of plagiarised materials, and has not been submitted for a higher degree to any other University or Institution.

08-12-2021

. . . . . .
Date

. . . . . .
SONAL KUMAR

Supervisor Declaration Statement

I have reviewed the content and presentation style of this thesis and declare it is free of plagiarism and of sufficient grammatical clarity to be examined. To the best of my knowledge, the research and writing are those of the candidate except as acknowledged in the Author Attribution Statement. I confirm that the investigations were conducted in accord with the ethics policies and integrity standards of Nanyang Technological University and that the research data are presented honestly and without prejudice.

08-12-2021

. . . . . .

Date

. . . . . .

PROF. MADHAVI SRINIVASAN

Authorship Attribution Statement

This thesis contains material from 5 papers published in the following peer-reviewed journal(s) in which I am listed as an author.

Chapter 2 is published as Verma V*, **Kumar S*,** Manalastas Jr W, Satish R, Srinivasan M. Progress in Rechargeable Aqueous Zinc- and Aluminum-Ion Battery Electrodes: Challenges and Outlook. Adv Sustainable Syst. 2019;3(1):1800111.

The contributions of the co-authors are as follows:

- Prof. Madhavi provided the initial project direction.
- Mr. Verma and I prepared the manuscript drafts with equal contribution.
- Prof. Madhavi, Dr. Rohit and Dr. William reviewed and provided supervision in refining the paper.

Chapter 4 is published as **Kumar S**, Satish R, Verma V, Ren H, Kidkhunthod P, Manalastas W, Srinivasan M. Investigating FeVO4 as a cathode material for aqueous aluminum-ion battery. J Power Sources. 2019;426:151-61.

The contributions of the co-authors are as follows:

- Prof. Madhavi provided the initial project direction.
- I wrote the drafts of the manuscript. The manuscript was revised together with Prof. Madhavi, Dr. Rohit and Dr. William.
- I co-designed the study with Mr. Verma and Dr. William.
- I performed the synthesis, electrochemical testing and in-lab materials characterizations at School of Materials Science and Engineering.
- Dr. Ren collected the transmission electron micrographs.
- Dr Rohit and Dr Pinit collected XAS data and helped in analysis.

Chapter 5 is published as Cai Y*, **Kumar S***, Chua R, Verma V, Yuan D, Kou Z, Ren H, Arora H, Srinivasan M. Bronze-type vanadium dioxide holey nanobelts as high performing cathode material for aqueous aluminium-ion batteries. J Mater Chem A. 2020;8(25):12716-22.

The contributions of the co-authors are as follows:

- Prof. Madhavi provided the initial project direction.
- Dr. Cai and I wrote the drafts of the manuscript. The manuscript was revised together with Prof. Madhavi, Dr. Cai and Dr. Du.
- Dr. Cai synthesized and provided the active material.
- Mr. Hemal Arora and I performed electrochemical testing and cell performance optimization.
- Dr. Rodney, Dr. Kou, Dr Cai and I carried out in-lab materials characterizations and further analysis.
- Dr. Ren collected the transmission electron micrographs.
- Mr. Verma helped in of XRD data analysis.

Chapter 6 is published as **Kumar S**, Verma V, Arora H, Manalastas W, Srinivasan M. Rechargeable Al-Metal Aqueous Battery Using NaMnHCF as a Cathode: Investigating the Role of Coated-Al Anode Treatments for Superior Battery Cycling Performance. ACS Applied Energy Materials. 2020;3(9):8627-35.

The contributions of the co-authors are as follows:

- Prof. Madhavi provided the initial project direction.
- I wrote the drafts of the manuscript. The manuscript was revised together with Prof. Madhavi, Dr. William and Mr. Verma.
- I synthesized the active materials, Mr. Hemal helped in electrochemical testing.
- I carried out in-lab materials characterizations and further analysis.
- Mr. Verma helped in of XRD data analysis.

Chapter 7 is submitted as **Sonal Kumar**, Teddy Salim, Vivek Verma, William Manalastas and Madhavi Srinivasan et al., Enabling Al-metal anodes for aqueous electrochemical cells by using eutectic mixtures as artificial protective interphase.

The contributions of the co-authors are as follows:

- Prof. Madhavi provided the initial project direction.
- I wrote the drafts of the manuscript. The manuscript was revised together with Prof. Madhavi, Dr. William, Dr Teddy and Mr. Verma.
- I performed the synthesis, electrochemical testing and in-lab materials characterizations at School of Materials Science and Engineering.
- Dr. William helped in collecting FTIR and Raman data.
- Dr. Teddy helped in XPS data collection and analysis.

08-12-2021

. . . . . .
Date

. . . . . .
SONAL KUMAR

Abstract

Rechargeable aluminum-ion aqueous battery (AIAB) is extremely attractive from the prospects of developing environmentally and economically sustainable battery energy storage systems. The usage of water as an electrolyte solvent in AIAB makes it inherently non-flammable and presents opportunities for open-air fabrication, making it safer and cheaper. At the same time, AIAB presents opportunities of getting rid of lithium while harnessing aluminium's (Al's) high volumetric capacity (~8000 mAh cm^{-3}) and low cost because of the high abundance in the earth's crust. Hence, AIAB is a strong contender for futuristic energy storage applications, challenging established commercial battery chemistries. However, the AIAB battery research is nascent and presents challenges on both the cathode and anode front, often raising questions about the feasibility and practicality of such viable battery chemistry. This thesis is an effort towards to studying Al-ion batteries and answering this feasibility question by testing novel cathodes and anodes in water-based electrolyte.

The thesis starts with a deep dive into the existing AIAB literature. Further, the research gaps are identified and problem statements are defined. The main objective is to study the feasibility of AIAB, essentially by demonstrating working AIAB cell. Hence the scope of the thesis includes (i)engineering new cathode materials which allow for reversible accommodation of Al-ion or its complexes in an Al-salt based aqueous electrolyte, (ii) engineering the surface of Al-metal to enable its usage as an anode in an Al-salt based aqueous electrolyte without significant electrolyte decomposition, and (iii) implementing electrochemical and materials characterization techniques to develop an understanding of the concomitant cell reactions.

The thesis can be broadly divided into two parts, one focusing on cathode and the other on anode development. $FeVO_4$, VO_2, and HCFs have been explored as potential cathode materials. $FeVO_4$ is reported by us for the first time as a host material showing Al-ion intake by a conversion type mechanism; VO_2 is shown to have excellent long-term cycling stability in an optimized electrolyte, and HCF has been developed as a standard

cathode material with stable cycling properties to complement anodic studies. On the anodic front, $AlCl_3$ based eutectic formulations have been proposed, which can be used to engineer an artificial protective layer on Al-metal. These layers protect Al from oxidation in ambient and improve the conductivity and kinetics at anode/electrolyte interface, making usage of Al-metal as an anode possible in aqueous electrolyte. A combination of in-house and synchrotron characterization techniques has also been used to understand the structural and compositional evolution in the cathode and study the evolution of Al anode surface chemistry under various conditions.

The thesis concludes that an aluminum-ion battery chemistry is possible in an aqueous electrolyte. However, such chemistry is currently limited by low cell voltage, which can be overcome by developing high voltage cathodes and new coating formulations which can exploit the actual reduction potential of Al-metal (-1.66 V vs SHE). The developments made in the thesis serve as a collection of important preliminary studies in the AIAB field and will be beneficial for researchers working in multivalent aqueous chemistry and metal surface engineering.

Lay Summary

The rapidly growing world economy and an ever-increasing world population are causing a paradigm shift towards using non-renewable energy sources like wind, tidal, and solar. However, the intermittent and dispersed nature of such energy creates demand for integrating battery energy storage systems (BESS) in the electric grid that can store and release harvested energy on demand as per consumption pattern. Considering high demand in future, these BESS will need to be low-cost investment, safe and environmentally sustainable. Among various battery chemistries, rechargeable aluminum-ion aqueous battery (AIAB) is a potential candidate for such applications owing to cheap, non-flammable water based electrolyte that can be handled in ambient conditions and highly abundant, cheap Al metal anode that makes AIAB economically and environmentally sustainable, therefore ideal for BESS or similar applications.

However, AIAB is still in the nascent stage, and lab-scale studies need to be done to ascertain the feasibility of such chemistry. This thesis does precisely that. In this study, various new cathode materials are engineered and tested for their applicability in AIAB. At the same time, the surface of the Al-metal anode has been engineered such that the naturally forming oxide layer on Al metal is rid of and the surface chemistry is activated towards chemical reaction in a battery. Finally, combinations of these cathodes and anodes are tried to see the possibility of making a successful AIAB. An effort has also been made to develop science and understanding of how this chemistry would function. At the cathode front, this study contributes $FeVO_4$, VO_2, and HCFs as new host materials and deciphers the underlying reaction mechanism of Al-intake. At the anode front, the study presents new $AlCl_3$ based coatings formulations. These formulations when coated on Al-metal foil protects it from oxidation in the open air and activates its surface, essentially making it possible to use Al as an anode in AIAB.

Overall, the findings in this thesis conclude that an aluminum-ion battery chemistry is possible in an aqueous electrolyte and sets a strong foundation for AIAB progress. Researchers working in aqueous multivalent battery chemistry and metal surface

engineering can benefit abundantly from this study. This thesis adds significant initial knowledge towards realizing cheaper and safer battery technology.

Acknowledgements

I would like to start my acknowledgement by thanking my supervisor, Professor Madhavi Srinivasan, for her constant guidance and providing the right balance of push and freedom, which allowed me to pursue various directions in my thesis and make rapid progress. I want to acknowledge the financial support from by National Research Foundation of Singapore (NRF) Investigatorship award number NRFI2017-08. I would also like to thank Synchrotron Light Research Institute (Public Organization), Muang, Nakhon Ratchasima, 30000, Thailand, for XAS measurements in Beamline 5.2. and its scientist Dr. Pinit and Dr. Suchinda, who helped in the successful usage of the beamline. I am most grateful to Professor Frank de Groot of Utrecht University for providing critical XAS analysis. I was fortunate to have support and guidance from amazing seniors and peers in the lab, including Dr. William, Dr. Rohit, Dr. Eldho, Dr. Rodney, Dr. Cai and Mr. Verma, who have indirectly contributed significantly to this thesis. I would also like to thank NTU Materials Science and Engineering and FACTS staff for their endless support and a pleasant learning journey together.

Finally, I would like to thank my friends and family who helped keep my morale high and pursue my goal even in challenging situations.

Table of Contents

Table Captions

Figure Captions

$Al(NO_3)_3$ electrolyte, based on TEM-EDX analyses (A–C; discharged to a particular depth-of-discharge) and (D-F; charged to a particular state-of-charge after a particular depth-of-discharge) and b) TEM EDX elemental mapping of CuFe–PBA for sample C in Fig 2.3(a). Reproduced with permission.[14]Copyright 2014, John Wiley and Sons. c) CV showing the reversible insertion mechanism of a variety of trivalent-ions in CuHCF in 1 M conc. of the respective nitrate based electrolytes at pH value 2. Reproduced with permission.[15]Copyright 2015, John Wiley and Sons. d) Cycling life of FF-PBA cathode in different electrolytes Al-WISE, 0.5 M $Al_2(SO_4)_3$, and 0.5 m $Al(OTF)_3$), e) Experiment with cathode dissolution. From left to right, the electrolytes Al-WISE, cycling stability, even though, authors claim the 1 M $Al(NO_3)_3$, and 0.5 M $Al_2(SO_4)_3$ are seen. The photos on top were taken before cycling, and the photos on the bottom were taken after 50 cycles. Functional electrode (WE): FFPBA, counter electrode: AC, and reference electrode: Ag/AgCl) were used in all electrochemical measurements. The voltage range is from 0.7 to 1.3 V vs Ag/AgCl) and the current density is 150 mA/g. Reproduced with permission [17] Copyright © 2019, American Chemical Society.

Figure 2.5 a) Specific capacity with cycle number at various current densities for Xero-V_2O_5 in 1 M $AlCl_3$ aqueous electrolyte, b) Ex-situ XRD patterns of cycled and pristine V_2O_5 at various states of charging/discharging at slow current-density. The peak at 26.4° belongs to graphite substrate of the electrode. Reproduced with permission.[23]Copyright 2016, RSC. c) Working-principle schematic of aqueous Al ion battery based on intercalation electrode using $VOPO_4$ as cathode and MoO_3 as anode, d) Long-term cycling performance 1 A g^{-1} and the corresponding coulombic efficiency for cell configuration c using Gelatin-PAM electrolyte. Reproduced with permission[25] Copyright 2019 Elsevier B.V. e) Digital photographs of cycled electrodes along with galvanostatic discharge/charge curves of aqueous Al electrochemical cells using V_2O_5 cathodes at 20mA/g. Reproduced with permission [26] Copyright © 2020,

John Wiley and Sons.

Figure 2.6 a) CV profiles of graphite in different electrolytes at scan rate of 1 mV s^{-1}. Reproduced/Adapted with permission.[27] Copyright 2016, ACS, b) Cyclic voltammograms at 0.1 mVs^{-1} between 0.2 and 1.0 V, c) Cycling stability performance at a current density of 50 mAg^{-1}, d) XPS analysis of N 1s regions for as-prepared, discharged and recharged electrodes. Reproduced with permission [28] Copyright 2020 Wiley-VCH GmbH. e) cycling performance for anthraquinone, f) Reaction mechanism between AQ and Al-ion assisted by protons. Reproduced with permission [22] Copyright © 2021, American Chemical Society.

Figure 2.7 a) The crystal structure of anatase TiO_2 (blue spheres: Ti, red spheres: O). b) SEM image of as-prepared anatase TiO_2 nanotube arrays, and c) cyclic voltammograms (CVs) of the as-prepared anatase TiO_2 nanotube arrays in 1 M $AlCl_3$, $MgCl_2$ and LiCl aqueous electrolytes, run at 20 mV s^{-1}. Reproduced with permission.[3] Copyright 2012, RSC.

Figure 2.8 a) Respective CVs for a) a graphene-TiO_2 composite and b) TiO_2, in 1 M $AlCl_3$ electrolyte at a scan rate of 5 mV s^{-1}. Reproduced with permission.[32] Copyright 2017, ACS. c) Ex situ XRD patterns of graphene-TiO_2 nanoparticle electrodes after the 1st & 5th negative-direction (-0.4V to -1.5V vs Ag/AgCl) and positive-direction CV scans at 5 mV s^{-1}, in 0.5 M $AlCl_3$ electrolyte (A represents reflections for the anatase TiO_2 phase). Reproduced with permission.[36] Copyright 2018, Springer-Verlag GmbH Germany. d) Typical CVs of as-prepared anatase TiO_2 nanotube arrays at 10 mV s^{-1} in electrolytes of 0.25 M $Al_2(SO_4)_3$ mixed with varying concentrations of NaCl. Reproduced with permission.[34] Copyright 2014, Elsevier Ltd. e) TiO_2 faradic resistance (RF) as a function of polarization time in chloride-based & sulfate-based electrolytes at various pH. Reproduced with permission.[35] Copyright 2016, Elsevier Ltd.

Figure 2.9 a) Comparative EIS study of symmetric Al batteries using various Al anodes and electrolyte combinations, b) Al plating/stripping in symmetric cells of Al and TAl (ionic liquid treated Al) at 0.2 mA cm^{-2} with each

cycle containing charge and discharge cycles of 1 hr. Reproduced from [8] Copyright 2018 Qing Zhao and AAAS, c) Plating stripping tests in symmetric cell of Zn substrate in 2 M $Al(OTF)_3$ and 2 M $Zn(OTF)_2$ at 0.2 mA cm^{-2}. Each cycle containing charge and discharge cycles of 0.5 hr. Inset - the magnification of selected periods, d) Comparative EIS study of symmetric cells using various anode-electrolyte combinations. e) schematic showing suppression process of dendrite formation leading to a uniform deposition. Reproduced from [10] Copyright 2020 American chemical society.

Figure 2.10 a) The electrochemical stability window of electrolytes Al-WISE, 1 M $Al(NO_3)_3$, and 0.5 M $Al_2(SO_4)_3$) done by linear sweep voltammetry at 10 mV/s, b) Free anion (FA), Loose ion pair (LIP), and Intimate ion pair (IIP) fit to Raman spectrum of 1, 3, and 5 m $Al(OTF)_3$ solution, c) solvation structure schematic. Reproduced from [17] Copyright 2019 American Chemical Society, d) Cycling performance of G-MoO_3 in different volume ratios of diglyme and water. Reproduced from [42] Copyright © 2019, Springer-Verlag GmbH Germany, Pourbaix diagram of e) manganese and f) vanadium in water. Reproduced with permission.[43] Copyright 2018, RSC.

Figure 2.11 a) Volcanic curve for different metal surface showing exchange currents for H_2 evolution with metal-H bond strength for various elements. Adapted with permission.[49]Copyright 1972, Elsevier B.V. b) Stability of $LiMn_2O_4$ electrodes in terms of specific capacity vs cycle number when fabricated on various current collectors and corresponding c) Photograph of the non-treated Al foil current collector after 15 cycles and Chromate Conversion Coated (CCC) Al foil after 50 cycles in 2.5 M Li_2SO_4 electrolyte (pH = 7). Reproduced with permission.[48]Copyright 2015, RSC.

Figure 2-12: a) Ragone plot of various ZIAB and AIAB electrodes[9]

Figure 3.1 a) Density-temperature plots of water with variable temperature, b) pressure-temperature correlation for water with variable filling factor of

the progression of cycling, the spectrum for all of the abovementioned species remain more or less the same. The binding energy of chemical species does not change as the cycling continues. Though there are modest quantitative shifts, there is no consistent pattern in the progression of cycling. As a result, the chemical composition of the TAl cycled surface does not change with repetitive cycling.

Figure 6.18 Cl 2p area spectra for TAl foil retrieved from a TAl | 2 m AlTFS | TAl cell after (a) 12 hours of soaking/rest, (b) 5, (c) 10, and (d) 20 cycles. XPS signals from two separate spots were obtained for each study. The existence of Cl on the TAl cycled is found to be quite random. And when Cl is found, it does not have a strong presence. This leads one to believe that Cl from the surface of TAl may leach out partially during cycling, but there is no strong pattern to suggest that more Cl dissolves in the electrolyte with longer cycling or that the dissolution of AlCl3 in the electrolyte improves efficiency.

Figure 7.1 Nyquist plot for (a) Al, (c) UTAl and (d) ETAl symmetric cells showing experimental and fitted spectra collected 5 hours after cell fabrication and after 30^{th} stripping cycle. (b) Schematic representing Al metal-barrier layer-electrolyte interface along with the equivalent circuit used to fit the EIS spectra collected for such systems.

Figure 7.2 Comparative stripping/plating test in symmetric coin cell for (a) Al and UTAl at 0.1 mA cm^{-2}, (b) Al and ETAl at 0.1 mA cm^{-2}, (c) ETAl and UTAl at 0.1 mA cm^{-2} and (d) ETAl and UTAl at 0.2 mA cm^{-2}.

Figure 7.3 (a) Stripping/plating testing in symmetric UTAl coin cell for various concentrations of AlTFS aqueous electrolyte (0.1 m, 1 m, 2 m, 3 m, 5 m) done at 0.1 mA cm^{-2} (b) Stripping/plating testing in symmetric UTAl cells using Al coated with the eutectic mix $AlCl_3$+Urea in three different ratios - 1.3: 1, 1.6:1 and 2:1, (b) Stripping/plating testing in symmetric UTAl cell at various rates including 0.2 mA cm^{-2}, 0.1 mA cm^{-2}, 0.05 mA cm^{-2}, (d) Stripping/plating testing in symmetric UTAl cell for coin cell and flooded beaker cell at 0.1 mA cm^{-2}, (e) Comparative stripping/plating test in

symmetric flooded beaker cell for Al and UTAl. Negative and positive current density of 0.1 mA cm^{-2} was applied for 1 hour each in an alternating sequence.

Figure 7.4 (a) SEM-EDX elemental mappings for Al, Cl and N on pristine UTAl surface, (b) SEM-EDX line scan for Al, Cl, N and C through the pristine UTAl cross section. FTIR spectra obtained for (c) as received Al, UTAl, air-exposed UTAl, (d) 2 m AlTFS, cycled UTAl (1S, 1P, 15S and 15P) after salvaging them from cycled symmetric cells (using 2 m AlTFS as electrolyte; cycled at 0.1 mA cm^{-2}), (e) Raman spectra for 2 m AlTFS, electrolyte obtained from flooded beaker cells post-plating/stripping (0.1 mA cm^{-2}) in the symmetric cells of Al and UTAl separately.

Figure 7.5 Al 2p region of XPS spectra (with deconvoluted peaks) for the surface, 1^{st} etched and 9^{th} etched layers of (a) Al foil as-received from supplier, (b) UTAl foil transferred from glovebox, (c) UTAl exposed to air for 48 hours, (d) UTAl foil subjected to one round of stripping in a symmetric cell (with 2m AlTFS as the electrolyte; cycled at 0.1 mA cm^{-2}). XPS data was first collected from the surface (labelled "surface"), followed by 5 rounds of etching (30 s Ar^+ sputtering) and subsequent data collection; which was followed by 4 more rounds of etching (60 s Ar^+ sputtering) and subsequent data collection.

Figure 7.6 (a) Al 2p region of XPS spectra (with deconvoluted peaks) for the surface, 1^{st} etched, and 9^{th} etched layers of UTAl salvaged after (a) 1^{st} plating, (b) 15^{th} stripping, (c) 15^{th} plating. XPS data was first collected from the surface, followed by 5 rounds of etching (30 s Ar^+ sputtering) and subsequent data collection; which was followed by 4 rounds of etching (60 s Ar^+ sputtering) and subsequent data collection.

Figure 7.7 **(**a) Cl 2p region of XPS spectrum for UTAl surface showing the presence of Cl, (b) F1s region of XPS spectrum from surface of Al stripped for one cycle (1S) showing the presence of metallic fluoride. (c) F1s region of XPS spectrum for 1S 1^{st} layer after etching, showing the presence of organic fluoride (low energy), (d) C1s region of XPS spectrum for UTAl

Abbreviations

AC	Activated Carbon
AIAB	Aluminum-ion aqueous Battery
AlTFS	Aluminum Trifluoromethanesulfonate
BESS	Battery Energy Storage Systems
BSE	Backscattered Electron
CV	Cyclic Voltammetry
DI	Deionised
EDX	Energy Dispersive X-ray
EIS	Electrochemical Impedance Spectroscopy
ETAl	$Et_3NHCl + AlCl_3$ (1:1.5) coated Al
EXAFS	Extended X-ray absorption fine structure
FeHCF	$Fe(Fe_{0.97}(CN)_6)_{0.88}(H_2O)_{0.473}$
FTIR	Fourier Transform Infrared
FTIR-ATR	Fourier Transform Infrared -Attenuated Total Reflectance
GCD	Galvanostatic Charge Discharge
HCF	Hexacyanoferrate
HRTEM	High Resolution Transmission Electron Microscopy
NMHCF	$Na_{1.68}Mn[Fe(CN)_6].1.7H_2O$
UTAl	Urea + $AlCl_3$ (1:1.3) coated Al
PBA	Prussian Blue Analog
SCE	Standard calomel electrode
SE	Secondary Electron
SEM	Scanning Electron Microscopy
SEI	Solid Electrolyte Interphase
SLRI	Synchrotron Light Research Institute
TAl	Ionic liquid + $AlCl_3$ treated Al
TEM	Transmission Electron Microscopy
VO_2-B	Bronze-type Vanadium Oxide
XAS	X-ray absorption spectroscopy

XANES	X-ray Absorption Near-Edge Structure
XRD	X-ray Diffraction
XPS	X-ray Photon Spectroscopy

Chapter 1

Introduction

This chapter introduces the background and significance of using non-lithium battery chemistry to enable battery energy storage systems for renewable energy harvesting. In this regard, the economic and environmental sustainability advantages of using aluminum chemistry have been discussed, along with the possible challenges that can be faced to develop such an electrochemical system. These challenges are further stated in the form of problem statements and lead to defining the thesis's objective and scope. Additionally, a brief overview of thesis chapters has is provided, and the major finding and outcomes are abridged.

1.1 Background and Significance

A rapidly expanding global economy coupled with an ever-increasing population is likely to surge our energy needs by more than 30% in the coming few years. [1] Considering this future demand, there is a paradigm shift towards using alternative and cleaner energy resources, including wind, solar and tidal. [2] But at the same time, the intermittent and dispersed nature of the abovementioned energy resources makes them unreliable for on-demand electricity needs of the population and industry centres. This means oversupplied energy during the off-peak hours and vice versa. This problem is statistically expressed in the form of a "duck curve" showing a mismatch in energy supplied vs energy demand throughout the day for a solar-powered community (Figure 1-1). [3] This is wherein stationary electrochemical storage units or battery energy storage systems (BESS) come in. These energy storage units can harvest intermittent energy and release it as per the consumption pattern, essentially facilitating load-levelling and peak-shaving.[4-8] Pondering infrastructural perspective, modular BESS can be connected to individual small battery units in residential and commercial buildings or at the main power station with megawatts of power capacity. Considering potentially large-scaled BESSs, sustainability and safety become the main criteria to produce battery materials, besides high power/energy density (145 Wh kg^{-1} at device scale)[1], long cycling life (2000 cycles at device scale) and low investment costs ((0.17 USD/usable kWh). [9-10]

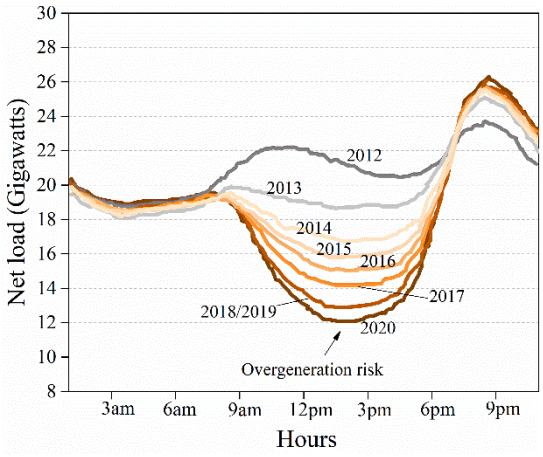

Figure 1-1: Typical duck chart showing the imbalances in peak demand and renewable energy production over the course of a day: Each line represents the hourly evolution of net load

(average load minus wind and photovoltaics generation) as sampled on every March 31st of consecutive years. With the yearly increase in PV installations, the spikes in energy production between ~1-2 pm grow much more significantly than energy demand (as shown by the dip in the curves). This represents excess energy, and a high risk of overgeneration during afternoons whereas the opposite scenario is expected during late evenings. Data sourced from ref.[3, 11]

For large-scale BESS, a water-based electrolyte is advantageous from an economic, safety, and sustainability perspective. This is because 1) using aqueous electrolyte means possible fabrication in ambient, essentially getting rid of the stringent fabrication process including the requirement for inert atmosphere, 2) water is cheap, 3) water, unlike their organic solvent, is non-flammable and non-volatile, essentially reducing the incendiary risks arising with battery short-circuiting failures.[12] Overall, using water as an electrolyte solvent implies better safety prospects and cost-efficiency.

Among several possible battery chemistries, the idea of using cheaper and more abundant elements like Na, K, Mg, Ca, Zn and Al has also been gaining popularity recently.[11, 13-14] Using these elements as anode not only satisfies the sustainability criteria for BESS but also tackles the severe supply risk of lithium arising from its uneven geo-distribution. Hence a battery system with a host material reversibly accommodating one of the abovementioned migrating metal-ion or its complexes while using an aqueous electrolyte fits the criteria for BESS very well.

1.2 Problem Statement

Among the several abovementioned chemistries, Al as an anode is particularly advantageous (Figure 1-2) [13, 15-28] because of its 1) highest volumetric capacity (~8000 mAh cm^{-3}), 2) high abundance in the earth's crust and 3) possible cheap costing provided by an already mature Al industry; thus opening up the possibilities for sustainable and affordable batteries for everyone.[11, 29-30] However rechargeable aluminum ion aqueous battery (AIAB) research is still in infancy and poses significant challenges in all three fronts of the cathode, anode and electrolyte which majorly are as follow. Firstly, very few

cathode materials have been explored for AIAB so far and most suffer from various problems such as low voltage [31-36], poor capacity[37-43], rapid cycling decay[44-47], and predominant capacitive reaction[48-49]. High charge density of Al^{3+} also adds more challenges as it limits the solid-state diffusivity in cathodes, often causing doubts over the feasibility of Al^{3+} insertion in the host structures. Secondly, Al metal used as anode offer very high plating/stripping overpotential because of readily forming Al-oxide layer on Al. This renders surface chemistry inert and requires high voltages for plating/stripping, causing unwarranted electrolyte degradation. Thirdly at electrolyte front 1) small (1.23 V) electrochemical window of aqueous electrolyte often causes electrolyte decomposition and gas evolution, essentially limiting the voltage of the cell and 2) highly acidic nature of electrolyte causes extreme corrosion of auxiliary parts of the cell. Though these encounters could have been dealt with one by one, their interdependence makes the problem more challenging. It becomes imperative to engineer cells so that the three components mentioned above work in tandem without countering the other.

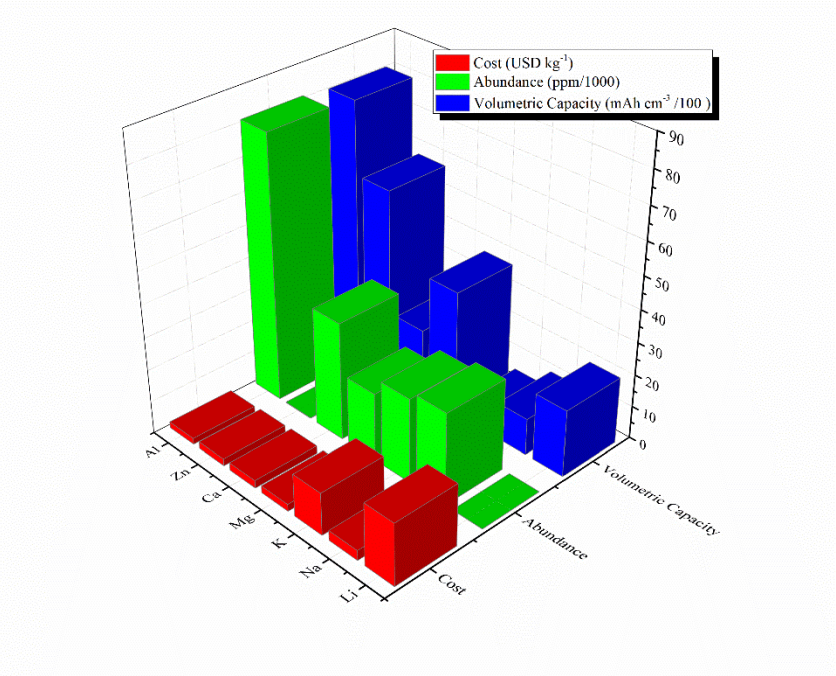

Figure 1-2: Comparison of volumetric charge capacities, costs and natural abundance for different metal anodes.[29, 50-51]

The problem statement will take the general form:

> "*This thesis describes and validates the feasibility of aluminum-ion aqueous electrochemical systems with engineered cathode and anode made to work in tandem in an optimized aqueous electrolyte to deliver high capacity and good cycling stability leading to the realization of a super cheap and environmentally friendly energy storage device potentially to be used in large scale applications such as electricity grid.*"

1.3 Objectives and Scope

The primary objective of this thesis is to investigate and study the feasibility of AIAB and eventually provide a proof of concept by demonstrating a working AIAB cell with high capacity and good cycling life of 300 Wh/kg and 1000 cycles, respectively. This aim is achieved by engineering cathode and anode for AIAB and optimizing electrolyte to enhance cell performance. Hence the scope of this thesis includes 1) synthesizing new cathode materials and testing them for reversible insertion of Al-ion/Al-ion complex in a Al-salt based aqueous electrolyte, 2) engineering Al metal anode surface to reduce the anodic plating/stripping overpotential in a Al-salt based aqueous electrolyte, 3) using in-lab and synchrotron characterization techniques exhaustively to study Al-ion/Al-ion complex insertion in host cathode and evolution of the Al-metal anode surface chemistry under various conditions, 4) optimizing the electrolyte's basic properties like concentration and pH to enhance cell performance and 5) demonstrate a full working AIAB cell.

1.4 Dissertation Overview

The thesis addresses the fundamental question of the scientific viability of AIAB and its implications for advancement in the field of multivalent battery research and development.

Chapter 1 introduces the background and significance of developing non-lithium aqueous

batteries and later explores the advantages of AIAB over other battery chemistries. Likely challenges and encounters concomitant to AIAB development are laid out. Furthermore, the objectives, including the scope of the thesis, are presented, and finally, an overview of the thesis is provided.

Chapter 2 reviews the literature concerning various aspects of AIAB and identifies the gaps in the research field that shaped the objectives of the thesis. The chapter includes both the historical and contemporary literature pertaining to rechargeable AIAB. To start with, AIAB is defined and some examples of working mechanism of AIAB are discussed. Further, a discussion on various cathodic materials tried and tested for AIAB follows. Important contemporary developments on the anodic side are highlighted, followed by a brief discussion on electrolyte.

Chapter 3 discusses the principles underlying the synthesis methodology adopted and the characterization techniques employed in this study. The discussion is made from both material and device standpoint, as appropriate, with an additional effort to justify the suitability of the technique. Furthermore, the fabrication protocol for AIAB has been detailed, including a discussion on the choice of auxiliary components of cells.

Chapter 4 investigates $FeVO_4$ as a potential cathode material for reversible Al-ion/Al-ion complex insertion. This study primarily explores the possibility of a conversion type material to accommodate a highly polarizing ion like Al^{3+}. The electrochemical performance of $FeVO_4$ has been studied, and the insertion mechanism has been explored in detail using electrochemical and material characterization techniques. Finally, the cycling life of the cell has been enhanced by modulating pH and concentration of the electrolyte.

Chapter 5 investigates VO_2 nanobelts potentially as a high performing cathode material for reversible Al-ion/Al-ion complex insertion. The prime idea herein is to exploit the unique shear structure and the 2D morphology of VO_2 to gain an enhanced performance in terms of capacity and cycling stability. Further, a combination of ex-situ

characterization techniques has been employed to reveal the reaction storage mechanism underlying superior performance.

Chapter 6 primarily investigates the role of ionic liquid+$AlCl_3$ anodic coating treatments in influencing the full-cell battery performance. For this purpose, a stable cathode material, showing successful Al-ion insertion, has been tested against treated Al metal anode. Further, the stability and compatibility of the coating layer in the ambient environment and during cell operation has also been studied in detail.

Chapter 7 focuses on engineering an artificial interfacial layer on an Al metal anode to improve the anodic interfacial ion transfer conductance and kinetics. Two different combinations of eutectic mixtures, including urea+$AlCl_3$ and triethylamine hydrochloride+$AlCl_3$, have been explored as potential coating treatments for Al-metal anodes. Further, modified interfacial anode surface is studied in detail for its potential application in aqueous electrochemical cells, using electrochemical and spectroscopy characterization techniques.

Chapter 8 concludes the overall study and summarizes the significant findings of the thesis. Further, a commentary has also been made on the possible opportunities and strategies that can be adopted in future in this research field.

1.5 Findings and Outcomes

The novelties of this study could be identified as follows:

1. Contributed the first conversion type material in the AIAB field. The study sets the precedent of using conversion cathode chemistry for Al-ion insertion in an aqueous electrolyte by successfully showing reversible intake of Al-ion. The study also supports the feasibility of AIAB chemistry.
2. A deterministic effect of electrolyte pH was shown on the cycling stability of the cathode material in an AIAB system. The study showed that in a less acidic electrolyte, the cathode material experiences suppressed side reactions and hence

longer cycling stability can be obtained.

3. Contributed VO_2 as a highly stable cathode material for AIAB, enabled by its unique shearing structure. This study showed a stable cycling performance for 1000 cycles of charge/discharge and elucidated Al-ion and H^+ co-intercalation mechanism.
4. Revealed the implications of using an ionic liquid + $AlCl_3$ coated Al in a full-cell. The study conclusively showed that the traditional knowledge that maximum concentrated electrolyte will lead to the most stable cycling performance does not necessarily translate when using a coated form of Al as an anode in the AIAB system.
5. Revealed that an ionic liquid + $AlCl_3$ coated Al is protected from oxidation in an ambient environment for at least 40 hours and forms an in-situ SEI like layer during cell operations.
6. Contributed urea+$AlCl_3$ and triethylamine hydrochloride+$AlCl_3$ as eutectic formulations that can be used to engineer artificial protective coating on Al. These coatings improve the interfacial conductance and kinetics at the anode/electrolyte interface, essentially enabling the usage of Al in an aqueous system.
7. Revealed urea+$AlCl_3$ coating to be stable in ambient for at least 48 hours and its role in forming in-situ type layer during battery cycling.

References

[1] L. Cozzi, T. Gould World Energy Outlook, 2017, International energy Agency. https://www.iea.org/weo2017/ (accessed July).

[2] China Is Adding Solar Power at a Record Pace. https://www.bloomberg.com/technology (accessed 25 Feb).

[3] P. Denholm, O'Connell, Matthew, Brinkman, Gregory, Jorgenson, Jennie Overgeneration from Solar Energy in California, A Field Guide to the Duck Chart. https://www.osti.gov/servlets/purl/1226167 (accessed July).

[4] K. C. Divya, J. Østergaard. *Electr. Power Syst. Res.* **2009,** *79*, 511-520.

[5] C. A. Hill, M. C. Such, D. Chen, J. Gonzalez, W. M. Grady. *IEEE Trans. Smart Grid.* **2012,** *3*, 850-857.

[6] J. B. Goodenough, H. D. Abruna, M. V. Buchanan Basic Research Needs for Electrical Energy Storage. Report of the Basic Energy Sciences Workshop on Electrical Energy Storage, April 2-4, 2007. https://science.energy.gov/~/media/bes/pdf/reports/files/ees_rpt_print.pdf (accessed July).

[7] E. E. Jessica Intrator, Andris Abele, Steven Weissman, Morgan Sawchuk, and Emily Bartlett 2020 Strategic Analysis of Energy Storage in California. http://www.energy.ca.gov/2011publications/CEC-500-2011-047/CEC-500-2011-047.pdf (accessed July).

[8] N.-K. C. Nair, N. Garimella. *ENERG. BUILDINGS.* **2010,** *42*, 2124-2130.

[9] H. Kim, J. Hong, K.-Y. Park, H. Kim, S.-W. Kim, K. Kang. *Chem. Rev.* **2014,** *114*, 11788-11827.

[10] J. O. G. Posada, A. J. R. Rennie, S. P. Villar, V. L. Martins, J. Marinaccio, A. Barnes, C. F. Glover, D. A. Worsley, P. J. Hall. *Renew. Sus. Energ. Rev.* **2017,** *68*, 1174-1182.

[11] V. Verma, S. Kumar, W. Manalastas Jr, R. Satish, M. Srinivasan. *Adv. Sustainable Syst.* **2019,** *3*, 1800111.

[12] E. P. Roth, C. J. Orendorff. *Electrochem. Soc. Interface.* **2012,** *21*, 45-49.

[13] R. Demir-Cakan, M. R. Palacin, L. Croguennec. *J. Mater. Chem. A.* **2019,** *7*, 20519-20539.

[14] Z. Liu, Y. Huang, Y. Huang, Q. Yang, X. Li, Z. Huang, C. Zhi. *Chem. Soc. Rev.* **2020**.

[15] A. Sonoc, J. Jeswiet. *Procedia CIRP*. **2014,** *15*, 289-293.

[16] C. Helbig, A. M. Bradshaw, L. Wietschel, A. Thorenz, A. Tuma. *J. Cleaner Prod.* **2018,** *172*, 274-286.

[17] K. R. Guduru, C. J. Icaza. *Nanomaterials.* **2016,** *6*, 1-19.

[18] T. Liu, X. Cheng, H. Yu, H. Zhu, N. Peng, R. Zheng, J. Zhang, M. Shui, Y. Cui, J. Shu. *Energy Storage Materials.* **2018**, 68-91.

[19] Z. Xing, S. Wang, A. Yu, Z. Chen. *Nano Energy.* **2018,** *50*, 229-244.

[20] S. Boyd, V. Augustyn. *Inorg. Chem. Front.* **2018,** *5*, 999-1015.

[21] D. Bin, F. Wang, G. Tamirat Andebet, L. Suo, Y. Wang, C. Wang, Y. Xia. *Adv. Energy Mater.* **2018,** *8*, 1703008.

[22] P. Canepa, G. Sai Gautam, D. C. Hannah, R. Malik, M. Liu, K. G. Gallagher, K. A. Persson, G. Ceder. *Chem. Rev.* **2017,** *117*, 4287-4341.

[23] J. Zhao, H. Ren, Q. Liang, D. Yuan, S. Xi, C. Wu, W. Manalastas, J. Ma, W. Fang, Y. Zheng, C.-F. Du, M. Srinivasan, Q. Yan. *Nano Energy.* **2019,** *62*, 94-102.

[24] D. Yuan, W. Manalastas Jr, L. Zhang, J. J. Chan, S. Meng, Y. Chen, M. Srinivasan. *ChemSusChem.* **2019,** *12*, 4889-4900.

[25] V. Verma, S. Kumar, W. Manalastas, Jr., J. Zhao, R. Chua, S. Meng, P. Kidkhunthod, M. Srinivasan. *ACS Applied Energy Materials.* **2019**, 8667-8674.

[26] H. Ren, J. Zhao, L. Yang, Q. Liang, S. Madhavi, Q. Yan. *Nano Research.* **2019,** *12*, 1347-1353.

[27] R. Chua, Y. Cai, Z. K. Kou, R. Satish, H. Ren, J. J. Chan, L. Zhang, S. A. Morris, J. Bai, M. Srinivasan. *Chem. Eng. J.* **2019,** *370*, 742-748.

[28] S. Kumar, V. Verma, R. Chua, H. Ren, P. Kidkhunthod, C. Rojviriya, S. Sattayaporn, F. M. F. de Groot, W. Manalastas Jr, M. Srinivasan. *Batteries & Supercaps.* **2020,** *n/a*.

[29] S. K. Das, S. Mahapatra, H. Lahan. *J. Mater. Chem. A.* **2017,** *5*, 6347-6367.

[30] D. Yuan, J. Zhao, W. Manalastas, S. Kumar, M. Srinivasan. *Nano Materials Science.* **2019**, 248-263.

[31] S. Liu, J. J. Hu, N. F. Yan, G. L. Pan, G. R. Li, X. P. Gao. *Energy Environ. Sci.* **2012,** *5*, 9743-9746.

[32] Y. Liu, S. Sang, Q. Wu, Z. Lu, K. Liu, H. Liu. *Electrochim. Acta.* **2014,** *143*, 340-346.

[33] M. Kazazi, P. Abdollahi, M. Mirzaei-Moghadam. *Solid State Ionics.* **2017,** *300*, 32-37.

[34] M. Kazazi, Z. A. Zafar, M. Delshad, J. Cervenka, C. Chen. *Solid State Ionics.* **2018,** *320*, 64-69.

[35] M. R. Lukatskaya, O. Mashtalir, C. E. Ren, Y. Dall'Agnese, P. Rozier, P. L. Taberna, M. Naguib, P. Simon, M. W. Barsoum, Y. Gogotsi. *Science.* **2013,** *341*, 1502.

[36] H. Lahan, S. K. Das. *Dalton Transactions.* **2019,** *48*, 6337-6340.

[37] Z. Li, K. Xiang, W. Xing, W. C. Carter, Y. M. Chiang. *Adv. Energy Mater.* **2014,** *5*, 1401410.

[38] S. Liu, G. L. Pan, G. R. Li, X. P. Gao. *J. Mater. Chem. A.* **2015,** *3*, 959-962.

[39] R. Y. Wang, B. Shyam, K. H. Stone, J. N. Weker, M. Pasta, H.-W. Lee, M. F. Toney, Y. Cui. *Adv. Energy Mater.* **2015,** *5*, 1401869.

[40] Y. Ru, S. Zheng, H. Xue, H. Pang. *Chem. Eng. J.* **2019**, 122853.

[41] P. Wang, Z. Chen, Z. Ji, Y. Feng, J. Wang, J. Liu, M. Hu, H. Wang, W. Gan, Y. Huang. *Chem. Eng. J.* **2019,** *373*, 580-586.

[42] Y. Gao, H. Yang, X. Wang, Y. Bai, N. Zhu, S. Guo, L. Suo, H. Li, H. Xu, C. Wu. *ChemSusChem.* **2020,** *13*, 732-740.

[43] J. Joseph, J. Nerkar, C. Tang, A. Du, A. P. O'Mullane, K. Ostrikov. *ChemSusChem.* **2019,** *12*, 3753-3760.

[44] Z. Hu, Y. Guo, H. Jin, H. Ji, L.-j. Wan. *Chem. Commun.* **2020,** *56*, 2023-2026.

[45] F. Nacimiento, M. Cabello, R. Alcántara, P. Lavela, J. L. Tirado. *Electrochim. Acta.* **2018,** *260*, 798-804.

[46] J. R. Gonzalez, F. Nacimiento, M. Cabello, R. Alcantara, P. Lavela, J. L. Tirado. *RSC Adv.* **2016,** *6*, 62157-62164.

[47] S. Kumar, R. Satish, V. Verma, H. Ren, P. Kidkhunthod, W. Manalastas, M. Srinivasan. *J. Power Sources.* **2019,** *426*, 151-161.

[48] S. Sun, C. Tang, Y. Jiang, D. Wang, X. Chang, Y. Lei, N. Wang, Y. Zhu. *Sol. Energy Mater. Sol. Cells.* **2020,** *207*, 110332.

[49] J. Joseph, A. P. O'Mullane, K. Ostrikov. *ChemElectroChem.* **2019,** *n/a*.

[50] W. M. Haynes, D. R. Lide, T. J. Bruno. *CRC handbook of chemistry and physics : a ready-reference book of chemical and physical data*, CRC Press: Boca Raton, Florida, 2016.

[51] M. Fleischer *Recent estimates of the abundances of the elements in the earth's crust*; 285; 1953.

Chapter 2*

Literature Review

This chapter starts with defining the AIAB in the context of this thesis, followed by few proposed working mechanisms for AIAB. A detailed literature review is done on cathodes materials tested for AIAB, including inorganics and organics. A literature review on anode and electrolyte has also been done, which is primarily contemporary to the duration of this thesis. Further, the significance of using the suitable auxiliary component, including the current collector, is also discussed. Overall, this chapter helps discover the research gaps in the AIAB field and asks some outstanding questions and puts this thesis in the context of the developing research.

This section published substantially as Verma V, Kumar S*, Manalastas Jr W, Satish R, Srinivasan M. Progress in Rechargeable Aqueous Zinc- and Aluminum-Ion Battery Electrodes: Challenges and Outlook. Adv Sustainable Syst. 2019;3(1):1800111. (No written permission from Wiley is necessary for thesis purpose).

2.1 Overview of Aqueous Rechargeable Aluminum-ion energy storage

Aluminum ion aqueous battery (AIAB) is a promising candidate for BESS because of sustainability and low-cost investment reasons.[1] Aluminum has garnered significant attention not only in the present but also in the past. The very first time Aluminum was reported in any battery system was as a positive electrode together with zinc.[2] This work was followed by a series of Al-based research. However, they can only be classified as primary batteries.[2] To the best of knowledge, the first work on aqueous secondary aluminum-ion battery was reported in 2012,[3] which also indicates how new this field is.

Currently, a clear definition for AIAB is missing, hence for the sake of clarity, AIAB in this thesis is defined as any energy storage system wherein a host material allows for reversible insertion of Al-ion or any of its complexes in an aqueous electrolyte. This will include both types of cells where metal Al is used as anode or not. Hence the minimum requirements for a cell to be termed as AIAB are Al-ions in the electrolyte, which can unidirectionally flow towards cathode during discharge and a host material allowing for its reversible accommodation. Though in the infancy stage, the most acceptable working mechanism of AIAB is analogous to the rocking-chair Li-ion battery. Typically, during discharging or when a load is connected, Al-ions extracted from anode moves towards cathodes through the electrolyte with the parallel movement of electrons in the outer circuit towards the cathode and vice-versa during charging (reaction below and Figure 2-1).[4-6]

Anode: $Al - 3e^- \overset{\leftarrow}{\rightarrow} Al^{3+}$

Cathode: $Al_xMnO_2.nH_2O + 3(y-x)e^- + (y-x)Al^{3+} \overset{\leftarrow}{\rightarrow} Al_yMnO_2 2.nH_2 0$

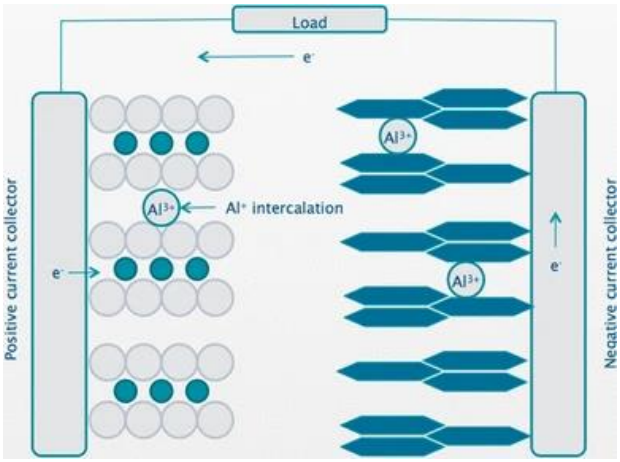

Figure 2-1: Working principle schematic of AIAB showing intercalation of Al-ion in host material during discharge. Reproduced from[4] Copyright 2018, A. Holland.

Some alternate mechanism for AIAB has also been proposed. These include: 1) dissolution of original Mn-based cathode materials to form Al-Mn complex in the electrolyte, followed by the reversible dissolution/deposition of $Mn^{2+}/Al_xMn_{(1-x)}O_2$ redox reaction and the stripping/plating of Al in the subsequent discharge/charge processes (Figure 2-2)[7] and 2) reaction of MnO cathode with the electrolyte to produce hydroxyl ion which then combines with Al-ions to from oxide.[8] See the following reaction:

Anode: $Al - 3e^- \overset{\leftarrow}{\rightarrow} Al^{3+}$

Cathode: $3H_2O \overset{\leftarrow}{\rightarrow} 3H^+ + 3OH^-$

$$xMnO_2 + 3e^- + 3H^+ \overset{\leftarrow}{\rightarrow} yMnO_{2-\frac{3}{2y}} + (x-y)MnO_2 + \frac{3}{2}H_2O$$

$$Al^{3+} + 3OH^- + e^- + z\,H_2O \overset{\leftarrow}{\rightarrow} Al(OH)_3e^-zH_2O$$

Despite some similarity with well-established electrochemical systems like lithium-ion batteries, AIAB brings its own challenges. These challenges come at all three fronts of

cathode, anode, and electrolyte[1]. The following sections critically review these three cell components while discussing concomitant existing problems and parallelly building up research gaps that will serve as the thesis problem statement. It is also to be noted that AIAB is a relatively new system. Most contents covered in the literature are contemporary research and have steered the research work in this thesis as and when they were reported.

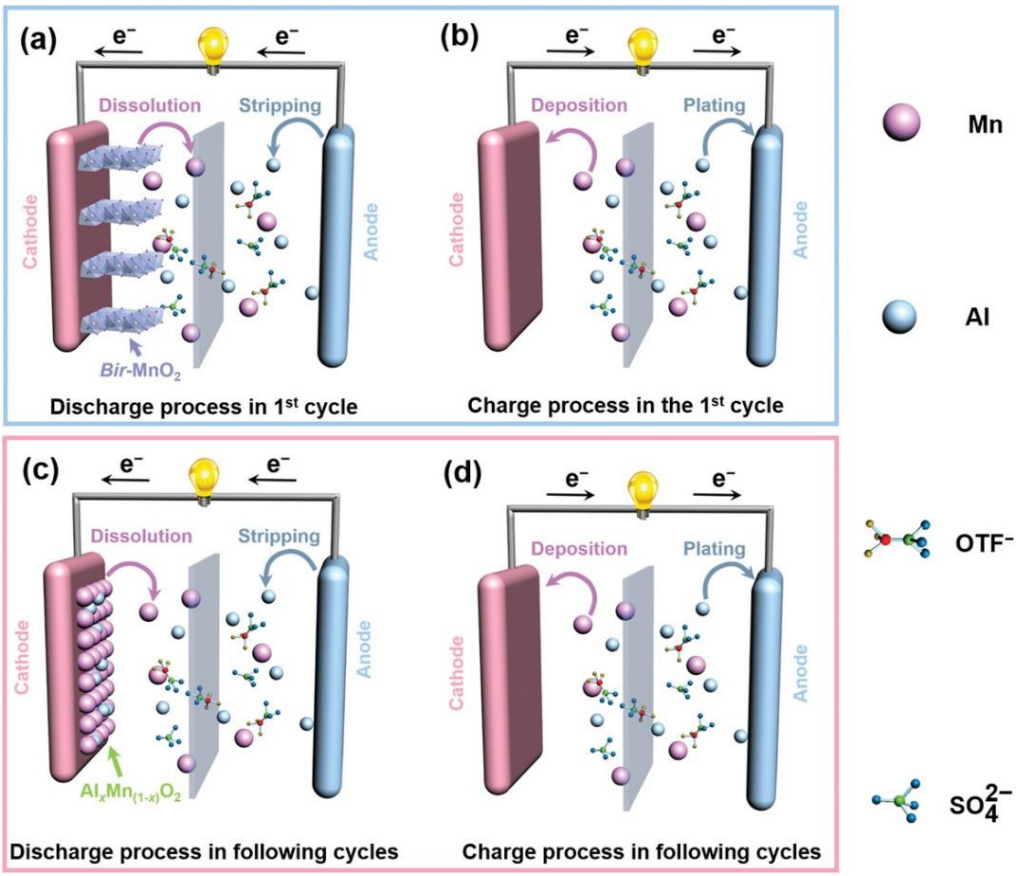

Figure 2-2: The schematic diagram of aluminum-manganese electrochemistry in a) the first discharge process, b) the first charge process, and c,d) the discharge process and charge process in following cycles. It is reproduced from [7] Copyright 2019, Wiley and Sons.

2.2 Cathodes for AIAB: Selection criteria and challenges

[1] Though electrolyte has been briefly covered in literature review, the scope of this thesis only includes selecting best electrolyte based on literature and optimizing its concentration and pH. Any further optimization/engineering is beyond the scope of this thesis.

2.2.1 MnO_2

MnO_2 has always been one of the most studied materials for any electrochemical system. This interest is because of 1) various possible oxidation states of Mn that can provide high voltages, 2) various polymorphs of MnO, which open up the possibilities of intercalation of all sorts of guest-ions, and 3) high capacity of MnO.[9] However, for AIAB, oxides of Mn has hardly been explored. This section discusses such studies, including the reasons behind lacking interest in MnOs for AIAB.

The first significant work on AIAB came in Nov. 2018, wherein α-MnO_2 was reported with a novel anode (discussed in the anode section).[8] A high capacity of 380 mAh/g was reported, though it decreased to 168 mAh/g in just 40 cycles. This rapid fading of cycling was attributed to the dissolution of Mn in the electrolyte. Following this, Chuan Wu et al. used an activated Mn_3O_4 for AlAB by introducing Al^{3+} and H_2O prior to testing.[6] Again, a high capacity of 520 mAh/g was reported. However, it decreased to 272 mAh/g in just 65 cycles Figure 2-3 a. Using a similar strategy of pre-insertion of Al, Chunshuang reported a high capacity of 650 mAh/g for Al_xMnO_2 paired with a Zn-Al alloy anode (discussed in anode section), which remains the highest capacity reported till date Figure 2-3 b.[10] The problem of dissolution was to some extent tackled by pre dissolving $MnSO_4$ in AlTFS electrolyte Figure 2-3 c.[7] This enabled plating/stripping of Al-Mn complex from the electrolyte (Figure 2-2), leading to improved stability. Though this strategy improves the cycling stability, it was not sufficiently suitable for very long cycling (Table 2-1).

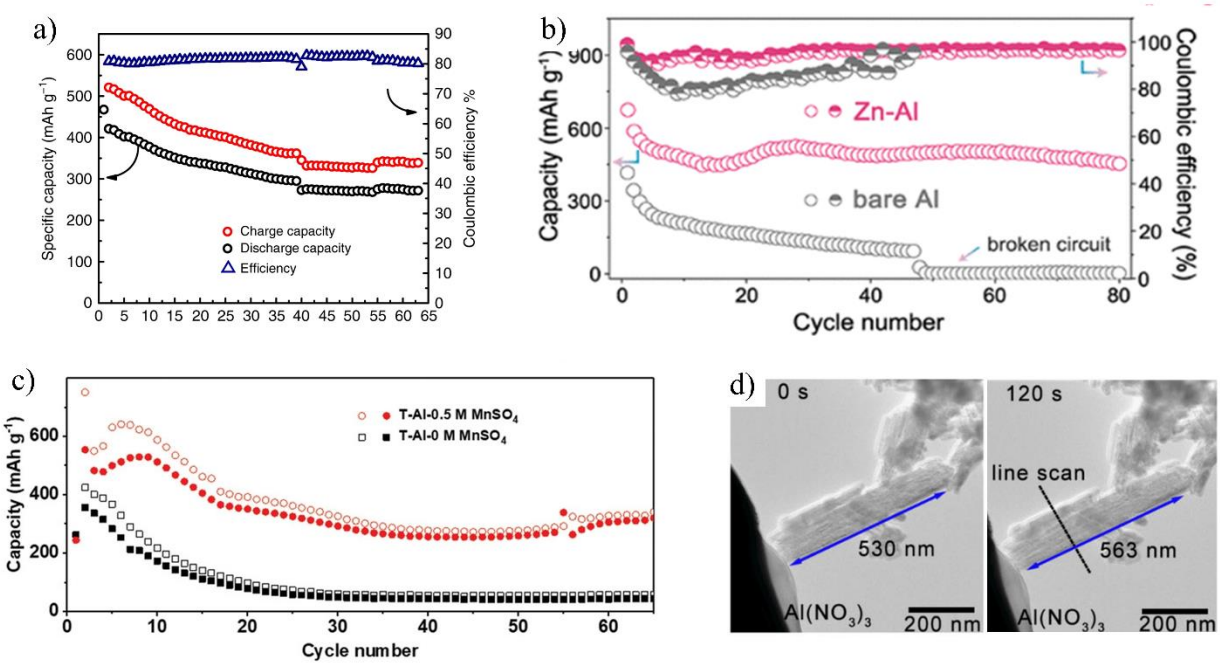

Figure 2-3: a) Efficiency and cycling ability of Al/Al(OTF)$_3$-H_2O/$Al_xMnO_2{\cdot}nH_2O$ rechargeable battery. Reproduced from [6] Copyright 2019, Chuan Wu, b) Cycling performance at a current density of 100 mA g^{-1} comparing metal/Al_xMnO_2 full cells using Al and treated Al anodes in 2 M Al(OTF)$_3$ electrolyte. Reproduced from [10] Copyright © 2020, American Chemical Society. c) Cycling performance of the T-Al/Bir-MnO_2 and T-Al/0.5Mn/Bir-MnO_2 batteries. Reproduced from [7] Copyright 2019, Wiley and Sons. d) TEM image acquired before applying a bias of -2 V and after 120 s. Reproduced from [11] copyright 2020, Wiley-VCH GmbH.

In another work, K-rich cryptomelane has been reported for AIAB.[12] Though a low initial capacity is observed, which fades to ~ 60 % in 60 cycles, the study is backed by simulation work claiming energy favourability for Al-ion to intercalate into MnO_2 to replace K. In another very interesting work, J. Joseph et al. have used in-situ TEM and DFT simulations to convincingly prove the insertion of Al-ion in Magnesium-doped Manjiroite (MnO_2).[11] Their in-situ TEM shows an increase in the length of nanoscale cathode material when the battery setup is negatively biased. A minor elongation of ~ 6.2 % has been reported without any significant changes in the cathode structure and morphology Figure 2-3 d. Additionally, the DFT study suggests lower formation energy of Al intercalated Mg-MnO_2 than Mg-rich MnO_2. Both in-situ and TEM strongly suggests

that Al-ion insertion in Mg-doped MnO_2 is very well possible. Simulation work by Alfaruqi et al. suggests multistage insertion of Al-ion in α-MnO_2.[13] This study also suggests significant structural distortion even in low concentration of Al insertion primarily because of high charge density of Al. The study also makes simulation-based suggestions of doping MnO_2 with Mg to obtain better structural integrity for intercalation of guest-ions.

Simulation studies on MnO do an excellent job of answering the possibility of Al-ion insertion in MnO. These studies suggest pre-inserting MnO host materials with ions like Al, K Mg etc. for better capacity and structural integrity. This strategy also seems to be working, as evidenced by experimental studies. But without doubt, cycling stability remains a major problem with MnO-based cathode materials as evidenced by non-existence of any study reporting cycling stability > 150. Hence, on one hand there is quite a lot of scope in exploring various polymorphs of MnO as a high energy density (because of high capacity and voltage) material for AIAB, MnO does not form a good candidate for fundamental studies in AIAB because of the extreme nature of electrode-electrolyte parasitic reactions discussed further in section 2.4.

Table 2-1: Electrochemical performance for various MnO materials as AIAB cathode.

Working Electrode	Electrolyte	Current rate (mA g^{-1})	Average voltage (vs.)	Capacity (mAh g^{-1})	Capacity Retention (% at 'n' cycles)	Ref.
Mg doped MnO_2	1 M $Al(NO_3)_3$	-	1.1 (Ag/AgCl)	-	-	[11]
α- MnO_2	2 m $Al(OTF)_3$	100 mA g^{-1}	1.3 (treated Al)	380	44% at 40	[8]
Birnessite MnO_2	2 m $Al(OTF)_3$ + 0.5 M $MnSO_4$	100 mA g^{-1}	1.3 (Al)	554	69% at 65	[7]
K rich Cryptomelane (MnO_2)	1 M $Al(NO_3)_3$	20 mA g^{-1}	1.4 (graphite)	109	61% at 60	[12]
Al_xMnO_2	5 M $Al(OTF)_3$	30 mA g^{-1}	1.3 (Al)	520	67% at 65	[6]

Al_xMnO_2	2 M $Al(OTF)_3$	100 mA g^{-1}	1.6 (vs Zn-Al)	650	70% at 80	[10]

2.2.2 Hexacyanoferrate (HCF)

Hexacyanoferrrates have gained considerable attention in multivalent-ion battery research.[9] Their open framework structure and their wide open channels make them an attractive host material for multivalent guest ions with relatively large diameter. For AIAB, there has been increasing attention in exploring HCFs as cathode materials. In this section, all such reports are discussed. It is to be noted that though HCFs, because of their open structure, forms a stable host cathode material, they do not show high capacity.[15]

The first-ever report on AIAB using HCF as a cathode material was made in 2015.[14] Zheng Li et al. made a noticeable and convincing case of Al-ion insertion in $K_{0.02}Cu[Fe(CN)_6]_{0.7}\cdot 3.7H_2O$ using ex-situ EDX and XRD. Figure 2-4 a shows the varying ratio of Al upon cycling, whereas Figure 2-4 b gives a qualitative proof of Al-insertion. Additionally, shifting peaks in the ex-situ XRD study gave conclusive evidence of insertion. Though reporting a low capacity, this study served as a starting point for studying HCFs for AIAB. Further, Richard et al. studied $K_{0.03}Cu[Fe(CN)_6]_{0.65}\cdot 2.6H_2O$ for various multivalent and trivalent ion-insertion.[15] The shapes of voltammograms were poorly defined and broader for trivalent ions (Figure 2-4 c), hinting at one of the possibilities including poor kinetics, low signal to noise ratio due to high non-faradaic current, resistance changes with continuous solid-state composition and multi-stepped insertion of ions in the host. Such broad peaks could also correspond to the gradual dehydration of ions to be inserted into various sites within the host structure. Later Liu et al. also observed a similar broad voltammogram for $KCu[Fe(CN)_6].8H_2O$ and reported a stable capacity of 25 mAh/g for 1000 cycles. [16] One of the most critical works on HCFs in AIAB has been by A, Zhou et al. wherein they implemented the concept of using high concentration electrolyte (called water in salt(WISE)). [17] An improved cycling stability of HCF was reported when using 5 m AlTFS (aluminum trifluoromethanesulphonate) as against 0.5 m AlTFS or 0.5 m $Al_2(SO_4)_3$ (Figure 2-4 d). The electrolyte aspect of this

work is discussed later in the electrolyte section. A very high cycling life of 1600 cycles was also reported recently for $K_2CoFe(CN)_6$ nano cubic assemblies.[18] In another work Ni-based HCF was studied for AIAB in 5 m AlTFS.[19] Interestingly, this study showed a relatively bad cycling stability performance even in a concentrated electrolyte. It is also to be noted that this study used Al-foil as anode, and the research was done in a coin cell. This could have

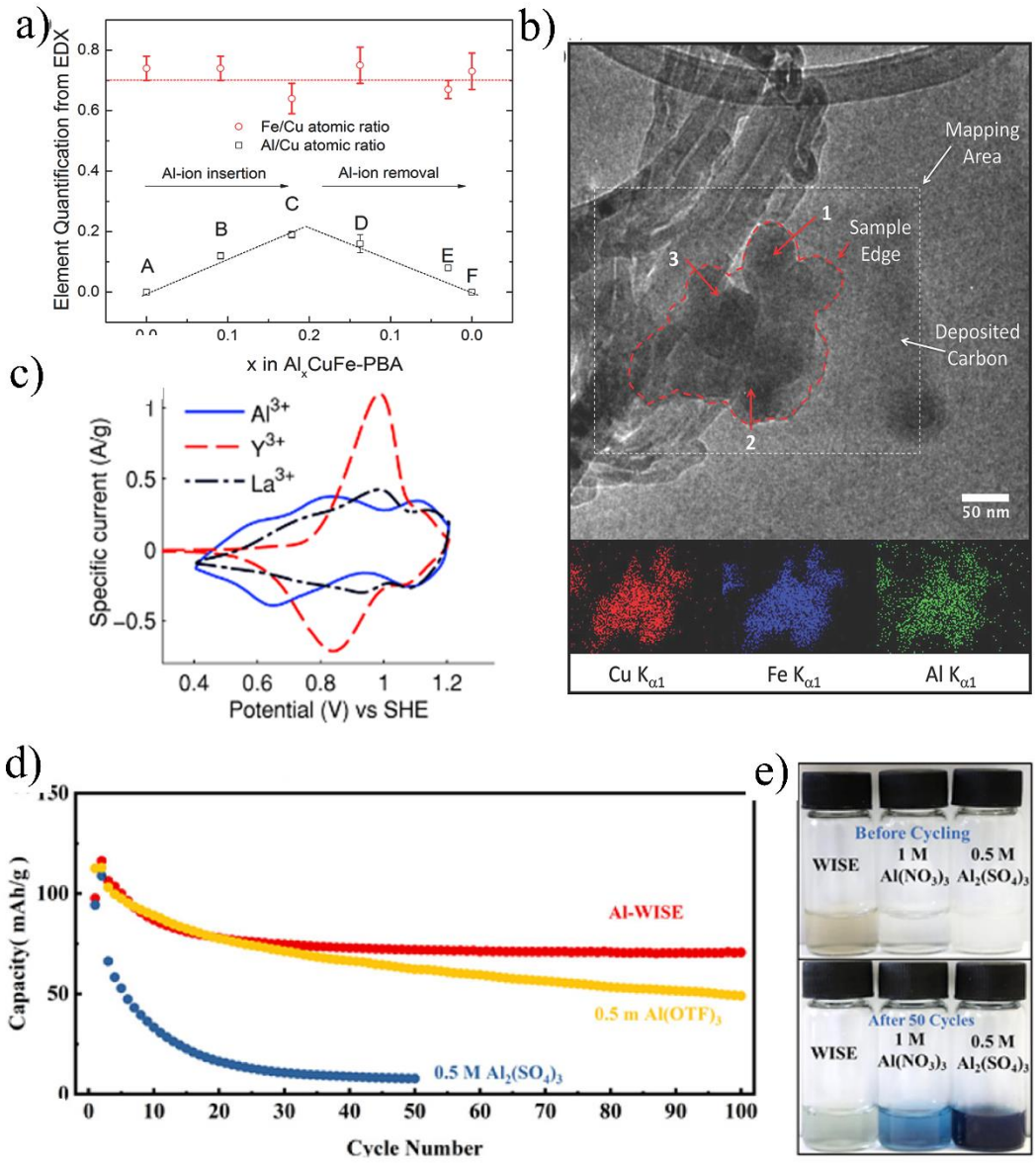

Figure 2-4: a) The elemental ratio (Fe/Cu and Al/Cu) detected for CuFe–PBA after electrochemical cycling against counter electrode $Al_xCuFe–PBA$ in 1 M $Al(NO_3)_3$ electrolyte,

based on TEM-EDX analyses (A–C; discharged to a particular depth-of-discharge) and (D-F; charged to a particular state-of-charge after a particular depth-of-discharge) and b) TEM EDX elemental mapping of CuFe–PBA for sample C in Fig 2.3(a). Reproduced with permission.[14]Copyright 2014, John Wiley and Sons. c) CV showing the reversible insertion mechanism of a variety of trivalent-ions in CuHCF in 1 M conc. of the respective nitrate based electrolytes at pH value 2. Reproduced with permission.[15]Copyright 2015, John Wiley and Sons. d) Cycling life of FF-PBA cathode in different electrolytes Al-WISE, 0.5 M $Al_2(SO_4)_3$, and 0.5 m $Al(OTF)_3$), e) Experiment with cathode dissolution. From left to right, the electrolytes Al-WISE, cycling stability, even though, authors claim the 1 M $Al(NO_3)_3$, and 0.5 M $Al_2(SO_4)_3$ are seen. The photos on top were taken before cycling, and the photos on the bottom were taken after 50 cycles. Functional electrode (WE): FFPBA, counter electrode: AC, and reference electrode: Ag/AgCl) were used in all electrochemical measurements. The voltage range is from 0.7 to 1.3 V vs Ag/AgCl) and the current density is 150 mA/g. Reproduced with permission [17] Copyright © 2019, American Chemical Society.

been a factor affecting the dissolution of Ni in the electrolyte as a prime reason for capacity fading. A manganese deficient hexacyanoferrate was also explored for AIAB in an aqueous and a nanofibrillated cellulose/polyacrylamide hydrogel electrolyte.[20] Authors claim to have obtained better rate capability due to these Mn deficiencies, which may expand the transport channels for Al-ion insertion. The use of gel electrolyte also allowed for the fabrication of flexible AAIB, which was tested after rigorous bending. A very high capacity of 64.7 mAh/g with 56% retention at the 200th cycle was observed for this flexible AIAB. A similar study on the flexibility of AIAB was done on a copper hexacyanoferrate cathode, and polypyrrole (PPy) coated MoO_3 full-cell sandwiching a PVA-$Al(NO_3)_3$ gel polymer electrolyte.[21] Here battery exhibits remarkable versatility and protection in the face of multiple deformations and mechanical tests, including stretching, pressing, folding, twisting, and arbitrary drilling and tailoring into any desired shape. A very recent work in Feb 2021 stands out among all (Table 2-2), reporting a high-capacity retention for 500 cycles at high rate of 500 mA/g, that too in low-cost sulphate electrolyte.[22]

Overall, HCFs appears to be a relatively stable material for studies in AIAB. Multiple reports demonstrating long cycling stability indicates less parasitic reactions at the electrolyte-cathode interface. Reports on flexible AIABs making use of HCFs as cathode also hint towards to rigorous nature of HCFs. But at the same time, HCFs fail to provide very high capacities. Hence HCFs can be considered a good option wherein high cathode stability is required, for instance, in AIAB studies on electrolyte or anodes.

Table 2-2: Electrochemical performance for various hexacyanoferrates as AIAB cathode. (Efficiency not included as lots of these studies includes parasitic reactions)

Working Electrode	Electrolyte	Current rate	Average voltage (V *vs.* SHE)	Capacity (mAh g^{-1})	Retention (% at cycles)	Ref.
$Al_{0.2}CuFe$-PBA	1 M $Al(NO_3)_3$	5 C	0.5	30	83.3% at 1000	[14]
CuHCF	0.5 M $Al_2(SO_4)_3$	400 mA g^{-1}	0.66, 0.83	40	54.9% at 1000	[16]
CuHCF	Nitric acid +1 M $Al(NO_3)_3$	5C	0.76	49	-	[15]
CuHCF	1 mol dm^{-3} $AlCl_3$ & 1 mol dm^{-3} KCl	20C	1.5 (full cell)	10 mAh g^{-1}	90% at 1814	[4]
$K_2CuFe(CN)_6$	1 M $Al_2(SO_4)_3$	0.5 A g^{-1}	0.85	58.6 mAh g−1		[22]
defective $Mn_4[Fe(CN)_6]_{2.88}\Delta_{0.29}\cdot 11.8H_2O$	1 M Al(OTF)$_3$	0.5 A g^{-1}	1.2 (full cell vs ILAl)	82.1	69.5% at 100	[20]
defective $Mn_4[Fe(CN)_6]_{2.88}\Delta_{0.29}\cdot 11.8H_2O$	NFC/PAM gel	0.2 A g^{-1}	1.2 (full cell vs ILAl)	64.7	56.4% at 200	[20]
$Fe[Fe(CN)_6]_{0.7}9\cdot 2.1H_2O$	5 M Al(OTF)$_3$	150 mA g^{-1}	0.4 (vs Ag/AgCl)	116	71% at 100	[17]
$K_2CoFe(CN)_6$	1 M $Al(NO_3)_3$	0.1 A g^{-1}	0.5 (Hg/Hg_2Cl_2)	50	50% at 1600	[18]
$K_{0.02}Ni_{1.45}[Fe(CN)_6]\cdot 2.6H_2O$.	5 M Al(OTF)$_3$	20 mA g^{-1}	0.8 (Al)	46.5	55% AT 500	[19]
$K_2CuFe(CN)_6$	1 M $Al_2(SO_4)_3$	500 mA g^{-1}	0.6 (SCE)	60	75 % at 500	[22]

2.2.3 Vanadium based cathodes

González et al. studied V_2O_5 xerogels in 1 M $AlCl_3$. They showed reversible intercalation of Al-ions (Figure 2-5 a) with specific capacity 150 mAh g^{-1}.[23] XPS results confirmed the reduction of vanadium in discharged V_2O_5 cathodes while ex-situ XRD results (Figure 2-5 b) indicated progressive amorphization of V_2O_5 with every charge. González proposed a side-reaction mechanism wherein Al-ion upon insertion reduces vanadium to a lower oxidation state (from +5 to +4) and forms a hydrated Al-V complex responsible for loss of crystallinity.

$$\frac{x}{3}Al(H_2O)_n^{3+} + (V^{5+})_2O_5 + xe^- \rightarrow (Al^{3+})_{x/3}[(V^{4+})_x,(V^{5+})_{2-x}]O_5.nH_2O$$

NASICON $Na_3V_2(PO_4)_3$ (NVP) was studied with rigorous characterization details using 0.1 M $AlCl_3$ aqueous electrolytes.[24] NVP/carbon nanocomposites were prepared to ensure that the conductivity is sufficient and dissolution slows down due to the carbon layer. Ex-situ XRD results in hints towards ion-intercalation/deintercalation in the contraction/expansion cycle for the unit cell. XPS results show the high Al peak intensity in discharged samples, whereas vanadium peaks shifted reversibly to lower and higher energy values following battery discharge and charge, respectively. NMR study was also used to confirm the presence of Al-ions in the lattice, along with surface-accommodated Al-ions (only two different types of Al could be distinguished using NMR).

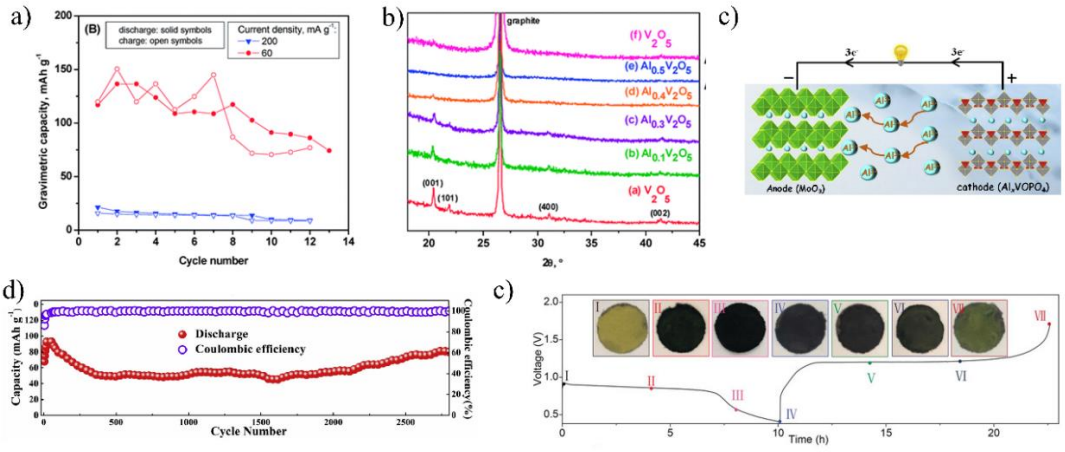

Figure 2-5: a) Specific capacity with cycle number at various current densities for Xero-V_2O_5 in

1 M $AlCl_3$ aqueous electrolyte, b) Ex-situ XRD patterns of cycled and pristine V_2O_5 at various states of charging/discharging (SOC) at slow current-density. The peak at 26.4° belongs to graphite substrate of the electrode. Reproduced with permission.[23]Copyright 2016, RSC. c) Working-principle schematic of aqueous Al ion battery based on intercalation electrode using $VOPO_4$ as cathode and MoO_3 as anode, d) Long-term cycling performance 1 A g^{-1} and the corresponding coulombic efficiency for cell configuration c using Gelatin-PAM electrolyte. Reproduced with permission[25] Copyright 2019 Elsevier B.V. e) Digital photographs of cycled electrodes along with galvanostatic discharge/charge curves of aqueous Al electrochemical cells using V_2O_5 cathodes at 20mA/g. Reproduced with permission [26] Copyright © 2020, John Wiley and Sons.

Thus, Nacimiento proposed a mechanism where NVP loses Na-ions during the first charging cycle, and bulk intercalation/deintercalation happens in subsequent cycles along with surface storage of Al-ions. Even though the stability of NVP in the study was not excellent, complimenting characterization techniques demonstrates a successful insertion of Al-ion.

In an another work a safe and flexible high-performance rechargeable AIB was reported using a mechanically robust gelatin-polyacrylamide hydrogel electrolyte and a MoO_3 anode and $VOPO_4$ cathode (Figure 2-5 c).[5] This AIB has a high-rate capability of 6 A g^{-1}, a high discharge power of 88 mAh g^{-1}, and long cyclic durability of 86.2 % capacity retention even after 2800 cycles (Figure 2-5 d), making it one of the best performing AIAB batteries reported until date. Further, Zhang et al. have shown the electrode dissolution phenomenon happening with V_2O_5. A distinctive change in colour of electrodes was observed at different stages of chare-discharge (Figure 2-5 e), which was also reversible in nature, essentially indicating the reversible reduction of V_2O_5. This dissolution problem was effectively tackled by using a cation-selective membrane that enhanced the cycling life of the cell by ~30% (Table 2-3). Authors also claim that insertion of at least one proton is always favoured in acidic media, and no proof of Al-ion intercalation was found in V_2O_5.

Vanadium based cathodes have scarcely been explored for AIAB, with reports so far showing the excessive dissolution of vanadium. At the same time, the question of Al-ion

getting inserted in V based host materials remains unclear and needs more exploration.

Table 2-3: Electrochemical performance for various vanadium oxides as AIAB cathode

Working Electrode	Electrolyte	Current rate	Average voltage (V *vs.* SHE)	Capacity (mAh g^{-1})	Retention (% at cycles)	Ref.
Xero-V_2O_5	1 M $AlCl_3$	60 mA g^{-1}	0.48	120	62.5% at 13	[23]
$Na_3V_2(PO_4)_3$	0.1 M $AlCl_3$	60 mA g^{-1}	0.62	100	40% at 40	[24]
$VOPO_4$	gelatinpolyacrylamide	1 A g^{-1}	0.5 (Ag/AgCl)	88	86.2 % at 2800	[5]
V_2O_5 (Nafion coated separator)	2 M $Al(OTF)_3$	-	1 V(Al)	180	66% at 50	[26]

2.2.4 Organics

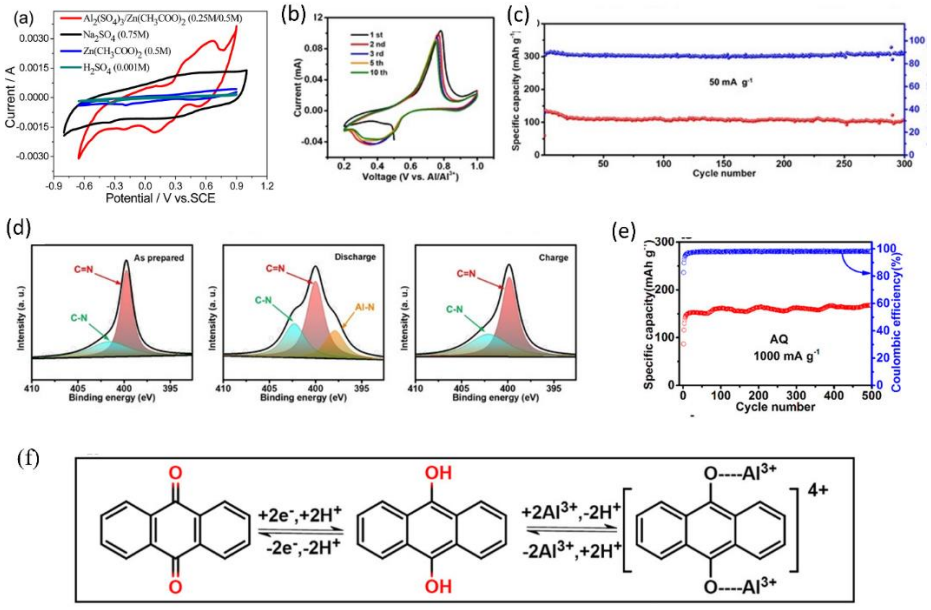

Figure 2-6: a) CV of graphite in different electrolytes at scan rate of 1 mV s^{-1}. Reproduced/Adapted with permission.[27]Copyright 2016, ACS, b) Cyclic voltammograms at 0.1 mVs^{-1} between 0.2 and 1.0 V, c) Cycling stability performance at a current density of 50 mAg^{-1}, d) XPS analysis of N 1s regions for as-prepared, discharged and recharged electrodes. Reproduced with permission [28] Copyright 2020 Wiley-VCH GmbH. e) cycling performance for anthraquinone, f) Reaction mechanism between AQ and Al-ion assisted by protons. Reproduced with permission [22] Copyright © 2021, American Chemical Society.

For AAIB, Wang presented an exfoliated graphite material as the first organic cathode showing electrochemical activity in a sulphate electrolyte (Figure 2-6 a).[27] An aqueous $Al_2(SO_4)_3/Zn(CHCOO)_2$ electrolyte was used to cycle this cathode with a Zn-foil anode. Using TEM studies, Wang found a 0.05 nm increase in the interlayer distance after discharging. The emergence of new phases was also suggested by SAED patterns. This is a compelling proof of the introduction of Al-ions in graphite. Very recently, two high performing organic cathodes have been reported. Phenazine, a heterocyclic compound derived from prokaryotes, has been reported as high-capacity stable material (Table 2-4) with compelling proof of Al-insertion.[28] As shown in Figures 2-6 b and c, Phenazine has very clearly defined electrochemical peaks and has a very stable cycling performance. Authors used ATR-FTIR and XPS (Figure 2-6 d) to study the reaction mechanism for Al-ion insertion and conclude that a -C=N- acts as an active centre of Phenazine to allow intercalation/deintercalation of large-size AlTFS. Phenazine with CN containing monolayer on Pt for Al insertion might be interesting. Anthraquinone was reported as another durable material for AIAB with an increasing capacity for 500 cycles (Figure 2-6 e).[22]. Authors claim anthraquinone (AQ) is practically insoluble in water because of the absence of alpha-hydrogen atoms. This may have resulted directly in a long cycling life. Mechanism-wise the AQ molecule receives two electrons from the external circuit and undergoes a one-step two-electron redox process with the aid of protons in the electrolyte to form anthrahydroquinone (AQH_2) (Figure 2-6 f). Further, this accumulated H_2 is exchanged with Al-ion for its insertion.

Table 2-4: Electrochemical performance for various organic materials as AIAB cathode

Working Electrode	Electrolyte	Current rate	Average voltage (V)	Capacity (mAh g^{-1})	Retention (% at cycles)	Ref.
9, 10-Anthraquinone	1 M $Al_2(SO_4)_3$	1 A g^{-1}	-0.3 (SCE)	86.7 mAh g−1	200% at 500	[22]
Phenazine	5 M Al(OTF)$_3$	50 mA g^{-1}	0.6 (Al)	132 mAh g^{-1}	76.5% at 300	[28]
Exfoliated Graphite	$Al_2(SO_4)_3$ /Zn(CHCOO)$_2$	0.5 A g^{-1}	0.1 (SCE)	80 mAh g^{-1}	94% at 200	[27]

2.2.5 TiO_2

TiO_2 exists in eight different types of crystal structures, with rutile, brookite and anatase as the common polymorphs.[29] The anatase TiO_2 crystal structure is composed of stacked TiO_6 octahedrons that form tunnels, generating suitably sized pathways for cation intercalation (Figure 2-7 a). Liu et al. demonstrated the first AIAB with reversible Al-ion intercalation in anatase TiO_2 nanotubes, prepared by anodizing titanium foil, in 2012 (Figure 9b). [3] Their reason for the increased electrochemical activity in nanotube TiO_2 compared to bulk TiO_2 was that nanotubes had shorter ion diffusion paths and a higher electrolyte-to-ion diffusion ratio because of their form factor. Liu demonstrated an electrochemical reduction of titanium (Ti^{4+} to Ti^{3+}/Ti^{2+}) using XPS and NMR, implying that the material is charge-compensated by the injection of Al-ions into the lattice. Furthermore, CV tests of TiO_2 in Al, Mg and Li chloride salts revealed significantly higher CV peak intensities for the $AlCl_3$ solution (Figure 2-7 c), indicating a propensity for Al-ion insertion in TiO_2.

However, when two fundamental considerations are made: 1) the hydrated radii of ions and 2) the higher charge density of multivalent ions, Liu's statement that Al^{3+} has a smaller radius than Li^+ and Mg^{2+} (53.5 pm for Al^{3+} and 76 pm & 72 pm for Li^+ and Mg^{2+}, respectively) results in facile electrochemical Al^{3+} insertion is counterintuitive. There are two competing ideas here. On one hand, the larger hydrated radius of Al^{3+} (4.75 for Al^{3+}, 4.30 for Zn^{2+}, and 3.82 for Li^+) may make insertion into TiO_2 more difficult unless the solvating water molecules' hydration sheath is partially or wholly removed from the intercalating-ion during the insertion process. On the other hand, non-hydrated Al^{3+} which has a high charge density, may encounter more resistance during its movement in the host material. Nonetheless, this problem can be eased if shielding can be provided by hydrating water molecules or pre-existing water molecules in the host crystal structure. Thus, given that smaller ions fit easier into lattice tunnel but a shielding effect is necessary for multivalent-ion mobility within the lattice, partial hydration seems to be the most likely scenario for facile insertion.

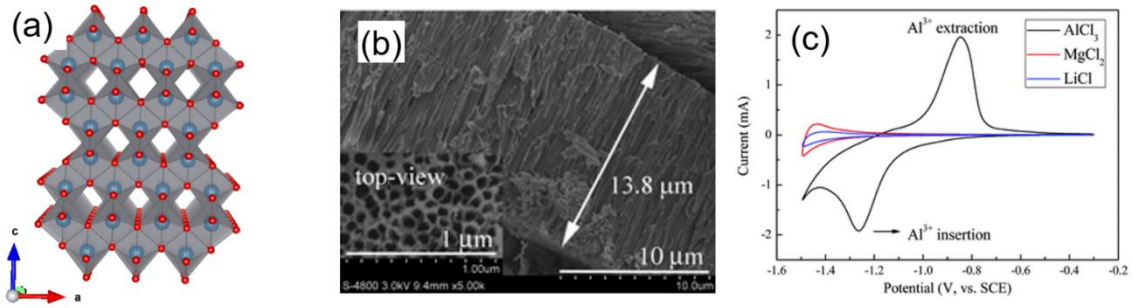

Figure 2-7: a) The crystal structure of anatase TiO_2 (blue spheres: Ti, red spheres: O). b) SEM image of as-prepared anatase TiO_2 nanotube arrays, and c) cyclic voltammograms (CVs) of the as-prepared anatase TiO_2 nanotube arrays in 1 M $AlCl_3$, $MgCl_2$ and LiCl aqueous electrolytes, run at 20 mV s^{-1}. Reproduced with permission.[3]Copyright 2012, RSC.

Kazazi et al. synthesized highly porous and high surface area TiO2 nanospheres in a related study, emphasizing the importance of narrow diffusion paths and electrolyte ions and electron accessibility to the intercalating host material. [30] At a low-rate of 0.15 C and a high-rate of 6 C, this material had an initial power of 108 mAh g^{-1} and 183 mAh g^{-1}, respectively. In continuation to this work, Kazazi improved the material by making a TiO_2/carbon nanotube (CNT) nanocomposite.[31]

Similarly, Lahan et al. tested anatase TiO_2 for Al-ion insertion by making different composites with conductive additives (Graphene, CNT and Ag).[32] Interestingly, Graphene-TiO_2 composites showed clear electrochemical peak whereas pure TiO_2 without any kind of additives did not (Figure 2-8 a, b). Lahan attributed this activity of Graphene-TiO_2 to the increasing electrical conductivity in the order, Graphene-TiO_2 > CNT- TiO_2 > Ag - TiO_2 > TiO_2, also observed in the same trend using EIS and Randles-Sevick equations. This study highlighted the importance of adding a suitable conductive additive to the active material. Following this work, Lahan detected two Al-based phases (Al_2TiO_5 & $Al_2Ti_7O_{15}$) in the discharged graphene wrapped TiO_2 electrode giving proof of Al-ion reaction. (Figure 2-8 c).

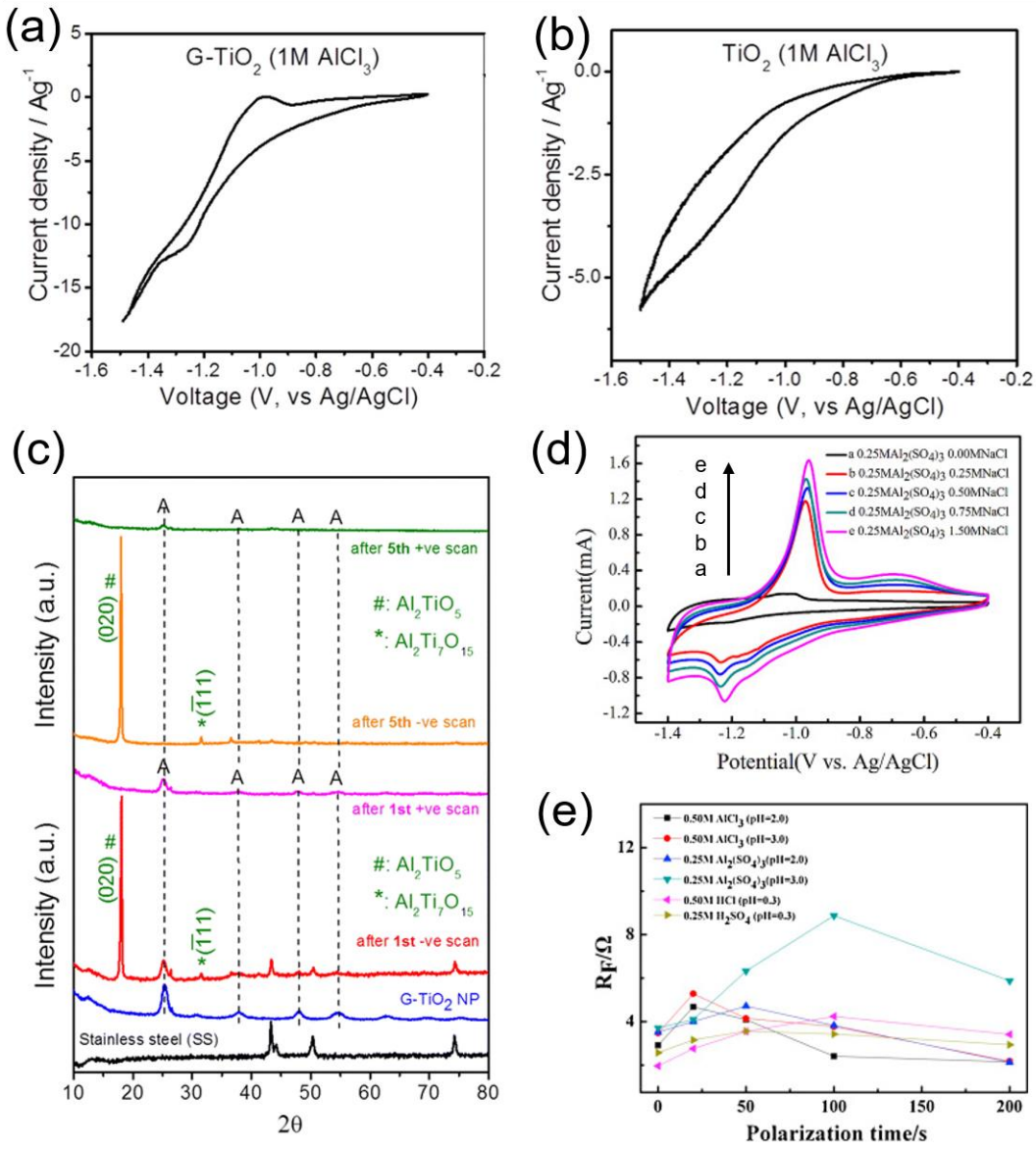

Figure-2-8: a) Respective CVs for a) a graphene-TiO_2 composite and b) TiO_2, in 1 M $AlCl_3$ electrolyte at a scan rate of 5 mV s^{-1}. Reproduced with permission.[32] Copyright 2017, ACS. c) Ex situ XRD patterns of graphene-TiO_2 nanoparticle electrodes after the 1st & 5th negative-direction (-0.4V to -1.5V vs Ag/AgCl) and positive-direction CV scans at 5 mV s^{-1}, in 0.5 M $AlCl_3$ electrolyte (A represents reflections for the anatase TiO_2 phase). Reproduced with permission.[33]Copyright 2018, Springer-Verlag GmbH Germany. d) Typical CVs of as-prepared anatase TiO_2 nanotube arrays at 10 mV s^{-1} in electrolytes of 0.25 M $Al_2(SO_4)_3$ mixed with varying concentrations of NaCl. Reproduced with permission.[34] Copyright 2014, Elsevier Ltd. e) TiO_2 faradic resistance as a function of polarization time in chloride-based & sulfate-based electrolytes at various pH. Reproduced with permission.[35]Copyright 2016, Elsevier Ltd.

Most of the AIAB work involves the usage of $AlCl_3$ as an electrolyte (Table 2-1), whereas weak or no activity has been observed in nitrate and sulphate based electrolytes.[36] Yingying et al. performed studied TiO_2 nanotube in an array of electrolytes with varying anionic species.[34] Unlike $Al_2(SO_4)_3$ electrolytes, electrochemical activity was observed in $AlCl_3$. The increased electrochemical activity was also observed with increasing concentrations of NaCl in $Al_2(SO_4)_3$ (Figure 2-8 d), suggesting a role of Cl^- ions in intercalation. However, no conclusive mechanism could be asserted.

Sang et al. used EIS (Figure 2-8 e) to investigate the influence of H^+ on the electrochemical behaviour of TiO_2 nanotube in an array of aqueous solutions with both H^+-Al^{3+} ions suggested: 1) Hydroxylation is dominant in the initial stage of Al-ion intercalation in TiO_2 but at a later stage H^+/Al^{3+} ion could begin intercalating. 2) the surface hydroxylation-dehydroxylation and/or intercalation-deintercalation occurs more readily in the presence of Cl^-, 3) H^+ was more active as compared to Al^{3+}. Therefore, Sang suggested the use of a lower acidity (pH≥3) electrolytes.[35]

Overall, good research work has gone into studying TiO_2 as a low voltage material for AIAB. Along with a focus on the mechanism, performance enhancement strategies of making cathode composites with carbon-based materials and vacancy generation have been successful. TiO_2 can undoubtedly be considered an anode for the AIAB system (however self-discharge studies for this material remains pending), but this will effectively mean not using Al-metal as an anode, losing cost and abundance advantages of Al.

Table 2-5: Electrochemical performance for various titanium oxides as AIAB cathode

Working Electrode	Electrolyte	Current rate	Average voltage (V *vs.* SHE)	Capacity (mAh g^{-1})	Retention (% at cycles)	Ref.
TiO_2 Nanotube Array	1 M $AlCl_3$	4 mA cm^{-2}	-0.81	75	>100 % at 13	[3]
TiO_2 Nanospheres	1 M $AlCl_3$	0.15 C	-0.84	183	96.67% at 25	[30]

TiO_2/CNT Nanocomposite	1 M $AlCl_3$	1C	-0.85	170	94.12% at 100	[31]
TiO_2 Nanotube Array	Different concentrations of $Al_2(SO_4)_3$, $AlCl_3$ with NaCl as additive	4 mA cm^{-2}	-0.77	74.8	-	[34]
TiO_2 Nanotube Array	$Al_2(SO_4)_3$ and $AlCl_3$ at different pH	-	-	-	-	[35]
G-TiO_2	0.25 M $AlCl_3$	6.25 Ag^{-1}	-0.73	50 mAh g^{-1}	64% at 125	[32]
G-TiO_2	0.5 M $AlCl_3$	6.25 Ag^{-1}	-0.73	40 mAh g^{-1}	>100% at 90	[33]
$Ti_{0.95}$ $\square_{0.05}$ $O_{1.79}$ $Cl_{0.08}$ $(OH)_{0.13}$	1 M NaCl + 1 M $AlCl_3$ (molar ratio 3.33 of Cl −/Al 3 +)	3 A g^{-1}	-0.7	78.3 mA h g^{-1}	81.7% at 100	[37]

2.2.6 Others

Other than the above-mentioned material, S.k Das's group has done very good work of identifying completely new materials for AIAB and making critical preliminary studies. WO_3 and Bi_2O_3 have been explored for Al-insertion (Table 2-6 for performances).[38] [39] Using ex-situ XRD formation of Al-based products have been shown to form during discharge, which serves as a suitable proof for Al-ion insertion or a probable conversion mechanism in this case.[38] A Al-S battery has also been reported by implementing the concept of water-in-salt like electrolyte.[40] A very high initial capacity of ~1400 mAh/g has been reported but it decreases very rapidly.

Table 2-6: Electrochemical performance for various other materials as AIAB cathode

Working Electrode	Electrolyte	Current rate	Average voltage (V *vs.* SHE)	Capacity (mAh g^{-1})	Retention (% at cycles)	Ref.
Bi_2O_3/Exf.Gr	1 M $AlCl_3$	0.5 A g^{-1}	0.65 (Al)	103	70 (increases)	[38]
MoO_3	1 M $AlCl_3$	2.5 A g^{-1}	-0.45 (AG/AgCl)	210	100 (increases)	[39]
S-C composite	$Al(OTF)_3$+LiTFSI+HCl	200 mA g-1	0.9 (Al)	1410	29% in 30	

2.3 Anodes for AIAB: Modification of Al-metal surface

Though Al-metal seems to be an apt candidate to be used as anode in aqueous batteries, it comes with its challenges. The primary and most stubborn of this is spontaneous forming of a passivating oxide layer on its surface. This oxide layer renders the anode surface inert and requires large voltage differences for the plating/stripping process. Such a large voltage difference can cause electrolytic degradation given the small electrochemical window of water. Prof. Archer et al. made a breakthrough in this area when they used a combination of $AlCl_3$ and ionic liquid to treat Al foil surfaces in an inert atmosphere chemically.[8, 14-15, 34] This coating created an artificial conductive layer on the surface and changed the surface chemistry by preventing native oxide formation, allowing Al plating/stripping with much lower overpotential. Figure 2-9a shows a comparative impedance study of symmetric cells for various anode and electrolyte configurations. It can be seen that Ionic liquid + $AlCl_3$ treated Al (TAl) symmetric cells offer way lesser impedance as compared to normal Al-metal anode. This also translated into plating stripping studies wherein TAl symmetric cells showed almost 1/10 overpotential compared to Al symmetric cells (Figure 2-9 b) at 0.2 mA cm^{-2}. This drop in overpotential is primarily attributed to the decrease in charge transfer resistance on the coated Al anodic interface as suggested by the EIS studies.

A similarly good and novel study exploring the possibilities of using alloyed Al in AIAB came out.[10] Authors tried to form a Zn-Al alloy by electrodepositing Zn on Al and claim that “alloying element Zn can mitigate the passivation and self-discharge behaviour, and improve the Coulombic efficiency (CE) by inhibiting H_2 evolution side reaction”. The significantly reduced plating/stripping overpotential can be seen for this Zn-Al symmetric cell (Figure 2-9 c). A significantly reduced impedance can also be seen for the same in Figure 2-9 d. It has also been suggested that the presence of Al^{3+} near Zn substrate helps suppress Zn dendrite formation by forming a positively charged electrostatic shield (Figure 2-9 d).

Both the abovementioned studies are likely to serve as an anchoring point for further

exploration or modification of the Al surface to enable its successful usage as an anode. Additional aspects like stability and compatibility of these modified surfaces can also be studied.

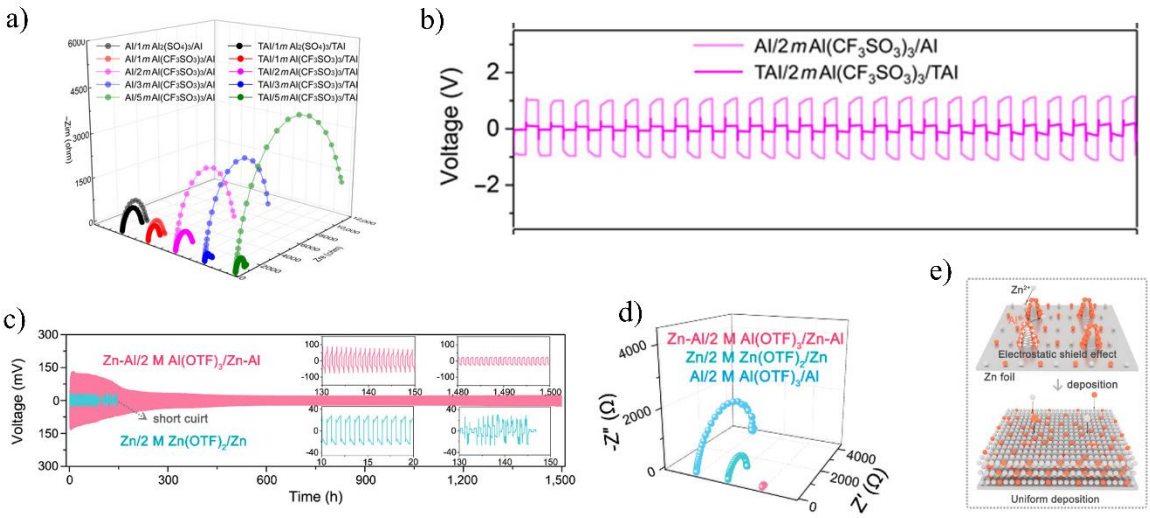

Figure-2-9: a) Comparative EIS study of symmetric Al batteries using various Al anodes and electrolyte combinations, b) Al plating/stripping in symmetric cells of Al and TAl (ionic liquid treated Al) at 0.2 mA cm^{-2} with each cycle containing charge and discharge cycles of 1 hr. Reproduced from [8] Copyright 2018 Qing Zhao and AAAS, c) Plating stripping tests in symmetric cell of Zn substrate in 2 M $Al(OTF)_3$ and 2 M $Zn(OTF)_2$ at 0.2 mA cm^{-2}. Each cycle containing charge and discharge cycles of 0.5 hr. Inset - the magnification of selected periods, d) Comparative EIS study of symmetric cells using various anode-electrolyte combinations. e) schematic showing suppression process of dendrite formation leading to a uniform deposition. Reproduced from [10] Copyright 2020 American chemical society.

2.4 Electrolytes for AIAB

Conventionally, chloride, nitrate and sulphate salt of Al have been used for AIAB because of low cost and ease of availability. However, these salts have a smaller electrochemical stability window, low solubility and are more corrosive, especially $AlCl_3$. On the other hand, AlTFS has emerged as the new electrolyte used widely in AIAB studies. AlTFS though acidic, is not as corrosive as $AlCl_3$ and has a significantly wider stability window

(Figure 2-10 a). This makes TFS based electrolyte more appealing to be used in AIAB.

Electrolyte's composition and concentration can play a key role in determining any electrode's performance and thus the overall cell performance. Using highly concentrated salts and electrolyte additives are popular strategies in aqueous battery research to mitigate parasitic side reactions. For instance, lithium aqueous research has been reported with highly concentrated electrolyte of 30 m.[14] However, given the low solubility of Al salts as compared to Li, AlTFS can only be dissolved upto 5 m at room temperature. Zhou et al. implemented the concept of water-in-salt[41] electrolyte by trying a 5 m concentrate form of AlTFS.[17] As shown in Figure 2-10 b, on increasing the concentration, the number of intimate ion pairs in the electrolyte increased significantly, whereas the free anion decreased. This led to a decreased water activity, thus potentially causing suppressed side reactions. This also led to cycle life performance improvement, as shown in Figure 2-4 d. In another study, diglyme and water combination was used to obtain better cycling life (Figure 2-10 d).[42] Essentially, this study also suppresses the water activity but by eliminating it from the system. It is to be noted here that higher concentration of salt may cause severe corrosion problem as discussed later in section 2.5.2.

Other than concentration, the pH of electrolyte has a key role in aqueous batteries. Transition-metal elements normally experience different stable phases when interacting with water molecules, depending on the pH and the applied potential. This data is summarized in an E-pH or Pourbaix diagrams, such as Figure 2-10 e,f for manganese and vanadium. [43-44] According to the Pourbaix diagram, a thermodynamic driving force exists to reduce solid MnO_2 to aqueous Mn^{2+} while MnO_2-cathodes cycle between 0 V and 1.2 V (vs SCE) at a slightly acidic pH. Manganese can only be stable as MnO_2 at applied potentials greater than 1.2 V (vs. SCE), as also observed experimentally.[45-46] On the other hand, when vanadium-based cathodes are cycled between 0 V to 0.6 V (*vs.* SCE) in mildly acidic conditions, the stable vanadium phase is not solid V_2O_5 but aqueous VO^{2+}.[47] It's important to remember that a transition metal's complex transitions between solid and aqueous phases aren't always reversible. This could result in structural failure

and "orphaned" active masses that are cut off from the electrode's electrical network, as has been observed experimentally.[46] Indeed, the dissolution of transition-metal redox-active centres in an electrode must be controlled and minimized by optimizing battery operating conditions and electrolyte. It is to be noted here that Pourbaix diagram does not provide any information about the kinetic parameters and is purely based on thermodynamic considerations.

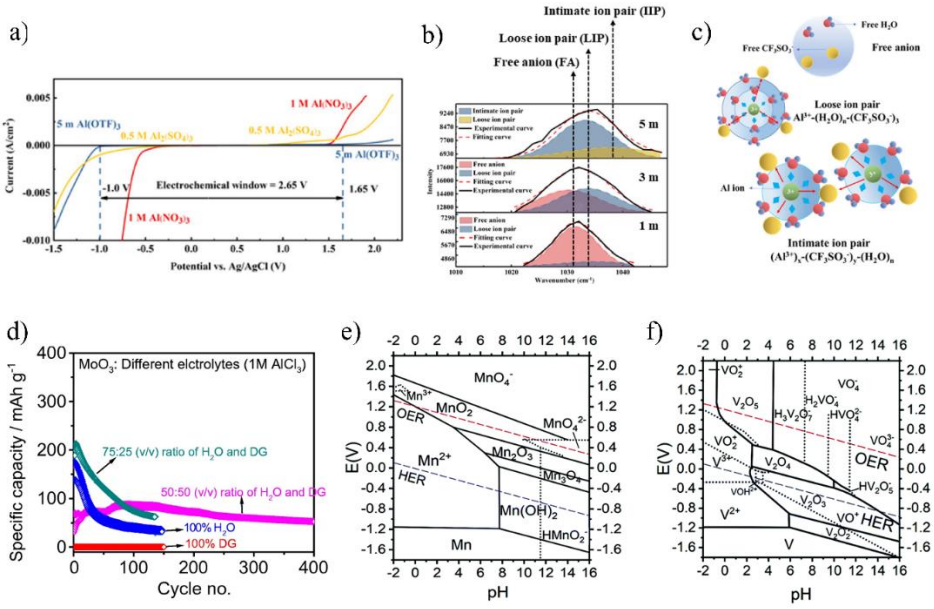

Figure-2-10: a) The electrochemical stability window of electrolytes Al-WISE, 1 M $Al(NO_3)_3$, and 0.5 M $Al_2(SO_4)_3$) done by linear sweep voltammetry at 10 mV/s, b) Free anion (FA), Loose ion pair (LIP), and Intimate ion pair (IIP) fit to Raman spectra of 1, 3, and 5 m $Al(OTF)_3$ solution, c) solvation structure schematic. Reproduced from [17] Copyright 2019 American Chemical Society, d) Cycling performance of G-MoO_3 in different volume ratios of diglyme and water. Reproduced from [42] Copyright © 2019, Springer-Verlag GmbH Germany, Pourbaix diagram of e) manganese and f) vanadium in water. Reproduced with permission.[43] Copyright 2018, RSC.

2.5 Role of current collector

2.5.1 H_2 Evolution

For an aqueous system, the current collector has a big role to play. Though it may seem the current collector's only role is to be sufficiently conductive and collect current, it is otherwise. The current collector significantly influences the electrochemical window of water. Figure 2-11 a gives an idea of which current collector shall be used for which experimentations. The metals like Pt, Re and Rh forms the top of the volcanic curve as they catalyze water batter than other metals to produce H_2 gas. Such low overpotential metal anodes can be used for experiments like electrolyte study where minimum electrochemical overpotential is needed. But for the electrode study, where we want maximum overpotential such that the electrolyte does not degrade, metals such as Ti and Pb are better, showing reduced H_2 evolution potential.

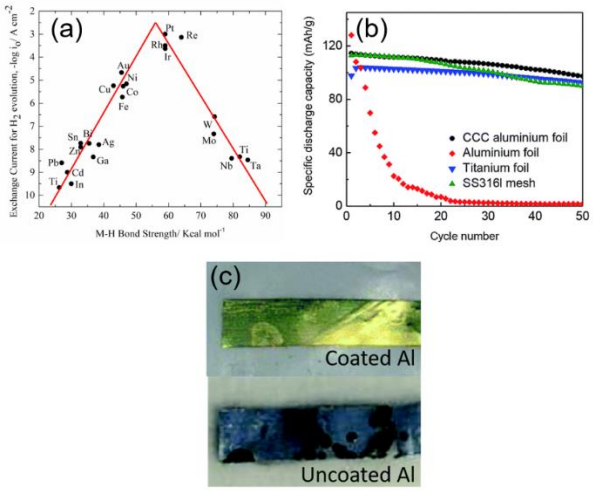

Figure 2-11: a) Volcanic curve for different metal surface showing exchange currents for H_2 evolution with metal-H bond strength for various elements. Adapted with permission.[48]Copyright 1972, Elsevier B.V. b) Stability of $LiMn_2O_4$ electrodes in terms of specific capacity vs cycle number when fabricated on various current collectors and corresponding c) Photograph of the non-treated Al foil current collector after 15 cycles and Chromate Conversion Coated (CCC) Al foil after 50 cycles in 2.5 M Li_2SO_4 electrolyte (pH = 7). Reproduced with permission.[49]Copyright 2015, RSC.

2.5.2 Corrosion

In acidic electrolytes, conventional Cu and Al current collectors corrode. Pt, Ti, and Ni are known to display corrosion resistance even in harsh environments, [44], but they are costly. Stainless steel has been documented to corrode strongly in acidic electrolytes of Al-salts,[32]. In 2.5 M Li_2SO_4, Gheytani et al. published chromate-conversion coated Al foil with comparable performance to titanium foil (Figure 2-11 b).[49] An uncoated Al current collector, on the other hand, showed substantial corrosion as compared to a coated one, which showed stable capacity over 50 cycles (Figure 2-11 c).

Overall, selecting a current collector material appears to be a minor consideration, but it is critical to prevent unnecessary hydrogen evolution and corrosion.

2.6 Outstanding questions

AIAB being a relatively new field, has various dimensions to explore. The historical and contemporary literature review presents various outstanding questions that need to be answered to establish AIAB as a feasible alternative to other battery systems. Those questions include the following:

1. Can the conventional battery testing setup be used for AIAB?
2. Are there new cathodes materials that can allow reversible insertion of a high charge density guest-ion like Al^{3+}?
2. Which Al-ion insertion mechanisms are possible?
3. Are there cathode materials or a class of materials for AIAB that can show minimal parasitic reactions and has long cycling life?
4. What structural/morphological modification can help enhance the performance of AIAB?
5. Can normal Al-metal be used directly as an anode AIAB?
6. What surface modification can be done onto the Al-metal surface to make it ionically more conducting?
7. How well does an Al-surface modification process sits with the fabrication process and during battery operations?
8. Which electrolyte can be used for AlAB, and how does electrolyte concentration and

pH affect the battery performance?

2.7 PhD in context of Literature

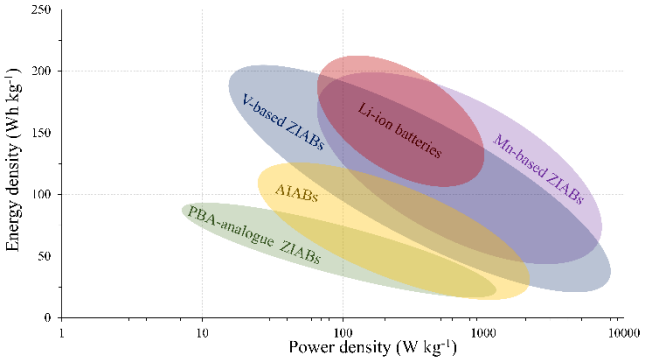

Figure 2-12: a) Ragone plot of various ZIAB and AIAB electrodes. Reproduced from[9]

In this thesis, a genuine attempt has been made to answer all the questions mentioned in the above section, drawn from the literature work. The original part of thesis starts with explorations of new cathode materials (Figure 2-12 showing gap in terms of energy density and power) that can show reversible Al-ion insertion. The reaction mechanism underlying such insertion is also studied to ascertain that AIAB chemistry is possible, and finally the preliminary understanding of working of a AIAB cell is also developed. Further, thesis address the challenges on the anodic side of the cell. Firstly, established work on Al anode are further explored to check their suitability to the cell assembly process and during cell-operations. Further, modifications are made on Al metal surface to enable its usage as an anode in aqueous electrolyte. In almost all the studies, the electrolyte has been optimized to improve cell performance. AIAB being a new field presents several opportunities to make developments in various areas. In this thesis, rather than focusing on just one cell component, an attempt has been made to develop both cathode and anode for AIAB, and finally demonstrate a working full cell.

References

[1] D. Yuan, J. Zhao, W. Manalastas, S. Kumar, M. Srinivasan. *Nano Materials Science.* **2020,** *2*, 248-263.

[2] T. Leisegang, F. Meutzner, M. Zschornak, W. Münchgesang, R. Schmid, T. Nestler, R. A. Eremin, A. A. Kabanov, V. A. Blatov, D. C. Meyer. *Frontiers in Chemistry*. **2019,** *7*, 268.

[3] S. Liu, J. J. Hu, N. F. Yan, G. L. Pan, G. R. Li, X. P. Gao. *Energy Environ. Sci*. **2012,** *5*, 9743-9746.

[4] A. Holland, R. D. McKerracher, A. Cruden, R. G. A. Wills. *J. Appl. Electrochem.* **2018**.

[5] P. Wang, Z. Chen, H. Wang, Z. Ji, Y. Feng, J. Wang, J. Liu, M. Hu, J. Fei, W. Gan, Y. Huang. *Energy Storage Materials.* **2019,** *25*, 426-435.

[6] C. Wu, S. Gu, Q. Zhang, Y. Bai, M. Li, Y. Yuan, H. Wang, X. Liu, Y. Yuan, N. Zhu, F. Wu, H. Li, L. Gu, J. Lu. *Nat. Commun.* **2019,** *10*, 1-10.

[7] S. He, J. Wang, X. Zhang, J. Chen, Z. Wang, T. Yang, Z. Liu, Y. Liang, B. Wang, S. Liu, L. Zhang, J. Huang, J. Huang, L. A. O'Dell, H. Yu. *Adv. Funct. Mater.* **2019,** *0*, 1905228.

[8] Q. Zhao, M. J. Zachman, W. I. Al Sadat, J. Zheng, L. F. Kourkoutis, L. Archer. *Sci. Adv.* **2018,** *4*, 1-7.

[9] V. Verma, S. Kumar, W. Manalastas Jr, R. Satish, M. Srinivasan. *Adv. Sustainable Syst.* **2019,** *3*, 1800111.

[10] C. Yan, C. Lv, L. Wang, W. Cui, L. Zhang, K. N. Dinh, H. Tan, C. Wu, T. Wu, Y. Ren, J. Chen, Z. Liu, S. Madhavi, X. Rui, Q. Yan, G. Yu. *J. Am. Chem. Soc.* **2020**.

[11] J. Joseph, J. F. S. Fernando, M. A. Sayeed, C. Tang, D. Golberg, A. Du, K. Ostrikov, A. P. O'Mullane. *ChemElectroChem.* **2021,** *8*, 1048-1054.

[12] J. Joseph, J. Nerkar, C. Tang, A. Du, A. P. O'Mullane, K. Ostrikov. *ChemSusChem.* **2019,** *12*, 3753-3760.

[13] M. H. Alfaruqi, S. Islam, J. Lee, J. Jo, V. Mathew, J. Kim. *J. Mater. Chem. A.* **2019,** *7*, 26966-26974.

[14] Z. Li, K. Xiang, W. Xing, W. C. Carter, Y. M. Chiang. *Adv. Energy Mater.* **2014,** *5*, 1401410.

[15] R. Y. Wang, B. Shyam, K. H. Stone, J. N. Weker, M. Pasta, H.-W. Lee, M. F. Toney, Y. Cui. *Adv. Energy Mater.* **2015,** *5*, 1401869.

[16] S. Liu, G. L. Pan, G. R. Li, X. P. Gao. *J. Mater. Chem. A.* **2015,** *3*, 959-962.

[17] A. Zhou, L. Jiang, J. Yue, Y. Tong, Q. Zhang, Z. Lin, B. Liu, C. Wu, l. suo, Y.-S. Hu, H. Li, L. Chen. *ACS Appl. Mater. Interfaces.* **2019,** *11*, 41356–41362.

[18] Y. Ru, S. Zheng, H. Xue, H. Pang. *Chem. Eng. J.* **2019**, 122853.

[19] Y. Gao, H. Yang, X. Wang, Y. Bai, N. Zhu, S. Guo, L. Suo, H. Li, H. Xu, C. Wu. *ChemSusChem.* **2020,** *13*, 732-740.

[20] D. Wang, H. Lv, T. Hussain, Q. Yang, G. Liang, Y. Zhao, L. Ma, Q. Li, H. Li, B. Dong, T. Kaewmaraya, C. Zhi. *Nano Energy.* **2021,** *84*, 105945.

[21] P. Wang, Z. Chen, Z. Ji, Y. Feng, J. Wang, J. Liu, M. Hu, H. Wang, W. Gan, Y. Huang. *Chem. Eng. J.* **2019,** *373*, 580-586.

[22] L. Yan, X. Zeng, S. Zhao, W. Jiang, Z. Li, X. Gao, T. Liu, Z. Ji, T. Ma, M. Ling, C. Liang. *ACS Appl. Mater. Interfaces.* **2021,** *13*, 8353-8360.

[23] J. R. Gonzalez, F. Nacimiento, M. Cabello, R. Alcantara, P. Lavela, J. L. Tirado. *RSC Adv.* **2016,** *6*, 62157-62164.

[24] F. Nacimiento, M. Cabello, R. Alcántara, P. Lavela, J. L. Tirado. *Electrochim. Acta.* **2018,** *260*, 798-804.

[25] P. Wang, Z. Chen, Z. Ji, Y. Feng, J. Wang, J. Liu, M. Hu, H. Wang, J. Fei, W. Gan, Y. Huang. *Energy Storage Materials.* **2019**.

[26] Q. Zhao, L. Liu, J. Yin, J. Zheng, D. Zhang, J. Chen, L. Archer. *Angew. Chem. Int. Ed.* **2019,** *n/a*.

[27] F. Wang, F. Yu, X. Wang, Z. Chang, L. Fu, Y. Zhu, Z. Wen, Y. Wu, W. Huang. *ACS Appl. Mater. Interfaces.* **2016,** *8*, 9022-9029.

[28] J. Chen, Q. Zhu, L. Jiang, R. Liu, Y. Yang, M. Tang, J. Wang, H. Wang, L. Guo. *Angew. Chem. Int. Ed.* **2021,** *60*, 5794-5799.

[29] L. Kavan, M. Grätzel, S. E. Gilbert, C. Klemenz, H. J. Scheel. *J. Am. Chem. Soc.* **1996,** *118*, 6716-6723.

[30] M. Kazazi, P. Abdollahi, M. Mirzaei-Moghadam. *Solid State Ionics.* **2017,** *300*, 32-37.

[31] M. Kazazi, Z. A. Zafar, M. Delshad, J. Cervenka, C. Chen. *Solid State Ionics.* **2018,** *320*, 64-69.

[32] H. Lahan, R. Boruah, A. Hazarika, S. K. Das. *J. Phys. Chem. C.* **2017,** *121*, 26241-26249.

[33] H. Lahan, S. K. Das. *Ionics.* **2018,** *24*, 1855–1860.

[34] Y. Liu, S. Sang, Q. Wu, Z. Lu, K. Liu, H. Liu. *Electrochim. Acta.* **2014,** *143*, 340-346.

[35] S. Sang, Y. Liu, W. Zhong, K. Liu, H. Liu, Q. Wu. *Electrochim. Acta.* **2016,** *187*, 92-97.

[36] S. K. Das, S. Mahapatra, H. Lahan. *J. Mater. Chem. A.* **2017,** *5*, 6347-6367.

[37] X. Wu, N. Qin, F. Wang, Z. Li, J. Qin, G. Huang, D. Wang, P. Liu, Q. Yao, Z. Lu, J. Deng. *Energy Storage Materials.* **2021,** *37*, 619-627.

[38] S. Nandi, S. K. Das. *Solid State Ionics.* **2020,** *347*, 115228.

[39] H. Lahan, S. K. Das. *J. Power Sources.* **2019,** *413*, 134-138.

[40] Z. Hu, Y. Guo, H. Jin, H. Ji, L.-j. Wan. *Chem. Commun.* **2020**.

[41] L. Suo, O. Borodin, T. Gao, M. Olguin, J. Ho, X. Fan, C. Luo, C. Wang, K. Xu. *Science.* **2015,** *350*, 938-943.

[42] H. Lahan, S. K. Das. *Ionics.* **2019,** *25*, 3493-3498.

[43] S. Boyd, V. Augustyn. *Inorg. Chem. Front.* **2018,** *5*, 999-1015.

[44] M. Pourbaix. *Atlas of electrochemical equilibria in aqueous solutions*, Houston, Texas : National Association of Corrosion Engineers, 1974.: 1966.

[45] B. Lee, C. S. Yoon, H. R. Lee, K. Y. Chung, B. W. Cho, S. H. Oh. *Sci Rep.* **2014,** *4*, 6066.

[46] N. Zhang, F. Cheng, J. Liu, L. Wang, X. Long, X. Liu, F. Li, J. Chen. *Nat Commun.* **2017,** *8*, 405.

[47] C. W. Mason, F. Lange. *ECS Electrochem. Lett.* **2015,** *4*, A79-A82.

[48] S. Trasatti. *J. Electroanal. Chem. Interfacial Electrochem.* **1972,** *39*, 163-184.

[49] S. Gheytani, Y. Liang, Y. Jing, J. Q. Xu, Y. Yao. *J. Mater. Chem. A.* **2016,** *4*, 395-399.

Chapter 3

Experimental Methodology

This chapter discusses the synthetic techniques and the implemented characterization techniques used in the revelation of the working mechanism of AIAB. The first part of the chapter emphasizes the synthesis techniques of the cathode and anode material. The second part of the chapter discusses the principle behind the material characterization techniques used, specifically focusing on the technique's suitability in the context of this thesis. The third part of the chapter discusses the principle and application of the electrochemical characterization techniques used to study the electrochemical properties of the active material.

3.1 Synthesis

Hydrothermal and coprecipitation techniques have been used in most of the synthesis process of AIAB cathode materials.

3.1.1 Hydrothermal/Solvothermal Synthesis

Hydrothermal synthesis is a bottom-up reaction-based approach that has been widely used for the synthesis of inorganic materials. It essentially involves chemical reactions in a sealed and heated vessel above ambient temperature and pressure. A combination of high pressure and temperature lowers the solvent's density, viscosity, and surface tension while the ionic product increases (Figure 3-1 a). The filling factor also influences the vessel's pressure (Figure 3-1 b). This leads to an increased reaction rate often enabling reactions that otherwise would not have been possible at room temperature. [1]

Such synthesis has two variants: 1) Hydrothermal, when water is used as a solvent for reaction, and 2) Solvothermal when other solvents are used for the reaction. The heating of the vessel is either isothermal, for cases like powder synthesis, or an increasing temperature gradient is given, for example, crystal growth. This synthesis approach can be used to make several morphologies, including nanoparticles, nanorods, nanospheres, nanotubes, and graphene nanosheets. The most important advantage of hydrothermal synthesis can obtain very high-temperature reaction products at a lower temperature.

For this thesis, this approach was chosen as it is quick and simple. A typical hydrothermal synthesis involved mixing the stoichiometric ratios of reactant in a solution and heating it isothermally in a Teflon lined vessel. Further, the reaction product is centrifuged and washed several times with DI water/ethanol to separate the non-reacted pre-cursor from the reactant product. Finally, the synthesized material is vacuum dried overnight.

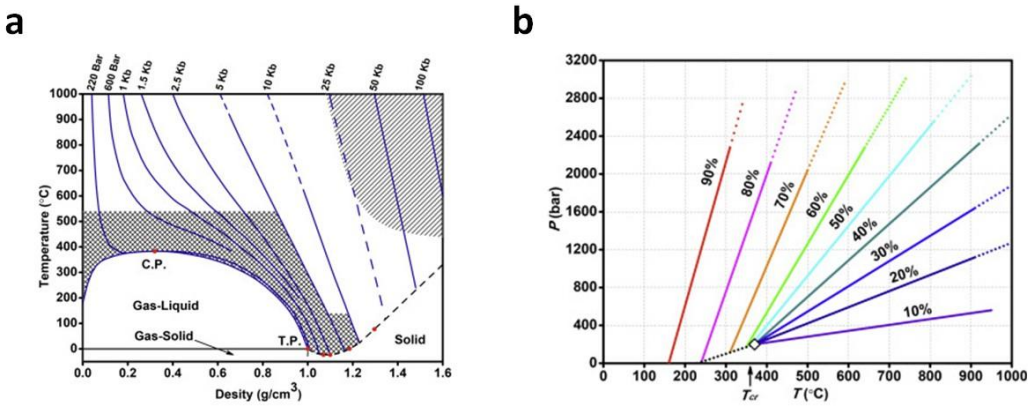

Figure 3-1: a) Density-temperature plots of water with variable temperature, b) pressure-temperature correlation for water with variable filling factor of the sealed reactor. [1]

3.1.2 Co-precipitation

The co-precipitation technique is a bottom-up synthesis approach that takes advantage of different solubility of different salts in water. Essentially, stoichiometric amounts of two or more water-soluble salts are first dissolved in water as reagents, leading to liquid phase precipitation of a water-insoluble salt. This insoluble salt precipitates out when its concentration exceeds its solubility product in the solvent, also called supersaturation. The reaction process involves nucleation, growth and coarsening at later stages. The coarsening step affects the size, morphology and hence the properties of the reaction product. [2]

This synthesis approach was adopted as it is simple, rapid and does not need high temperature for reaction. Typically, the reacting agents are first dissolved in water separately in stoichiometric amounts. Then they are slowly added to another solution slowly and dropwise to form the reaction products. At times the dissolution and precipitation are also controlled by changing the pH of the solution. Usually, a low pH is used for dissolving reactants and a high pH to precipitate the formed product out.[2]

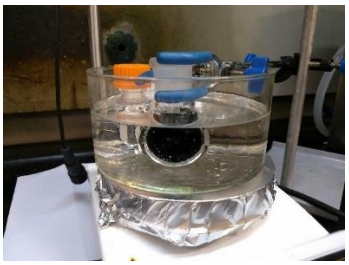

Figure 3-2: Co-precipitation reaction in progress.

3.1.3 Dip coating of anodes

In some studies, Al-metal anodes were dip-coated to create an artificial layer over them. The process involved simply preparing a eutectic mix inside the glovebox by mixing the required ratios of a precursor followed by polishing Al foil to remove the oxide layer on it and then dipping it in the eutectic mix for about 24 hours. The dipped foils were also flipped once in these 24 hours for an effective coating. Further these coated foils are removed, and excessive coating is wiped off. The polishing of Al foil was done using P800 grit size paper. Similar to metallurgical specimen sample preparation, polishing was done in horizontal and vertical direction, making sure that eventually the surface is free of any observable scratch. It is to be noted here that polishing was done inside the glovebox in an inert atmosphere and the polished Al foil was dipped in eutectic coating mixture right after polishing. This essentially eliminates the chances of oxide layer formation on the Al metal foil.

3.2 Materials Characterization

3.2.1 X-Ray Diffraction (XRD)

Diffraction is an important tool to study the crystal structure of materials and is handy for checking the purity of a compound. XRD works on principle of Bragg's Law that relates the lattice distance (d) of crystal to the diffraction angle (θ) for a given source of X-ray. In very simple terms few percentages of the incident rays on the crystal gets reflected and interfere constructively. These interferences occur at certain angles (θ) only and are

detected as high-intensity peaks in the detector (Figure 3-3). A set of such peaks is unique and is characteristic of only one particular phase. Thus the exact crystal structure of a material can be determined with an intelligent guess. The non-destructive and simple nature of this technique makes it quite versatile. This technique has been exhaustively used in the studies included in this thesis to study the crystal structure of the synthesized materials and cycled electrodes. Rietveld refinement and Pawley fitting techniques were used to refining certain known crystal structures and fit them to the experimentally obtained diffraction pattern. Whereas the Rietveld refinement method aimed at overlapping experimental peak intensity and positions with the fitted pattern of intensity and positions, Pawley implements only the overlapping of peak positions. Both these fitting methods were implemented as and when required.

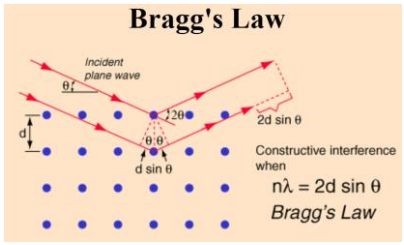

Figure 3-3: Bragg's Law Schematic [3]

For experiments in this report, crystal structures were determined using a Bruker D8 Advance diffractometer operating in a Bragg-Brentano geometry and using a Lynxeye-type detector with CuKα radiation. The obtained XRD pattern was subsequently refined using the TOPAS 4.1 software for the synthesised powder when needed. For the charged/discharged electrode samples, the electrodes were extracted from the electrochemical cells and scanned without removing the Ti current collector mesh. To facilitate pattern-to-pattern comparisons, the collected XRD patterns were calibrated against the Ti peak position. The pattern intensities were subsequently normalized against the most intense peak.

3.2.2 Scanning Electron microscopy (SEM)

SEM uses a focused electron beam that interacts with the material to be scanned and produces several signals. These signals are detected and provide morphological and compositional information based on the type and capabilities of the detector. Secondary electrons are detected to provide morphological information as they interact and emitted from the specimen surface. In contrast, back scattered electrons are emitted from deeper locations in the specimen (Figure 3-4) and are highly dependent on atomic number, thus useful for analytical SEM. Characteristic X-rays emitted from the materials are characteristics of the elements present in the material and can provide quantitative compositional information.

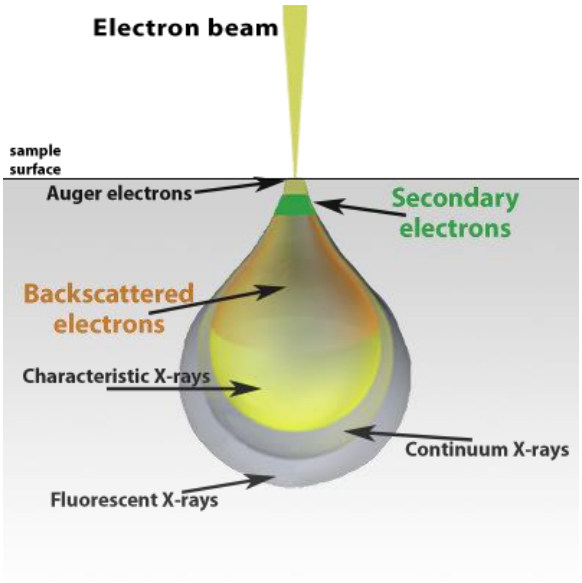

Figure 3-4: Electron beam interaction with specimen [4]

For characterizations in this report, morphological analysis was conducted using a field emission scanning electron microscope (JEOL, JSM-7600F) in SEI mode with an accelerating voltage of 5kV and at 3-8 mm working distance. EDX elemental analyses of powder and electrode samples were conducted using silicon-drift detectors as implemented in the microscope-attached EDS systems (Oxford Aztec Energy). Each sample was probed at 20 kV or more accelerating voltage for about 600 seconds while

maintaining an optimum deadtime between 20% to 30%. Due to the nanometric dimensions of some samples, a JEOL JEM-2100F TEM set at an accelerating voltage of 200kV was also used at times to probe the finer details of the powder morphologies.

3.2.3 Transmission Electron Microscopy (TEM)

TEM, just like SEM, uses an accelerated electron beam to gather morphological and compositional information. However, unlike SEM, it does not collect the scattered electron to generate the electron image. Rather, the incoming electrons which gets modified upon interaction with the specimen are collected over a fluorescent screen at the bottom of the microscope. The electrons are accelerated at one order higher voltage as compared to SEM. This high energy provides a better resolution than SEM, which is advantageous to study morphology at higher magnification. TEM is done in transmission mode(Figure 3-5). Advanced TEM can generate images at the atomic scale.

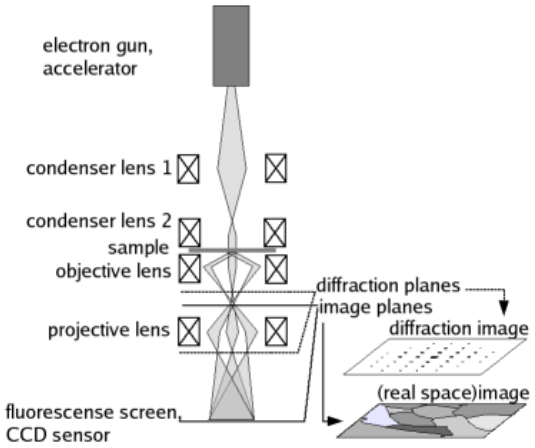

Figure 3-5: TEM column [4]

3.2.4 Raman Spectroscopy

This technique is used as a finger printing tool to identify the molecules by observing their vibrational, rotational and other frequencies. Fundamentally, laser light of a certain wavelength (with small bandwidth) interacts with molecular vibration causing a shift in

laser energy with various possibilities (Figure 3-6). This shift is unique for vibrations from different molecules. Thus, any change in the energy is characteristic of a particular bonding configuration. Raman is advantageous when it comes to studying short-range ordering as it cannot be done using techniques such as XRD.

In the context of this report, Raman shifts were measured on a WITec, Alpha300 SR Confocal Raman spectrometer. Powder and electrode samples were exposed to a 488 nm wavelength Argon type laser. Further, each spectrum was normalized with respect to the most intense peak, background subtracted and analyzed based on the available literature.

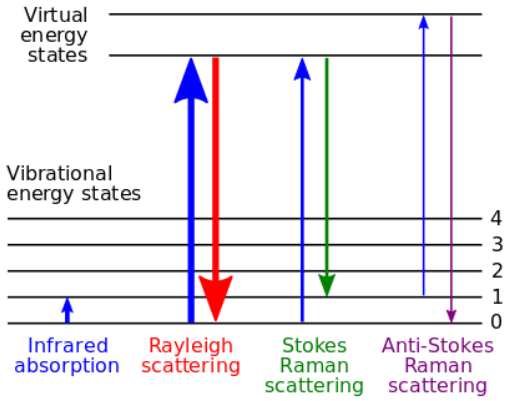

Figure 3-6: Raman spectroscopy based on inelastic scattering.[5]

3.2.5 X-ray photoelectron Spectroscopy (XPS)

XPS is essentially a surface technique (~ 10 nm), primarily used to study the changes in the oxidation state occurring on the surface and for compositional analysis. As illustrated below sample is targeted with photons to excite the electronic state of atoms leading to the ejection of electrons of different energy. These electrons are filtered via a hemispherical analyser and detected for defined energy values. Since every element has its unique core level energy, electrons ejected for different elements have different energy. The same energy concept applies for one single element with different oxidation states or different binding energy. Hence XPS can is sensitive to elements, oxidations state and molecular bonding.

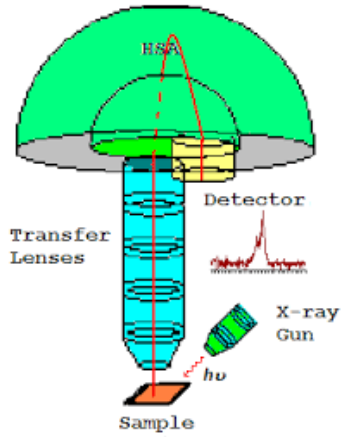

Figure 3-7: Schematic of XPS instrument [6]

In this report, Kratos AXIS Supra XPS, which uses monochromated radiation (Al K_α, 1486.69 eV) operating at 225 W, was used to study the surface chemistry of synthesized powder, cycled electrodes and electrolytes as and when required. Obtained spectra were deconvoluted using the Casa XPS software. Each spectrum was calibrated with adventitious C1s peaks (Other peaks like N1s were also used in some cases wherein a low amount of carbon was detected), the background was removed using a non-linear (Shirley) baseline, and fitting was done with peaks defined as a combination of Lorentzian (30%) and Gaussian distribution (70%). This study supplemented by surface etching has been used exhaustively to study the surface and subsequent layers of the anodes. It is to be noted that Shirley background was used here because of the typical step like background which emerges in XP spectrum as a result of the inelastic scattering of the valence electrons. Empirically, it has been found that using a non-linear background like Shirley helps in accounting for such step. However, in cases where the spectrum background decreases when moving from lower to higher binding energy values, Shirley background cannot be used. In the context of this thesis, Shirley background was found to be a better alternative as compared to linear or a Tougaard background. It can also be noted that XPS studies here have not been used to produce any quantitative results, hence background, though usually important, does not significantly affect any conclusions made in this thesis. A GL(30) peak combination was used for peak

fitting as empirically this combination has been found to be the most useful and versatile. Adding to that, the XPS peak shape gets defined not only by the atomic level considerations but also by the instrumentation. The XPS instrument used here also uses a database including peaks with GL(30) profile. Hence, it was sensible to use GL(30).

3.2.6 X-ray Absorption Spectroscopy (XAS)

XAS is a widely used X-ray technique primarily used to determine the matter's local geometry and electronic structure. Usually, XAS is carried out at a synchrotron facility as it requires high energy and intensity photon. The fundamental principle in XAS is the same as XPS, wherein each element's unique electronic structure is its fingerprint. As opposed to measuring electrons of defined energies, XAS involves detecting ionising radiation that has been either absorbed or generated through fluorescence. A typical XAS spectrum consists of two parts as shown below: 1) XANES (X-Ray absorption near edge structure)- This region is sensitive to active site geometry and changes in oxidation state. It includes two region including free edge and rising edge. 2) EXAFS (Extended X-ray absorption fine structure)- This region provides information about ligands surrounding the active site/absorbing atom (Figure 3-8).

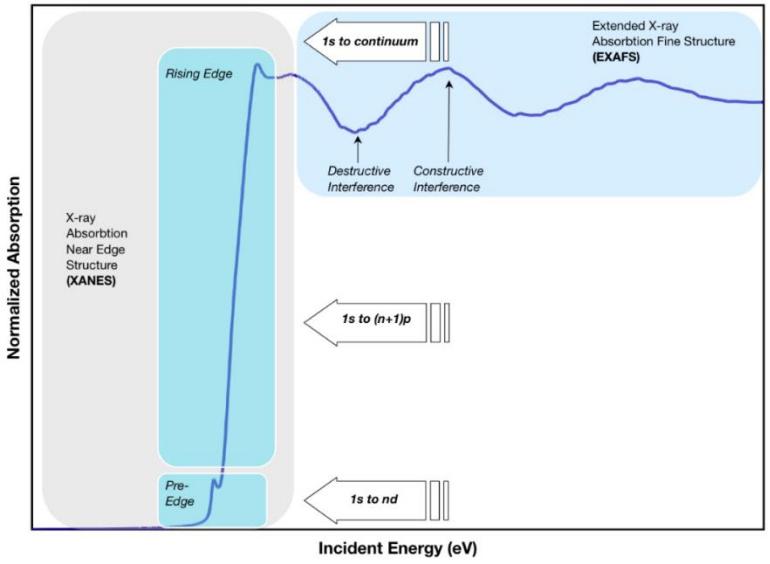

Figure 3-8: Typical XAS spectrum showing its different region [7]

XAS schematic and actual setup are shown below. A typical setup includes bending magnets which accelerate electrons to a produce white beam. This goes through a double crystal monochromator to produce a monochromatic beam that finally interacts with the sample. Further, the ionizing radiations from the material are collected using a detector depending on the mode of measurement (transmission or fluorescence).

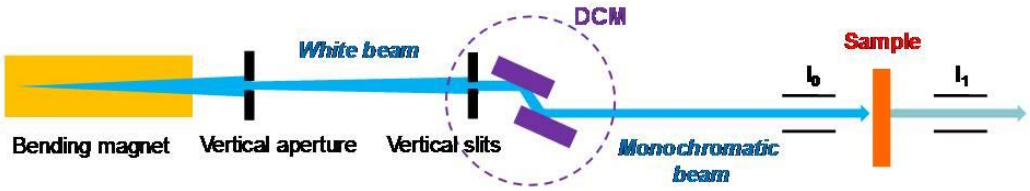

Figure 3-9: Typical XAS schematic.

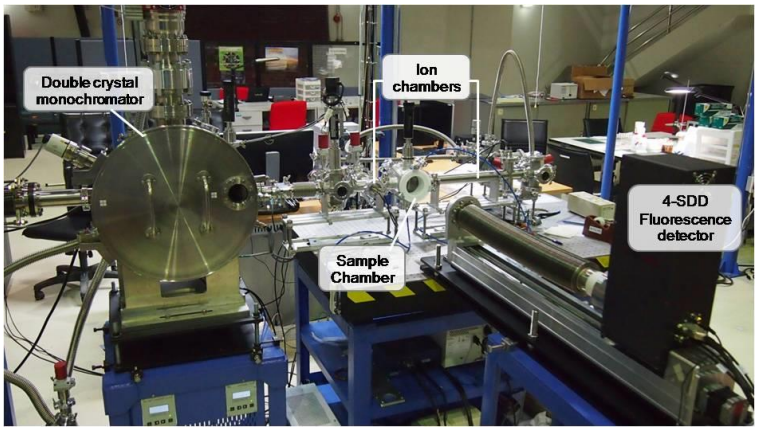

Figure 3-10: Actual XAS instrumentation setup of beamline 5.1 at SLRI, Thailand.

In the context of this report, the XAS characterization was carried out at beamline 5.2 and beamline 8.1 at SLRI, Thailand. A software suite called Demeter, which includes Athena and Artemis, was used for XAS data analysis.[8] Whereas Athena was used for XAS data processing, Artemis was used for EXAFS data analysis using theoretical standards. The obtained spectrum was processed using Athena by removing background contributions and were further normalized to unity to eliminate variations due to samples and/or equipment.

3.2.7 Uv-Vis Spectroscopy

This is an absorption spectroscopy technique usually used in analytical chemistry. It can be used to determine the presence of analytes such as transition metal ions. Molecules with π–π*, n–π*, σ–σ* and n–σ* bonding absorb energy to excite electrons to higher anti-bonding molecular orbitals, thus absorbing energy in visible and adjacent energy region. Here, UV-Vis was used to detect the presence of transition metal ion in the cycled electrolyte.

In the context of this report, PerkinElmer, Lambda950 was used to measure the absorbance of electrolytes in the 190 nm to 800 nm wavelength range of light. Liquid samples were diluted down by a factor of 10 and then measured in clean quartz cuvettes (PerkinElmer, B0631009) for absorbance. For the cycled electrolytes, the equivalent non-cycled electrolyte was used as a reference for background subtraction.

3.2.8 Fourier Transform Infrared (FTIR) Spectroscopy

FTIR spectroscopy technique is used to obtain an infrared spectrum of absorption or emission of a solid, liquid or gas. Typically, a sample is irradiated with polychromatic infrared electromagnetic radiation. Depending on the sample's molecular composition and radiation, some of this radiation is absorbed by the sample while the rest is transmitted as it is. Unknown products, additives inside polymers, surface contamination on a material, and more can be identified using FTIR analysis. The results of the experiments can be used to determine the molecular composition and structure of a sample. An interferometer, a simple device that generates an optical signal with all of the IR frequencies encoded in it, is used to distinguish samples. The measured signal is then decoded using the Fourier transformation, a mathematical process. The spectral information is then mapped using a computer-generated method.

In the context of this literature, FTIR spectra for Al foils were recorded using a Perkin-Elmer Frontier machine in the spectral range of 600-4000 cm-1. FTIR for liquids was recorded in transmission mode by first mixing them with KBr powder and pressing them

in a tablet form. FarIR was measured using NicoletTM iSTM 50, Thermo scientific machine in ATR mode.

3.3 Battery Assembly and Testing

Battery testing was done either in a coin cell setup (CR2016) or a flooded beaker cell setup with two or three-electrode arrangement as required. Most of the initial stage study (chapter 3 and 4) included working with a three-electrode setup with C/Pt/Ti foil as an anode and Ag/AgCl as reference electrode (Figure 3-11) which was calibrated with another standard electrode and showed drifting potential only in mV range. Such electrode choices were made partially because of the corroding nature of $AlCl_3$ electrolyte and partially because of a lacking anode. It was only after treated Al-metal anode was successfully reported[9] as an active anode for AIAB, coin cell studies could be done.

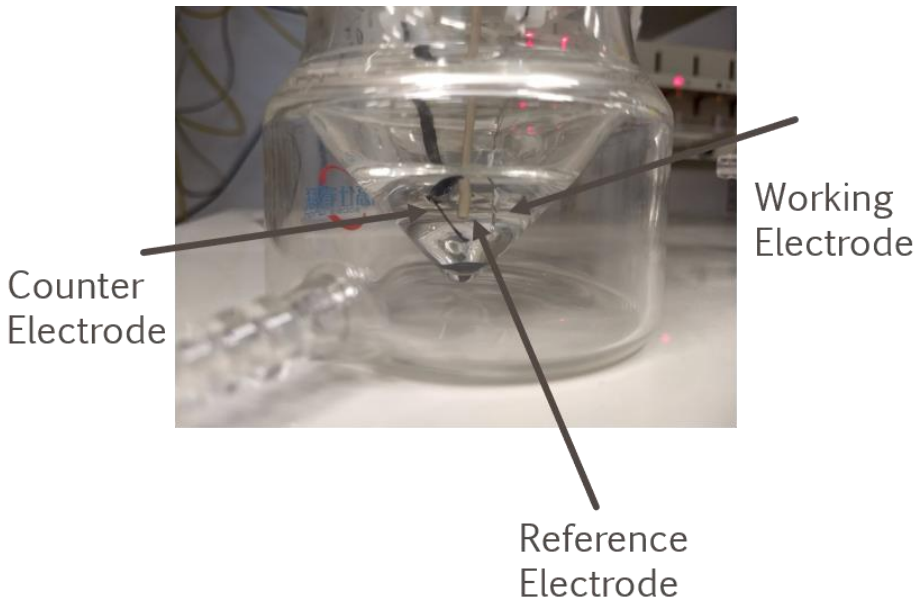

Figure 3-11: Three electrode setup used in the AIAB study

The selection of the current collector was also critical to the aqueous study as a conventional current collector like Cu and Al would corrode in an aqueous environment and would also allow for a smaller thermodynamic chemical stability window.[10] Hence Ti

foil/mesh was chosen as a current collector. As discussed in section 2.5, Ti does not corrode even in a low pH environment and does not catalyze water to H_2 rigorously.

Cathode preparation was done either in 8:1:1 or 6:2:2 ratios of active material, conducting carbon and binder. Cathode preparation varied slightly for the three electrode setup and the coin cell. For the 3 electrode setup, active material was mixed with conducting carbon (Acetylene black or Super P), and TAB (teflonized acetylene black) was used as the binder. This mix was then pressed several times, forming a tablet-like uniform film which was further pressed on Ti mesh using a press machine (Figure 3-12). Finally, this electrode was vacuum dried overnight. Cathodes for coin cell were prepared differently. Initially, the required amounts of active material and super P were mixed in a mortar-pestle until it formed into a uniform colour. Further, this mix was added into N-methyl-2-pyrrolidone solvent already containing the required amount of pre-dissolved PVDF. Subsequently, the slurry was left to stir overnight and later painted on titanium foils to make cathodes, which were finally dried overnight to get rid of the solvent.

Figure 3-12: Cathode for three-electrode setup

Anode preparation varied according to the study required. In the initial stages of the study, wherein the focus was on the cathode, an anode for three-electrode setups included using a cleaned Ti/C/Pt foil of the required size. In later stages, coated Al-metal anodes were used for both coin cell and flooded beaker cell. The fabrication process included polishing as received Al-foil ((0.25mm thick, annealed, 99.99% (metals basis) Alfa Aesar) in the Ar-filled glovebox (<0.1 ppm O_2; <0.1 ppm H_2O) and dipping them for about 24 hours in the coating mixture. The dipped Al was flipped from time to time for improved coating. Further, the coated Al was softly wipe-dried of all the liquid from the surface and taken out of the glovebox for the cell preparation.

3.4 Electrochemical Characterization

3.4.1 Cyclic Voltammetry (CV)

This is a fundamental electrochemical characterization technique. Here the potential of a working electrode is cycled between two fixed voltages, at a fixed rate, with respect to the potential of a reference electrode. In the case of a coin cell, the counter electrode acts as the reference electrode (keeping in mind that potential on such references may drift during the cell operation as continually passing current may result in overpotential.). As an output, the variation in current is observed and recorded as a function of voltage. This technique is primarily used to investigate the activity of material toward cation intake and determine the window in which the material is active. This same window is usually further used for GCD. In the context of this report, CV experiments were carried out in Solartron 1470E. The discharging (cathodic sweep) step of the cell essentially would result in the insertion of guest-ion, Al-ion/Al-ion complex in this case, in the cathode material. This process can also be called as alumination. Similarly, the charging would result in de-alumination. Any new host material that was to be tested for activity towards Al-insertion was first scanned in various range of cycling window, which was expanded with each cycle. Having scanned the activity of the material until the electrolyte decomposition voltage values on either extreme, a potential range was chosen for cycling such that the pair of cathodic/anodic peak falls within the cycling range and at the same time keeping the window small enough not to decompose the electrolyte. Considering the small electrochemical stability window of aqueous electrolyte, all the cycling range in this this are ~ 1.3 V or less.

Figure 3-13 depicts a typical voltammogram. It shows a cathodic peak and an anodic peak representing the electrochemical redox processes happening during the discharge and charge cycle. The presence of peak as observed here indicates the electrochemical activity of the host material with the ions in the electrolyte. Such activity can include intercalation of guest-ion, conversion process in host material or any parasitic reaction of

host material with the electrolyte.

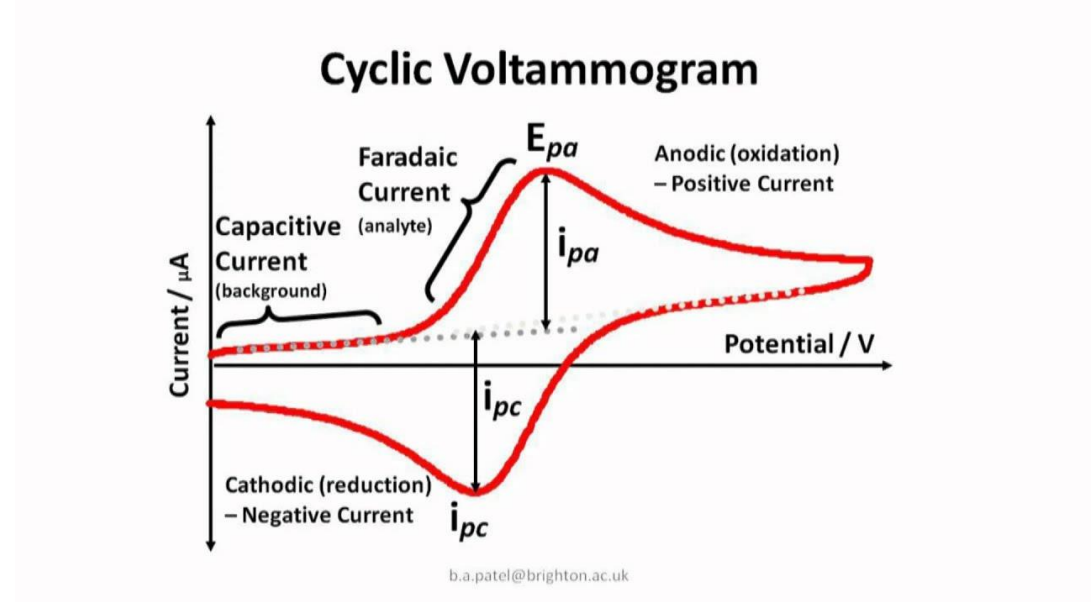

Figure 3-13. Cyclic voltammogram depicting redox process.[11]

3.4.2 Galvanostatic Charge and Discharge (GCD)

This electrochemical characterization technique includes applying a constant current between the working electrode and counter electrode within set cutoff voltages (w.r.t the reference electrode). As an output, the voltage response to constant current is observed and recorded to gauge the capacity of the material. The longer it takes the voltage to change, the higher is the capacity. The GCD profile also provides important information about the chemical potential and thermodynamics of the system. Typically, a first-order phase transformation is indicated by a flat plateau, whereas a smooth slope indicates the formation of a solid solution in the host material or a capacitive behaviour (typically at high rates).

3.4.3 Electrochemical impedance Spectroscopy (EIS)

EIS is an electrochemical technique that measures the impedance response of a system with respect to the varying AC frequencies. This technique takes advantage of the fact that different electrochemical cell components respond differently to varying AC

frequencies. A small alternating potential is applied across the cell, and the resultant current response is measured at various specified frequency values. Using I and V, one can find the value of the impedance of the system. The figure below shows one such impedance spectrum plotted in a complex plane and an equivalent circuitry with various components that can be used to fit the spectrum. Typically, such spectrum consist of a semicircle (indicative of the charge transfer as well as the electrode-electrolyte interfacial capacitance) starting from a certain impedance value (indicative of the charge transfer resistance in the system) and ending up into a sloping line (indicative of the diffusion kinetics in the system). The shape of the spectrum is determined by the number and type of components present in the system.

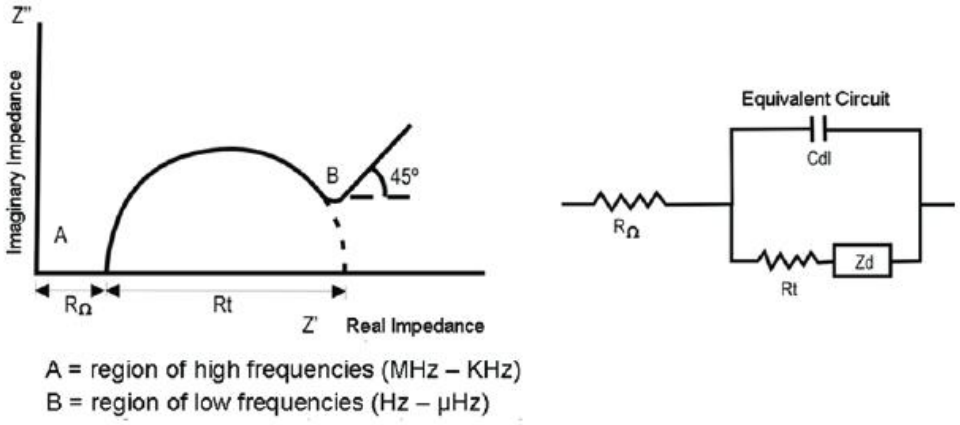

Figure 3-14. Impedance spectrum and the corresponding equivalent circuit of a lithium-ion battery illustrated as Nyquist plot.[11]

References

[1] S. H. Feng, G. H. Li. Chapter 4 - Hydrothermal and Solvothermal Syntheses. In *Modern Inorganic Synthetic Chemistry (Second Edition)*; Xu, R.,Xu, Y., Eds.; Elsevier: Amsterdam, 2017; pp 73-104.

[2] A. V. Rane, K. Kanny, V. K. Abitha, S. Thomas. Chapter 5 - Methods for Synthesis of Nanoparticles and Fabrication of Nanocomposites. In *Synthesis of Inorganic Nanomaterials*; Mohan Bhagyaraj, S., Oluwafemi, O. S., Kalarikkal, N.,Thomas, S., Eds.; Woodhead Publishing: 2018; pp 121-139.

[3] http://hyperphysics.phy-astr.gsu.edu/hbase/quantum/bragg.html (accessed 7 Feb).

[4] https://www.nanoscience.com/techniques/scanning-electron-microscopy/ (accessed 10 Feb).

[5] T. Dieing, O. Hollricher, J. Toporski. *Confocal Raman Microscopy*, Springer Science & Business Media: 2011; Vol. 158.

[6] http://www.casaxps.com/ebooks/XPS%20AES%20Book%20new%20margins%20rev%201.2%20for%20web.pdf (accessed 11 Feb).

[7] https://maths.tcd.ie/~bmurphy/thesis/thesisse4.html (accessed 15 Feb).

[8] B. Ravel, M. Newville. *J. Synchrotron Radiat.* **2005,** *12*, 537-541.

[9] J. Zhi, A. Z. Yazdi, G. Valappil, J. Haime, P. Chen. *Sci. Adv.* **2017,** *3*.

[10] V. Verma, S. Kumar, W. Manalastas Jr, R. Satish, M. Srinivasan. *Adv. Sustainable Syst.* **2019,** *3*, 1800111.

[11] A. J. Bard, L. R. Faulkner. *Electrochemical Methods: Fundamentals and Applications, 2nd Edition*, John Wiley and Sons: 2000; p 864.

Chapter 4*

Investigating $FeVO_4$ as a cathode material for aqueous aluminum-ion battery

This chapter explores the possibility of inserting Al-ion in a host material by a conversion-type mechanism. $FeVO_4$ has been explored as a potential conversion-type cathode material. It is first synthesized in the form of nanorods and studied for electrochemical activity towards Al-ion insertion. Further, its structural and compositional evolution during cycling has been studied in detail, revealing Al-ion intake by a conversion mechanism. A deterministic effect of increasing electrolyte pH on cycling stability has also been demonstrated, which reduces the side reactions between the host material and the electrolyte.

---

*This section published substantially as Kumar S, Satish R, Verma V, Ren H, Kidkhunthod P, Manalastas W, et al. Investigating FeVO4 as a cathode material for aqueous aluminum-ion battery. J Power Sources. 2019;426:151-61. (No written permission from Elsevier is necessary for thesis purpose) Copyright 2019 Elsevier B.V.

4.1 Introduction

AIAB being a new field, has very few numbers of electrode materials explored for Al-insertion. Most of these materials typically show insertion type mechanism.[1] However, the high charge density of Al-ion limits its diffusion in the host material. This often leads to limited capacity, structural disintegration and excessive non-reversible capacity causing capacity fading. One way to circumvent this problem is using a host material that would potentially show a conversion type reaction mechanism. Such materials react with guest-ions and form thermodynamically favourable phases, thus circumventing the excessive charge resistance occurring during intercalation. However, the reversibility of those new phases formed is not guaranteed and needs experimentation for confirmation. To the best of knowledge, such conversion type material has not been explored for AIAB, leaving a big research gap in this domain.

In this chapter $FeVO_4$ has been explored as a cathode material for AIAB. The electrochemical performance and the Al-ion insertion mechanism has been studied in detail. $FeVO_4$ is particularly chosen for this purpose because 1) It can potentially show conversion type mechanism as evidenced from previous reports[2-3], 2) it can be cycled within the thermodynamic stability window of water, and 3) It has demonstrated exceptional capacity in non-aqueous Li-ion batteries, allowing up to 8 Li-ions to be inserted. [2, 4] The synthesis of $FeVO_4$ is reported, followed by its demonstration as cathode material for AIAB. Further, the pH and concentration of the electrolyte have been modulated to enhance the battery performance. This material can deliver a specific capacity of ~350 mAh g^{-1} at 60 mA g^{-1}, which was pointedly higher than previously reported cathode materials for AIAB.[5] Further, the reaction mechanism for Al-ion insertion is studied in detail using a combination of in-house and synchrotron-based technique.

4.2 Experimental methods

4.2.1 Material Synthesis

$FeVO_4$ nanorods were produced by combining hydrothermal and dry annealing in a stepwise fashion, as stated elsewhere with minor changes. [4] 1 mmol $Fe(NO_3)3.9H_2O$ (Sigma-Aldrich, purity >99.9%) was dissolved in 15 mL deionized (DI) water at room temperature in this process. At 80°C, a stoichiometric volume of NH_4VO_3 (Sigma-Aldrich, purity >99%) was dissolved in 15 mL DI water. The two solutions were then combined as follows: under magnetic stirring, the NH_4VO_3 solution was slowly applied to the $Fe(NO_3)_3$ solution. After that, the resulting mixture was stirred for about 4 hours, allowing the solution enough time to react and transform into a homogeneous orange liquid. This mixture was then placed in a tight-sealed 50-mL Teflon-lined autoclave and heated to 160°C for a 5-hour dwell in a heating oven. After allowing the residue to cool to room temperature, it was filtered and washed three times with water and acetone (2 washings). This residue was dried in a vacuum oven overnight, then calcined in air for 2 hours at 500°C, recovered, and analyzed for purity.

Synthesis reaction:

$$Fe(NO_3)_3 + NH_4VO_3 + (x+1)H_2O \rightarrow FeVO_4.xH_2O + NH_4NO_3 + 2HNO_3$$

Upon calcination:

$$FeVO_4.xH_2O \rightarrow FeVO_4 + xH_2O$$

4.2.2 Material Characterization

XRD: Crystal structures were determined using a Bruker D8 Advance diffractometer with a Lynxeye-type detector and CuKα radiation in a Bragg-Brentano geometry (40 kV, 40 mA, 0.6 mm slit size). With a step size of 0.0248°, a scan time of 4 seconds per step was used. To achieve zero-background diffraction peaks, all runs used commercially available monocrystalline Si-based sample holders (Panalytical). The obtained XRD pattern for the synthesized $FeVO_4$ powder was then refined using the TOPAS 4.1 program.

The electrodes were removed from the electrochemical cells and screened without cutting the Ti current collector mesh for the charged/discharged electrodes samples A0-C4.

Instead of using offsets from routine refinement techniques, which were poorly converged due to the nanocrystallinity of the active material and extraneous binder/carbon phases, the collected XRD patterns were adjusted against the high, sharp Ti peak position to facilitate pattern-to-pattern comparisons. After that, the pattern intensities were normalized towards the most intense peak.

Microscopy: Morphological analysis was performed using a JEOL JSM-7600F field emission scanning electron microscope in SEI mode with a 5kV accelerating voltage and an 8mm working distance. The silicon-drift detectors used in the microscope-attached EDS systems were used to perform EDX elemental analyses of powder and electrode samples (Oxford Aztec Energy). Each sample was probed for around 600 seconds at a 20kV accelerating voltage while maintaining an optimum deadtime of 20% to 30%. Since the $FeVO_4$ rods are nanometric in size, a JEOL JEM-2100F TEM with a 200kV accelerating voltage was used to investigate the finer details of the powder morphologies.

Raman Spectroscopy: A WITec Alpha300 SR Confocal Raman Spectrometer was used to measure Raman shifts. A 488 nm Argon type laser was used to expose powder and electrode samples. In addition, spectra were standardized using the most extreme peak in each spectrum and analyzed using literature.

XPS: The oxidation state of the surface particles was investigated using the Kratos AXIS Supra XPS, which operates at 225 W and uses monochromated radiation (Al K_α, 1486.69 eV). The energy of the pass was set to 20 eV. With the aid of Casa XPS software, the obtained spectra were deconvoluted. Initially, each spectrum was tuned so that the adventitious C1s peaks were located at a binding energy of 284.8 eV. A non-linear (Shirley) baseline was used to eliminate the background. A combination of Lorentzian (30%) and Gaussian distributions were used to describe each suitable peak. It should be noted that narrow scans obtained for Fe were often indistinguishable from Fe satellite peaks. Hence, only Fe $2p_{3/2}$ peaks were analyzed.

4.2.3 Electrochemical Characterization

The active material, binder (Teflonized Acetylene Black), and conductive carbon (acetylene black) were combined in a ratio of 6:2:2 (3mg:1mg:1mg) and repeatedly pressed to form a pellet, which was then pressed onto a Ti mesh under a 7-ton force. Prior to testing, the shaped electrode was dried for 1 hour in a vacuum oven. All electrochemical testing was carried out in a 3-electrode flooded beaker cell with a Solartron Analytical 1470 E for CV and a BTS Neware for galvanostatic charge-discharge (GCD) studies. Except for the Ti current collector, no metal was submerged in the electrolyte during applied-bias testing. The pressed tablet composite served as the working electrode in this device, while carbon paper (AV carb GDS221OO) served as the counter electrode, and Ag/AgCl (in 3.5 KCl) electrodes served as voltage reference systems. All tests were carried out in either aqueous $AlCl_3$ solution prepared as-is or aqueous $AlCl_3$ solution that had been pH-modified (basified dropwise using ammonium hydroxide solution).

4.3 Results and discussion

4.3.1 Crystal structure and morphology

Acquired XRD patterns were Rietveld refined based on the *P-1* space group with full occupancy of Fe, V and O at 2i sites (Figure 4-1 a). With a crystallite size of 62.9 nm, the resulting lattice parameters were determined to be as a = 6.72 Å, b = 8.07 Å, c = 9.35 Å, $\alpha = 96.65°$, $\beta = 106.57°$, $\gamma = 101.6°$. (Full details of refinement in Table 4-1). The $FeVO_4$ structure has three distinct Fe atoms, similar to the Ziminaite phase (PDF no. 38-1373). Two of these non-equivalent Fe (Fe1 & Fe3) are in a distorted octahedral oxygen environment, whereas the third Fe (Fe2) is in a trigonal bipyramidal oxygen environment (Figure 4-1 b). Finally, the three V atoms form a distorted tetrahedral environment (red polyhedra).

Table 4-1: Rietveld refinement calculations for as synthesized $FeVO_4$ powder with Rwp and Rp of 1.48 and 1.3, respectively.

Atom	Wyckoff Sites	X	Y	Z	Occupation factor
Fe1	2i	0.75204	0.69423	0.40881	1
Fe2	2i	0.46597	0.88944	0.21160	1
Fe3	2i	0.96885	0.30568	0.01195	1
V1	2i	0.00496	0.99694	0.25674	1
V2	2i	0.19955	0.60155	0.34332	1
V3	2i	0.52063	0.29906	0.12734	1
O1	2i	0.64510	0.48440	0.25140	1
O2	2i	0.25480	0.43750	0.42600	1
O3	2i	0.05260	0.69900	0.42800	1
O4	2i	0.15860	0.09540	0.42910	1
O5	2i	0.45300	0.73880	0.36110	1
O6	2i	0.76110	0.86700	0.26490	1
O7	2i	0.52730	0.12770	0.21970	1
O8	2i	0.15140	0.87200	0.17720	1
O9	2i	0.35690	0.73080	0.01930	1
O10	2i	0.26410	0.29600	0.03850	1
O11	2i	0.94950	0.14520	0.15240	1
O12	2i	0.05370	0.52730	0.14720	1

The morphological characteristics of the synthesized $FeVO_4$ are shown in Figures 4-1 d-g. The obtained material crystallized in a predominantly nanorod morphology with seed-like particles, according to SEM images. The elemental maps obtained using SEM-EDX (Figure 4-1 h) revealed a uniform distribution of Fe, V, and O in the nanostructure. No other elements were detected in the EDS energy spectrum. The seed-like morphology on nanorod formations was supposed to be $FeVO_4$ crystals since no crystalline impurities were found in the XRD study. These could be $FeVO_4$ that nucleated but could not develop within the reaction time. It has been shown by researchers in past that longer reaction time in the hydrothermal vessel results in disappearance of these seed-like particles. The SEM micrograph in Figure 4-1 e has a high aspect ratio of about 10, and average diameter and average length of 190.5 nm and 1.70 m, respectively, according to statistical analysis (Figure 4-1 i, j).

4.3.2 Electrochemical performance

Figure 4-2 a shows the voltammogram of $FeVO_4$ cathode as cycled within a voltage range of -0.8V to 1V (vs Ag/AgCl). Two cathodic peaks at 0.2 and -0.2 V (vs Ag/AgCl) and two anodic peaks at 0.1 and 0.5 V (vs Ag/AgCl) can be found in the first cycle; these

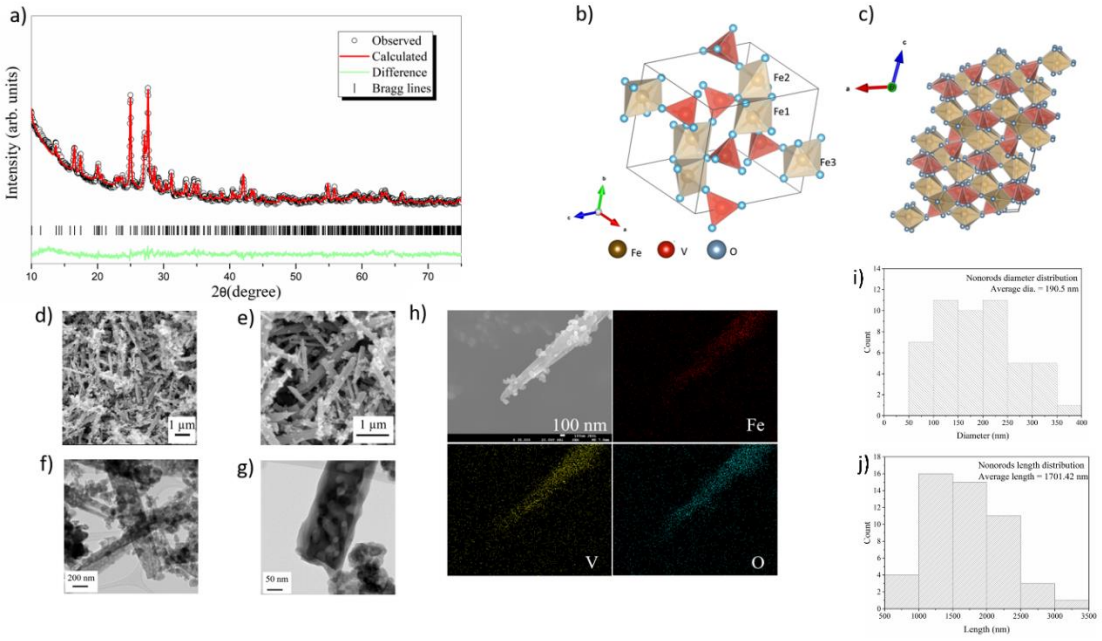

Figure. 4-1: Structural characterization of as synthesized $FeVO_4$ powder: (a) Rietveld-refined structure fitted to the experimental pattern, (b) unit cell of $FeVO_4$ (Fe1, Fe2, & Fe3 are three different environments of Fe) and (c) Crystal structure of $FeVO_4$ as viewed from the *b*-axis. $FeVO_4$ morphology study: (d) & (e) SEM micrographs, (f) & (g) TEM micrographs, (h) EDX elemental mappings of Fe, V, and O distributions in the synthesized $FeVO_4$ powder, and Statistical representation of nanorod size distribution (i) diameter and (j) length.

peaks become more established in subsequent cycles. The presence of these peak pairs may be attributed to reduction/oxidation processes occurring on $FeVO_4$'s transition metal centres, indicating a reversible electrochemical phenomenon. It is to be noted here that since there are parallelly occurring side reactions on the cathode, attributing these peaks to specific reduction phenomenon based on the thermodynamic values is not possible. Similar to what has been observed for Mg-ion in $FeVO_4$[6] and Al-ion in CuHCF, [7-9] the broadened profiles of the CV plots point to a complex insertion/reaction mechanism and weak insertion kinetics. In the absence of Al-ion in the electrolyte, controlled CV tests (Figure 4-2 b) was also performed, and no redox peaks in the NH_4OH or NH_4Cl

electrolyte were observed. This means that the electrochemical activity found in our sample is primarily due to Al-ion insertion/reaction, as other spectator ions (NH^{4+}, Cl^-, and OH^-) did not react.

The charge capacity of $FeVO_4$ was measured using a GCD study on the electrodes in 1 M $AlCl_3$ at 60 mA g^{-1}. Though the capacity was initially 250 mAh g^{-1}, it quickly degraded to 25 mAh g^{-1} after only three cycles (Figure 4-2 d, pH 1.9). After the first few cycles, an initially translucent electrolyte turned yellowish, suggesting possible vanadium dissolution into the electrolyte, as also predicted by the Pourbaix diagram of V.[10] To tackle dissolution, the pH of 1 M $AlCl_3$ electrolyte was raised from 1.9 to 3.5 by adding ammonium hydroxide solution, ensuring that the electrolyte remained homogeneous and no precipitate produced.

This step greatly decreased the electrolyte's apparent colour change during cycling. In the charge/discharge analysis, the initial capacity increased to 350 mAh g^{-1} (Figure 4-2 c), and the cycling stability improved in high pH electrolyte (Figure 4-2 d).

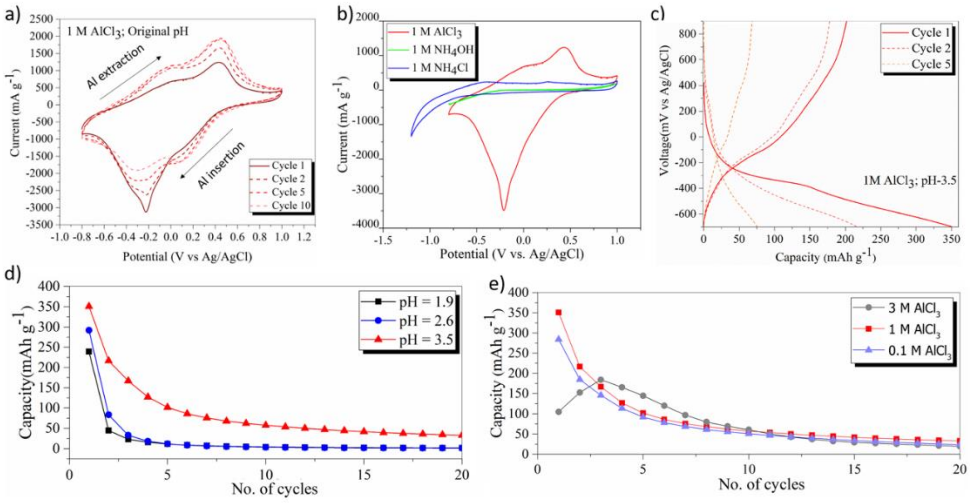

Figure 4-2: (a) Voltammograms in 1 M $AlCl_3$ with pH~1.9 at 10mV sec^{-1} (-ve scan followed by +ve). (b) Voltammograms in different electrolytes as a control experiment at 10mV sec^{-1}. (c) GCD plot in 1 M $AlCl_3$ with pH=3.5 at 60 mA g^{-1} (d) Cycling life in 1 M $AlCl_3$ under various pH (e) Cycling life at pH=3.5 for several concentrations of $AlCl_3$.

4.3.2 Effect of electrolyte pH

The thermodynamic trend centered on the equilibrium between a discharged cathode material (here: Al-reacted $FeVO_4$) and ionic/molecular species present in the aqueous electrolyte (here: H^+, OH^-, O_2, H_2, and H_2O) can explain this electrochemical change.

$$Al\ (intercalated) + \left(\frac{3}{4}\right)O_2 + (\frac{3}{2})H_2O \ \Leftrightarrow\ Al^{3+} + (3)OH^-$$

The introduction of cations into a host material results in a reduced oxidation state for redox-active centres to maintain charge balance. However, this cation reduction mechanism is limited to a certain amount of cation intake. This limit can also be expressed in terms of the host material's minimum reduction potential (V_{min}), beyond which the material becomes unstable. In this case, forcing current beyond this potential limit can result in irreversible decomposition of the electrode, the electrolyte, or both. In other words, a lower applied potential (V_{app}) than V_{min} would push the above reaction forward, resulting in host material destabilization. V_{min} for Al can be derived as a function of electrolyte pH and reacting ion concentration (here Al) as follows (derivation details in reference [5, 11-12]):

$$V_{min} = 4.290 - 0.059\,pH - 0.0066\log[\,Al^{3+}]\left(vs\,\frac{Li^+}{Li}\right)$$

A high pH electrolyte will result in a lower V_{min}, as can be deduced from the above equation. As a result, there exits a larger potential window for cycling the host material in a higher pH electrolyte with less chance of electrode destabilization and parallel electrolyte decomposition. It can be concluded that electrolyte with a higher pH value improved cycling stability based on this thermodynamic pattern. Cycling stability as a function of $AlCl_3$ concentration (Figure. 4-2 e) was also studied, finding that there was no discernible increase in cycling stability with the concentration increase. Eventually, 1 M $AlCl_3$ (pH =3.5) was considered the optimum electrolyte based on improved cycling performance and less amount of salt requirement.

4.3.3 Mechanism study

Ex-situ SEM-EDX, XRD, Raman spectroscopy, XPS, and XAS were used to investigate whether Al-ions were truly interacting with the electrode and gain insight into the Al-ion charge/discharge process. A0, A1, A2, A3, A4, B2, B4, C2, and C4 electrode samples were discharged/charged at 60 mA g^{-1} in 1 M $AlCl_3$, pH 3.5 (Sample specifics in Table 4-2 and represented in Fig. 4-4 c) and halted at various depths of discharge/charge. The electrodes were then retrieved, thoroughly washed with deionized (DI) water, cleaned, and characterized further.

Table 4-2: Details on charged/discharged electrode samples

Sample	Discharge (D)/ Charge (C) (vs. Ag/AgCl)
A0	Pristine electrode
A1	*1st cycle:* -0.2 V (D)
A2	*1st cycle:* -0.7 V (D)
A3	*1st cycle:* -0.7 V (D) and -0.3 V (C)
A4	*1st cycle:* -0.7 V (D) and 0.9 V (C)
B2	*2nd cycle:* -0.7 V (D)
B4	*2nd cycle:* -0.7 V (D) and 0.9 V (C)
C2	*5th cycle:* -0.7 V (D)
C4	*5th cycle:* -0.7 V (D) and 0.9 V (C)

EDX - SEM-EDX maps for fully discharged sample A2 (Figure 4-3) display a uniform distribution of Al in the scanned region that matches the elemental Fe, V, and O distributions well, suggesting a uniformly reacted electrode surface. SEM-EDX spectra were also obtained for the other samples in the A0-C4 series to investigate variations in Al material, and these EDX spectra were then used to compute the Al/V (Figure 4-4 a) and Fe/V (Figure 4-4 b) ratios. The Fe/V ratio was about 1 in all of the samples, indicating that the ratio was stable. Furthermore, the Al/V ratios followed a very clear trend, with all discharged samples (A1, A2, B2, C2) having a higher Al/V ratio and all charged samples (A3, A4, B4, C4) having a lower Al/V ratio. This finding clearly shows that Al-ions responded reversibly during the charging and discharging processes.

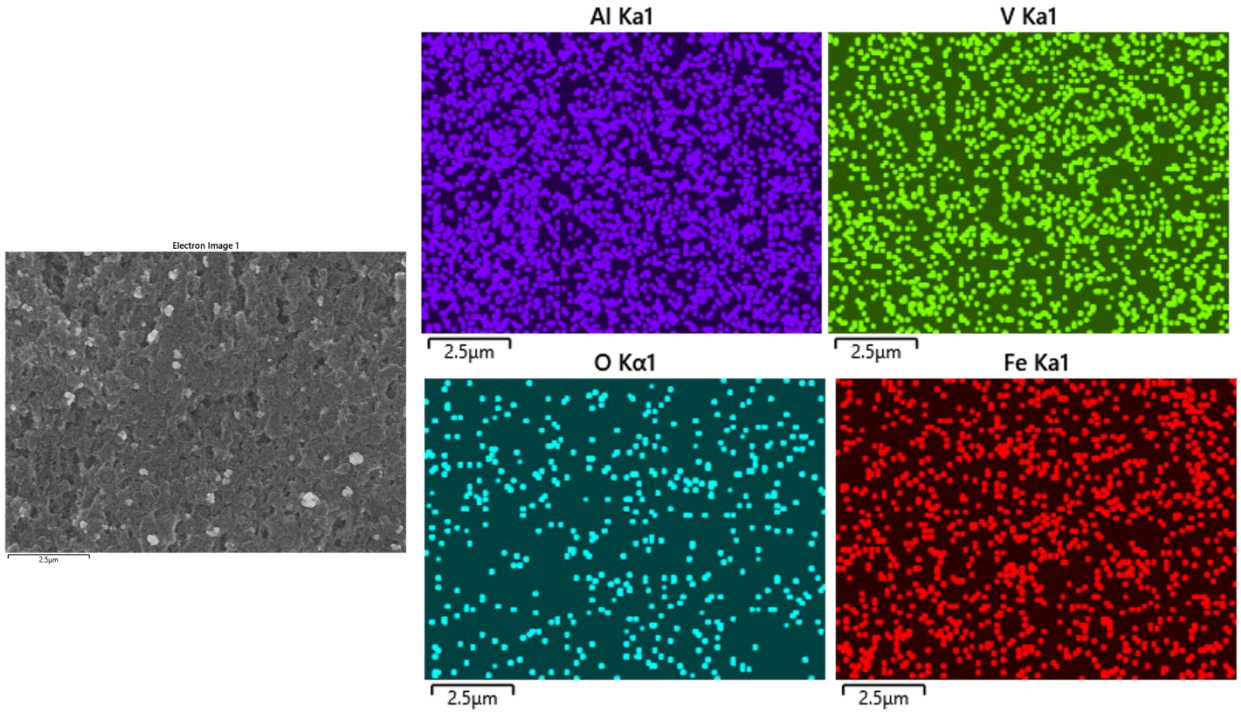

Figure 4-3: EDX elemental mappings of Al, O, V and Fe for electrode sample-A2.

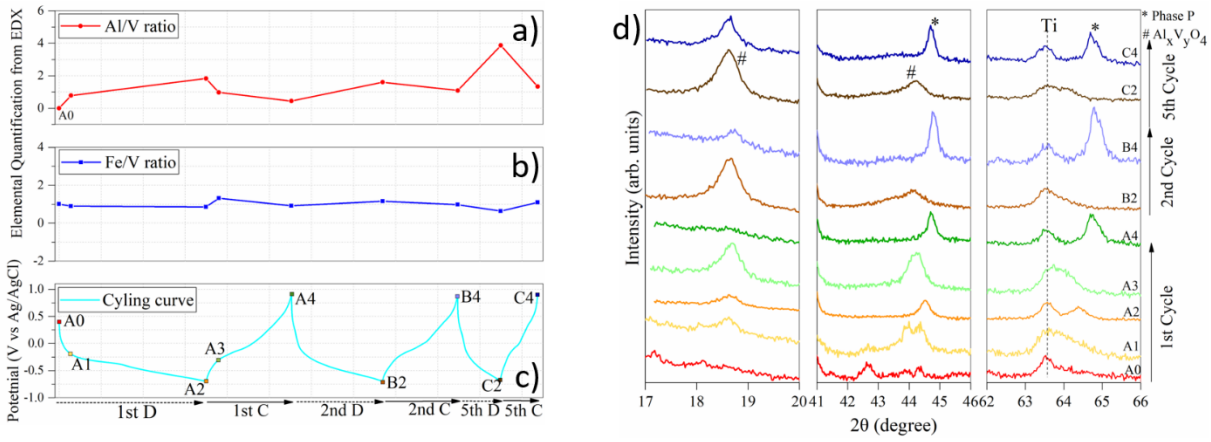

Figure 4-4: EDX quantification of electrode samples A0-C4: (a) Al/V ratio and (b) Fe/V ratio. (c) GCD profile with the charge/discharge state for electrodes A0-C4. (d) Ex-situ diffraction pattern of electrode samples A0-C4

XRD - The reaction of Al-ions with the $FeVO_4$ lattice is further confirmed by ex-situ XRD patterns of samples A0-C4. The most important portions of the scans in the XRD patterns are shown in Figure 4-4 d.

17 to 20°: There were no peaks in the pristine sample A0; however, a new peak occurs in the discharge phases (A1 and A2), rises in intensity at the start of charging (A3), and then vanishes entirely in the fully-charged sample (A4) (A4). This peak reappears during discharge (B2), weakens with charging (B4), and reappears with discharge (C2) and weakens with charging on subsequent cycling (C4). Except for sample A3, the new peak occurs in all discharged electrodes and fades/disappears in charged electrodes, in a clear pattern for all samples. Sample A3 is from the first charge/discharge period, implying that the material has gone through some kind of initial activation. In subsequent cycles, the Al-ion reaction produces a new phase that was not present in the electrode material when it was first prepared. This latest peak parallels spinel AlxVyO4 phases ($AlVO_3$, AlV_2O_4) and appears to be reversible [13-14]. AlV_2O_4 and $AlVO_3$ are trigonal and cubic crystal systems, respectively. This shows that Al-ions interact with the active materials to transform the triclinic $FeVO_4$ lattice into a more symmetrical system.

41 to 46°: There are two peaks of interest in this area: one at 44.3° (found in discharged samples) and another at 44.8°. (appearing in charged samples). The peak at 44.3° closely resembles the AlxVyO4 phase and occurs at the same time as the peak in the 17° to 20° θ region. The peak at 44.8°, on the other hand, was difficult to index, so it can be called as phase "P" for now and discussed later.

62 to 66°: There are two peaks in this range. The Ti substrate is responsible for the peak at 63.5°. The other peak, at 64.5°, is not visible in the pristine sample, but it emerges after cycling. This peak has a trend where it occurs in charged samples, more prominently in A4, B4, and C4, and then vanishes in discharged samples (B2 and C2). This means that Al-ion extraction results in forming a new phase that was not present in the electrode material before. This peak appears/disappears at the same time as the peak at 44.8°. As a result, we consider the peaks at 44.8° and 64.5° to be part of the same phase, “P,” which will be addressed further down in the XAS section.

The $FeVO_4$ cathode material does not accommodate Al-ions through a typical

intercalation process, according to XRD. It is seen that right after the first discharge, the original long-range order is permanently lost, but new phases appear reversibly as they appear systematically in all the discharged samples. The formation of an AlxVyO4 process upon Al intake and forming a phase P upon Al removal are both reversible. A conversion-type mechanism agrees with this permanent transformation to new phases entirely unrelated to the original crystal structure. These findings are consistent with previous findings on the reaction of lithium with $FeVO_4$ in non-aqueous batteries. [2, 15] Researchers in previous reports have stated that during the early stages of lithiation, the original $FeVO_4$ reflections vanish, and new peaks emerge that correspond to new phases such as $LiFeO_2$.[15]

Raman Spectroscopy: All of the samples A0 - C4 were then subjected to Raman analysis. The pristine $FeVO_4$ sample A0 has four characteristic Raman peak, as shown in Figure 4-5. These features are a combination of multiple undulations corresponding to various $FeVO_4$ bond vibrational modes and stretching: 1) shifts in the 880 to 950 cm^{-1} range arise from terminal V–O stretching modes; 2) shifts in the 700 to 880 cm^{-1} range represent bridging V–O···Fe stretching; 3) shifts from 550 to 700 cm^{-1} are mixed V–O···Fe & V···O···Fe stretching; and 4) shifts between 300 and 550 cm^{-1} correspond to V-O-V deformation and Fe-O stretching.[16-18]

The Raman spectra show a strong pattern, with $FeVO_4$ peaks diminishing or weakening in all discharged samples (A1, A2, B2, and C2) but re-emerging in charged samples (A4, B4 and C4). This shows two things: 1) The local environments of V and Fe shift drastically. The initial $FeVO_4$ may have vanished due to interactions with Al-ions, resulting in the formation of a new solid phase (invisible to Raman), or it may have undergone selective dissolution, leaving only carbon residue from the binder and conductive additive. The probability of $FeVO_4$ from the electrode surface dissolving into the electrolyte as V^{+5} and leaving metallic Fe_3Al phase on the surface will be discussed later; 2) The reappearance of the characteristic peaks suggests that $FeVO_4$ is structurally reversible, at least locally. It should be noted that XRD reflections indicated a non-reversible structural transformation of $FeVO_4$ upon discharge which is contrasting to the

Raman studies. This may be because XRD is a bulk technique, while Raman is a localized technique.

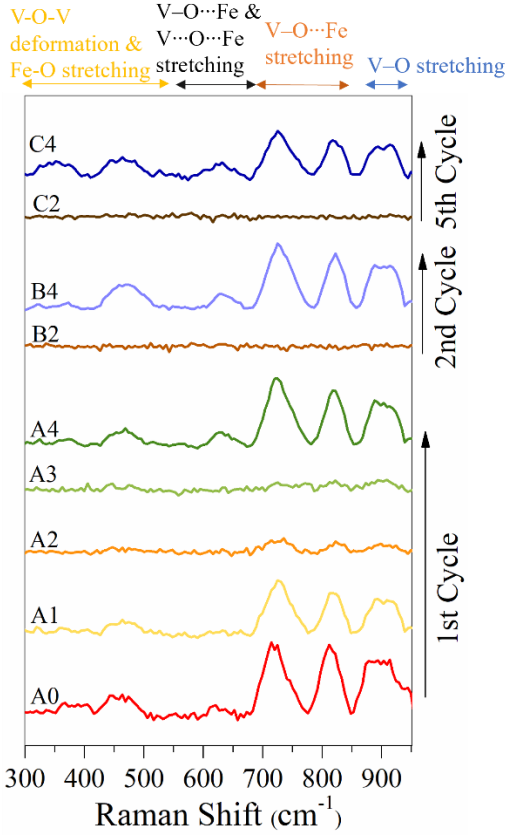

Figure 4-5: Ex-situ Raman shifts of samplesA0-C4

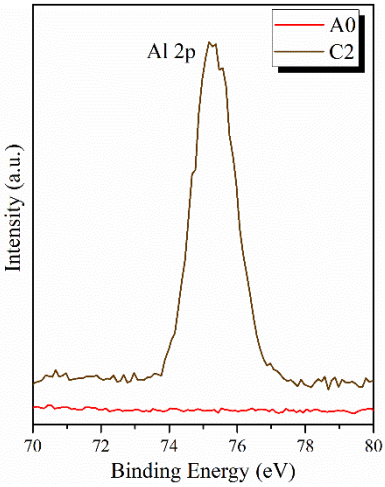

Figure 4-6: XPS of sample A0 and C2 showing Al 2p peaks.

Ex-situ XPS: In comparison to the pristine electrode A0, C2 showed clearly established Al 2p peaks (Figure 4-6) that reflect the Al oxide presence[19-21] and indicate Al-ion reaction with the electrode. It's probably the same phase $AlxVyO_4$, which was also detected in XRD analysis.

The evolution of V (Figure 4-7) and Fe (Figure 4-8) oxidation states are also studied for all samples A0-C4. The discharged electrode samples' V $2p_{3/2}$ peaks were substantially wider than the pristine and charged samples. This result suggests that the discharged samples have several V oxidation states (as wide peak will be fitted with more than one V peak).[22] It is observed: 1) In the first step, partial discharge produces a small amount of low-oxidation phase (A1). The initial $FeVO_4$ peak splits into two peaks at maximum discharge (A2), reflecting a high and low oxidation state of V (discussed in next paragraph). The peak narrows as charging progress, with maxima close to the initial $FeVO_4$ value 517.31 eV. 2) In the second and fifth cycles, a similar finding is made as in the first.

Based on the preceding observations, it can be deduced that at least two separate oxidation states of V form during discharge (lower oxidation state: simulated in green & higher oxidation state: simulated in blue). Spinel phases AlxVyO4 (also detected in XRD) have lower oxidation states of vanadium, with average oxidation states of +3 and +2.61. [13-14, 23] V in pristine $FeVO_4$ is already in the +5 state and cannot be further oxidized for the higher oxidation state. As a result, the change in V's coordination environment explains the shift to higher binding energy. The V $2p_{3/2}$ energy peak (517.9-518.5 eV) corresponds to a V_2O_5/Al_2O_3 phase.[22, 24] As a result, it is expected that during the Al-ion reaction, V_2O_5 will form, which will coexist with an Al oxide phase. V_2O_5 is one of the thermodynamically stable phases that $FeVO_4$ will disintegrate into, so its formation is very probable.[25] Since the V $2p_{3/2}$ peaks in the charged sample are narrow and recover a peak maxima close to the original energy value of the pristine sample, the reversible transformation back into $FeVO_4$ is also inferred.

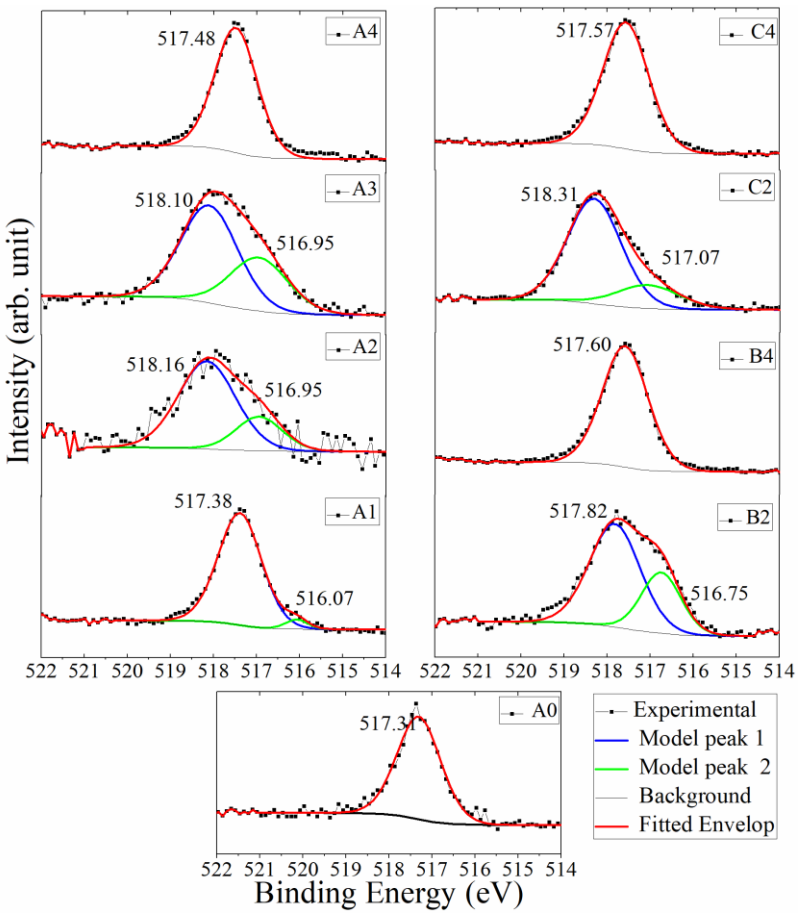

Figure 4-7: XPS spectra of samples (A0-C4) showing experimentally obtained and fitted V $2p_{3/2}$ peaks.

For discharged samples, all of the Fe 2p3/2 peaks have a broader FWHM, causing the Fe $2p_{3/2}$, Fe satellite peak, and Fe $2p_{1/2}$ peaks to become indistinct. 1) The low energy peak (blue) transitions to lower binding energy upon discharge and returns to its original location upon charging; the high energy peak (green) stays stationary. 2) All discharged and charged samples have a low binding energy peak (706-708 eV; brown model peak). The following is inferred from these findings: 1) discharged samples form a reversible low-oxidation phase (represented by the blue line), 2) a small amount of a new phase formed at ca. 707 eV after the 1st discharge can be attributed to metallic Fe_3Al.[26] Denis et al. previously documented the formation of such a metallic phase in a non-aqueous battery, in which Fe undergoes a metallic phase upon Li absorption and is reoxidized upon charging.[3] Both charged and discharged samples display this Fe_3Al phase. During

discharging, this metallic phase forms alongside V_2O_5, wherein some amount of V is likely to dissolve in the electrolyte. As a result, a portion of Fe_3Al could remain in the sample indefinitely.

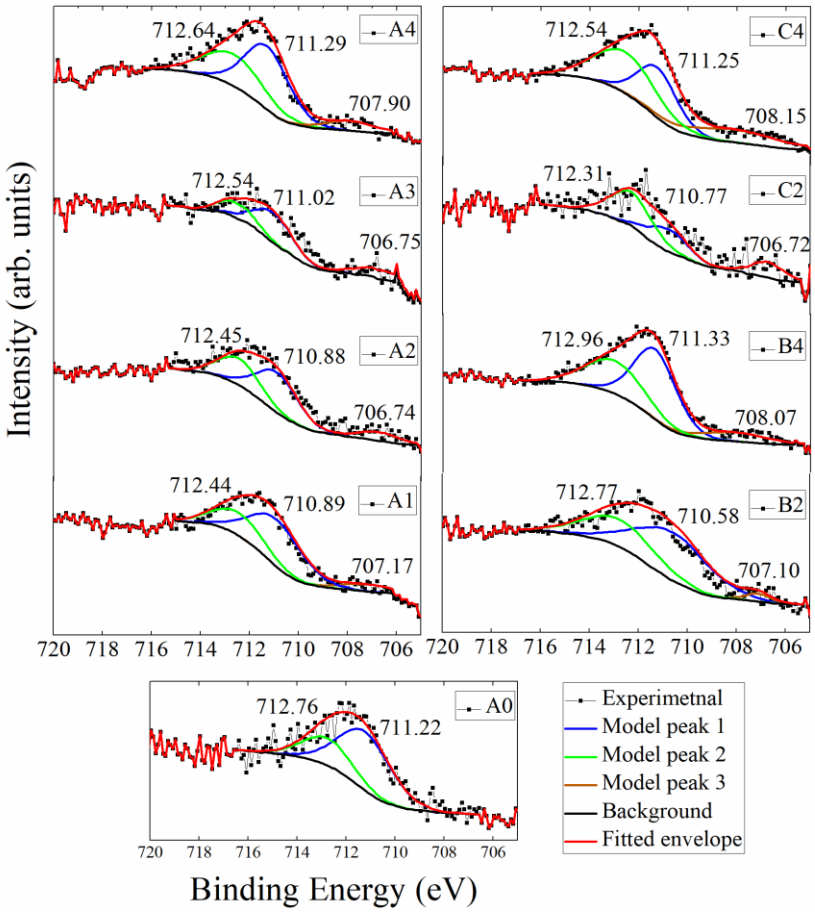

Figure 4-8: XPS spectra of samples (A0-C4) showing experimentally obtained and fitted Fe $2p_{3/2}$ peaks.

Ex-situ XAS: A comparison of samples A0 and A2 was performed. Three distinct peaks can be found: Peak A – It corresponds to local quadrupolar transitions in which an electron is excited from a central 1s orbital of Fe to an empty 3d orbital; [27] Peak B- It corresponds to a similar *1s3d* excitation which is non-local. Here a *1s* electron of the central atom - metal M (here: Fe) is excited to the unoccupied *3d* state of a next-nearest–neighbour metal M' (here: Fe') atom. Such a transition proceeds through an intersite hybridization M(*4p*)-O(*2p*)-M'(*3d)* (here: Fe(*4p*)-O(*2p*)-Fe'(*3d*)). The intensity of peak B

is a direct representation of the strength of this oxygen-mediated *4p-3d* hybridization, which depends on M-O-M' bonding;[28-29] and Peak C – It corresponds to the *1s4p* dipolar excitations, wherein excitation takes place from the core *1s* to the *4p* conduction band.[27]

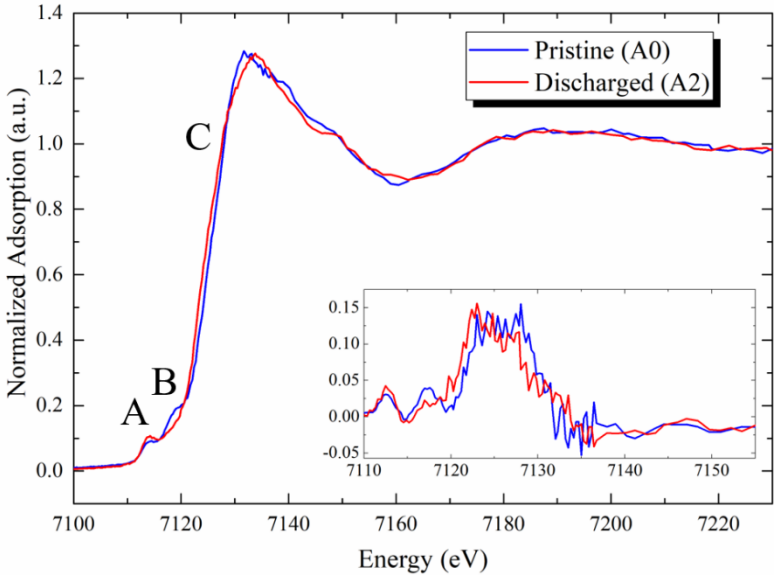

Figure 4-9: Ex-situ XAS spectra of samples A0 and A2.

The XANES spectra reveal that: 1) A2's peak C changes to a lower energy value (clearly seen in the first derivate of the spectrum in the inset of Figure 4.9). This suggests that the Fe-oxidation state has decreased[30] (also observed in the XPS study). This change of 1.5 eV is notable (Figure 4.10), implying that Fe could have been only partially reduced, as a shift of 4 eV is required when Fe^{+3} reduces to Fe^{+2}.[30]; 2) for the discharged sample, A2, the peak A strength increases. This indicates partial breaking of inversion symmetry for the Fe shell, wherein the Fe octahedral coordination is changing to a lesser symmetrical system causing *3d-4p* wavefunction mixing that allows electronic excitation to the *4p* character of the *3d* band.[27] 3) When peak B is discharged, its amplitude drops dramatically. This corresponds to the factors that can affect Fe(4p)-O(2p)-Fe'(3d) hybridization, namely Fe-O-Fe bond length and/or Fe-O-Fe bond angle.[27] Based on the above findings, we infer that Fe decreases upon Al-intake, forming a phase with weaker or no Fe-O-Fe bonds.

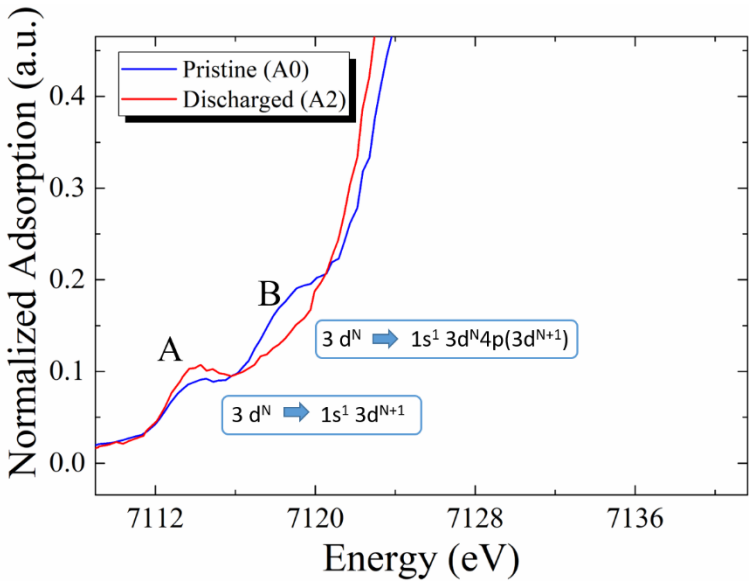

Figure 4-10: Zoomed in XAS spectra of samples A0 and A2. Peaks A and B with their respective electronic transition

A fitted Fourier transform of XAS spectra is shown in Figure 4-11. According to EXAFS fitting, the average Fe-O bond length for sample A2 is around 0.03 Å shorter than for pristine samples, A0. Normally, upon reduction, the length of the bond increases; however, the reverse is true here. Fe in oxides has been shown to have such an anomaly. [31] The ionic radii of Fe in oxidation states +3 and +2 are, for example, 1.759 Å and 1.734 Å, respectively. [32] As has been observed for related octahedral environments in $FeAlO_3$ and $FeGaO_3$ in terms of shorter than normal Fe-O bond lengths, this phenomenon may very well be an effect of increased covalence character in Fe-O bonds.[31] It is to be noted here that EXAFS fitting in figure 4-11 has been done using only Fe-O (absorbing atom and immediate neighbour) scattering path as the data of interest was only Fe-O bond length. For any typical EXAFS data, the scattering signals from the immediate neighbours are good enough to fit the first shell, however it will not fit the next shells well. This essentially means that the fitting beyond 2 Å will not be good. The last two peaks could only have been fitted well if more scattering paths (ex-Fe-Fe, fe-O-Fe, Fe-V etc) were also used for the fitting.

Overall, an amorphous (as no crystalline FeO phase was found for A2 in the XRD study) Fe oxide with a shorter covalent Fe-O bond is predicted to form where the average

oxidation state of iron is between +3 and +2. This phase has a weak or non-existent Fe-O-Fe bond, suggesting that it is a Fe-O-Al phase. This phase is most likely converting to a crystalline Fe-O phase, which was detected by XRD as phase "P" when charged.

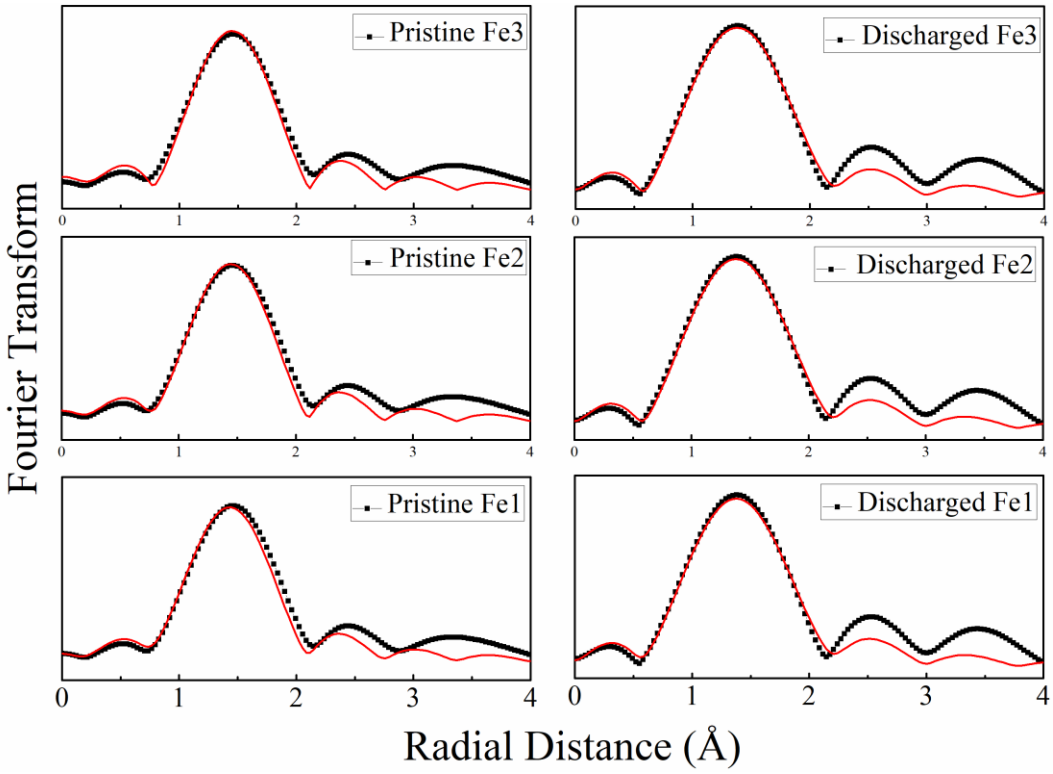

Figure 4-11: First shell EXAFS fitting for samples A0 (pristine) and A2 (discharged) electrodes in Hanning window of 1-3.

Table 4-3: EXAFS fitting results CN: Coordination number; σ^2: EXAFS Debye-Waller factor; R: Bond length (Å); R-factor: Goodness of fit.

Sample	**Fe (environment)**	**CN**	**σ^2**	**R**	**R-factor**
Pristine	Fe 1 (Oct)	6	0.010	1.960	0.025
	Fe2 (Tri. Bipy)	4 1	0.007 0.007	1.951 2.045	0.018 0.018

	Fe3 (Oct')	4 2	0.001 0.001	1.936 2.073	0.018 0.018
Discharged	Fe 1 (Oct)	6	0.015	1.933	0.016
	Fe2 (Tri. Bipy)	4 1	0.012 0.012	1.920 2.015	0.015 0.015
	Fe3 (Oct')	4 2	0.009 0.009	1.901 2.038	0.015 0.015

UV-Vis Spectroscopy: While the dissolution of the electrode was delayed to some degree by increasing the pH value, it could not be completely stopped. The UV-Vis spectrum of a high pH electrolyte cycled for 100 cycles are shown in Figure 4-12. This spectrum is similar to sodium metavanadate and sodium orthovanadate in an aqueous solution, where V is in the +5 oxidation state.[33]

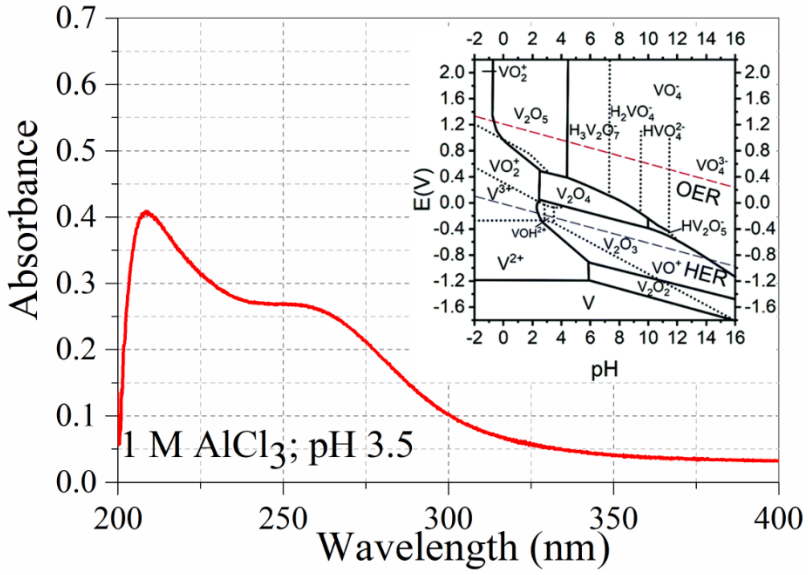

Figure 4-12: Uv-Vis spectrum for 1M $AlCl_3$, pH -3.5 electrolyte obtained after 100 cycles of charge/discharge (inset: E vs pH diagram for V; Reproduced from.[10] Copyright 2018, RSC).

4.4 Conclusion

In conclusion, $FeVO_4$ was investigated as a possible cathode material for AIAB, showing

Al-ion intake by a conversion type mechanism. It demonstrated an unprecedented capacity of 350 mAh g^{-1}. A pH modulated $AlCl_3$ was used to show that increasing pH positively impacts the cathode capacity retention. Ample proof of Al-ion intake in $FeVO_4$ has been provided, and the likely mechanism in action is explored using a combination of various characterization techniques.

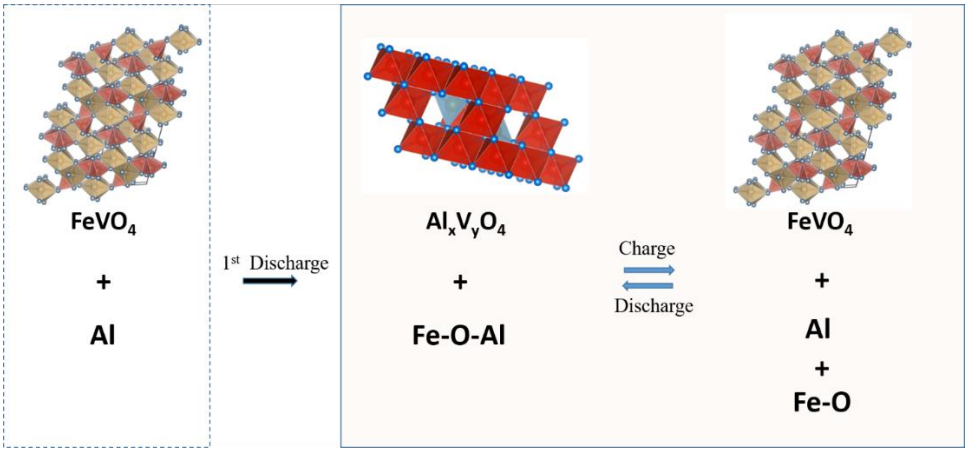

Figure 4-13: Predicted reaction mechanism of $FeVO_4$ showing only reversible phases.

There are two sets of reactions going on at the same time: "$FeVO_4$ reacting with Al" and "$FeVO_4$ reacting with electrolyte." Though the ongoing parasitic reactions make determining the exact mechanism of Al reaction with $FeVO_4$ difficult, it is suggested that Al-ion intake into $FeVO_4$ results in the creation of an AlxVyO4 spinel phase and an amorphous Fe-O-Al phase, both of which are reversible and electrochemically active (Figure 4-13). $FeVO_4$ from the surface reacts with the electrolyte to form V_2O_5 and metallic Fe_3Al at the same time. Furthermore, $FeVO_4$ and Fe-O phases form during charging, V_2O_5 dissolves into the electrolyte as V^{+5}, and metallic phase Fe_3Al is still present on the surface. Per cycle, some V^{+5} dissolves and stays trapped in the electrolyte, where it could have been converted back to $FeVO_4$ reversibly. This is most likely why capacity decreases with each cycle.

References

[1] V. Verma, S. Kumar, W. Manalastas Jr, R. Satish, M. Srinivasan. *Adv. Sustainable Syst.* **2019,** *3*, 1800111.

[2] S. Denis, E. Baudrin, F. Orsini, G. Ouvrard, M. Touboul, J. M. Tarascon. *J. Power Sources.* **1999,** *81-82*, 79-84.

[3] S. Denis, R. Dedryvère, E. Baudrin, S. Laruelle, M. Touboul, J. Olivier-Fourcade, J. C. Jumas, J. M. Tarascon. *Chem. Mater.* **2000,** *12*, 3733-3739.

[4] X. Liu, Y. Cao, H. Zheng, X. Chen, C. Feng. *Appl. Surf. Sci.* **2017,** *394*, 183-189.

[5] V. Verma, S. Kumar, W. Manalastas, R. Satish, M. Srinivasan. *Adv. Sustainable Syst.* **2018,** *0*, 1800111.

[6] H. Zhang, K. Ye, K. Zhu, R. Cang, J. Yan, K. Cheng, G. Wang, D. Cao. *Chem-Eur. J.* **2017,** *23*, 17118-17126.

[7] S. Liu, G. L. Pan, G. R. Li, X. P. Gao. *J. Mater. Chem. A.* **2015,** *3*, 959-962.

[8] R. Y. Wang, B. Shyam, K. H. Stone, J. N. Weker, M. Pasta, H.-W. Lee, M. F. Toney, Y. Cui. *Adv. Energy Mater.* **2015,** *5*, 1401869.

[9] Z. Li, K. Xiang, W. Xing, W. C. Carter, Y. M. Chiang. *Adv. Energy Mater.* **2014,** *5*, 1401410.

[10] S. Boyd, V. Augustyn. *Inorg. Chem. Front.* **2018,** *5*, 999-1015.

[11] J.-Y. Luo, W.-J. Cui, P. He, Y.-Y. Xia. *Nat. Chem.* **2010,** *2*, 760.

[12] W. Li, W. R. McKinnon, J. R. Dahn. *J. Electrochem. Soc.* **1994,** *141*, 2310-2316.

[13] K.-i. Matsuno, T. Katsufuji, S. Mori, Y. Moritomo, A. Machida, E. Nishibori, M. Takata, M. Sakata, N. Yamamoto, H. Takagi. *J. Phys. Soc. Jpn.* **2001,** *70*, 1456-1459.

[14] A. F. Reid, T. M. Sabine. *J. Solid State Chem.* **1970,** *2*, 203-208.

[15] M. Hayashibara, M. Eguchi, T. Miura, T. Kishi. *Solid State Ionics.* **1997,** *98*, 119-125.

[16] L. Grazia, D. Bonincontro, A. Lolli, T. Tabanelli, C. Lucarelli, S. Albonetti, F. Cavani. *Green Chem.* **2017,** *19*, 4412-4422.

[17] A. Š. Vuk, B. Orel, G. Dražič, F. Decker, P. Colomban. *J. Sol-Gel Sci. Technol.* **2002,** *23*, 165-181.

[18] H. Tian, I. E. Wachs, L. E. Briand. *J. Phys. Chem. B.* **2005,** *109*, 23491-23499.

[19] S. L. Chang, J. W. Anderegg, P. A. Thiel. *J. Non·Cryst. Solids.* **1996,** *195*, 95-101.

[20] I. Olefjord, H. J. Mathieu, P. Marcus. *Surf. Interface Anal.* **1990,** *15*, 681-692.

[21] A. M. Venezia, C. M. Loxton, J. A. Horton. *Surf Sci.* **1990,** *225*, 195-205.

[22] N. K. Nag, F. E. Massoth. *J. Catal.* **1990,** *124*, 127-132.

[23] E. J. W. Verwey, E. L. Heilmann. *J. Chem. Phys.* **1947,** *15*, 174-180.

[24] K. V. R. Chary, C. P. Kumar, D. Naresh, T. Bhaskar, Y. Sakata. *J. Mol. Catal. A: Chem.* **2006,** *243*, 149-157.

[25] J. Walczak, J. Ziollkowski, M. Kurzawa, J. Osten-Saacken, M. Lysio. *Pol. J. Chem.* **1985,** *59*.

[26] I. N. Shabanova, V. A. Trapeznikov. *J. Electron. Spectrosc. Relat. Phenom.* **1975,** *6*, 297-307.

[27] G. Frank de, V. György, G. Pieter. *J. Phys.: Condens. Matter*. **2009,** *21*, 104207.

[28] J. A. Sigrist, M. W. Gaultois, A. P. Grosvenor. *J. Phys. Chem. A.* **2011,** *115*, 1908-1912.

[29] F. M. F. de Groot, P. Glatzel, U. Bergmann, P. A. van Aken, R. A. Barrea, S. Klemme, M. Hävecker, A. Knop-Gericke, W. M. Heijboer, B. M. Weckhuysen. *J. Phys. Chem. B.* **2005,** *109*, 20751-20762.

[30] W. M. Heijboer, P. Glatzel, K. R. Sawant, R. F. Lobo, U. Bergmann, R. A. Barrea, D. C. Koningsberger, B. M. Weckhuysen, F. M. F. de Groot. *J. Phys. Chem. B.* **2004,** *108*, 10002-10011.

[31] P. Ravindran, R. Vidya, H. Fjellvåg, A. Kjekshus. *Phys. Rev. B.* **2008,** *77*, 134448.

[32] N. E. Brese, M. O'Keeffe. *Acta Crystallogr. B.* **1991,** *47*, 192-197.

[33] E. Mutlu, T. Cristy, S. W. Graves, M. J. Hooth, S. Waidyanatha. *Environ. Sci. Pollut. R.* **2017,** *24*, 405-416.

Chapter 5*

Investigating Vanadium dioxide holey nanobelt as a cathode material for aqueous aluminum-ion battery

In this chapter, bronze-type vanadium dioxide (VO_2–B) holey nanobelts have been designed as a high performing cathode material in terms of both the capacity and cycling stability. Benefiting from the unique shear structure and two-dimensional holey nanobelt morphology, the VO_2–B electrode delivers a superior specific capacity of up to 234 mAh g^{-1} at 150 mA g^{-1} and exhibits high-capacity retention of 77.2% over 1000 cycles at 1 A g^{-1}, which are among the best cathode performances reported for AIAB. Moreover, electro-kinetic analysis and ex-situ structural and compositional evolution characterization experiments reveal the reaction storage mechanism.

This section published substantially as Cai Y, Kumar S*, Chua R, Verma V, Yuan D, Kou Z, et al. Bronze-type vanadium dioxide holey nanobelts as high performing cathode material for aqueous aluminium-ion batteries. J Mater Chem A. 2020;8(25):12716-22. (No written permission from RSC is necessary for thesis purpose).

5.1 Introduction

Vanadium oxides have emerged as a popular candidate for multi-valent ion insertion. Its various oxidation states allow for the formation of robust and voided crystal structures which can tolerate the insertion of large-sized ions. Recent investigations have also demonstrated that a tunnel structured may be more robust and stable for insertion of such large-sized ions as compared to a layered structure.[1-3] Hence there remains a research gap in exploring a tunnel structured vanadium oxide for AIAB. It is to be noted here that in an aqueous electrolyte, the size of ions (0.53 Å for Al^{3+}, 0.74 Å for Zn^{2+} and 0.76 Å for Li^{+1}, +0.72 Å Mg^{2+}, respectively) changes to larger values because of hydration (1.89 Å for Al^{3+}, 2.08 Å for Zn^{2+}, 2.10 Å for $Mg^{2+}$and 1.95 Å for Li^{+})[29-33]. Hence for systems like AIAB, the large sized tunnels of VO_2 are quite critical for successful insertion.

In this chapter, 2-dimensional holey nanobelts of vanadium dioxide (VO_2) have been explored as a potential cathode material for AIAB. This bronze-type crystal has a bilayer shear structure forming a tunnel-like framework by the corner and edge-sharing of VO_6 octahedra.[26] This kind of shear structure is likely to strengthen the material's structural integrity due to the increased edge-shearing, and the consequent resistance offered to lattice shearing during insertion/de-insertion. [27, 28] Theoretically, this particular structure of VO is quite promising for the storage of high-charge density Al-ion which is likely to experience high resistance during diffusion in the host material. Additionally, the final synthesized product is in a porous and 2-dimensional form. This will provide a larger interfacial contact area with the electrolyte & hence enhance the electrochemical activity. Testing this material, a high capacity of 234 mAh g^{-1} at 150 mA g^{-1} is reported. At a higher rate of 1 A g^{-1}, remarkable long-term cycling stability for 1000 cycles with a capacity retention of 77.2% is also reported. The concomitant mechanism of insertion/de-insertion is also studied via ex-situ studies focusing on the evolution of elemental composition, crystal structure and valence states during cycling.

5.2 Experimental methods

5.2.1 Material Synthesis

VO_2 was synthesized by a simple hydrothermal reduction of V_2O_5 using glucose. Analytical grades of solvent and reactants were used for the synthesis. V_2O_5 and glucose were dispersed in 30 ml of deionized water in a molar ratio of 1.25:1 and then stirred for about 1 hour. The solution was further transferred to a 50 ml Teflon stainless steel autoclave and maintained isothermally for 24 hours at 180 °C. Finally, the precipitate was cleaned with water and ethanol several times and dried at 80 °C overnight in a vacuum oven. The final product was further taken for XRD and cathode fabrication.

5.2.2 Material Characterization

A Bruker D8 Advance powder diffractometer with Cu-Kα radiation was used to obtain the product's X-Ray diffraction (XRD) pattern. Scanning electron microscopy (SEM, JSM-7600F, JEOL) and transmission electron microscopy (TEM, JEOL 2100F) were used to examine the morphologies. A Confocal Raman Microscopy (WITec) was used to capture Raman spectra at room temperature using a 488 nm excitation wavelength. The surface electronic states were studied using X-ray photoelectron spectroscopy (Kratos AXIS Supra). The spectra's binding energies were calibrated using C1s = 284.6 eV.

5.2.3 Electrochemical Characterization

VO_2-B powder, super P carbon, and teflonized acetylene black (TAB) were mixed in a weight ratio of 6: 2: 2 to make the working electrodes. The mixture was then pressed against titanium wire (Good Fellow). Three electrodes set up cells were used to perform electrochemical measurements. The counter and reference electrodes were made of graphite paper and Ag/AgCl (saturated KCl), respectively. Solartron 1256 B was used to perform cyclic voltammetry (CV) measurements. The Neware BTS device was used to perform galvanostatic charge and discharge measurements. Both electrochemical experiments were carried out at room temperature.

5.3 Results and discussion

5.3.1 Crystal structure and morphology

Shown in Figure 5-1 a is the diffraction pattern of the synthesized VO_2-B. The peaks could be indexed well with the monoclinic crystal structure of VO_2-B (PDF No. 96-153-0871, *C2/m* space group).[4] The sequence of peaks corresponding to the planes (110), (40-1), (31-1), and (020) are sharper than those corresponding to the planes (002) and (003), suggesting a favoured orientation. The corresponding crystallographic presentation is shown in figure 5-1 b. The fundamental units of the structure are the distorted VO_6 octahedra which share corners and edges along the c direction of the unit cell. Such a structure is likely to tolerate the lattice strain because of possible edge shearing. Additionally, the large tunnel size (3.281 × Å 4.984 Å) in this structure is sufficient for the intercalation of Al^{3+} (0.53 Å; hydrated Al^{3+}- 1.89 Å).[5]

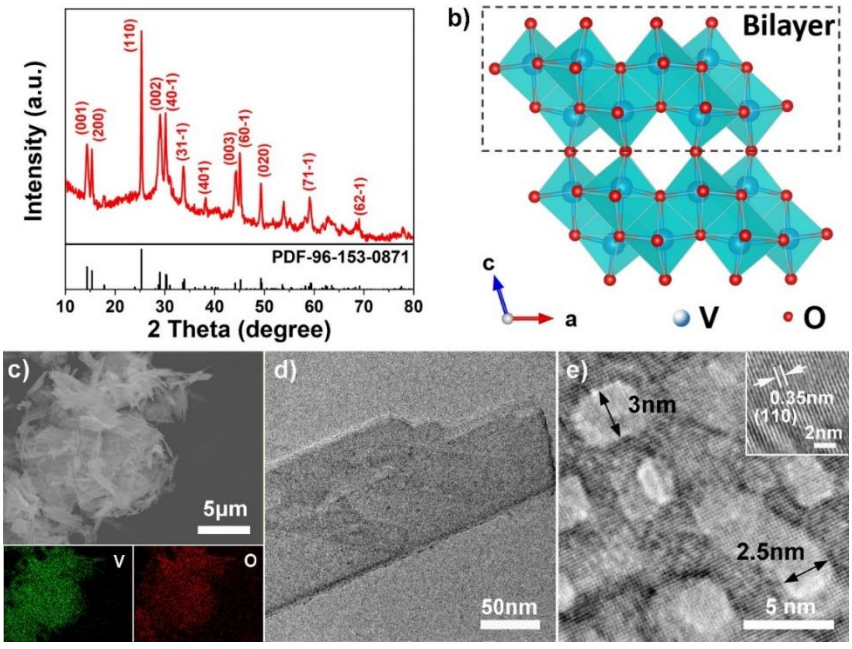

Figure 5-1: Structural and morphological characterizations of the VO_2-B powder: a) Diffraction pattern, b) crystal structure, c) SEM image with EDS mapping of the as-synthesized powder B, d) TEM and e) high-resolution TEM images of as-synthesized powder.

SEM was further used to investigate the morphology of the final synthesized powder. The material has a 2-dimensional, belt-like morphology with an aggregate length of ~ 5 μm (Figure 5-1 c). Such belt-like morphology is in line with the previous reports which show a nucleation and growth mechanism for VO_2, wherein, only a small percentage of nuclei survives and grows to form the long belt like morphology. Hence no nanoparticles forms. An EXD analysis also shows the uniform distribution of V and O throughout the material indicating the homogeneity in the synthesized powder. TEM analysis indicates high aspect ratio of powder showing a width of about 100 nm (Figure 5-1 d). Furthermore, some holes of about 3 nm can also be seen on the nanobelts (Figure 5-1 e). This unique morphology is likely to enhance the ion-diffusivity and increase the electrode-electrolyte (due to holes and high aspect ratio at nanoscale) contact facilitating improved electro-kinetics. In the inset of Figure 1e, a high-resolution TEM (HRTEM) image shows well-resolved lattice spacing of 0.35 nm, which belongs to the monoclinic VO_2-B structure's (110) crystal plane (PDF No.- 96-153-0871).

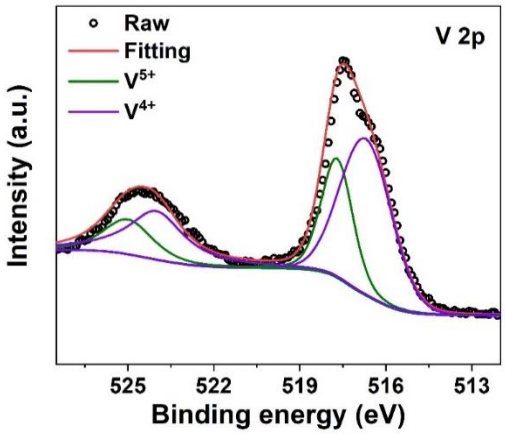

Figure 5-2: V 2p region of XPS spectrum for the as-synthesized powder

The oxidation state of the powder was determined using XPS (Figure 5-2). As can be seen, the collected spectrum could be deconvoluted into two-component peaks. V $2p_{3/2}$ peak was resolved into two peaks at 517.7 eV and 516.7 eV, which corresponds to the pentavalent (V^{5+}) and tetravalent (V^{4+}) oxidation states of the vanadium, respectively.[6-7] It

is speculated that the presence of pentavalent V can be due to partial surface oxidation, which is in line with previous studies.[38] In addition, previous research has shown that multivalent vanadium on the surface can improve the electronic conductivity of vanadium oxides.[8-10] Hence it will only be advantageous.

5.3.2 Electrochemical performance

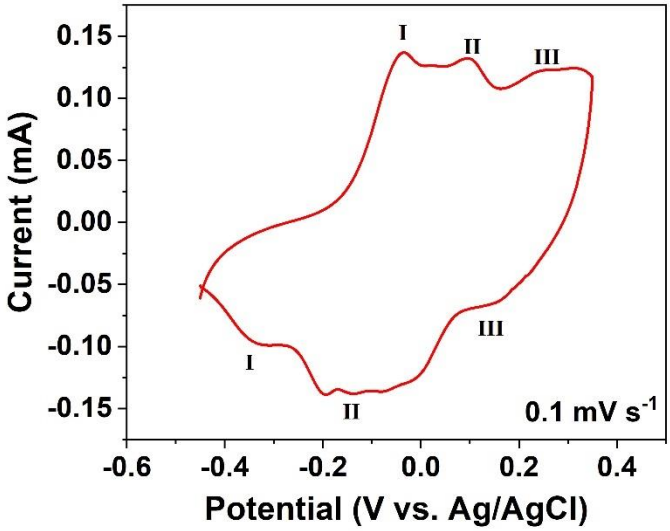

Figure 5-3: Cyclic voltammogram for VO_2-B cathode material tested in 5 m AlTFS electrolyte.

First and foremost, the active material was tested for its activity towards Al-insertion by doing a slow rate cyclic voltammetry in 5 m AlTFS electrolyte (Figure 5-3). The broad nature of the voltammogram with multiple peaks indicates a rather complex and multi-stepped insertion process. Such broad peaks have been observed in the past for multivalent ions like Mg^{2+} in $FeVO_4$[11] and Al^{3+} in CuHCF.[12-14]

Further, a capacity retention study was done on the active material. Initially, a rapid capacity fading was observed when the material was tested 2 m AlTFS electrolyte. Based on the knowledge that salt concentration can change the physical and chemical properties of the electrolyte, eventually leading to enhanced cycling performance,[15-18] the concentration was optimized for better performance. As shown in figure 5-4 a, the

capacity retention of the active material improved with the increase in the electrolyte concentration. This can be attributed to the significantly reduced activity of the water molecule because of the increased numbers of intimate ion-pair in the high concentration electrolyte. [19-20]

It cannot be denied here that even after concentration modulation, there is a substantial loss of initial capacity. One strategy to improve the performance further could have been to increase the salt concentration further. However, making a more concentrated AlTFS is not possible as ~ 5 m is the maximum solubility of the AlTFS electrolyte in DI water and an increased concentration would lead to precipitation. Alternatively, one could make a hybrid electrolyte by adding some salt of Li with high solubility in water. However, the study of such concentrated hybrid electrolyte is outside the scope of this study because that leads to adding the complexity of the insertion process, making it even more difficult to decipher the same. The dissolution observed here can be explained using the Pourbaix diagram of vanadium.[21] At low pH, as is the case here, thermodynamically favourable species such as $HV_2O_5^-$, $H_3V_2O_7^-$, or VO^{2+} can form by vanadium dissolution from the cathode material.[22-23] This partial dissolution is observed in the initial stages of cycling; however, once a certain amount of the above-mentioned species has dissolved into the electrolyte, the electrode attains equilibrium with the vanadium compound in the electrode. Hence in the later stage of the cycling, the stability does not drop significantly.

This is also reflected in the long-term cycling performance of VO_2-B (Figure 5-4 c). This material can maintain a capacity of 56.6 mAh g^{-1} after 1000 cycles at a high cycling rate of 1 A g^{-1}. As expected, the specific capacity of the material is reduced at this high rate, speculated to be due to kinetic limitations because of rapid insertion and de-insertion. Such long-term stability is unprecedented with the contemporary AIAB literature.[21]

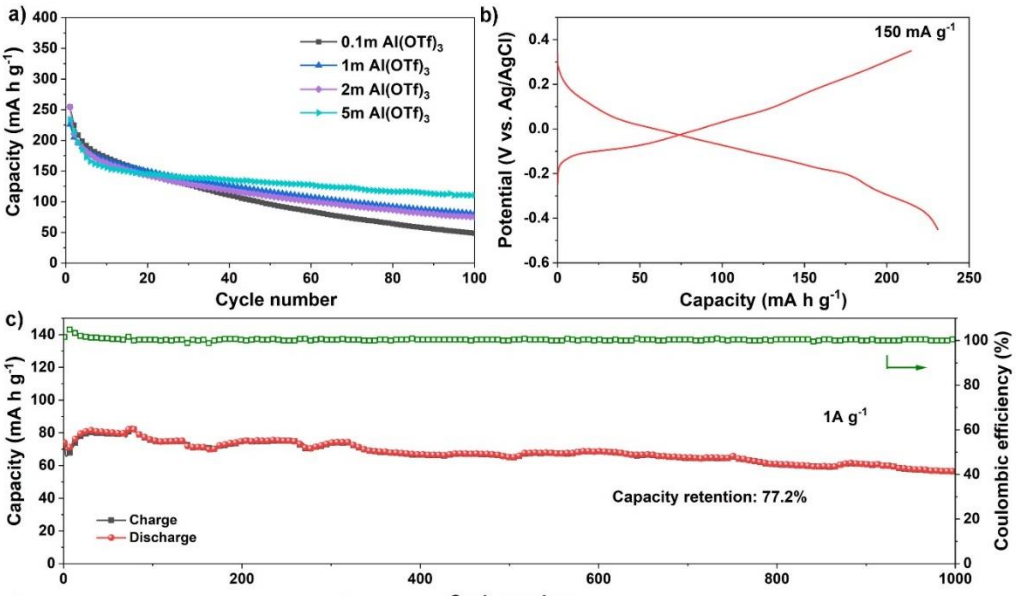

Figure 5-4: Cycling performances of the VO_2-B cathode: (a) stability study in different concentrations of the AlTFS electrolyte at 150 mA g^{-1}. b) Galvanostatic charge/discharge profile in the 5 m AlTFS electrolyte, c) long-term cycling study at 1 A g^{-1} in 5 m AlTFS electrolyte

5.3.3 Mechanism study

Material VO_2-B shows the excellent capacity and capacity retention and proves to be a good cathode candidate for AIAB. However, it is also equally important to decipher the concomitant electrochemical reactions here. In this section, the guest-ion storage mechanism in VO_2-B has been studied using a combination of ex-situ studies.

The crystal structural changes in VO_2-B is first studied by doing ex-situ XRD of fully discharged and fully charged electrodes and then comparing them with the pristine electrode and with themselves (Figure 5-5 a). Compared with the diffraction pattern of the pristine cathode, minor changes are noticeable in the pattern of the discharged cathode. This indicates a robust crystal structure of VO_2-B which did not dis-integrate upon insertion of guest ions. A closer look at the main peak reveals a shift to lower theta values indicating a volume expansion of the lattice upon guest-ion insertion. Similarly, upon charging, this peak shifts back to higher values indicating a reversible structural change mostly because of de-insertion. The corresponding unit-cell parameters (a, b, c, β)

calculated from Pawley fitting are presented in Table 5-1 and clearly show an increase and decrease in unit cell volume upon discharging and charging. The volume change is minor (0.1%) and can be speculated because of the unique shear structure of VO_2-B, which could effectively compensate for the volume changes and effectively would have resulted in a stable host-material as was observed in GCD studies.

Table 5-1: Lattice parameters of the VO_2-B electrode at different states.

	Pristine	**Discharge**	**Charge**
a (Å)	12.055(2)	12.047(3)	12.048(5)
b (Å)	3.6928(7)	3.696(1)	3.694(1)
c (Å)	6.421(1)	6.429(1)	6.426(1)
β	107.04(2)	106.97(2)	106.97(3)
V ($Å^3$)	273.3(1)	273.8(1)	273.5(1)
R_{wp}	5.742	6.094	6.071

Further, Raman spectroscopy was used to probe the local structural variations in the cathode material upon cycling (Figure 5-5 c). The two bands at 408 cm^{-1} and 288 cm^{-1} in the pristine VO_2-B electrode can be assigned to V-O and V_2-O bending vibration modes, respectively. [24] V_2-O & V_3-O bridging modes are assigned to the broad band between 400 cm^{-1} and 600 cm^{-1}. V_2-O and V=O stretching modes are responsible for the bands at 685 cm^{-1} and 991 cm^{-1}, respectively.[25] There is a red shift of the V=O bond from pristine to fully discharged state, changing from 991 cm^{-1} to 987 cm^{-1}. Ion intercalation into the VO_2-B tunnels might have triggered a shift in bond length. After being fully charged, such a shift in bond length is retrieved, consistent with the above XRD result. Minor changes in Raman spectra during cycling also indicates high structural integrity even in small range order.

The changing oxidation state of the transition metal and the surface composition of the cathode was studied using XPS. As can be seen in figure 5-5 d, for the pristine sample, no Al signals were detected, and a small peak was observed at 70 eV corresponding to V 3s.[26] Upon discharge, the peak for Al element appear at ~ 74.4 eV. This peak is at different binding energy as compared to the reported value (75.8 eV) for AlTFS electrolyte, indicating: 1) a modification in the environment of Al-ion when moving from electrolyte to cathode and 2) the signal collected corresponds to the intercalated Al-ion and is not from the absorbed electrolyte on the cathode surface. Elemental mapping (Figure 5-5 e) also shows the presence of Al-ion in the cathode, supporting its intercalation into the host material.

O 1s region of the XPS spectrum reveals interesting information about the co-insertion of H^+ in the host material. The H-O-H bond at 532.6 eV for absorbed crystal water, the -OH bond at 531.4 eV for the hydroxide, and the V-O bond at 530.1 eV can be assigned to the deconvoluted peaks of the O1s spectrum (Figure 5-5 f). Clearly, upon discharge, the integrated area under peaks corresponding to -OH and H-O-H increases, indicating a possible proton co-insertion with the Al-ion.[27-28] The possibility of proton co-insertion is very real here as in an Al-ion aqueous acidic environment, the hydrated Al^{3+} ions ($[Al(H2O)_6]^{3+}$) are hydrolysed to provide H^+.[19]

Meanwhile, the diminished V-O bond characteristic peaks suggest structural rearrangements in VO_2-B, possibly caused by Al-ion intercalation, as was also shown by the changes in the Al 2p spectrum in Figure 5-5 d. Furthermore, the V $2p_{3/2}$ peak of the discharged VO_2-B electrode can be decoupled into two peaks, corresponding to V^{3+} and V^{4+}, respectively (Figure 5-6 a).[6, 29] In particular, compared to the pristine state, the intensity of the V^{4+} peak decreases while the intensity of the V^{3+} peak increases, indicating the reduction of V^{4+} to V^{3+} while Al^{3+} and H^+ intercalate. The flaky morphology of VO_2 is also seems to be maintained after cycling (Figure 5-6 b).

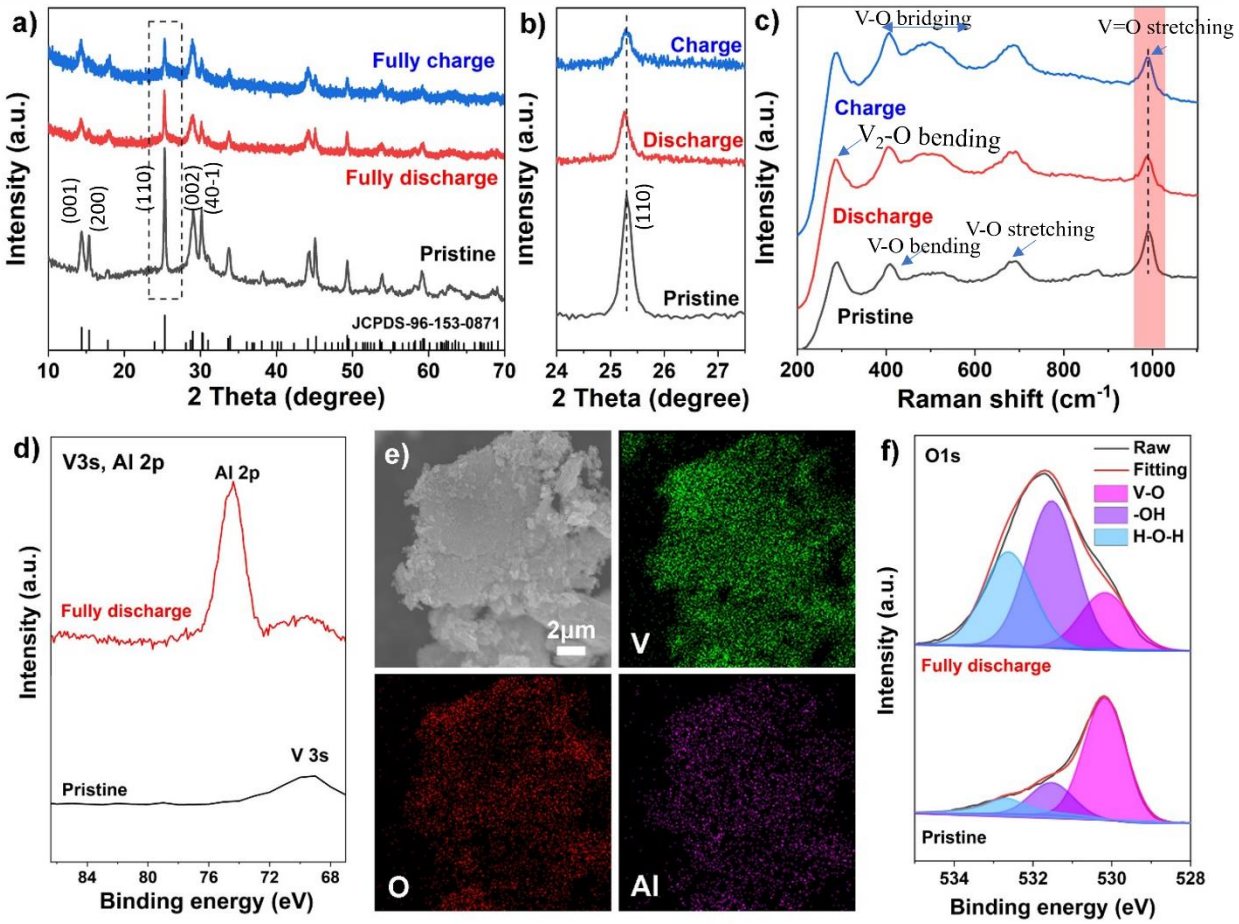

Figure 5-5. a) Ex-situ diffraction patterns and b) selected magnified diffraction patterns of the pristine and cycled VO_2-B cathodes, c) ex-situ Raman spectra for pristine, discharged and charged cathodes, d) V 3s and Al 2p region of XPS spectra for pristine & fully discharged states of VO_2-B, e) SEM-EDX elemental mapping of the discharged VO_2-B cathode, and f) O 1s region of XPS spectra for pristine and discharged states of VO_2-B cathode.

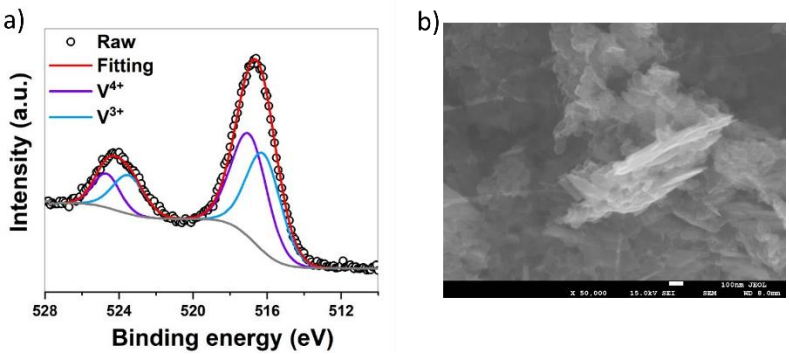

Figure 5-6: (a) V 2p XPS spectrum of the fully discharged VO_2-B electrode and (b) SEM image of electrode cycled for 3 cycles.

Based on the ex-situ analysis, a proton and Al^{3+} co-insertion mechanism can be proposed here, which is also reversible. It can be noted here that the transport number study of various ions present in the electrolyte can add more insight into the capacity contributions from respective ions, however such study is out of the scope of this chapter. The overall rection can be speculated to be as follow:

In the electrolyte: $Al(H_2O)_6{}^{3+} \leftrightarrow Al(OH)(H_2O)_5^{2+} + H^+$

On cathode: $VO_2 + x\ H^+ + y\ Al^{3+} + (x + 3y)\ e^- \leftrightarrow H_xAl_yVO_2$

In short, the hydrated Al-ions complexes form by a hydrolysis reaction in an Al-ion aqueous acidic system, resulting in the formation of H^+. These protons and Al-ions co-intercalate into the tunnel structure of VO_2-B sheets during the discharge process. The proton and Al-ions are reversibly deintercalated from VO_2-B during subsequent charge processes. The holey nanobelts morphology proves to be advantageous here as it provides short ion diffusion pathways and abundant electrolyte/electrode interaction, resulting in high capacity and cycling stability of VO_2-B cathode.

5.4 Conclusion

This chapter investigates a supposedly robust crystal structure of VO_2 with an aim to develop high performing cathode material and expand understanding of guest-ion uptake mechanism in the oxides of vanadium for an aqueous electrolyte.

Active material, VO_2-B, shows a high initial capacity of 234 mAh g^{-1} at 150 mA $g^{-1,}$ which fades rapidly in the initial charge/discharge cycles because of the high acidity of the electrolyte. This capacity fading is dependent on the electrolyte concentration and slows down with an increase in the concentration of Al salt in the electrolyte. A long-term specific capacity of 72.9 mAh g^{-1} could be obtained for 1000 cycles at 1 A g^{-1} in a 5 m AlTFS electrolyte. Such long stability performance surpasses the contemporary

cathode performances reported for AIAB and is likely enabled by the robust shearing structure of VO_2-B.

A combination of ex-situ studies focused on studying the structural and compositional evolution of VO_2-B during cycling reveals superior structural integrity and reversible compositional changes in VO_2-B. Notably, even after parallelly ongoing parasitic reactions, the structure maintains both long and short-range ordering, and reversible changes in oxidation state can be seen after a full cycle of charge/discharge. Further, in terms of guest-ion uptake mechanism, it is revealed that both H^+ and Al^{3+} co-inserts in the host material, which is likely given the high acidity of the electrolyte. We also note here that simulation studies of VO_2 solvated in electrolyte can add more insight to this study from a thermodynamic point of view.

Without a doubt, VO_2-B is one of the potential cathodes for the AIAB system. Additional electrolyte engineering like the synthesis of hybrid electrolyte and pH modulation can improve the capacity retention further.

References

[1] G. Fang, J. Zhou, A. Pan, S. Liang. *ACS Energy Letters.* **2018,** *3*, 2480-2501.

[2] B. Tang, G. Fang, J. Zhou, L. Wang, Y. Lei, C. Wang, T. Lin, Y. Tang, S. Liang. *Nano Energy.* **2018,** *51*, 579-587.

[3] F. Wan, Z. Niu. *Angew. Chem. Int. Ed.* **2019,** *58*, 16358-16367.

[4] F. Théobald, R. Cabala, J. Bernard. *Journal of Solid State Chemistry.* **1976,** *17*, 431-438.

[5] J. Ni, W. Jiang, K. Yu, Y. Gao, Z. Zhu. *Electrochimica Acta.* **2011,** *56*, 2122-2126.

[6] J. Mendialdua, R. Casanova, Y. Barbaux. *Journal of Electron Spectroscopy and Related Phenomena.* **1995,** *71*, 249-261.

[7] G. Silversmit, D. Depla, H. Poelman, G. B. Marin, R. De Gryse. *Journal of Electron Spectroscopy and Related Phenomena.* **2004,** *135*, 167-175.

[8] J. Lai, H. Zhu, X. Zhu, H. Koritala, Y. Wang. *ACS Applied Energy Materials.* **2019,** *2*, 1988-1996.

[9] F. Cui, J. Zhao, D. Zhang, Y. Fang, F. Hu, K. Zhu. *Chemical Engineering Journal.* **2020**, 124118.

[10] V. Verma, S. Kumar, W. Manalastas Jr, J. Zhao, R. Chua, S. Meng, P. Kidkhunthod, M. Srinivasan. *ACS Applied Energy Materials.* **2019**.

[11] H. Zhang, K. Ye, K. Zhu, R. Cang, J. Yan, K. Cheng, G. Wang, D. Cao. *Chem-Eur. J.* **2017,** *23*, 17118-17126.

[12] S. Liu, G. L. Pan, G. R. Li, X. P. Gao. *J. Mater. Chem. A.* **2015,** *3*, 959-962.

[13] R. Y. Wang, B. Shyam, K. H. Stone, J. N. Weker, M. Pasta, H.-W. Lee, M. F. Toney, Y. Cui. *Adv. Energy Mater.* **2015,** *5*, 1401869.

[14] Z. Li, K. Xiang, W. Xing, W. C. Carter, Y. M. Chiang. *Adv. Energy Mater.* **2014,** *5*, 1401410.

[15] L. Suo, O. Borodin, T. Gao, M. Olguin, J. Ho, X. Fan, C. Luo, C. Wang, K. Xu. *Science.* **2015,** *350*, 938-943.

[16] L. Suo, O. Borodin, Y. Wang, X. Rong, W. Sun, X. Fan, S. Xu, M. A. Schroeder, A. V. Cresce, F. Wang. *Advanced Energy Materials.* **2017,** *7*, 1701189.

[17] D. P. Leonard, Z. Wei, G. Chen, F. Du, X. Ji. *ACS Energy Letters.* **2018,** *3*, 373-374.

[18] W. Pan, Y. Wang, Y. Zhang, H. Y. H. Kwok, M. Wu, X. Zhao, D. Y. Leung. *Journal of Materials Chemistry A.* **2019,** *7*, 17420-17425.

[19] A. Zhou, L. Jiang, J. Yue, Y. Tong, Q. Zhang, Z. Lin, B. Liu, C. Wu, L. Suo, Y.-S. Hu. *ACS applied materials & interfaces.* **2019,** *11*, 41356-41362.

[20] A. Zhou, L. Jiang, J. Yue, Y. Tong, Q. Zhang, Z. Lin, B. Liu, C. Wu, l. suo, Y.-S. Hu, H. Li, L. Chen. *ACS Appl. Mater. Interfaces.* **2019,** *11*, 41356–41362.

[21] V. Verma, S. Kumar, W. Manalastas Jr, R. Satish, M. Srinivasan. *Adv. Sustainable Syst.* **2019,** *3*, 1800111.

[22] Q. Zhao, L. Liu, J. Yin, J. Zheng, D. Zhang, J. Chen, L. A. Archer. *Angewandte Chemie International Edition.* **2020,** *59*, 3048-3052.

[23] A. M. Engstrom. *Vanadium Oxide Electrochemical Capacitors: An Investigation into Aqueous Capacitive Degradation, Alternate Electrolyte-Solvent Systems, Whole Cell*

Performance and Graphene Oxide Composite Electrodes, University of California, Berkeley: 2013.

[24] F. D. Hardcastle, I. E. Wachs. *The Journal of Physical Chemistry.* **1991,** *95*, 5031-5041.

[25] R. Li, C.-Y. Liu. *Materials Research Bulletin.* **2010,** *45*, 688-692.

[26] R. Zimmermann, R. Claessen, F. Reinert, P. Steiner, S. Hüfner. *Journal of Physics: Condensed Matter.* **1998,** *10*, 5697.

[27] S. Islam, M. H. Alfaruqi, V. Mathew, J. Song, S. Kim, S. Kim, J. Jo, J. P. Baboo, D. T. Pham, D. Y. Putro. *Journal of Materials Chemistry A.* **2017,** *5*, 23299-23309.

[28] Z. Li, S. Ganapathy, Y. Xu, Z. Zhou, M. Sarilar, M. Wagemaker. *Advanced Energy Materials.* **2019,** *9*, 1900237.

[29] C. Huan, X. Zhao, X. Xiao, Y. Lu, S. Qi, Y. Zhan, L. Zhang, G. Xu. *Journal of Alloys and Compounds.* **2019,** *776*, 568-574.

Chapter 6*

Investigating the role of coated-Al anode treatments for superior battery cycling performance using a hexacyanoferrate cathode

This chapter makes a transit from cathode materials towards anode studies. Firstly, a hexacyanoferrate cathode material is electrochemically tested for activity towards Al-ion insertion followed by mechanistic studies, which establishes it to be a stable cathode material that can be implemented to test unknown anodes. Secondly, an already developed treatment for Al-metal anode is studied against this cathode for its suitability to the long-term assembling of the full cell. The implications of using such an anode in a full cell are also revealed.

*This section published substantially as Kumar S, Verma V, Arora H, Manalastas W, Srinivasan M. Rechargeable Al-Metal Aqueous Battery Using NaMnHCF as a Cathode: Investigating the Role of Coated-Al Anode Treatments for Superior Battery Cycling Performance. ACS Applied Energy Materials. 2020;3(9):8627-35. Reprinted with permission. Copyright 2020, American Chemical Society.

6.1 Introduction

The premise for the low cost and sustainability of AIAB comes from the usage of Al-metal as an anode in the battery system, which takes advantages of the abundance of Al in the earth crust, making the battery system potentially cheaper. However, the oxide layer that forms readily on the Al-metal surface renders the surface inert and hinders its usage as an anode. This stubborn oxide layer increases the plating/stripping overpotential at the anode, often causing electrolytic degradation, especially in the aqueous electrolyte systems (as they have smaller electrochemical stability window). The main challenge here is to stop the formation of the oxide layer on the Al surface in an ambient environment that will make it compatible with the aqueous cells' fabrication process, which happens out in the open.

A breakthrough in this direction came from a recent work[1] wherein researchers created an artificial layer on the Al-metal surface such that it would block the ambient environment to come in contact with the Al-metal surface, thus effectively preventing the oxidation of Al. This was made possible by coating the surface of the Al with a eutectic mixture of $AlCl_3$ and ionic liquid (1-ethyl-3-methyl imidazolium chloride ([EMIm]Cl)) in an inert atmosphere. This conductive artificial layer (about 1 µm thick) increased the interface conductivity and reduced plating/stripping potential effectively. Following this work, studies making use of a similar approach have been reported,[2-5] however, they do not focus on the role of $AlCl_3$ + ionic liquid treated Al-anode (TAl) in regulating the overall battery performance. At the same time, it is not clear whether TAl: 1) is stable in an ambient environment and 2) compatible in an operating AIAB cell.

In this chapter, the abovementioned two aspects of TAl have been explored in a full-cell context. To make full cell studies wherein the effect of an anode on the full cell performance can be observed, a stable cathode, which can reversibly accommodate Al-ion, is needed. Hence the study has been done in three phases: 1) Firstly, a novel host material $Na_{1.68}Mn[Fe(CN)_6].1.7H_2O$ (NMHCF) is synthesized and tested for Al-ion

insertion, and the electrochemical performance has been studied along with the concomitant insertion mechanism. A high energy density for at least 275 cycles is reported. 2) Secondly, the active influence of TAl on the overall battery performance has been recognized. A combination of TAl and electrolyte is responsible for taking the battery system in a diffusion polarization regime which is also reflected in plating/stripping overpotential. 3) Thirdly, the stability of the coating material is examined under atmospheric ageing & postmortem from the working cells. Overall, a comprehensive study accounting for the effects of using TAl has been done while developing a new cathode material parallelly.

6.2 Experimental Method

6.2.1 Material Synthesis

NMHCF was synthesized using a co-precipitation method close to that described in a previous report.[6] To begin, 0.23 g of $MnSO_4.H_2O$ [Sigma Aldrich, > 99% purity] was dissolved in 50 ml DI water, followed by 0.197 g $K_4Fe(CN)_6.3H_2O$ (Sigma Aldrich, > 99.95 % purity) in 50 ml DI water. Both these solutions were added dropwise simultaneously to an aqueous solution containing 14 g of NaCl. The result was a white suspension that was aged overnight, washed with DI water, and then dried overnight at 60 °C.

For control experiments, $FeVO_4$ was also used as an active material. Its synthesis mechanism and physical-chemical properties are identical to those previously stated in chapter 4.

6.2.2 Material Characterization

The crystal structure of the synthesized powder and cycled electrodes was determined using a Bruker D8 Advance diffractometer with a Lynxeye-type detector configuration in a Bragg-Brentano geometry. The probing beam was Cu K alpha radiation (40 mA, 40 kV) with a beam knife to sever the low angle background signals. As a zero background

holder for samples, a single-crystal Si ingot was sliced at a particular misorientation angle. Low angle peaks were easily identified as a result of this. The cycled electrodes were removed from the cell, thoroughly washed with DI water, cleaned, and subjected to any required characterization. Since the Ti substrate in the electrode remained unchanged, the diffractogram of the cycled electrode included prominent Ti peaks, which were later used to calibrate the XRD signal and thereby facilitated pattern-to-pattern comparison. To accurately estimate lattice parameters, XRD data was Pawley fitted in TOPAS 3 program. A field emission scanning electron microscope was used to examine the powder's morphology (FESEM; JEOL, JSM-7600F). The Raman shifts for cycled electrodes were measured using a WITec Alpha300 SR Confocal Raman spectrometer using a 488 nm argon laser.

The Kratos AXIS Supra instrument was used to conduct X-ray photoelectron spectroscopy (XPS) on cycled cathodes and Al anode using a monochromatic Al K, (1486.69 eV) radiation. When gathering narrow scan signals for cycled cathodes, pass energy of 20 eV with a step size of 0.1 eV was used, while after etching, a pass energy of 40 eV with a step size of 0.1 eV was used. XPS was used to investigate various Al foil, such as obtained Al foil, TAl foil, air-exposed TAl foil for 40 hours, and cycled TAl foil. The composition of one of these foils was characterized, as well as two layers underneath it. Ar+ sputtering was used for the etching, which took 60 seconds each. While the signal selection was done with a smaller slit of 110, the etching was done with a 700 * 300 slit, ensuring that the signal was only obtained from the etched field. In the Casa XPS program, peak deconvolution was performed using a mixture of Lorentzian and Gaussian distribution (30:70) model peak. Due to aromatic C in the super P, each cathode spectrum was calibrated to 284 eV. Since the as obtained Al foil is conductive and Al metal peak was found to be at the literature metal Al binding energy value of 72.6 eV, no calibration was performed for its layers. [7-8] Each XPS spectrum of TAl foil was calibrated with N1s (C=N) at 401.6 eV[9] which happened to be the common species forming a part of the coating on Al. Notably, adventitious carbon was not used for this purpose as after etching the adventitious carbon is likely to get removed. TAl foil exposed to air was calibrated the same as TAl. The surface of TAl cycled in a cell was calibrated with -CF_3 at 293.8

eV[10-11] (No calibration with N1s was done here because the protective coating was partially destroyed upon cycling). Next two layers of TAl cycled in a cell were calibrated with metal Al peak at 72.6 eV.

6.2.3 Electrochemical Characterization

The battery was tested in a CR2016 coin cell with NMHCF as the cathode and TAl as the anode. By making a slurry in N-methyl-2-pyrrolidone solvent, a 6:2:2 weight ratio of NMHCF, super P, and PVDF binder were combined. This slurry was painted on Ti foil (mesh not used as it is more expensive) to prepare the cathode and allowed to dry overnight (same method for $FeVO_4$). Similar to a process previously mentioned, [1] TAl was prepared as an anode by coating Al foil (0.25mm thick, annealed, 99.99 per cent (metals basis) Alfa Aesar). Al foil was first punched out into 16 mm circles and placed inside a glovebox (H_2O < 0.1 ppm; O_2 <0.4 ppm) as obtained. It was then polished until smooth with P800 grit sandpaper before being dipped in a 1.3:1 eutectic solution of $AlCl_3$/ [EMIm]Cl (1-ethyl-3-methylimidazolium chloride). The Al foil was left in the mixture for 24-36 hours, flipped every 12 hours, and then removed. Later, the foil was removed from the solution, cleaned to clear excess coating liquid, and placed in a sealed vial in the glovebox. It can be emphasized here that TAl foil was only exposed to the atmospheric air for a few minutes during fabrication after it was removed from the glovebox.

Solartron Analytical 1470E was used for cyclic voltammetry (CV) measurements, while BTS-Neware was used for galvanostatic charge-discharge (GCD) experiments. Conductivity was measured using an Orion Star A322 conductivity meter optimized with KCl (0.1 M and 0.001 M) solutions.

6.3 Results and Discussion

6.3.1 Crystal Structure

The X-ray diffractogram of the synthesized powder is shown in Figure 6-1 a. It closely resembles the monoclinic phase -$Na_{1.68}Mn[Fe(CN)_6].xH_2O$ (PDF 04-022-3444).[12] A simulated fitting done to this pattern by Pawley method renders the lattice parameters as a = 10.5807 (6) Å, b = 7.513 (1) Å, c = 7.3187 (9) Å, $\alpha = \gamma = 90°$, β = 92.16 (1)°. The percentage of water in the synthesized powder was determined using thermogravimetric analysis (Figure 6-1 b). Water loss happened in two steps:1) gradual weight loss of 1.8% corresponding to desorption of water from the surface and 2) sudden weight loss of 9.25% corresponding to the elimination of interstitial water.[12] This 9.25% loss of water is equivalent to 1.73 water molecules for each $Na_{1.68}Mn[Fe(CN)_6]$ unit. NMHCF has a 3D open structural framework formed with MnN_6 & FeC_6 octahedron bridged by C-N anions, leading to the creation of large interstitial voids. Such large voids (~ 4.6 Å) are suitable for accommodating high charge density Al^{3+} ions and/or its hydrated complexes, which have relatively large diameters (1.89 Å-hexahydrated M-O covalent radius; 4.75 Å-M-O covalent radius+oxygen ion (O_2) radius of 1.4 Å).[13-14] PBA's crystal structure is suitable for researching multivalent battery chemistries because of this.

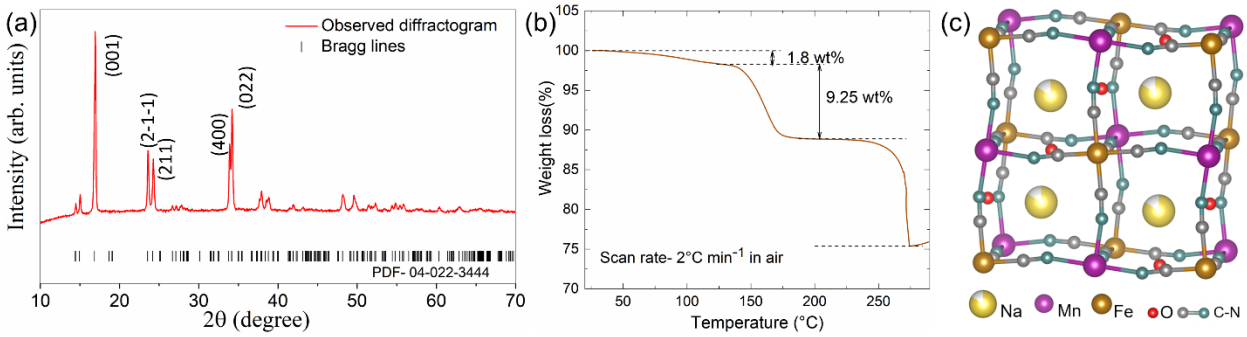

Figure 6-1: (a) Experimental diffraction pattern of as-synthesized powder with matched phases' sBragg lines, (b) TGA curve and (c) Crystal structure of as synthesized powder.

6.3.2 Electrochemical Performance

Cyclic voltammogram shows the prominent broad nature of cathodic (1.75 V) and anodic (1.1 V) peaks which averages out to a voltage of 1.42 V vs Al^{3+}/Al (Figure 6-2 a). The characteristic broad peaks indicate a rather complex insertion mechanism and/or de-solvation of hydrated guest-ions,[15] which can occur because of their large size, as has

been reported for HCFs.[14, 16-17] The GCD curves in consistency with CV study show one flat plateau each for charge and discharge (Figure 6-2 b). Noticeably, these plateaus grow apart in later cycles of charge/discharge; however, their profile remains almost constant. This indicates an increase in the overpotential of the cell in later cycles, mainly contributed from the anode as the cathode shows consistency in the charge-discharge profile.

Further, a cycling stability study was done in varying concentrations of AlTFS electrolyte (0.1m, 0.7m, 2m, 2.5m, 3m, 5m). The cycling performance improves with increasing concentration of the electrolyte but only until 2 m (Figure 6-2 c). This observation contrasts with the conventional wisdom that cycling stability improves in an increased electrolyte salt concentration because of reduced activity of water molecules (leading to a wider electrochemical window and reduced side reactions with cathode). [18] As a matter of fact, in chapter 5, best performance for VO_2-B cathode was seen in the 5 m of AlTFS aqueous electrolyte. This disparity is investigated in the later part of this chapter (Section 6.3.4)

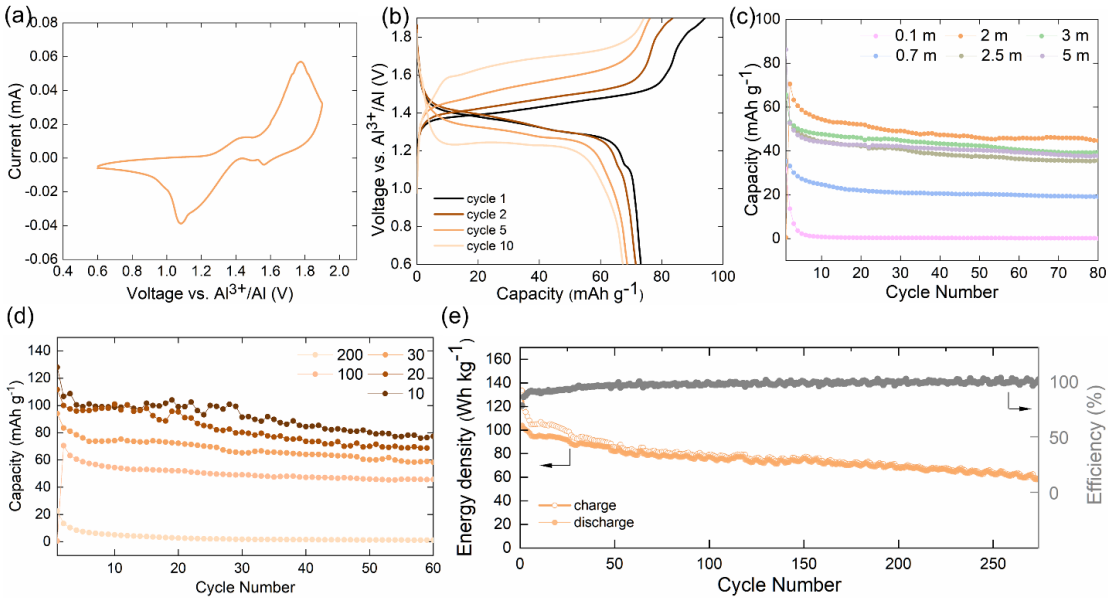

Figure 6-2: Electrochemical study of NMHCF cathode in a full cell context with TAl as anode: (a) Cyclic voltammograms in 2 m AlTFS cycled between 0.6 V & 1.9 V (scan rate of 0.1 mV s^{-1}; OCV ~0.8 V) (b) Galvanostatic charge-discharge profile in 2 m AlTFS at a current rate of 30

mA/g, (c) Cycling stability study in several concentrations of AlTFS electrolyte at the current rate of 100 mA/g, (d) Cycling stability study at several current rates in 2 m AlTFS aqueous electrolyte, (e) Extended cycling performance & corresponding coulombic efficiency in 2 m AlTFS aqueous electrolyte at 30 mA/g.

Cycling performance was also studied as a function of cycling rate. A ~ 10 folds improvement in stable cycling performance was noted as the rate was dropped to 10 mA g^{-1} from 200 mA g^{-1}. This is likely because 1) at lower rates of cycling there is sufficient time for guest ion to insert and de-insert into the host material (while at high rates ions may not insert into the host material and rather just accumulate at the surface) and 2) reduced anodic overpotential at slower rates (Figure 6-3). Finally, having optimized the rate and electrolyte concentration, the extended cycling life study was done at 30 mA g^{-1} in a 2 m (not M) electrolyte. A high discharge capacity of ~ 73 mAh g^{-1} is observed, which reduces to ~ 41 mAh g^{-1} over 275 cycles. This corresponds to an initial discharge energy density of 104 Wh kg^{-1}, which is better than HCF full studies in AIAB reporting energy densities of 100 Wh kg^{-1},[19] 60 Wh kg^{-1},[20] 15 Wh kg^{-1}, & 40 Wh kg^{-1}.[21-22]

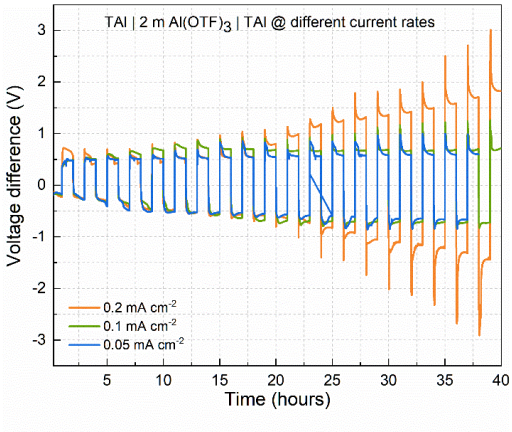

Figure 6-3: Stripping/plating testing in "TAl | 2m $Al(OTF)_3$ | TAl" at different current densities. At slow cycling rates lesser overpotential is observed on anode side, subsequently resulting in better cycling performance at slower rates.

6.3.3 Reaction Mechanism

In this section, the reaction mechanism for Al-ion insertion is studied in detail using ex-situ characterization techniques. The presence of Na and Al in the electrodes was detected using XPS. As predicted, the Na 1s region of the XPS spectra (Figure 6-4 a) shows a significant presence of Na in the pristine cathode. This number drops dramatically after charging, only to rise marginally after discharging. This means that the majority of the Na was eliminated during the first charging process, and that Na does not play a significant role in the discharge capacity. The abundant occurrence of Al in the discharged cathode, which was absent in the pristine cathode, was visible in the Al 2p region of XPS spectra (Figure 6-4 b), implying insertion of Al-ion during discharge. The Al 2p binding energy in the discharged cathode was 3 eV lower than in the AlTFS salt,[18] suggesting a different chemical environment than AlTFS salt around Al-ion, resulting from Al-ion insertion in the host material.

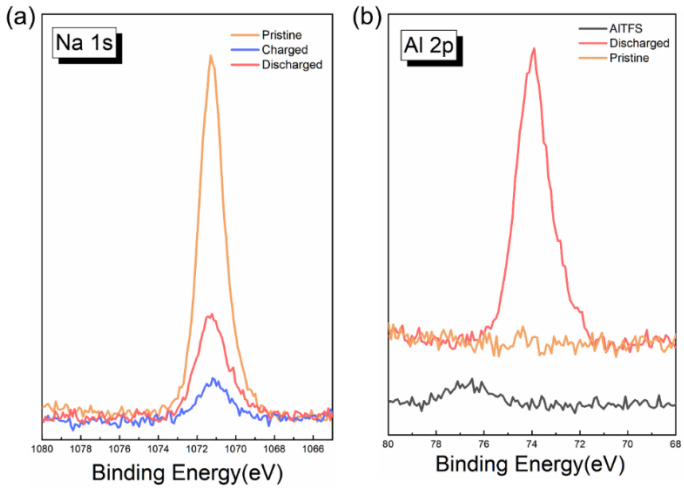

Figure 6-4: (a) Na 1s region of XPS spectra for pristine, charged and discharged NMHCF electrode and (b) Al 2p region of XPS spectra for pristine and discharged NMHCF electrode, and for $Al(OTF)_3$ salt.

Further, the evolution of the surface oxidation state in the transition metal centres, Fe and Mn, has been studied using XPS. Fe (Figure 6-5 a) originally present in bivalent oxidation state (Fe $2p_{1/2}$ -720.85 eV; Fe $2p_{3/2}$ – 707.97 eV),[23-24] partially oxidizes to a +3 state on charging (Fe $2p_{1/2}$ -720.78 eV and 722.82 eV; Fe $2p_{3/2}$ – 707.82 eV and 708.81

eV)[21] On subsequent discharging, the oxidation state is reverts back to +2 (Fe $2p_{1/2}$ - 720.80 eV; Fe $2p_{3/2}$ – 707.93 eV). Mn (Figure 6-5 b) originally present in a mixed oxidation state of +3 and +2 with a Mn^{3+}/Mn^{2+} ratio of ~ 2:3 (Mn $2p_{1/2}$ - 652.75 eV & 654.30 eV; Mn $2p_{3/2}$ – 640.69 eV & 641.85 eV),[5] oxidizes upon charging evident from a Mn^{3+}/Mn^{2+} ratio 1:1. Upon subsequent discharge, Mn^{3+}/Mn^{2+} ratio restores back to ~ 2:3. Overall, the evolution of oxidation states on both transition metal centres supports the reversible insertion of Al-ion in MNHCF and indicate the participation of both the transition metal centers in accommodating the concomitant charge variations.

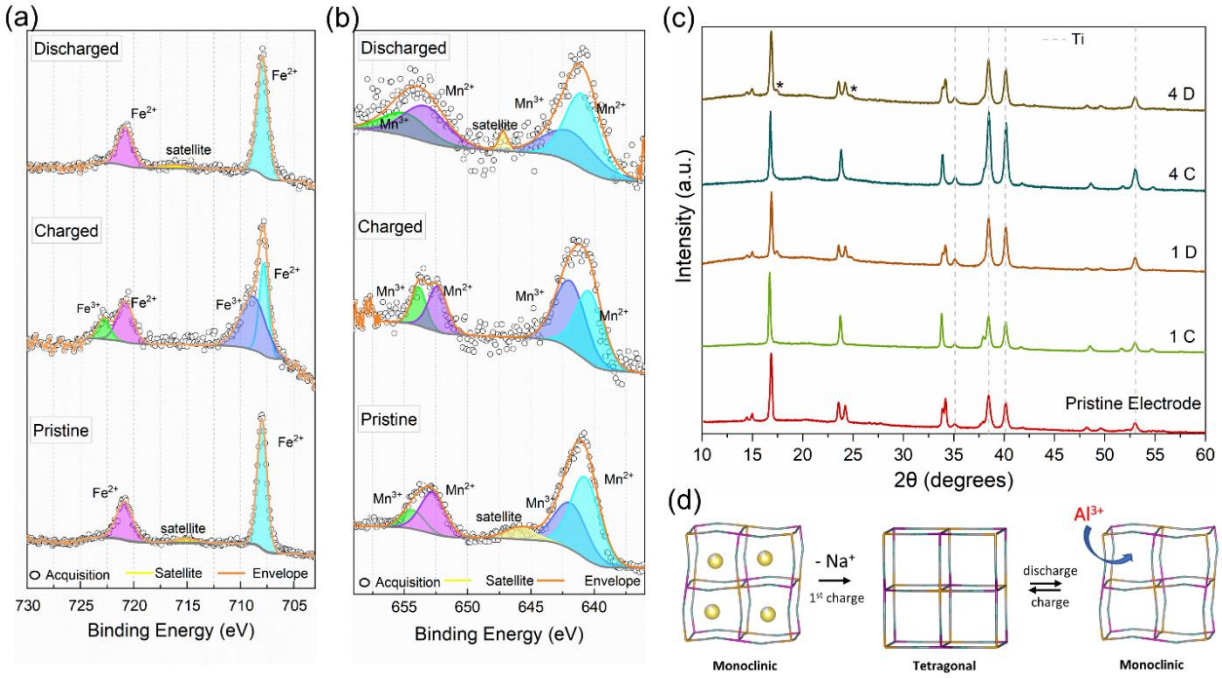

Figure 6-5: (a) and (b) Fe 2p and Mn 2p region of XPS spectra for the pristine, fully-charged & fully-discharged NMHCF cathodes. (c) Ex-situ X-ray diffraction pattern of the cathode in pristine state, at 1st & 4th charge (1 C & 4 C) & discharge (1 D & 4 D) state. (d) Schematic showing structural evolution in NMHCF upon cycling (based on XRD study).

XRD analysis (Figure 6-5 c) also supports the reversible insertion mechanism by showing a reversibly changing crystal structure of NMHCF from monoclinic to tetragonal phase (Figure 6-5 d). Pawley fitting the diffractogram of pristine cathode reveals a monoclinic phase (P21/n, space-group). Upon charging, few prominent peaks start to disappear and

suggest structural transformation to a more symmetrical system. A good Pawley fitting with a tetragonal space group, **I$\bar{4}$**m2m confirms this transformation from a monoclinic to a tetragonal phase. Such transformations have been observed before for Na and K battery chemistries using HCF as the cathode.[12, 24-25] Further, upon subsequent discharge, the original monoclinic peaks reappear, and the structure is transformed back to the monoclinic phase. The resultant lattice parameters from the Pawley fitting of cycled electrodes are presented in Figure 6-6. Comparing the lattice evolution in 1st and 4th cycle, a consistently reversible structural change can be seen. This is also reflected in increasing lattice volume, increasing lattice parameter *c*, and changing lattice angle, *β*. Two new shoulder peaks (marked with a star in the diffractogram of 4 C) also emerged in the discharged cathode diffractogram. These peaks may belong to a cubic phase of HCF,[26] that formed halfway during charging/discharging, as also reported previously.[12, 24-25]

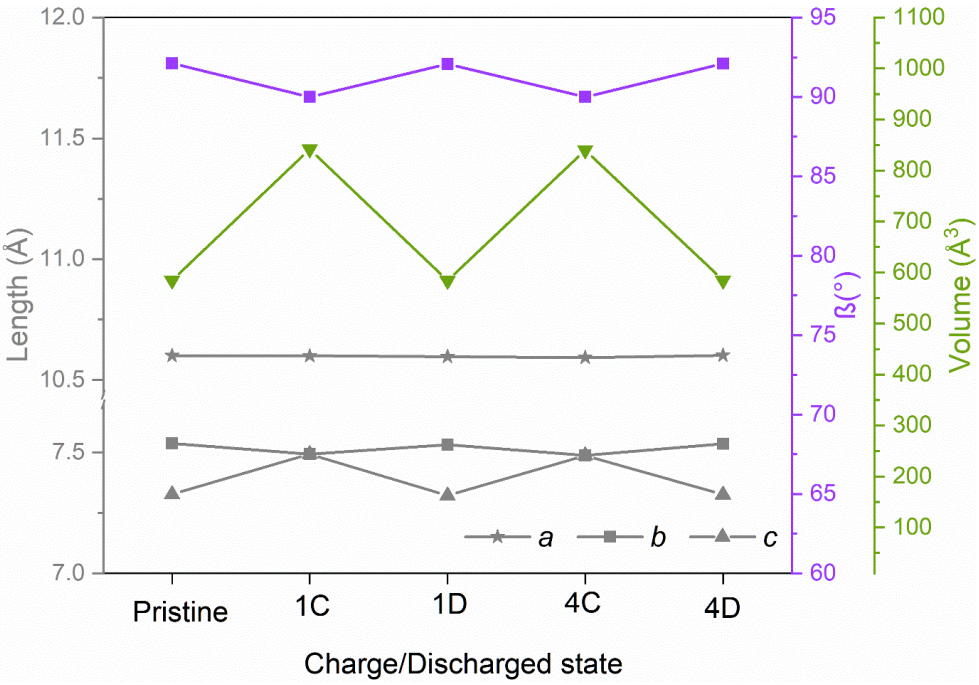

Figure 6-6: Lattice parameter & volume variation upon cycling of NMHCF cathode. The data plotted are from the Pawley fitting of the diffractograms presented in Figure 6-5 c.

Short-range order structural reversibility is also observed for MNHCF using Raman analysis (Figure 6-7). The pristine electrode showed two main peaks at 2105 cm^{-1} &

2026 cm^{-1} which can be attributed to the mixture of Fe^{II}-CN-Mn^{III} & Fe^{II}-CN-Mn^{II}.[27-28] These peaks vanish almost completely upon charging (1 C & 4 C) and reappear when the cathode is discharged (1 D & 4 D). This means that NMHCF's local structure is highly reversible as well as robust to allow for guest-ion insertion.

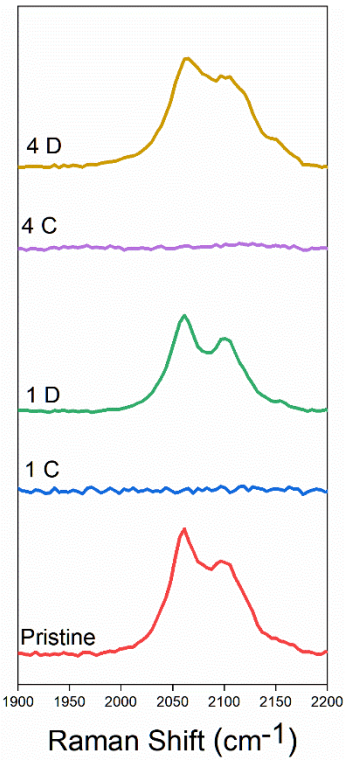

Figure 6-7: Ex-situ Raman spectra for the pristine and cycled electrodes for 1st and 4th cycle.

For completeness, a NMHCF was also tested for activity towards proton insertion in an HCl solution. The presence of no anodic peak (Figure 6-8) confirmed that proton insertion was negligible and had no contribution to the capacity.

Figure 6-5 d shows the proposed process of insertion/extraction along with host crystal structure transformation based on inferences from all ex-situ studies, showing removal of Na in the first charge stage followed by reversible insertion/extraction of Al-ion in subsequent cycling, resulting in a reversible phase transformation from monoclinic to tetragonal phase.

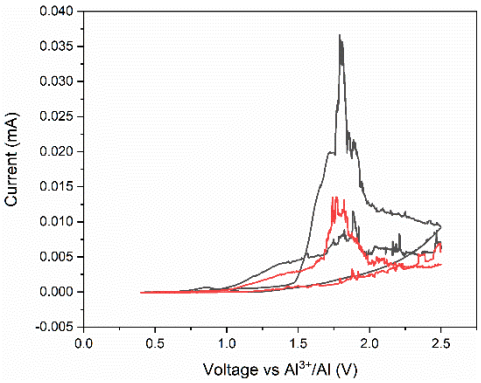

Figure 6-8: Stripping/plating testing in "NMHCF | 2m HCl | TAl" at current density of 0.2 mA cm^{-2} (High noise level because of possible corrosion of coin cell parts)

6.3.4 Role of treated Al-Anode

The practice of using highly concentrated electrolytes (also known as water-in-salt) is widely popular in aqueous battery chemistries. This is because, at high concentrations, the activity of water molecules are reduced, leading to wider electrochemical stability window and reduced parasitic reactions of cathode with water. This usually enables an improved cycling stability performance. Even for AIAB batteries using HCF cathode, the water-in-salt concept was implemented previously using 5 m AlTFS, either in HCF-Al full cell[21] or three-electrode setup[18]. However, in section 6.3.2, the best cycling stability was observed for 2 m AlTFS salt concentration. In this section, the reasons behind this discrepancy are investigated and related to the usage of TAl as an anode.

A clear trend of varying overpotential for full cell (MNHCF - TAl) can be seen in figure 6-9. Charge/discharge profiles show that the plateau difference for 2 m AlTFS electrolyte cell is less/comparable to other cells with different electrolyte concentrations. Interestingly, this low voltage difference is maintained only in 2 m concentration over a few cycles (as evident from the 5^{th} and 20^{th} cycle overpotential). This full cell overpotential development is also plotted for different electrolyte concentrations (Figure 6-10). Plotting, conductivity against electrolyte concentration on the same plot provides interesting insights. Clearly, overpotential and conductivity form inverse pattern to each

other. Electrolyte conductivities estimated at concentrations ranging from 0.1 to 5 m form a bell curve, with maxima that nearly coincide with overpotential-concentration minima. This suggests that the conductivity of the electrolyte can play a role in deciding the battery overpotential and, ultimately, the battery cycling stability performance. However, previous reports on AIAB using HCF as the cathode in 3-electrode configurations have shown that the best cycling outputs are obtained in the most concentrated AlTFS electrolytes, despite the fact that they do not have the highest conductivity.[18] This inconsistency suggests that electrolyte optimization alone is inadequate since other components could have synergistic or antagonistic consequences with specific electrolyte compositions that are yet to be discovered.

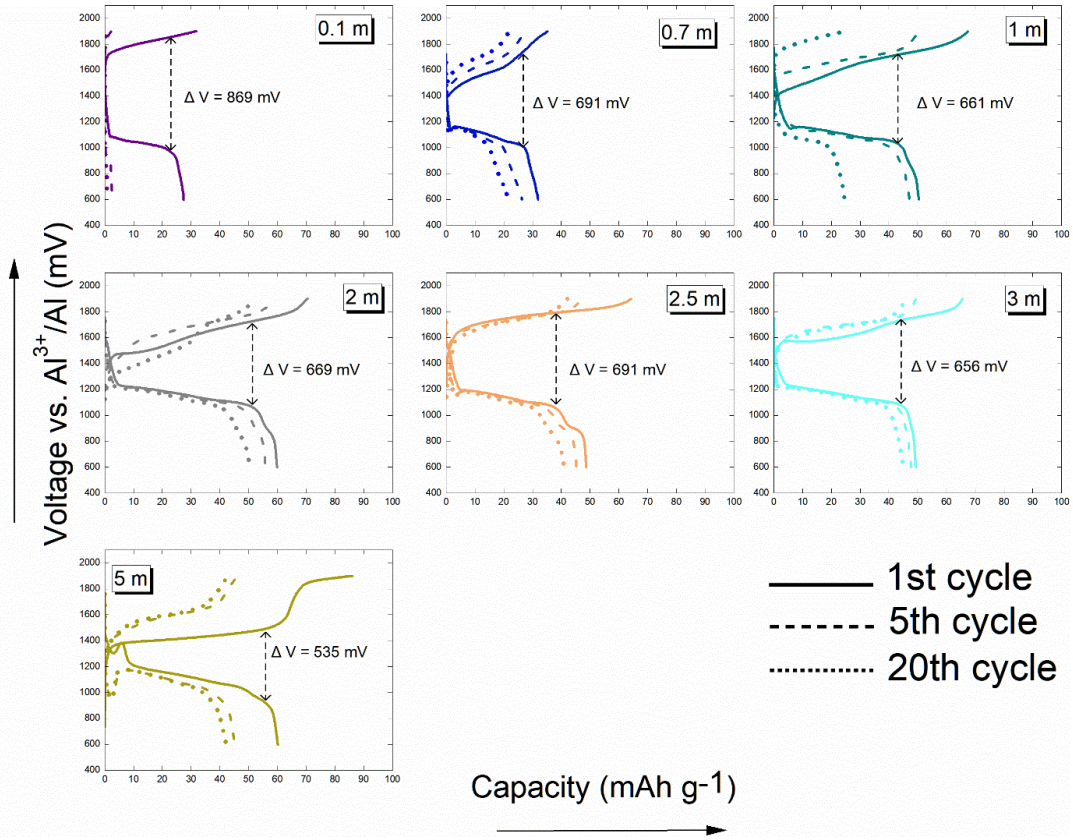

Figure 6-9: Voltage vs capacity profile for NMHCF-TAl cells cycled in various concentrations of $Al(OTF)_3$ electrolyte. Each graph shows three plots, including 1st, 5th and 20th cycle, and the cell overpotential in each case for the 1st cycle.

It's likely that the combination of "electrolyte + cathode" is responsible for affecting battery cycling longevity. To check this, a controlled study can be done with a different electrode. If similar trending overpotential observations are also made even for this new cathode, the trend will be not a function of “electrolyte + cathode”. For this purpose, $FeVO_4$ was chosen. As seen in chapter 4, $FeVO_4$ shows a conversion type reaction, thus making this controlled study independent of the intercalation mechanism of Al-ion insertion as is observed for MNHCF. [29] For $FeVO_4$, the best cycling life is observed in 2 m AlTFS and not in 5 m (Figure 6-10 b). Just like NMHCF full cell, the $FeVO_4$-TAl full cell overpotential is observed to be low in 2 m AlTFS (Figure 6-11). Because adjusting the cathode did not interrupt the pattern of getting the best cycle life with a less concentrated electrolyte, it is fair to assume that different “electrolyte + cathode” pairings will provide similar overall cell performances and cathode immersion in the electrolyte was not restricting the capacity retention.

Another hypothesis is that the mixture of "electrolyte + anode" was responsible for affecting battery cycling longevity. Stripping-plating experiments were performed in symmetric TAl-TAl cells to investigate the formation of overpotential for various electrolyte concentrations (Figure 6-10 c). Surprisingly, the 2 m electrolyte had the lowest Al plating/stripping overpotential, while higher overpotentials were found in lower (0.1 m & 1 m) and higher (5 m) concentrations. This follows the same pattern as the variation in cycling life for different electrolyte concentrations found in both NMHCF and $FeVO_4$ host materials. As a result, it's fair to assume that the "electrolyte + anode" pairing is affecting battery cycling performance here. It is hypothesized that due to their reduced conductivity, very highly concentrated electrolytes can obstruct ionic transport at the electrolyte-TAl surface interface, resulting in increased overpotential and poor cycling performance.

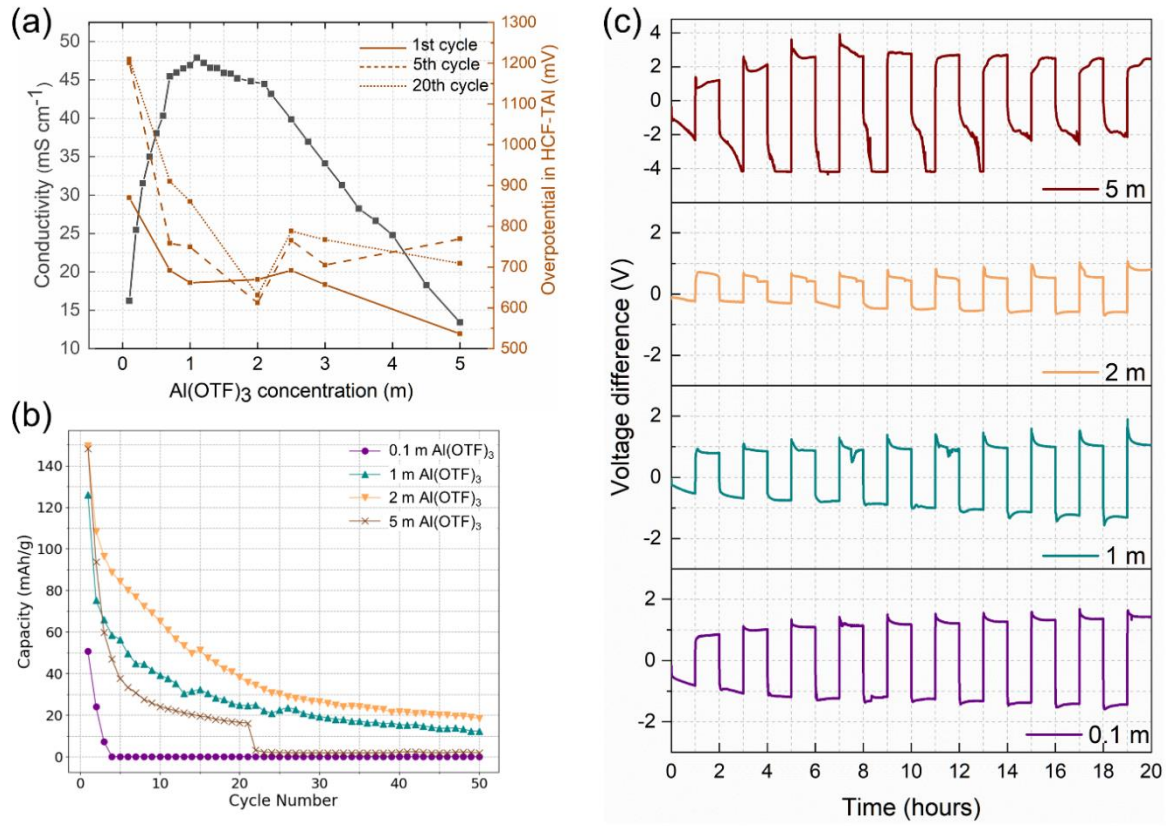

Figure 6-10: (a) Conductivity of different concentrations of AlTFS electrolyte (in grey); & cell overpotential for NMHCF | x m AlTFS | TAl configuration wherein x = 0.1 m, 1 m, 0.7 m, 2 m, 2.5 m, 3 m, & 5 m (shown for 1st, 5th & 20th cycle). (b) Cycling stability study for $FeVO_4$ | x m AlTFS | TAl cell configuration where x = 0.1 m, 1 m, 2 m and 5 m (current rate of 150 mA g^{-1}). (c) Stripping/plating test in TAl | x m AlTFS | TAl symmetric cells for x = 0.1 m, 1 m, 2 m and 5 m. Negative and positive current of 0.2 mA cm^{-2} was applied for 1 hour each in an alternating sequence.

It is also highlighted here that the observation will be different when not using TAl as an anode. In such a case, the battery cycling life is likely to improve along with increasing salt concentration, as was also observed by Suo et al. in a three-electrode setup. [18]

At this point, it's obvious that using TAl as an anode in a full-cell AIAB has serious consequences. The Al stripping/plating over-potential is highly influenced by the electrolyte conductivity, which determines the overall battery cycling stability performance. When fabricating a complete cell using TAl, the "electrolyte + anode"

combination becomes the core factor influencing cycling life. Simultaneously, concepts like water-in-salt, which can operate in three-electrode setups, do not always lead to comparable benefits when switching to TAl anodes.

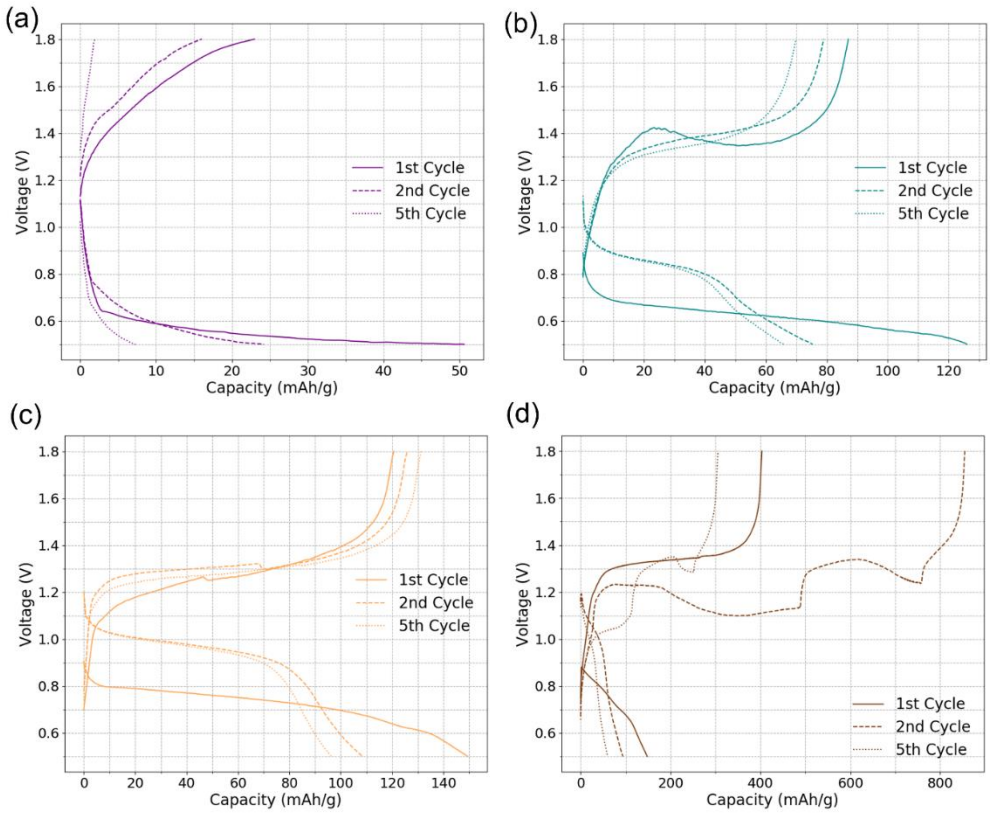

Figure 6-11: Charge-discharge profile for $FeVO_4$ | x m AlTFS | TAl cell configuration for x = a) 0.1 m, b) 1 m, c) 2 m and d) 5 m. Each graph shows 3 plots for 1st, 2nd & 5th cycle.

6.3.5 Stability/Compatibility study of the Treated Al

The introduction of TAl by Prof Archer et al. is causing a shift in how AIAB research is done.[1] Studies conventionally done in 3-electrode setups are shifting to more rational scenarios that use TAl as an anode. For example, post reporting of TAl AIAB reports have emerged which Al foil as it is, [2, 5, 21, 30-32] or in a modified form. [3-4, 33] However, all of these studies are either cathode focused, or electrolyte focused, and not much has gone into the TAl coating stability in ambient and its compatibility with the aqueous AlTFS electrolyte. Documenting this is important because: 1) the coating layer gets exposed to

the moisture and oxygen as fabrication of AIAB is done in ambient. This can change the surface chemistry, resulting in bad battery performance and 2) there does not exist any knowledge of how the coating layer behaves in an operating cell.

In this section, the surface and beneath layers of various TAl samples have been studied to document the effect of exposure to the environment (for coating stability study) and the effect of cycling in the cell. For this purpose, Al, TAl, TAl exposed to air for 40 hours (TAl_air) & cycled TAl (TAl_cycled) were characterized using XPS (Figure 6-12).

For as-received Al foil surface (non-porous, 0.25mm thick, annealed, 99.99% (metals basis) Alfa Aesar) (Figure 6-12 a), the Al 2p peak could be deconvoluted into three component peaks- metal Al[7-8], Al_2O_3[34-36] & the native-oxide on Al called AlO_x here[34-36]. Upon 1st etching, the intensity of both the oxide peaks decreases, indicating an expected reduction in their amount. Upon 2nd etch, the XPS spectrum remained the same. The shift of the O 1s region to higher energy values (Figure 6-13) upon etching also supports removing most of the metal oxide from the surface, and the remaining oxygen is likely from organics. Notably, there is no hydroxide found in either of the three layers, as the O1s spectrum binding energy remained smaller than that known for hydroxides (534 eV).[37]

An appreciable change in surface chemistry is seen in the treated Al foil (Figure 6-12 b). The surface shows major presence of chloride salts of Al with the negligible presence of the native oxide layer.[38] The Cl would have come from the originally used $AlCl_3$ in the eutectic coating. Noticeably, even after 2nd round of etching, the spectrum envelop do not change, indicating a robust and thick layer.

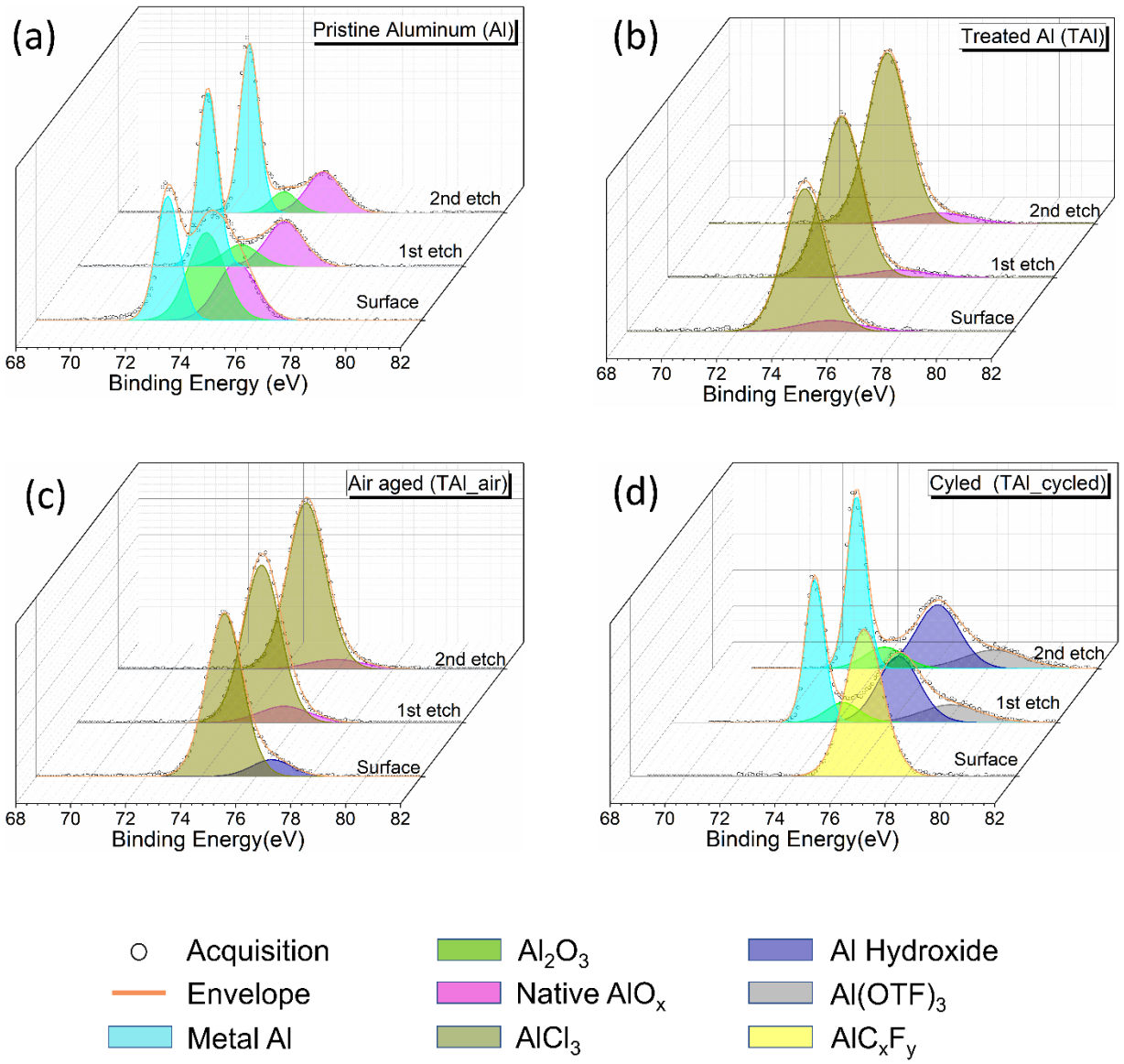

Figure 6-12: XPS spectra showing Al 2p region for surface and two etched layers of a) as received Al foil, b) TAl foil, c) TAl exposed to air for 40 hours, d) TAl foil salvaged from a cycled symmetric cell.

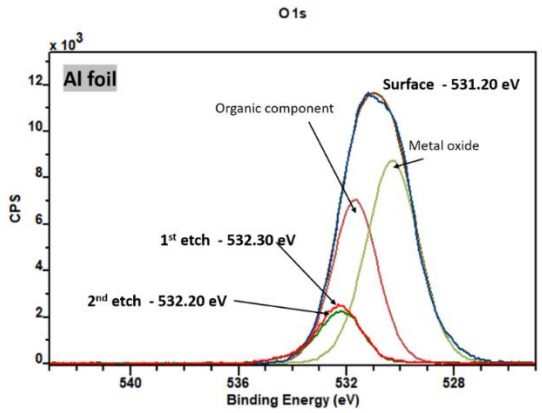

Figure 6-13: O1s region of XPS spectra for all three layers of Al foil.

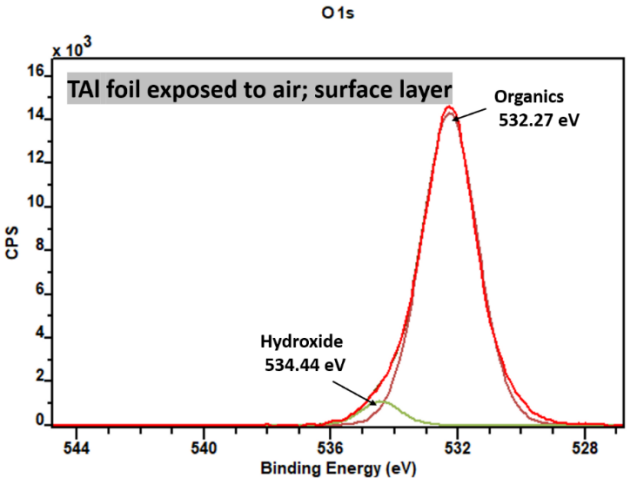

Figure 6-14: O1s region of XPS spectrum for the surface layer of Al foil which was exposed to the ambient air.

Upon 40 hours of exposure to the ambient environment, only minor changes can be observed (Figure 6-12 c). The surface layer is still majorly enriched with Cl salt of Al, and a small amount of Al hydroxide is also detected (high energy components peak of O1s spectrum (Figure 6-14) at 534.44 eV also confirms the hydroxide presence). [37, 39-40] After etching, the uncovered surface revealed an overabundance of $AlCl_3$, with the hydroxide layer gradually disappearing and only a small amount of the native Al oxide layer remaining. Here, in the battery fabrication process adopted here, TAl was only exposed to the ambient environment for a few minutes before being assembled in a coin cell. As a result, the coating layer is adequate for the fabrication phase.

The surface chemistry of TAl changes dramatically as it is cycled (Figure 6-12 d). For starters, there is only one peak for Al at 76.50 eV, which is a non-metallic Al peak. At the same time, new peaks in the C1s XPS spectrum appear (Figure 6-15 a), corresponding to the various functional groups C-N, C=N, CF_3, COOH, and C-S. CF_3 and C-S are most likely from the AlTFS electrolyte, while C=N and C-N are likely from the ionic liquid used in coating, and COOH may have formed in-situ. With two peaks at 533.64 eV and 534.21 eV, O 1s has also been moved to a higher energy state (Figure 6-15 b). The major peak at 533.64 eV corresponds to the oxygen in SO_3^{-}[41], which may have come from the AlTFS electrolyte. F is also detected (Figure 6-15 c), which resembles organic-flouride[42]. Hence a complex compound AlC_xF_y can be proposed to be forming here. [38] The detection of AlC_xF_y and organic functional groups indicates a possible reaction between coating layer and electrolyte to form a new set of compounds, forming part of an in-situ SEI (solid electrolyte interphase). Upon etching, hydroxide and small amounts of oxide are detectable in the cycled TAl (Figure 6-12 d etched layer). XPS of TAl soaked in 2 m AlTFS show that oxide and hydroxide may have formed once the TAl comes in contact with the electrolyte (Figure 6-16). However, once cycling starts, SEI like interface starts to form, and it remains there even after repeated cycling (Figure 6-17) showing that the SEI does not dissolve into the eelctrolyte. As far as the question of Cl dissolution in the electrolyte is concerned, Cl presence on the TAl surface was detected to be random (Figure 6-18). This indicated that originally formed coating layer may have broken partially once the TAl surface interacted with the aqueous electrolyte, however, a SEI like layer enriched with organic functional groups and Al complex forms.

The breaking of original coating may affect the onset magnitude of plating/stripping overpotential. However, it should not affect the plating/stripping overpotential magnitude in the subsequent cycles because the reaction and partial breaking of the coating on the surface takes place when the cell was at rest (right before plating/stripping). Further, the formation of a new SEI like layer can have both positive and negative implications. Positive because continual SEI formation means self-healing of the coating on the anode and negative because continual SEI formation would result in losing electrolyte continuously.

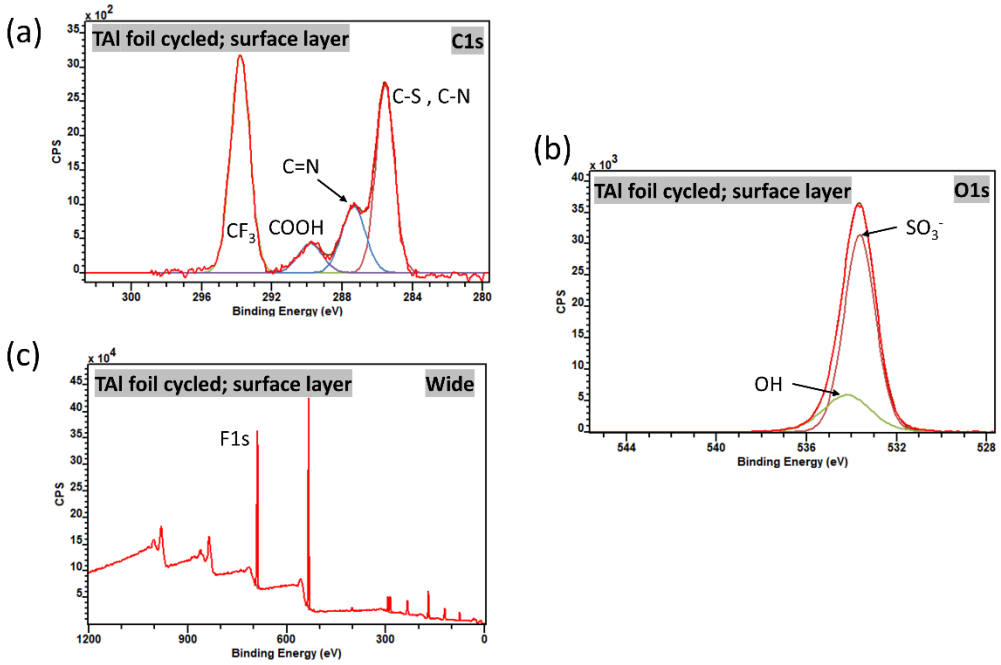

Figure 6-15: (a) C1s region, (b) O1s region and (c) wide spectrum for the surface layer of TAl foil which was cycled. The presence of new carbon species, SO_3^- and F confirms the formation of some kind of SEI layer.

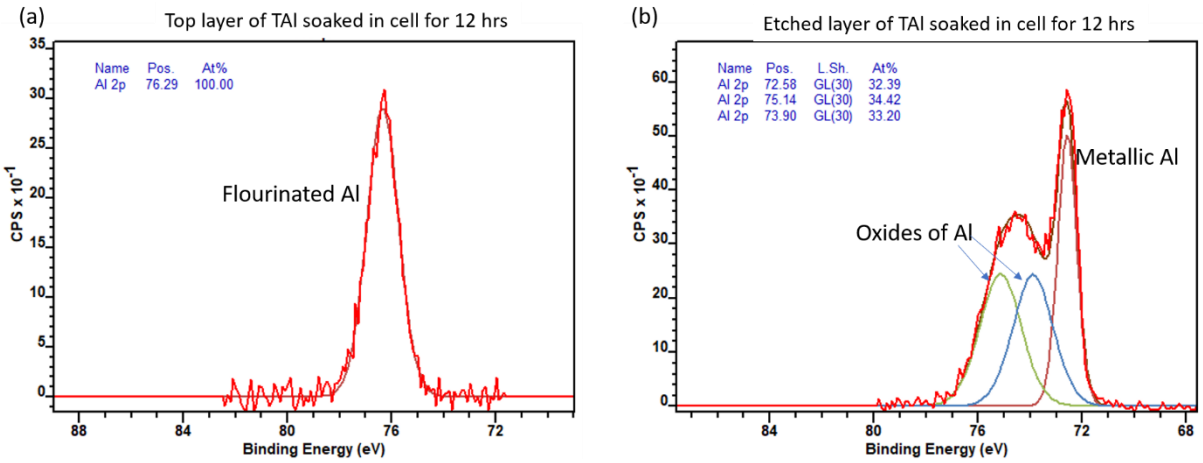

Figure 6-16: Al2p XPS region for TAl foil salvaged from TAl | 2 m AlTFS | TAl cell left at rest for 12 hours: (a) surface and (b) 1st etched surface.

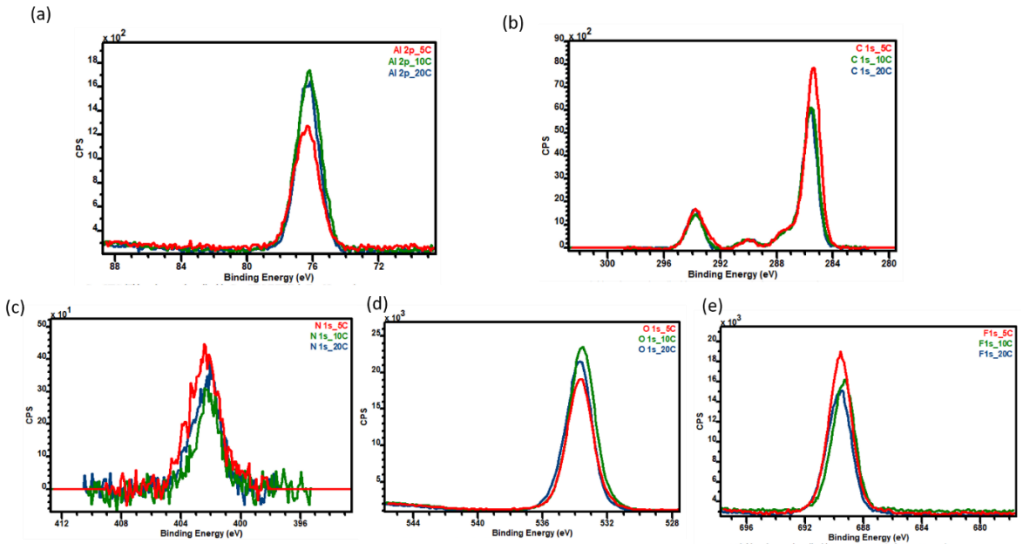

Figure 6-17: XPS spectra of TAl foil retrieved from TAl | 2 m AlTFS | TAl cell after 5, 10, and 20 cycles (labeled 5C, 10C, and 20C, respectively): (a) Al 2p area, (b) C 1s region, (c) N 1s region, (d) O 1s region, and (e) F 1s region. For the progression of cycling, the spectra for all of the above-mentioned species remain more or less the same. The binding energy of chemical species does not change as the cycling continues. Though there are modest quantitative shifts, there is no consistent pattern in the progression of cycling. As a result, the chemical composition of the TAl cycled surface does not change with repetitive cycling.

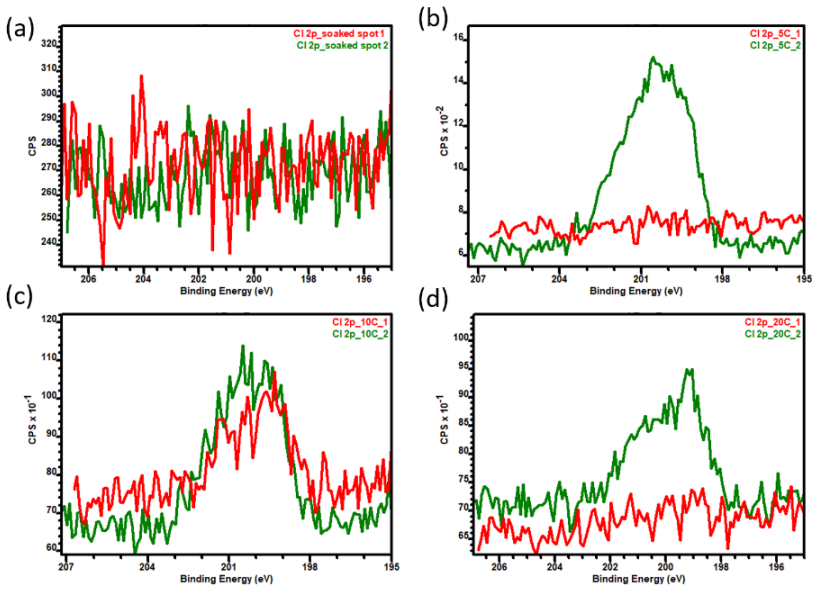

Figure 6-18: Cl 2p area spectra for TAl foil retrieved from a TAl | 2 m AlTFS | TAl cell after (a) 12 hours of soaking/rest, (b) 5, (c) 10, and (d) 20 cycles. XPS signals from two separate spots were obtained for each study. The existence of Cl on the TAl cycled is found to be quite random.

And when Cl is found, it does not have a strong presence. This leads one to believe that Cl from the surface of TAl may leach out partially during cycling, but there is no strong pattern to suggest that more Cl dissolves in the electrolyte with longer cycling or that the dissolution of AlCl3 in the electrolyte improves efficiency.

Overall, it is concluded that the protective coating is stable in the environment and aids in the prevention of oxide forming when Al is moved from the inert atmosphere and installed into a cell. However, this coating is incompatible with a functioning aqueous cell and partially breaks down once the TAl surface interacted with the aqueous electrolyte. The "partially broken protective coating + SEI" sheet, on the other hand, aids in preventing extreme oxidation of Al during cell operation. Despite this, the protective coating on the inside did crack when cycling. Therefore, there is still a need to find a new kind of coating that is more stable in-situ cycling. There are few directions that can be pursued from here: 1) exploring new and cheaper $AlCl_3$ based eutectic coatings (as done in next chapter), 2) exploring electrolyte additives that can form in-situ coating and c) making ex-situ coating by sophisticated method like PLD, CVD etc..

6.4 Conclusion

This chapter makes a phased transition from cathode towards anodic studies by first investigating an HCF type cathode for Al insertion and then studying a treated Al foil as anode against this cathode and exploring the implications of using this anode in a full-cell context.

To begin, a highly stable PBA analogue, NaMnHCF, that can easily store Al-ion by transitioning from monoclinic to tetragonal phase is presented. During repetitive charge/discharge, such a transition is strongly reversible, and Al-ion insertion in the host material is primarily due to vast interstitial voids and charge mitigation by multiple transition centres in the host, namely Fe and Mn. A high energy density of 130 Wh kg^{-1} that decays over 275 cycles to 60 Wh kg^{-1} is recorded. Such performance is above par full

cell reports in AIAB using HCF as cathode & the performance improvement is attributed to the usage of right combination of "cathode+electrolyte+anode".

Next, the crucial implications of using TAl in an aqueous system has been identified. A combination of "TAl + electrolyte" is responsible for influencing plating/stripping potential at the anode, affecting overall cell performance. Most importantly, it becomes clear that water-in-salt principles should be reconsidered because they do not lead to comparable advantages when switching to TAl anodes. It is also shown that: 1) the coating layer on TAl is sufficiently stable in atmospheric conditions and helps to cut its interaction with the foil; 2) Although the coating layer can partially break during battery operations, an in-situ SEI layer forms, which helps to prevent extreme oxidation of the Al anode.

This research adds to the understanding of how to make stable AIAB and strengthens belief in the use of TAl in the AIAB.

References

[1] Q. Zhao, M. J. Zachman, W. I. Al Sadat, J. Zheng, L. F. Kourkoutis, L. Archer. *Sci. Adv.* **2018,** *4*, 1-7.

[2] S. He, J. Wang, X. Zhang, J. Chen, Z. Wang, T. Yang, Z. Liu, Y. Liang, B. Wang, S. Liu, L. Zhang, J. Huang, J. Huang, L. A. O'Dell, H. Yu. *Adv. Funct. Mater.* **2019,** *0*, 1905228.

[3] Q. Zhao, L. Liu, J. Yin, J. Zheng, D. Zhang, J. Chen, L. Archer. *Angew. Chem. Int. Ed.* **2019,** *n/a*.

[4] Z. Hu, Y. Guo, H. Jin, H. Ji, L.-j. Wan. *Chem. Commun.* **2020,** *56*, 2023-2026.

[5] C. Wu, S. Gu, Q. Zhang, Y. Bai, M. Li, Y. Yuan, H. Wang, X. Liu, Y. Yuan, N. Zhu, F. Wu, H. Li, L. Gu, J. Lu. *Nat. Commun.* **2019,** *10*, 1-10.

[6] Z. Hou, X. Zhang, X. Li, Y. Zhu, J. Liang, Y. Qian. *J. Mater. Chem. A.* **2017,** *5*, 730-738.

[7] R. Hauert, J. Patscheider, M. Tobler, R. Zehringer. *Surf Sci.* **1993,** *292*, 121-129.

[8] K. Hirakawa, Y. Hashimoto, T. Ikoma. *Appl. Phys. Lett.* **1990,** *57*, 2555-2557.

[9] H. Nie, M. Li, Q. Li, S. Liang, Y. Tan, L. Sheng, W. Shi, S. X.-A. Zhang. *Chem. Mater.* **2014,** *26*, 3104-3112.

[10] *J. Chem. Educ.* **1993,** *70*, A25.

[11] D. T. Clark, D. Kilcast, W. K. R. Musgrave. *Journal of the Chemical Society D: Chemical Communications.* **1971**, 516b-518.

[12] J. Song, L. Wang, Y. Lu, J. Liu, B. Guo, P. Xiao, J.-J. Lee, X.-Q. Yang, G. Henkelman, J. B. Goodenough. *J. Am. Chem. Soc.* **2015,** *137*, 2658-2664.

[13] W. Manalastas Jr, S. Kumar, V. Verma, L. Zhang, D. Yuan, M. Srinivasan. *ChemSusChem.* **2019,** *12*, 379-396.

[14] R. Y. Wang, B. Shyam, K. H. Stone, J. N. Weker, M. Pasta, H.-W. Lee, M. F. Toney, Y. Cui. *Adv. Energy Mater.* **2015,** *5*, 1401869.

[15] Y. Mizuno, M. Okubo, E. Hosono, T. Kudo, H. Zhou, K. Oh-ishi. *J. Phys. Chem. C.* **2013,** *117*, 10877-10882.

[16] Z. Li, K. Xiang, W. Xing, W. C. Carter, Y. M. Chiang. *Adv. Energy Mater.* **2014,** *5*, 1401410.

[17] Y. Liu, S. Sang, Q. Wu, Z. Lu, K. Liu. *Electrochim. Acta.* **2014,** *143*, 340-346.

[18] A. Zhou, L. Jiang, J. Yue, Y. Tong, Q. Zhang, Z. Lin, B. Liu, C. Wu, l. suo, Y.-S. Hu, H. Li, L. Chen. *ACS Appl. Mater. Interfaces.* **2019,** *11*, 41356–41362.

[19] D. Wang, H. Lv, T. Hussain, Q. Yang, G. Liang, Y. Zhao, L. Ma, Q. Li, H. Li, B. Dong, T. Kaewmaraya, C. Zhi. *Nano Energy.* **2021,** *84*, 105945.

[20] L. Yan, X. Zeng, S. Zhao, W. Jiang, Z. Li, X. Gao, T. Liu, Z. Ji, T. Ma, M. Ling, C. Liang. *ACS Appl. Mater. Interfaces.* **2021,** *13*, 8353-8360.

[21] Y. Gao, H. Yang, X. Wang, Y. Bai, N. Zhu, S. Guo, L. Suo, H. Li, H. Xu, C. Wu. *ChemSusChem.* **2020,** *13*, 732-740.

[22] A. Holland, R. D. McKerracher, A. Cruden, R. G. A. Wills. *J. Appl. Electrochem.* **2018**.

[23] X. Tang, H. Liu, D. Su, P. H. L. Notten, G. Wang. *Nano Research.* **2018,** *11*, 3979-3990.

[24] Y. Tang, W. Li, P. Feng, M. Zhou, K. Wang, Y. Wang, K. Zaghib, K. Jiang. *Adv. Funct. Mater.* **2020,** *30*, 1908754.

[25] X. Bie, K. Kubota, T. Hosaka, K. Chihara, S. Komaba. *J. Mater. Chem. A.* **2017,** *5*, 4325-4330.

[26] H. J. Buser, D. Schwarzenbach, W. Petter, A. Ludi. *lnorg. Chem.* **1977,** *16*, 2704-2710.

[27] T. Suemoto, K. Ohki, R. Fukaya, M. Nakajima, H. Tokoro, S. Ohkoshi. *J. Lumin.* **2009,** *129*, 1775-1778.

[28] L. Wang, Y. Lu, J. Liu, M. Xu, J. Cheng, D. Zhang, J. B. Goodenough. *Angew. Chem. Int. Ed.* **2013,** *52*, 1964-1967.

[29] S. Kumar, R. Satish, V. Verma, H. Ren, P. Kidkhunthod, W. Manalastas, M. Srinivasan. *J. Power Sources.* **2019,** *426*, 151-161.

[30] S. Sun, C. Tang, Y. Jiang, D. Wang, X. Chang, Y. Lei, N. Wang, Y. Zhu. *Sol. Energy Mater. Sol. Cells.* **2020,** *207*, 110332.

[31] S. Nandi, S. K. Das. *Solid State Ionics.* **2020,** *347*, 115228.

[32] W. Pan, Y. Wang, Y. Zhang, H. Y. H. Kwok, M. Wu, X. Zhao, D. Y. C. Leung. *J. Mater. Chem. A.* **2019,** *7*, 17420-17425.

[33] S. Nandi, S. K. Das. *ACS Sustainable Chemistry & Engineering.* **2019**.

[34] Y.-C. Kim, H.-H. Park, J. S. Chun, W.-J. Lee. *Thin Solid Films.* **1994,** *237*, 57-65.

[35] Y. Okamoto, K. Nagata, T. Adachi, T. Imanaka, K. Inamura, T. Takyu. *J. Phys. Chem.* **1991,** *95*, 310-319.

[36] G. Mattogno, G. Righini, G. Montesperelli, E. Traversa. *Appl. Surf. Sci.* **1993,** *70-71*, 363-366.

[37] M. Textor, M. Amstutz. *Anal. Chim. Acta.* **1994,** *297*, 15-26.

[38] G. E. McGuire, G. K. Schweitzer, T. A. Carlson. *lnorg. Chem.* **1973,** *12*, 2450-2453.

[39] S. L. Chang, J. W. Anderegg, P. A. Thiel. *J. Non·Cryst. Solids.* **1996,** *195*, 95-101.

[40] T. J. Carney, P. Tsakiropoulos, J. F. Watts, J. E. Castle. *International Journal of Rapid Solidification.* **1990,** *5*, 189-217.

[41] W. Yao, Z. Zhang, J. Gao, J. Li, J. Xu, Z. Wang, Y. Yang. *Energy Environ. Sci.* **2009,** *2*, 1102-1108.

[42] M. Davies, High resolution XPS of organic polymers: The Scienta ESCA300 database: G. Beamson and D. Briggs John Wiley, Chichester, UK 1992. Elsevier: 1994.

Chapter 7*

Enabling Al-metal anodes for aqueous electrochemical cells by using eutectic mixtures as artificial protective interphase

This chapter explores Urea + $AlCl_3$ and Et_3NHCl + $AlCl_3$ as *two new eutectic formulations which can be used to coat Al and create artificial interphase on it, essentially enabling its usage as an anode in AIAB. These new formulations improve the conductivity and ion transfer kinetics at the Al-metal anode/electrolyte interface and protect Al from severe oxidation in the ambient environment. In the latter half of the chapter, Urea + $AlCl_3$ is identified as the superior coating mixture and further studied for its stability in the ambient environment and during cell operation. Finally,* Urea + *$AlCl_3$ coated Al is implemented in a full cell, providing a proof of concept of a working full-cell with a OCP of 1.2 V.*

*This section submitted substantially as "Enabling Al-metal anodes for aqueous electrochemical cells by using eutectic mixtures as artificial protective interphase."

7.1 Introduction

Prof Archer's work on enabling Al-metal's usage in an AIAB by creating an artificial layer is an important developmental step.[1] It keeps the promise of creating a low-cost and easily disposable battery alive. However, it can also be noticed that the coating mixture used in this particular study requires ionic liquid as one of the precursors for the [EMIm]Cl + $AlCl_3$ eutectic mixture. Ionic liquids are expensive, adding significant cost, and toxic to the environment. At the same time, it was concluded in chapter 6 that though the ionic liquid-based eutectic coating is stable in ambient, it breaks partially while the battery is in operation. Considering above two aspects, it is very much desirable to explore new compositions of coating materials for Al-anode that can replace the expensive IL used as a precursor in [EMIm]Cl + $AlCl_3$ and also form a coating which is stable during cell operation.

Hence, in this chapter, two new pre-cursors have been explored, which can form eutectic mixtures with $AlCl_3$ and can be potentially used to coat Al-metal. The selection of these pre-cursors is inspired by the non-aqueous Al-ion battery studies. These systems commonly employ corrosive electrolytes containing chloride ions which can effectively erode the passivating oxide film on Al.[2] These corrosive electrolytes, if employed as a coating material on Al-metal, can potentially rid of unwanted oxide layer as well. Urea + $AlCl_3$ and Triethylamine hydrochloride + $AlCl_3$ are two such electrolytes recently developed as ionic liquid analogues for non-aqueous Al-ion batteries.[3-5] Both the precursors, urea and triethylamine hydrochloride (Et_3NHCl), are advantageous as they: 1) form eutectic mixtures with $AlCl_3$, creating an opportunity to replace the expensive IL in [EMIm]Cl + $AlCl_3$ and 2) are cheaper than [EMIm]Cl. Price comparison from the Sigma-Aldrich website for analytical grades suggests Urea (0.26 SGD/g) and Et_3NHCl (0.16 SGD/g) to be at least 50 times cheaper than [EMIm]Cl (18 SGD/g). It can also be highlighted here that the exploration of new pre-cursors is also done from the perspective of adding new knowledge in the domain of coating materials for Al-metals, which would enable its usage as anode in AIAB.

Firstly, the electrochemical performance of Urea + $AlCl_3$ (1:1.3) coated Al (UTAl) and Et_3NHCl + $AlCl_3$ (1:1.5) coated Al (ETAl) has been studied and compared with the performance of normal Al-metal. Following this, the urea-based eutectic mixture is identified as the superior coating mixture and further studied for its stability in the ambient environment and during cycling. Finally, this UTAl is used as anode in a full-cell "FeHCF | 2 m AlTFS | UTAl", demonstrating its successful usage.

7.2 Experimental Method

7.2.1 Material Synthesis

Preparation of cathode

$FeFe(CN)_6$ (FeHCF), the active material in the cathode, was made using a method similar to that described elsewhere.[6-7] Under continuous stirring, an aqueous solution of $K_3Fe(CN)_6$ (Sigma-Aldrich; 455946) and an aqueous solution of $FeCl_3$ (Sigma-Aldrich; 236489) were added dropwise to 60 mL of DI water. To avoid $FeCl_3$ hydrolysis, a few drops of 37 per cent HCl solution were applied to the solution. This produced a brownish solution kept at 100°C for about 6 hours to allow the water and HCl to evaporate. This solution was then centrifuged and washed five times with DI water before being dried overnight in a vacuum oven. The obtained powder was further characterized for purity and prepared in the form of the cathode.

The cathode preparation slurry was made with a 6:2:2 weight ratio of active material, super-P, and PVDF binder. The requisite quantities of active material and super P were first mixed in a mortar-pestle until a uniform colour was achieved. This mixture was then added to an N-methyl-2-pyrrolidone solvent that already had the requisite amount of PVDF pre-dissolved. The slurry was then stirred overnight before being painted on titanium foils to create cathodes, which were then dried overnight to remove the solvent.

Preparation of anode

In this study, either Al or UTAl has been used as an anode. Al foil ((0.25mm thick, annealed, 99.99% (metals basis) Alfa Aesar) as received by the company was directly used in cells after punching them out in the form of disks of 16 mm diameter (to be used in coin cells) or in the form of rectangular foils (to be used in flooded beaker cell). Coated Al was readied by polishing Al-foil inside an Ar-filled glovebox (<0.1 ppm O_2; <0.1 ppm H_2O) with 800-grit size sandpaper and then coating it with a mix of $AlCl_3$ and urea or $AlCl_3$ + Et_3NHCl. The urea mix was prepared inside the glovebox by adding anhydrous $AlCl_3$ to pre-dried urea (dried in a vacuum oven overnight at 70° C) in different ratios, including 1.3:1, 1.6:1 and 2:1, and leaving it for rigorous stirring overnight. Similarly, anhydrous $AlCl_3$ was added to Et_3NHCl in different ratios. It is to be noted here that only the ratios combination which gave clear eutectic liquids were chosen for further study. This included 1.3:1 ratio for $AlCl_3$ + Urea and 1.5:1 ratio for $AlCl_3$ + Et_3NHCl. The coating methodology involved dipping polished Al foil in the eutectic mix for ~ 24 hours and flipping it from time to time to cover the coating material on the foil better. Further, the coated Al was softly wipe-dried of all the liquid from the surface and taken out of the glovebox for the cell preparation. (Though no weight measurements were made during this process, there was observable change in the surface lustre after polishing as-received Al and after coating the polished as received Al; As received Al-dull, after polishing-shiny, after coating- dull)

7.2.2 Material Characterization

The Raman shifts for the electrolytic liquids were measured using a WITec Alpha300 SR Confocal Raman spectrometer with a 488 nm argon laser. In the spectral range of 600-4000 cm^{-1}, FTIR spectra for Al foils were reported using a Perkin-Elmer Frontier unit. By first mixing liquids with KBr powder and pressing them into a tablet, FTIR for liquids was registered in transmission mode. FarIR was measured using NicoletTM iSTM 50, Thermo scientific machine in ATR mode.

MI-600, Kratos AXIS Supra XPS instrument equipped with 1486.69 eV, Al Kα radiation was used to investigate the surface of the Al foil at various stages, including- as received

foil by company, foil after coating with $AlCl_3$ + urea eutectic (UTAl), UTAl exposed to air for 48 hours, and UTAl foils recovered from the symmetric cells after various cycles of plating/stripping. For narrow scan, pass energy of 40 eV with a step size of 0.1 eV was used. All foils were characterized at the surface, etched and subsequently characterized 9 times. The etching was performed with an ion gun (5 keV Ar^+). The first 5 etching was done for 30 sec each, followed by 4 more 60-sec etching. The etching was done over 1500 μm * 1500 μm and with an analysis area of 110 μm to ensure that the signals were collected only from the etched area. Peak deconvolution was done in CASA XPS software using Shirley background and a combination of Lorentzian & Gaussian distribution (30:70) model peak. All the spectra for non-coated Al foil and etched layers of cycled UTAl were not calibrated as the dominant Al metal peak was observed to be at the literature metal Al binding energy value of ~ 72.6 eV. [8-9] Surface spectra for UTAl, UTAl exposed to air and cycled UTAl were calibrated to 284.8 eV, owing to the presence of adventitious carbon. Spectra for etched layers of UTAl and UTAl exposed to the air were calibrated to 399.8 eV (N1s) owing to the presence of nitrogen from urea[10].

7.2.3 Electrochemical Characterization

Battery testing was done either in a CR2016 coin cell or a flooded beaker cell as required. For plating/stripping studies, symmetric cells using Al or coated Al were fabricated with Whatman filter paper (Grade-1825-110, thickness 420 μm, filter size 110 mm) as separator (only in coin cells) and aluminum trifluoromethanesulphonate (AlTFS) electrolyte, and a constant current was applied for 1 hour each in alternating sequence using a Solartron Analytical 1470E. Galvanostatic charge-discharge studies were done on FeHCF cathodes with UTAl/Al as anode using BTS-Neware.

EIS study on Al foils was carried out in a three-electrode symmetric cell setup, flooded with 2 m AlTFS electrolyte, with 2 cm^2 of Al or coated Al foils facing each other. EIS spectra of WE and CE electrode were collected separately, using a Biologic SP-200. Saturated Ag/AgCl was used as the reference electrode. EIS measurements were recorded 5 hours after cell fabrication (OCV 1.2 V) and with a 5 min delay after required cycles of

plating/stripping. For each measurement, 6 frequency points were distributed logarithmically per decade in the range of 100 kHz to 8 mHz with an amplitude voltage of 10 mV with no dc voltage bias.

7.3 Results and Discussion

7.3.1 Impedance Study

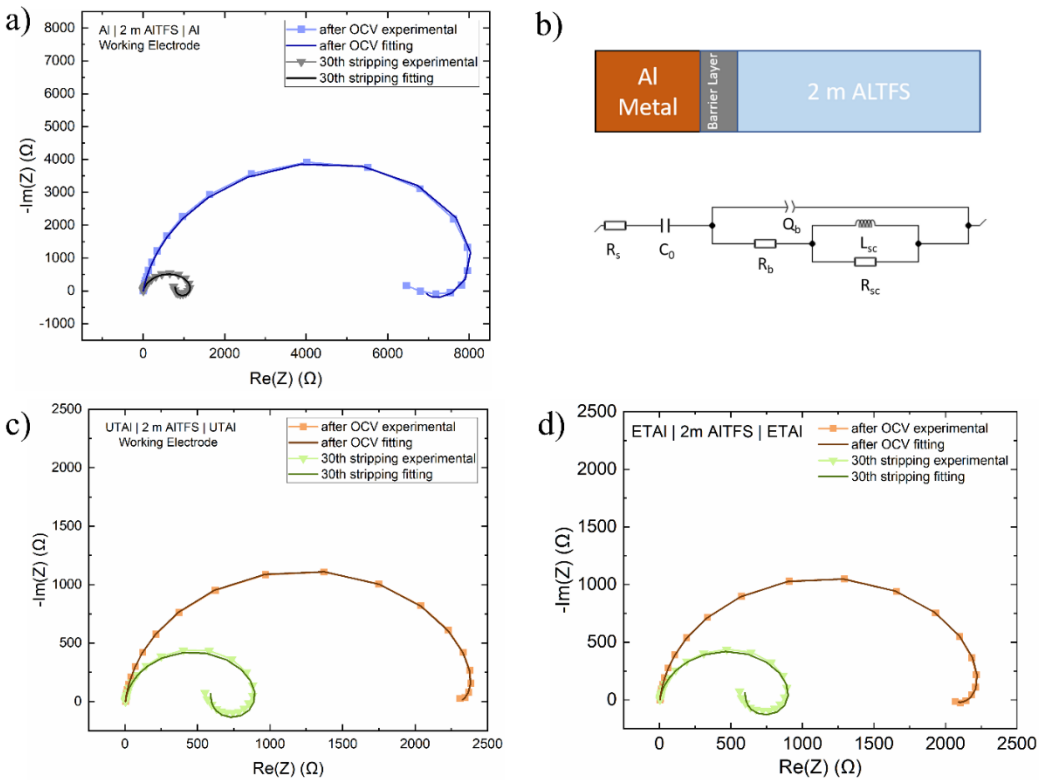

Figure 7-1: Nyquist plot for (a) Al, (c) UTAl and (d) ETAl symmetric cells showing experimental and fitted spectra collected 5 hours after cell fabrication and after 30th stripping cycle. (b) Schematic representing Al metal-barrier layer-electrolyte interface along with the equivalent circuit used to fit the EIS spectra collected for such systems.

The superiority of UTAl and ETAl is reflected in detailed impedance study done on their respective symmetric cells. A comparative EIS study was done on the working electrodes of Al, UTAl and ETAl symmetric cells, 5 hours after cell fabrication and after 30 cycles of plating/stripping (Figure 7-1). The fitting of all EIS spectra was done using an

equivalent electrical circuit model, similar to the ones used in the surface charge approach for metal/oxide/electrolyte systems (Figure 7-1 b).[11-14] This equivalent circuit consists of element R_s, representing solution resistance; constant phase element, Q_b, representing barrier layer capacitance where its impedance is defined as $Z_{CPE} = 1/Q(j\omega)^n$ with $-1 \leq n \leq 1$ while Q is a frequency-independent constant, being defined as pure capacitance for $n = 1$, resistance for $n = 0$, the inductance for $n = -1$; R_b, representing barrier layer resistance; C_0, faradaic pseudocapacitance representing the variation of barrier layer thickness with potential; resistance R_{sc} and inductance L_{sc} elements representing the diffusion and kinetic parameters, respectively, due to the surface charge at the barrier layer/electrolyte interface.[14] The barrier layer for the case of Al is spontaneously forming oxide layer and for coated Al is the artificially formed protective coating on it.

It can be seen that coating with either eutectic composition leads to a significantly improved conductivity. The overall impedance for UTAl and ETAl reduces to ~1/3 compared to uncoated Al (Table 7-1). This decrease is also reflected in reduced resistance of the barrier layer (R_b) and reduced resistance at the barrier layer/electrolyte interface (R_{sc}). Notably, the inductance value for UTAl and ETAl also decreases ~1/4 as compared to the uncoated Al. These observations and corresponding fitting from EIS studies indicate that the eutectic coating is not only less resistive to the ionic migration through the barrier layer but also enables a more conductive and faster ionic transport at the eutectic coating/electrolyte interface when compared to Al-oxide/electrolyte interface.

Table 7-1. Circuit element values obtained after fitting equivalent circuit given in figure 7-1 a,b, c for the to the EIS spectra collected for Al, UTAl and ETAl symmetric cells after OCV.

Components	Al | 2m AlTFS | Al	**UTAl | 2m AlTFS | UTAl**	**ETAl | 2m AlTFS | ETAl**
C_0	1.252 F	144.6 F	144.6 F
Rs	3.921 Ohm	4.019 Ohm	4.065 Ohm
R_b	6938 Ohm	2302 Ohm	2071 Ohm

L_{sc}	5974 H	1370 H	1328 H
R_{sc}	2262 Ohm	161 Ohm	238.5 Ohm
Q_b	59.86e-6 mho.s^n	223.0 1e-6 mho.s^n	165.7 1e-6 mho.s^n
n	0.902	0.938	0.943

A similar EIS study was also done after 30 cycles of plating and stripping for all three cases of Al, UTAl and ETAl. It can be seen that even after 30 cycles, the overall impedance of UTAl and ETAl was lesser than uncoated Al. This reduction of impedance, similar to data after OCV, is partially because of reduced resistance (Rb and Rsc) and partially because of reduced inductance value. This consistency in reduced impedance as an effect of coating even after 30 cycles indicates that either the original coating layer is still intact, or the formation of a new layer enables more conductive and faster ion migration path from the electrolyte to the metal.

Table 7-2. Circuit element values obtained after fitting equivalent circuit given in figure 7-1 a,b, c for the to the EIS spectra collected for Al, UTAl and ETAl symmetric cells after 30 cycles of plating/stripping.

Components	Al | 2m AlTFS | Al	**UTAl | 2m AlTFS | UTAl**	**ETAl | 2m AlTFS | ETAl**
C_0	0.123 F	0.216 F	0.224 F
Rs	3.75 Ohm	4.233 Ohm	3.998 Ohm
R_b	779.1 Ohm	584.8 Ohm	593 Ohm
L_{sc}	1009 H	519.8 H	558.6 H
R_{sc}	498.8 Ohm	342.2 Ohm	348.9 Ohm
Q_b	188.6e-6 mho.s^n	88.78e-6 mho.s^n	114 1e-6 mho.s^n
n	0.861	0.941	0.927

7.3.2 Plating/Stripping Performance

In this section, a comparative plating/stripping study has been done for the symmetric cells of Al, UTAl and ETAl. An overpotential comparison of UTAl vs Al clearly shows reduced voltages for the cells using UTAl (Figure 7-2 a). Similar observations are made for the ETAl vs Al plating/stripping voltage (Figure 7-2 b). A comparison of the UTAl vs ETAl plating/stripping study shows almost similar overpotential in the initial 25 cycles, which increases more rapidly for ETAl (Figure 7-2 c). An equivalent comparison of UTAl vs ETAl at a higher cycling rate of 0.2 mA cm^{-2} (Figure 7-2 d) also shows the superiority of UTAl over ETAl. Plating/Stripping studies demonstrates that coating reduces the overpotential at Al-anode, and at the same time $AlCl_3$ + urea eutectic based outperforms the Et_3NHCl + $AlCl_3$ coating. Hence, going forward, further studies are done only with UTAl.

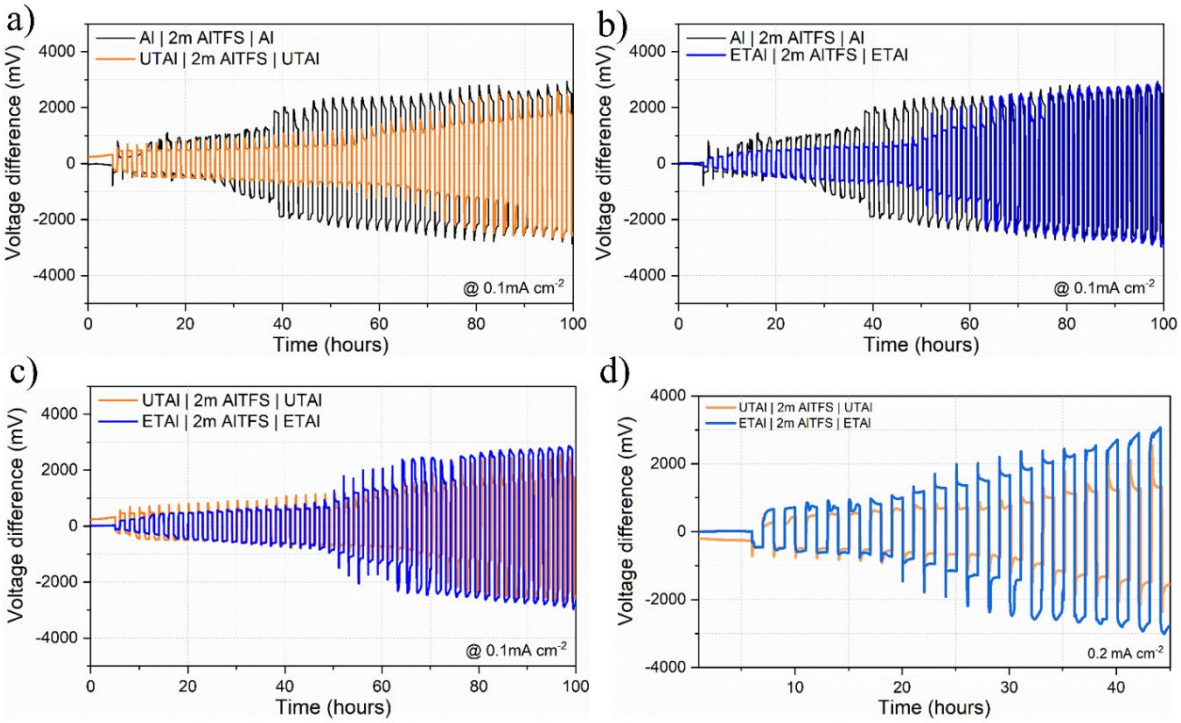

Figure 7-2: Comparative stripping/plating test in symmetric coin cell for (a) Al and UTAl at 0.1 mA cm^{-2}, (b) Al and ETAl at 0.1 mA cm^{-2}, (c) ETAl and UTAl at 0.1 mA cm^{-2} and (d) ETAl and UTAl at 0.2 mA cm^{-2}.

UTAl was also tested in different concentrations of electrolyte form 0.1 m to 5 m (Figure 7-3 a). An optimum overpotential was observed for the case of 2 m AlTFS. A link between overpotential, electrolyte concentration and low conductivity had been speculated in the past,[1, 15], but surprisingly here, the onset overpotential in higher concentration electrolyte (3 m and 5 m) was lower than that in 2 m.[15] This difference could be due to the different nature of the coating materials.

UTAl coated with different ratio combinations of $AlCl_3$ + urea was also tested under the same conditions (Figure 7-3 b). No major difference in the overpotential was observed; however, the study continued with a 1.3:1 ratio because of the homogenous nature of the eutectic. Plating/stripping was also done at different rates to demonstrate the effect of rate on the overpotential (Figure 7-3 c). The overpotential value increase with the increase in the rate.

It was also observed that overpotential starts to increase after about 30 cycles. This can be due to the limited amount of electrolyte (100 µl) in the coin-cell, which keeps on getting decomposed (because of subjecting it to a large testing window) as the cycling progresses. Hence a comparative plating/stripping study of UTAl symmetric cell was also done in flooded beaker symmetric cell, showing better performance in flooded beaker cell (Figure 7-3 d). When comparing UTAl vs Al in beaker cell (Figure 7-3 e), it can be observed that for all 175 cycles (or 350 hours), the UTAl|UTAl overpotential is consistently less than half that of Al|Al. This indicates that 1) the coating layer is likely intact and durable even after repeated cycles of plating/stripping and 2) the increasing overpotential observed with cycling in coin cells is an experimental anomaly due to the limited amount of electrolyte in the coin cell.

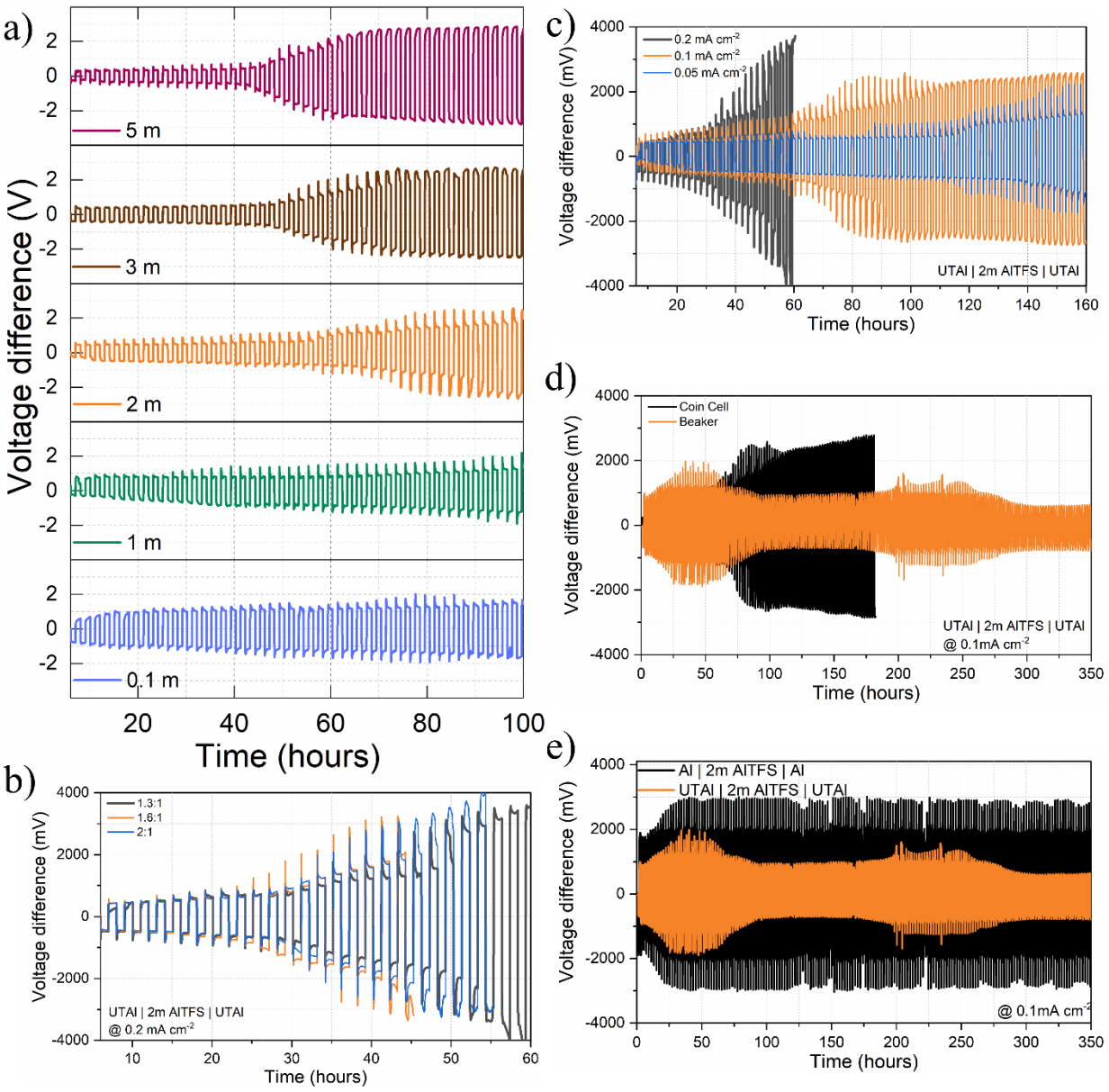

Figure 7-3: (a) Stripping/plating testing in symmetric UTAl coin cell for various concentrations of AlTFS aqueous electrolyte (0.1 m, 1 m, 2 m, 3 m, 5 m) done at 0.1 mA cm^{-2} (b) Stripping/plating testing in symmetric UTAl cells using Al coated with the eutectic mix $AlCl_3$+Urea in three different ratios - 1.3: 1, 1.6:1 and 2:1, (b) Stripping/plating testing in symmetric UTAl cell at various rates including 0.2 mA cm^{-2}, 0.1 mA cm^{-2}, 0.05 mA cm^{-2}, (d) Stripping/plating testing in symmetric UTAl cell for coin cell and flooded beaker cell at 0.1 mA cm^{-2}, (e) Comparative stripping/plating test in symmetric flooded beaker cell for Al and UTAl. Negative and positive current density of 0.1 mA cm^{-2} was applied for 1 hour each in an alternating sequence.

7.3.3 Structural and Compositional Analysis

This section focuses on the compositional study of the UTAl surface 1) right after coating, 2) after exposure to the atmosphere, and 3) after cycling. The aim is essentially to reveal the modification in the Al surface after coating and to check the stability of UTAl in air and during cycling.

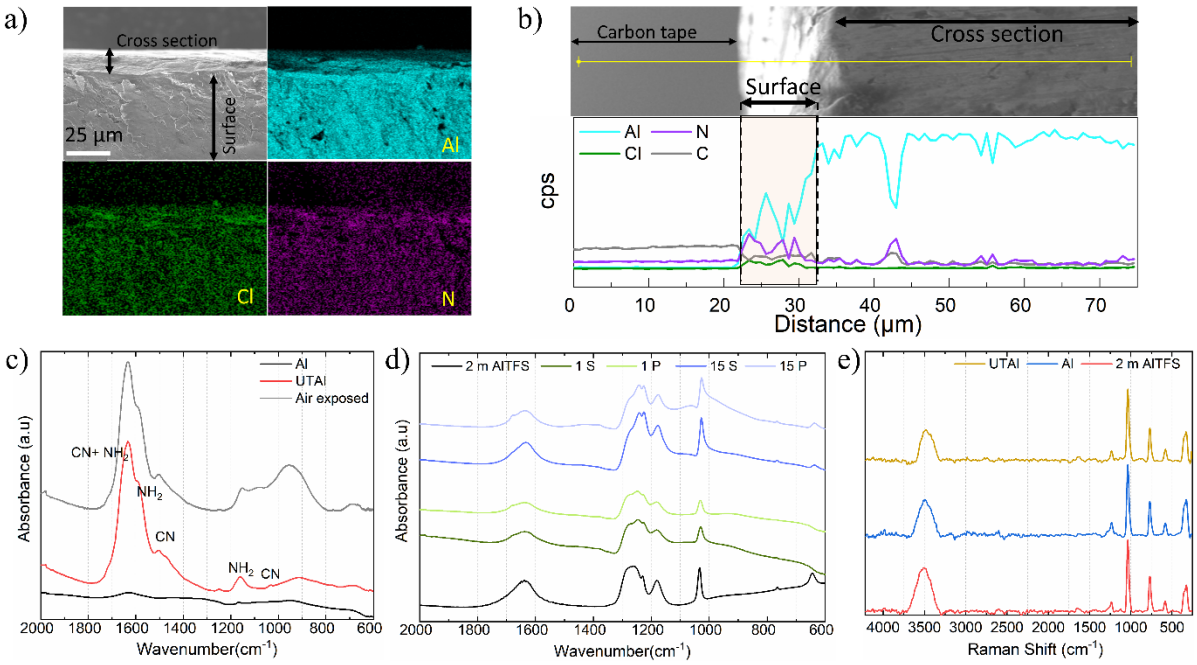

Figure 7-4: (a) SEM-EDX elemental mappings for Al, Cl and N on pristine UTAl surface, (b) SEM-EDX line scan for Al, Cl, N and C through the pristine UTAl cross section. FTIR spectra obtained for (c) as received Al, UTAl, air-exposed UTAl, (d) 2 m AlTFS, cycled UTAl (1S, 1P, 15S and 15P) after salvaging them from cycled symmetric cells (using 2 m AlTFS as electrolyte; cycled at 0.1 mA cm^{-2}), (e) Raman spectra for 2 m AlTFS, electrolyte obtained from flooded beaker cells post-plating/stripping (0.1 mA cm^{-2}) in the symmetric cells of Al and UTAl separately.

EDX elemental mapping of UTAl surface (Figure 7-4 a) and UTAl cross-section (Figure 7-4 b) provides visual insight into the newly formed protective layer on the Al surface. The presence of Cl and N (which come from $AlCl_3$ and urea, respectively) in the surface

is visible in EDX imaging, suggesting a changed surface with uniform coating. Line scan across the cross-section also shows the presence of N and Cl at the surface. Further, the presence of N is confirmed from FTIR analysis (Figure 7-4 c) which shows functional groups like NH_2 and CN. These functional groups remained attached even after 48 hours of exposure to the ambient environment, indicating the stable nature of the coating. The FTIR spectra of UTAl plated (P) or stripped (S) for 1 or 15 cycles primarily showed the presence of peaks characteristic of the 2 m AlTFS electrolyte (Figure 7-4 d). Though the overlap between AlTFS peaks with those of the originally present functional group makes it difficult to unravel the changes happening on the surface, the absence of new peaks over several cycles of plating/stripping indicates no significant changes on the surface interface in between the 1^{st} and 15^{th} cycle.

Furthermore, the non-dissolution of the coating layer into the electrolyte was determined by comparing the Raman spectra of the electrolytes salvaged from the flooded beaker symmetric cells used in plating/stripping of UTAl and Al. The Raman spectrum of the UTAl electrolyte remained the same as that of the Al electrolyte, as shown in figure 7-4 e (both of which is the same as that for 2 m AlTFS). This simply means that the dissolution in the electrolyte is not significant and the surface coating layer is still intact.

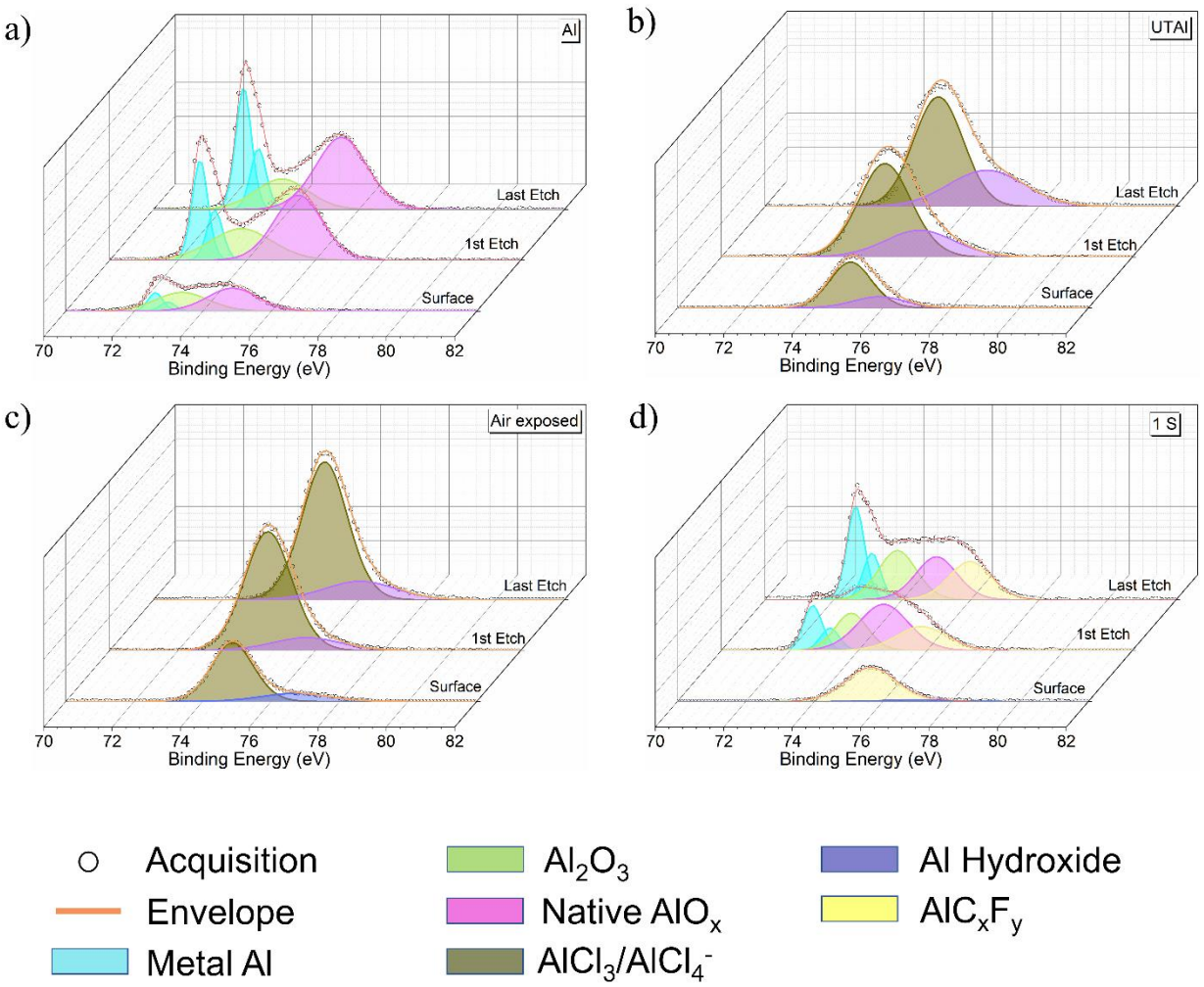

Figure 7-5: Al 2p region of XPS spectra (with deconvoluted peaks) for the surface, 1st etched and 9th etched layers of (a) Al foil as-received from supplier, (b) UTAl foil transferred from glovebox, (c) UTAl exposed to air for 48 hours, (d) UTAl foil subjected to one round of stripping in a symmetric cell (with 2m AlTFS as the electrolyte; cycled at 0.1 mA cm^{-2}). XPS data was first collected from the surface (labelled "surface"), followed by 5 rounds of etching (30 s Ar^+ sputtering) and subsequent data collection; which was followed by 4 more rounds of etching (60 s Ar^+ sputtering) and subsequent data collection.

By probing Al species on the surface and below, XPS research adds to our understanding of surface chemistry. It supports the FTIR study by demonstrating that the eutectic coating is air-stable, preventing the formation of oxide on the metallic Al surface while also providing protection during cell cycling by allowing the formation of an SEI-like

layer on the UTAl. The company's as-received Al foil, UTAl, UTAl exposed to air for 48 hours, and UTAl foils retrieved from the symmetric cells after various plating/stripping cycles were all subjected to layer-wise XPS characterization. For each case, the surface was characterized, followed by 5 rounds of 30-sec etching with 5 keV Ar^+ and an-immediate spectroscopy characterization, which was followed by 4 more rounds of 60-sec etching and characterization. Figure 7-5 and Figure 7-6 selectively shows the surface, 1st etch and last etch Al 2p region of XPS spectra with the deconvoluted peaks. Essentially, the interpretation of the chemical species present on the surface and beneath reveals information about the stability of the coating layer. The binding energy of all the species mentioned in this section with their respective references is presented in Table 7-3, 7-4 and 7-5.

The as-received Al-metal foil showed the presence of Al metal[8-9] (modelled as a pair of peaks because of spin-orbit components) along with two different kinds of oxides including Al_2O_3 and the native oxide layer on Al, AlO_x (Figure 7-5 a).[8-9, 16-21] As predicted, etching reduced the relative amount of Al_2O_3 and increased the prominence of the Al metal component, while the relative amount of native oxide remained nearly constant. The large increase in strength observed after etching was most likely due to the removal of surface contaminant, exposing the metallic surface underneath. Upon coating, there was a significant modification in the surface chemistry associated with the appearance of a new chemical species, which corresponds to the chloride salts of Al ($AlCl_3$/ $AlCl_4^-$) (Figure 7-5 b).[22-23] The presence of Al-based chloride salts was also corroborated by the detection of Cl^- on the surface (Figure 7-7 a).[22] This Cl salt of Al confirms the existence of the eutectic mix products formed according to the equations below.[24] On the surface of the Al, a significant amount of oxide was missing compared to the as-received Al. Surprisingly, the Al chloride salts were still predominant after nine rounds of etching, and the amount of AlO_x barely increased (this increased amount can be due to the removal of adventitious carbon from the surface, which also explains lower intensities of the surface spectra in all the cases). The above study clearly demonstrates that the eutectic coating has effectively covered the Al surface and is applied to it as a dense artificial layer.

$$n(urea) + 2AlCl_3 = [AlCl_2 . (urea)_n]^+ + AlCl_4^-$$

$$AlCl_4^- + AlCl_3 = Al_2Cl_7^-$$

Further, UTAl was exposed to the ambient environment for ~48 hours and characterized. With the presence of a relatively small amount of Al hydroxide (Figure 7-5 c), presumably formed as the sample interacted with moisture in the open air, the surface remained effectively covered by the chloride salts of Al.[25] The abundant presence of Al chloride salts with a small amount of AlO_x is still visible on the first and last etched surfaces, close to what was found for pristine UTAl. This demonstrates the coating layer's effectiveness in forming a protective barrier between Al and the atmosphere, preventing substantial oxidation on the Al surface. It's worth noting that the pristine or "new" UTAl is only exposed to the environment for a few minutes from glovebox to cell assembly.

In a symmetric UTAl | 2m AlTFS | UTAl cell, UTAl was also plated/stripped and characterized to see how efficient the coating layer was at preventing oxide formation during cell operations. After 1st stripping (Figure 7-5 d), a new peak in the high energy range of Al 2p core-level state was observed on the surface, which can neither be chloride salt of Al nor hydroxide of Al, as no Cl or any high energy oxygen peak (534 eV)[26] was observed parallelly. Therefore, here it has been attributed to the presence of fluoride salt of Al[27]. The detection of fluoride F 1s peak at high energy (Figure 7-7 b) also confirms the presence of Al fluoride salts.[28] Since there was no fluorine in the coating mixture, to begin with, this new fluoride-based species may have formed by the reaction of the protective barrier layer with the AlTFS electrolyte. Since there was no fluorine in the coating mixture, to begin with, this new fluoride-based specie may have formed by the reaction of the protective barrier layer with the AlTFS electrolyte. After etching, the Al spectra could be fitted with a mixture of Al and Al oxide peaks, similar to how the as-received Al was done. A high-energy peak with the same binding energy as the fluoride salt of Al found on the surface could also be fitted. However, the F1s spectrum (Figure 7-7 c) show the existence of organic fluorine rather than metal fluoride.[28-29] Hence, this fluoride species has been attributed as AlC_xF_y. Additionally, a high energy C peak on 1S surface (Figure 7-7 e) was also detected which was not present in UTAl (Figure 7-7 d) and has been attributed to C-F bond which may come from AlC_xF_y complex. The

presence of this new carbon fluoride species is highly indicative of the formation of an SEI-like layer. Compared to the precycling point, the relative amount of Al oxide on UTAl has increased after cycling.

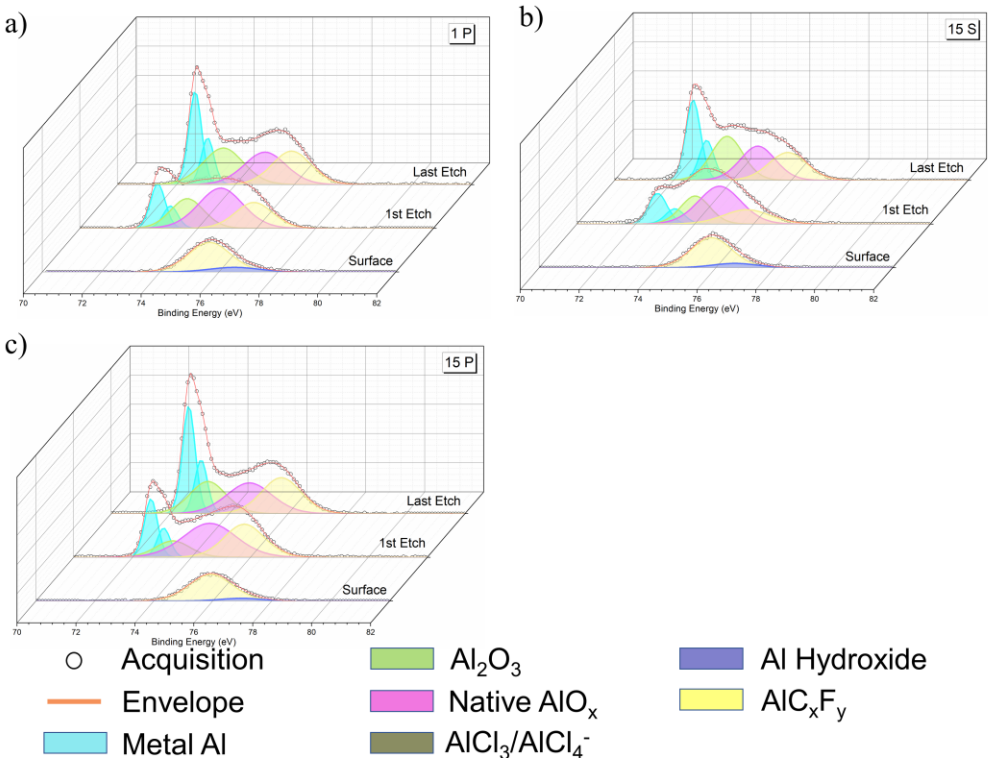

Figure 7-6: (a) Al 2p region of XPS spectra (with deconvoluted peaks) for the surface, 1st etched, and 9th etched layers of UTAl salvaged after (a) 1st plating, (b) 15th stripping, (c) 15th plating. XPS data was first collected from the surface, followed by 5 rounds of etching (30 s Ar^+ sputtering) and subsequent data collection; which was followed by 4 rounds of etching (60 s Ar^+ sputtering) and subsequent data collection.

However, it is not as strong as what was discovered for the Al as obtained. The overall spectrum and respective deconvoluted peaks remained identical to 1S after plating (Figure 7-6 a). Also, after the 15th stripping and plating, a similar profile could be seen (Figure 7-6 b, c).

Overall, it is concluded that the protective barrier layer effectively prevents oxidation in

the ambient environment and assists in forming an SEI-like layer while the cell is in operation. The formation of new AlC_xF_y species right from the 1st stripping with no major observable changes occurring even after 15th round of plating/stripping indicates that an in-situ layer had formed right from the beginning of the cell operation and effectively inhibits excessive oxide formation on Al during cell operation. These observations are very similar to what has been reported in previous work which included studying ionic liquid coated Al developed by Prof Archer et. al.[1]

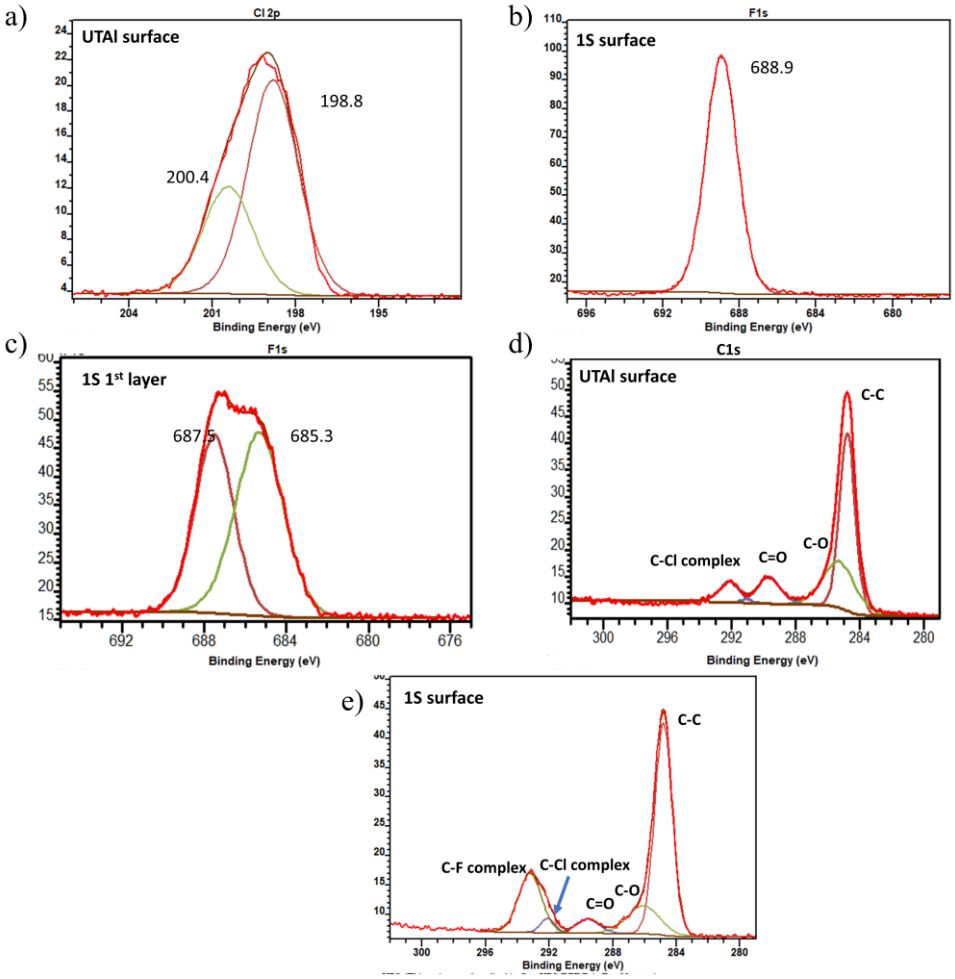

Figure 7-7: (a) Cl 2p region of XPS spectrum for UTAl surface showing the presence of Cl, (b) F1s region of XPS spectrum from surface of Al stripped for one cycle (1S) showing the presence of metallic fluoride. (c) F1s region of XPS spectrum for 1S 1st layer after etching, showing the presence of organic fluoride (low energy), (d) C1s region of XPS spectrum for UTAl surface showing the presence of a new C-Cl complex which likely is a part of the eutectic coating on Al.

(e) C1s region of XPS spectrum for 1S surface showing the appearance of a new C-F like complex, likely formed from the reaction of AlTFS electrolyte with the eutectic coating.

Table 7-3: Binding energy of species from Al2p region of XPS spectra discussed in the XPS section.

Species	Binding Energy (eV)	References
Metal Al	72.6-72.8	8-9
Al_2O_3	73.39-74.44	16-19
$AlCl_4^-$	75.4	22
$AlCl_3$	74.32-74.85	23
Al Hydroxide	75.71-76.71	25
Native AlO_x	75.29-76.47	20-21
$AlF_{2.3}(OH)_{0.7}.H_20$	75.8	27
AlF_y	76.50	23
$Al(OTF)_3$	77.6	7

Table 7-4: Binding energy of species from O1s region of XPS spectra discussed in the XPS section.

Species	Binding Energy (eV)	References
Al oxide	530.3-531	30-31
Organic species (C=O)	532.30	32-33
Al hydroxide	534.44-534.66	26
SO_3^-	533.64	34

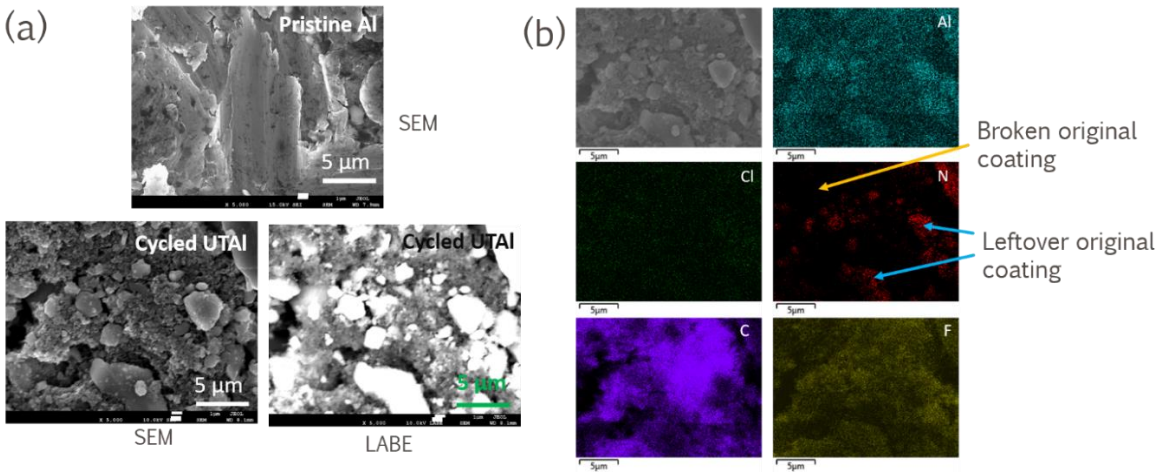

Figure 7-8: (a) SE image of Pristine Al, Cycled UTAl and LABE image of Cycled UTAl. (b) SEM-EDX elemental mapping of Cycled UTAl (same area as in (a)).

Table 7-5: Binding energy of species from C1s region of XPS spectra discussed in the XPS section.

Species	Binding Energy (eV)	References
CF_3	293.81	33, 35
COOH	289.82	36-37
C=N	287.35	38
C-N	285.57	38
C-S	285.57	39

The formation of an in-situ SEI layer was also confirmed from the SEM studies post cycling. Firstly, a comparison of surface morphology of pristine Al and cycled Al indicated some deposition/crystallization on the surface during cycling (Figure 7-8 a). A LABE analysis on the same cycled UTAL surface indicated the presence of more than one element. Hence, an EDX analysis of the same surface was done. The original protective later, composed of N and Cl species, was found to be broken partially. But very interestingly, all such vacant space from the broken original coating layer had presence of C and F species. Presence of such species was also found in XPS study above and was attributed to AlC_xF_y complex which would have formed the main component of an in-situ SEI like layer.

The presence of AlCxFy complex on the surface throughout cycling, irrespective of whether on stripped (1S, Fig-7-5d and 15S, Fig-7-6b) or plated samples (1P, Fig-7-6a and 15P, Fig-7-6c) indicates clearly that it is a part of the in-situ formed SEI layer. Presence of AlCxFy is pivotal in providing an anode surface with reduced charge transfer resistance as compared to bare Al (evident from the 30th cycle EIS study in Fig 7-1)). EIS data shows that impedance of modified anode after 30th cycle is 1/3rd that of bare Al after 30th cycle. We believe that it is the presence of AlCxFy complex that is facilitating less resistive ion migration path at the interface.

7.3.4 Full cell Battery Performance

A proof of concept is given in this section by demonstrating a working full cell using

UTAl as an anode and FeHCF as a cathode. FeHCF was chosen for this application because: 1) it has been documented for AlAB with reasonably stable cycling stability, implying that it will not affect the cycling stability of the entire cell; and 2) FeHCF has a 3D open structure with large interstitial voids (~ 4.6 Å) which makes its crystal structure ideal for studying multivalent battery chemistry like Al^{3+} or its hydrated complex which have a large diameter(~ 3.8 Å).[40-41].

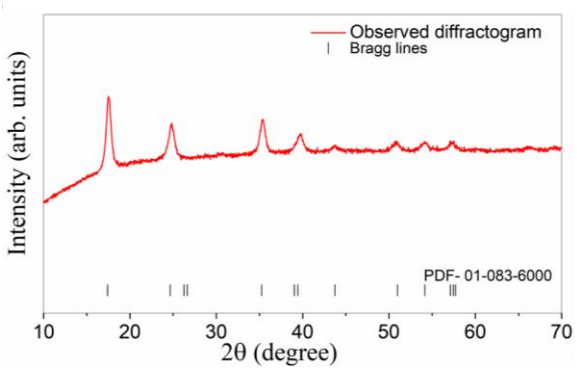

Figure 7-9: Experimental XRD pattern of synthesized FeHCF powder with Bragg lines of matched phase

Figure 7-9 show the x-ray diffractogram of the synthesized powder indicating a high-purity compound matching well with the cubic phase $Fe(Fe_{0.97}(CN)_6)_{0.88}(H_2O)_{0.473}$. The CV plot for the full cell (WE- HCF) is shown in Figure 7-10 a, demonstrating that FeHCF is reversibly active towards Al insertion. The broadened nature of the peaks suggests a complex insertion mechanism, which has previously been observed for HCFs., including possibly a de-solvation of hydrated Al-ion complex at cathode-electrolyte interphase.[42] Further, as a control test for H^+ insertion, the activity of FeHCF was also tested in HTFS (trifluoromethanesulfonic acid) and a 1:1 mix of AlTFS and HTFS (Figure 7-10 b). CV peaks observed in HTFS are non-significant and do not occur at the same potential as in AlTFS indicating insignificant H^+ insertion. On adding AlTFS to HTFS, new peaks start to appear, indicating it is Al which is actively inserting into the host material and H^+ does not have a significant contribution to the capacity. The galvanostatic charge-discharge profile for FeHCF | 2 m AlTFS | UTAl cell is shown in Figure 7-10 c for different cycles. Over repeated cycles, the charge-discharge profile remains the same, with only a minor rise in the overpotential. The urea-coated Al cell

outperforms the FeHCF | 2 m AlTFS | Al cell in the same voltage range and at the same rate of 100 mAh g^{-1} in a comparative analysis. As shown in Figure 7-10 d, the voltage difference of charge and discharge plateau is significantly large, effectively reducing the capacity harnessed in the given voltage range.

UTAl was also tested in a full cell at various cycling rates to show its applicability at both low and high rates (Figure 7-10 e). The capacity observed at high rates was lower, as predicted, but the cycling stability performance was more stable when compared to low rates. A high energy density of 100 Wh kg-1 was observed at low rates, but after 100 cycles, this dropped to 60 Wh kg-1. UTAl was also tested in a full cell at various cycling rates to show its applicability at both low and high rates (Figure 7-10 e). The capacity observed at high rates was lower, as predicted, but the cycling stability performance was more stable when compared to low rates. A high energy density of 100 Wh kg^{-1} was observed at low rates, but after 100 cycles, this dropped to 60 Wh kg^{-1}. This performance is at par with our previous study on NaMnHCF cathode that used ionic liquid coated Al as the anode. [29] If compared to other groups, this performance is significantly better than the only two HCF-Al full cell reports in the AIAB field, reporting energy densities of 15 Wh kg^{-1} and 40 Wh kg^{-1}. [43-44] Demonstrating a stable and comparable performance of the FeHCF cathode with our UTAl, we establish our coating to be effective and better than using bare Al.

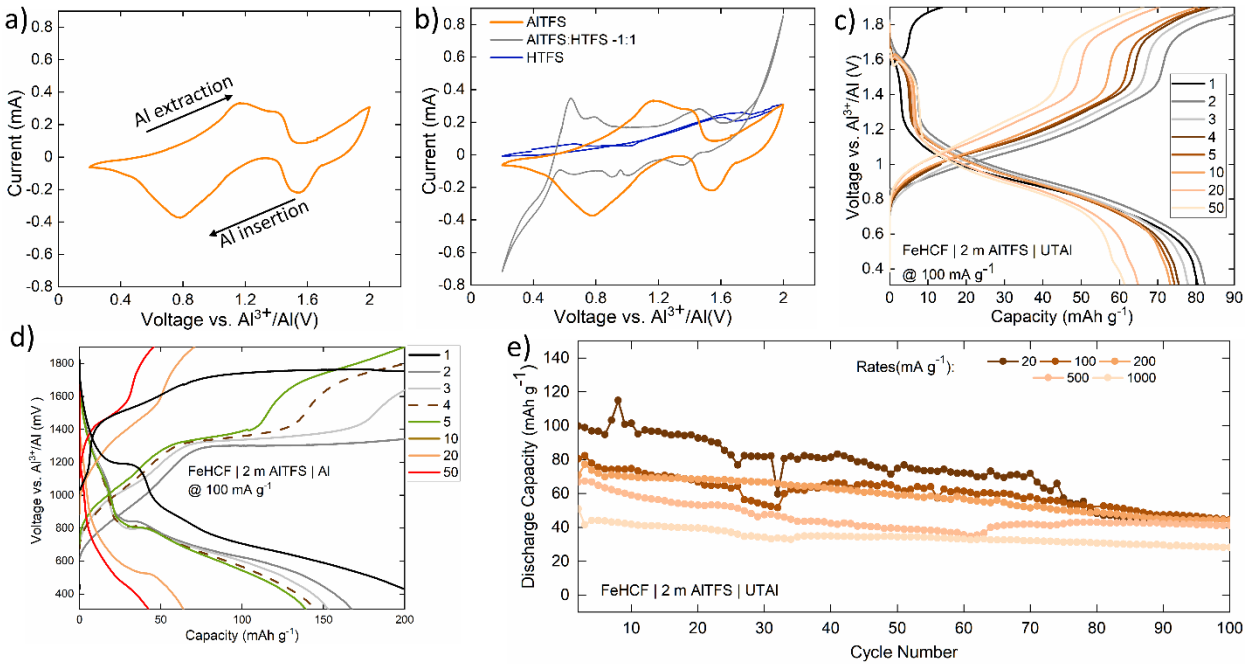

Figure 7-10: (a) Cyclic voltammogram (CV) of FeHCF | 2 m AlTFS | UTAl at 1mV s^{-1}, (b) CV for control test in trifluoromethanesulfonic acid and AlTFS combinations at 1mV s^{-1} (c) Galvanostatic charge/discharge profile at various cycles for FeHCF | 2 m AlTFS | UTAl cell at a current rate of 100 mA g^{-1}, (d) Galvanostatic charge/discharge profile at various cycles for FeHCF | 2 m AlTFS | Al at a current rate of 100 mA g^{-1}, (e) Cycling stability study at various current rates for FeHCF | 2 m AlTFS | UTAl cell.

7.4 Conclusion

The $AlCl_3$ + urea eutectic mixture has been introduced in this chapter as a less expensive alternative to $AlCl_3$ + ionic liquid mixture for coating Al and allowing its use as an anode in aqueous battery systems.

Firstly, the superiority of UTAl over non-coated Al was established by employing electroplating/ stripping and EIS studies in symmetric cells. The UTAl cell showed reduced plating/stripping overpotential which remained less than half of Al cell overpotential even for 175 cycles. EIS studies confirm the coating superiority by indicating a less resistive and faster ion migration path enabled by coating on Al. This artificial UTAl coating is observed to be 9 times less resistive than the oxide layer on

non-coated Al before plating/stripping, and 5 times less resistive after the 30th cycle of stripping. A 6 times higher value of inductance for UTAl also establishes the faster ionic transfer at the coating/electrolyte interface.

Secondly, the surface composition of coated Al has been investigated, as well as its stability in open-air and during cell operations. Coating fully transforms the Al surface chemistry from oxide to chloride composition with organic functional groups, as has been shown. This new interface is stable for at least 48 hours in an ambient environment. Despite the fact that the coating was observed to partially break down during cell operation, it could still aid in the creation of a new SEI-like layer, which is important for reducing Al surface oxidation during cell operations. Finally, a proof of concept that UTAl can be easily integrated into battery cells has been provided by demonstrating a stable full cell using FeHCF cathode with UTAl.

Overall, a new path has been demonstrated toward allowing the use of Al metal foil in aqueous electrolyte, and these results are not only a next step in establishing aluminum-ion aqueous batteries as a seminal principle, but they also pave the way for the commercialization of super-cheap batteries.

References

[1] Q. Zhao, M. J. Zachman, W. I. Al Sadat, J. Zheng, L. F. Kourkoutis, L. Archer. *Sci. Adv.* **2018,** *4*, 1-7.

[2] G. A. Elia, K. Marquardt, K. Hoeppner, S. Fantini, R. Lin, E. Knipping, W. Peters, J.-F. Drillet, S. Passerini, R. Hahn. *Adv. Mater.* **2016,** *28*, 7564-7579.

[3] M. Angell, C.-J. Pan, Y. Rong, C. Yuan, M.-C. Lin, B.-J. Hwang, H. Dai. *Proceedings of the National Academy of Sciences.* **2017,** *114*, 834.

[4] K. L. Ng, T. Dong, J. Anawati, G. Azimi. *Adv. Sustainable Syst.* **2020,** *4*, 2000074.

[5] H. Xu, T. Bai, H. Chen, F. Guo, J. Xi, T. Huang, S. Cai, X. Chu, J. Ling, W. Gao, Z. Xu, C. Gao. *Energy Storage Materials.* **2019,** *17*, 38-45.

[6] Z. Liu, G. Pulletikurthi, F. Endres. *ACS Appl. Mater. Interfaces.* **2016,** *8*, 12158-12164.

[7] A. Zhou, L. Jiang, J. Yue, Y. Tong, Q. Zhang, Z. Lin, B. Liu, C. Wu, l. suo, Y.-S. Hu, H. Li, L. Chen. *ACS Appl. Mater. Interfaces.* **2019,** *11*, 41356–41362.

[8] R. Hauert, J. Patscheider, M. Tobler, R. Zehringer. *Surf Sci.* **1993,** *292*, 121-129.

[9] K. Hirakawa, Y. Hashimoto, T. Ikoma. *Appl. Phys. Lett.* **1990,** *57*, 2555-2557.

[10] J. Ederer, P. Janoš, P. Ecorchard, J. Tolasz, V. Štengl, H. Beneš, M. Perchacz, O. Pop-Georgievski. *RSC Adv.* **2017,** *7*, 12464-12473.

[11] S. Cattarin, M. Musiani, B. Tribollet. *J. Electrochem. Soc.* **2002,** *149*, B457.

[12] S. Guo, J. J. Leavitt, X. Zhou, E. Lahti, J. Zhang. *RSC Adv.* **2016,** *6*, 44119-44128.

[13] M. B. Kannan, C. Moore, S. Saptarshi, S. Somasundaram, M. Rahuma, A. L. Lopata. *Sci. Rep.* **2017,** *7*, 15605.

[14] M. Bojinov. *Electrochim. Acta.* **1997,** *42*, 3489-3498.

[15] S. Kumar, V. Verma, H. Arora, W. Manalastas, M. Srinivasan. *ACS Applied Energy Materials.* **2020,** *3*, 8627-8635.

[16] Y.-C. Kim, H.-H. Park, J. S. Chun, W.-J. Lee. *Thin Solid Films.* **1994,** *237*, 57-65.

[17] Y. Okamoto, K. Nagata, T. Adachi, T. Imanaka, K. Inamura, T. Takyu. *J. Phys. Chem.* **1991,** *95*, 310-319.

[18] G. Mattogno, G. Righini, G. Montesperelli, E. Traversa. *Appl. Surf. Sci.* **1993,** *70-71*, 363-366.

[19] G. Mattogno, G. Righini, G. Montesperelli, E. Traversa. *J. Mater. Res.* **1994,** *9*, 1426-1433.

[20] S. L. Chang, J. W. Anderegg, P. A. Thiel. *J. Non·Cryst. Solids.* **1996,** *195*, 95-101.

[21] T. J. Carney, P. Tsakiropoulos, J. F. Watts, J. E. Castle. *International Journal of Rapid Solidification.* **1990,** *5*, 189-217.

[22] M.-C. Lin, M. Gong, B. Lu, Y. Wu, D.-Y. Wang, M. Guan, M. Angell, C. Chen, J. Yang, B.-J. Hwang, H. Dai. *Nature.* **2015,** *520*, 324-328.

[23] G. E. McGuire, G. K. Schweitzer, T. A. Carlson. *lnorg. Chem.* **1973,** *12*, 2450-2453.

[24] M. Malik, K. L. Ng, G. Azimi. *Electrochim. Acta.* **2020,** *354*, 136708.

[25] R. H. J. Lindsay J.R., Swartz W.E., Watts P.H., Rayburn K.A. *Appl. Spectmsc.* **1973,** *27*, 1.

[26] M. Textor, M. Amstutz. *Anal. Chim. Acta.* **1994,** *297*, 15-26.

[27] A. Hess, E. Kemnitz, A. Lippitz, W. E. S. Unger, D. H. Menz. *J. Catal.* **1994,** *148*, 270-280.

[28] M. Davies, High resolution XPS of organic polymers: The Scienta ESCA300 database: G. Beamson and D. Briggs John Wiley, Chichester, UK 1992. Elsevier: 1994.

[29] E. Kemnitz, A. Kohne, I. Grohmann, A. Lippitz, W. E. S. Unger. *J. Catal.* **1996,** *159*, 270-279.

[30] T. L. Barr. *Zeolites.* **1990,** *10*, 760-765.

[31] Y. Okamoto, T. Imanaka, S. Teranishi. *J. Catal.* **1980,** *65*, 448-460.

[32] K. Endo, C. Inoue, N. Kobayashi, M. Aida. *J. Phys. Chem. Solids.* **1994,** *55*, 471-478.

[33] *J. Chem. Educ.* **1993,** *70*, A25.

[34] W. Yao, Z. Zhang, J. Gao, J. Li, J. Xu, Z. Wang, Y. Yang. *Energy Environ. Sci.* **2009,** *2*, 1102-1108.

[35] D. T. Clark, D. Kilcast, W. K. R. Musgrave. *Journal of the Chemical Society D: Chemical Communications.* **1971**, 516b-518.

[36] G. Barth, R. Linder, C. Bryson. *Surf. Interface Anal.* **1988,** *11*, 307-311.

[37] F. Bournel, C. Laffon, P. Parent, G. Tourillon. *Surf Sci.* **1996,** *350*, 60-78.

[38] H. Nie, M. Li, Q. Li, S. Liang, Y. Tan, L. Sheng, W. Shi, S. X.-A. Zhang. *Chem. Mater.* **2014,** *26*, 3104-3112.

[39] F. E. H. J. Peeling, D.M. Mckinnon, M.S. Chauhan, N.S. Mclntyre. *Can. J. Chem.* **1978,** *56*.

[40] W. Manalastas Jr, S. Kumar, V. Verma, L. Zhang, D. Yuan, M. Srinivasan. *ChemSusChem.* **2019,** *12*, 379-396.

[41] R. Y. Wang, B. Shyam, K. H. Stone, J. N. Weker, M. Pasta, H.-W. Lee, M. F. Toney, Y. Cui. *Adv. Energy Mater.* **2015,** *5*, 1401869.

[42] Y. Mizuno, M. Okubo, E. Hosono, T. Kudo, H. Zhou, K. Oh-ishi. *J. Phys. Chem. C.* **2013,** *117*, 10877-10882.

[43] Y. Gao, H. Yang, X. Wang, Y. Bai, N. Zhu, S. Guo, L. Suo, H. Li, H. Xu, C. Wu. *ChemSusChem.* **2020,** *13*, 732-740.

[44] A. Holland, R. D. McKerracher, A. Cruden, R. G. A. Wills. *J. Appl. Electrochem.* **2018**.

Chapter 8

Conclusions and Recommendations

In this chapter, the major conclusions of the studies carried out are put into perspective and summarized. The novel contributions and findings are highlighted and compared to existing AIAB literature. The scope for future work and the possible strategies to further improve the performance of AIAB has also been discussed. These include exploration of methods to stabilize cycling performance of high voltage cathodes, exploration of robust coating techniques for Al-metal anode, exploration of hybrid electrolyte to improve cycling stability further and studying the gas evolution during cell operation.

8.1 Perspective

The main aim of this thesis was to study the feasibility of AIAB by engineering cathode and anode materials and to implement them in an aqueous electrolyte. The thesis started with a deep literature review on the historical developments on the AlAB. AIAB being a new and rapidly developing field, contemporary literature was also visited regularly. Indeed, the nature of this project has been very dynamic, and contemporary literature had a major role in pivoting the direction of this thesis. The starting phase of this thesis aimed only at engineering new cathode materials, but the need to optimize electrolyte and engineer anode surface became abundantly clear as the thesis progressed.

In the initial stages of this project, it was important to establish the feasibility of the Al-insertion in a cathodic material. Hence the first study, done on $FeVO_4$, included exhaustive characterization to study the insertion mechanism. This study introduced the first conversion-type material for Al-ion insertion in an aqueous electrolyte by conclusively showing the reversible formation of Al-containing phases. This study gave the initial confidence needed to pursue AIAB as a thesis subject. The second study, done on VO_2, was essentially aimed at coming up with a material that could show long cycle life. Further, it was realized that the economic and high volumetric capacity advantages of AlAB could only be realized by using Al as an anode in the system. Hence the thesis pivoted towards anodic study. At this stage, firstly, HCFs were established as stable cathodic material, which could be used to do full-cell studies using Al metal as anode without deteriorating full-cell performance. Later, anodes coated with various eutectic formulations were tested for their performance and suitability to the cell assembling process.

Overall, this thesis makes a significant contribution in the field of aluminum-ion aqueous battery. The details on Al-ion insertion mechanism in novel host materials and detailed study on the surface chemistry evolution of coated-Al contributes significant knowledge not only in the field of AIAB but in general for multivalent aqueous battery chemistry. It can also be added here that development in AIAB, including contributions from the thesis,

may seem inadequate compared to currently existing commercial battery systems. However, it is speculated that these developments will form parts of the backbone on which AIAB will develop.

8.2 Summary of results

8.2.1 Investigating $FeVO_4$ as a cathode material for aqueous aluminum-ion battery

- A novel Al-ion battery using $FeVO_4$ as a cathode material is reported with a high initial capacity of 350 mA h g^{-1}.
- A conversion mechanism is elucidated via XRD, XPS, XAS and Raman spectroscopy. The discharged states involve the formation of $Al_xV_yO_4$ & Fe-O-Al, which conclusively show the reversible reaction of Al-ion with the host material.
- Electrolyte pH is shown to have a deterministic effect on electrode stability. A high pH of the electrolyte reduces the side reactions between electrolyte and host material, improving the cycling stability.

8.2.2 Investigating Vanadium dioxide holey nanobelt as a cathode material for aqueous aluminum-ion battery

- 2 dimensional holey nanobelts of vanadium dioxide (VO_2) has been synthesized and explored as a potential cathode material for AIAB.
- Testing this material, a high capacity of 234 mAh g^{-1} at 150 mA g^{-1} is reported. At a higher rate of 1 A g^{-1}, remarkable long-term cycling stability for 1000 cycles with a capacity retention of 77.2% is also reported.
- An Al-ion and H^+ co-insertion mechnism has been revealed using complementary charcterization tecnhiques.

8.2.3 Investigating the role of coated-Al anode treatments for superior battery cycling performance using a hexacyanoferrate cathode

- A novel host material $Na_{1.68}Mn[Fe(CN)_6].1.7H_2O$ (NMHCF) is synthesized and tested for Al-ion insertion, and the electrochemical performance has been studied along with the concomitant insertion mechanism. A high energy density for at least 275 cycles is reported.

- The active influence of TAl on the overall battery performance has been recognized. A combination of TAl and electrolyte is responsible for taking the battery system in a diffusion polarization regime which is also reflected in terms of plating/stripping overpotential.

- The stability of the coating material is examined under atmospheric ageing & postmortem from the working cells.

8.2.4 Enabling Al-metal anodes for aqueous electrochemical cells by using eutectic mixtures as artificial protective interphase

- Urea + $AlCl_3$ and Et_3NHCl + $AlCl_3$ have been proposed as novel coating formulations that reduced anodic overpotential on Al-metal anode. These coating improves the conductivity and kinetics at the Al-anode/electrolyte interface.

- Urea based eutectic mixture is identified as the superior coating mixture and further studied for its stability in the ambient environment and during the cycling.

- UTAl is used as anode in a full cell “FeHCF | 2 m AlTFS | UTAl”, demonstrating its successful usage as an anode.

8.3 Novel Contribution

The novelties of this study could be identified as follows:

1. Reported the first conversion type material in the AIAB field, which sets a precedent of using conversion cathode chemistry for Al-ion insertion in an aqueous electrolyte. Revealed a deterministic effect of electrolyte pH on the cycling stability of the cathode material.
2. Implemented a robust structured VO cathode material for AIAB, showing remarkable long-term cyling stability for 1000 cycles with a capacity retention of

77.2% (Figure 8-1 a).

3. Revealed the implications of using an ionic liquid + $AlCl_3$ coated Al in a full cell. The study conclusively demonstrated that traditional knowledge of the highest concentrations of electrolyte leading to most stable cycling performance does not hold when using coated Al as an anode.

5. Contributed NMHCF and FeHCF as highly stable cathode materials that showed long-term cycling stability and could be used as standard cathodes in anodic studies (Figure 8-1 b).

6. Contributed urea+$AlCl_3$ as a low-cost eutectic formulation that can protect Al from oxidation in an ambient environment and assists in in-situ SEI like layer formation during cell operation. The usage of such an anode reduced the overall cell potential (Figure 8-1 c), essentially enabling usage of Al in an aqueous electrolyte.

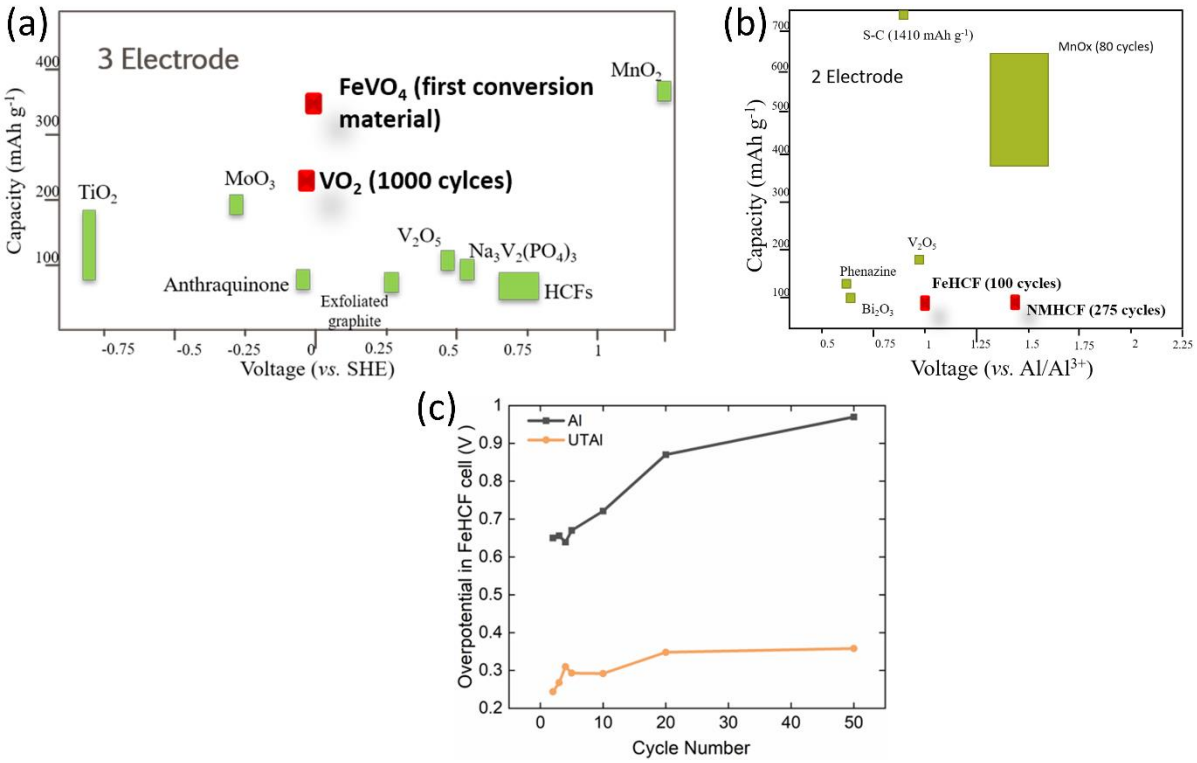

Figure 8-1: (a) Comparison of two novel cathode materials ($FeVO_4$ and VO_2) introduced in this study with historical and contemporary cathode materials studied in 3 electrode setup, (b) Comparison of two novel HCFs (NMHCF and FeHCF) introduced in this study with historical

and contemporary cathode materials studied in 2 electrode setup using coated Al as anode and (c) Full cell overpotential when using FeHCF cathode, and then comparing Al anode vs UTAl anode (the overpotential values are based on voltage difference of charge and discharge plateaus for the respective cases).

8.4 Recommendations

8.4.1 Anode

The anodic study done in this thesis makes use of the dip-coating technique to coat Al-metal with eutectic formulations. There is certainly room to make improvements in the coating techniques. Techniques like spin coating and spray coating can be adopted for better adhesion of the formulations to the Al metal. At the same time, alternative coating formulations aimed at increasing the cell voltage can also be adopted. The voltage of a typical FeHCF | 2 m AlTFS | UTAl cell can be seen to be about ~1.2 volts. This is because the actual redox potential of Al, which is -1.66 V (w.r.t. SHE), is not realized. The coating done on Al is likely not allowing for Al^{3+}/Al reduction process. New formulations which can practically realize such redox potentials can be explored and implemented in AIAB.

Some preliminary study done on anode included replacing high purity Al (>99.9%) with cheaper Al metal foil (Al substrate used as current collectors for cathode), coating it with eutectic formulations and implementing it in a full cell (Figure 8-2). However, reproducibility remained a problem in such experiments, speculated to be caused by the non-uniform coating because of the fragile nature of the foils. Hence, more exploration is needed in this direction as using cheap Al can significantly bring down the cost at the cell stage.

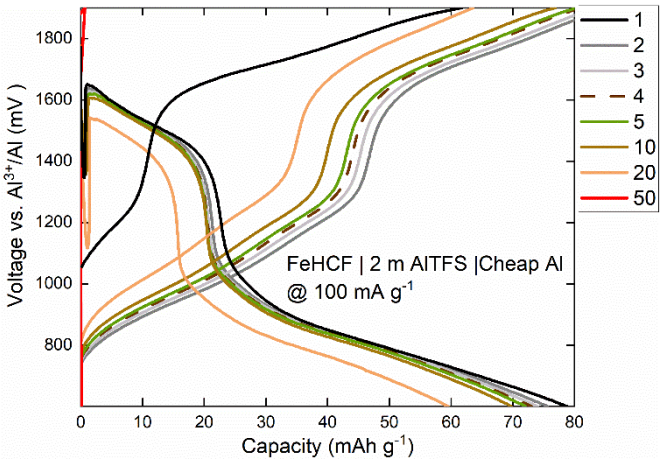

Figure 8-2: Galvanostatic charge/discharge profile at various cycles for FeHCF | 2 m AlTFS | cheap Al at a current rate of 100 mA g^{-1}.

8.4.2 Electrolyte

The scope of this thesis in terms of electrolyte improvement was limited to optimizing the concentration and the pH of the electrolytes formulated by dissolving Al-salts in water. Alternative hybrid formulations were not explored as the thesis aimed at studying the feasibility of aluminum chemistry, hence keeping the electrolyte chemistry purely of Al-ion species. As discussed in earlier chapters, AlTFS forms a maximum of 5 m solution in water, making room to explore more concentrated electrolyte forms. These concentrated electrolytes can be hybrid electrolytes known to enhance battery cycling life [1-3]. Combinations like 5 m AlTFS + 25 m LiTFS can be explored to realize the maximum advantage of water-in-salt concept.

Adding SEI layer forming additive in the electrolyte is one of the strategies to improve the cycling stability of the electrolyte as it reduces the side reactions between the cathode and the electrolyte.[4] [5-7] Since AIAB systems suffered badly with cathode material dissolution in the electrolyte, such SEI forming strategies can be adopted as next immediate steps in AIAB field.

8.4.3 Cathode

This thesis introduces three cathode material, namely, $FeVO_4$, VO_2 and HCFs, in the AIAB field. Though these materials introduce conversion chemistry and stable performances in the AIAB field, there is still a need for high voltage material with high capacity. MnO_x fits very well in that category. However, their stability in acidic Al aqueous electrolyte remains a big challenge in the field.[8-11] Preliminary study done on alpha-MnO also show such rapidly degrading cycling performance. Stabilizing the cycling performance of MnO_x for the AIAB system would be a good development.

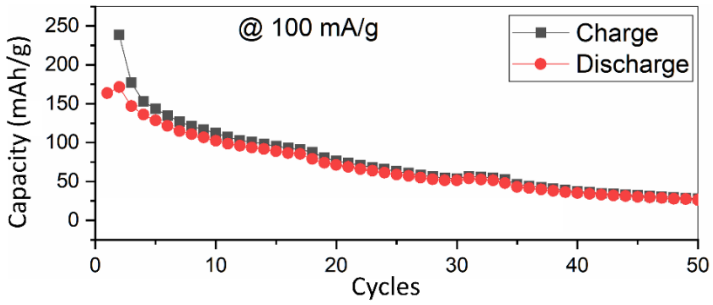

Figure 8-3: Galvanostatic charge/discharge profile at various cycles for alpha MnO | 2 m AlTFS | TAl at a current rate of 100 mA g^{-1}.

8.4.4 Other

One of the major challenges that have not been addressed in this thesis is the evolution of gases during cell cycling. These gaseous products are mainly formed by the catalysis of water on the metallic anode. It is speculated that O_2 and H_2 evolution may be happening during cell cycling. Several experiments in this thesis includes data where capacity dropped instantaneously because of coin-cell popping. This may also have been because of electrolyte reacting with coated Al and forming gases. Studies aimed at characterizing these gaseous species would add more knowledge in the field. Experiment design and discussion around the widely different transport numbers of ions present in the electrolyte can also be considered. It will help in adding new insights in the capacity contribution by different ions.

8.5 Concluding Remarks

In conclusion, this thesis titled "Engineering Cathode and Anode for Rechargeable Aluminum-ion Aqueous Battery" achieves its objective of studying the feasibility of aluminum chemistry in an aqueous electrolyte. The development made on cathode (shown below in figure 8-4) as well as anode front adds important initial knowledge in the field. New cathodic materials are introduced in the field with a detailed investigation of the guest-ion insertion mechanism in the host. New coating formulations, backed by detailed investigation of surface chemistry evolution under various conditions, make usage of Al-metal possible in an aqueous electrolyte. Finally, the implementation of engineered cathode and anode in a full-cell with optimized electrolyte demonstrates the feasibility of this chemistry.

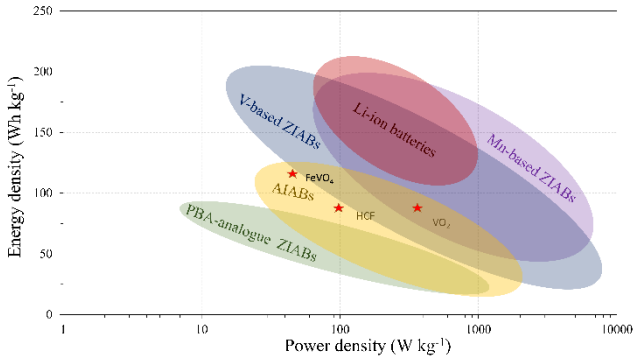

Figure 8-4: Ragone plot of various ZIAB and AIAB electrodes[9] with the current work

This thesis serves as a collection of important preliminary studies in the AIAB field, concluding that Al-ion battery chemistry in an aqueous electrolyte is possible. This chemistry has advantages in terms of safety, environmental and economic sustainability. However, it is also recognized that this chemistry, based on developments made in this thesis, has limitations in achieving high cell voltage (>1.5 V). These limitations can be overcome by exploring new high voltage cathode materials. The study overall provides an impetus to future multivalent battery researchers and would open new avenues for research into conversion-based cathodes and modification of Al-metal anode for Al-ion batteries.

References

[1] A. R. Mainar, E. Iruin, J. A. Blázquez. *Energy Technology.* **2020,** *8*, 2000476.

[2] J.-Q. Huang, X. Guo, X. Lin, Y. Zhu, B. Zhang. *Research.* **2019,** *2019*, 2635310.

[3] S. Wu, S. Hu, Q. Zhang, D. Sun, P. Wu, Y. Tang, H. Wang. *Energy Storage Materials.* **2020,** *31*, 310-317.

[4] I. B. Stojković, N. D. Cvjetićanin, S. V. Mentus. *Electrochem. Commun.* **2010,** *12*, 371-373.

[5] F. Wang, Y. Lin, L. Suo, X. Fan, T. Gao, C. Yang, F. Han, Y. Qi, K. Xu, C. Wang. *Energy Environ. Sci.* **2016,** *9*, 3666-3673.

[6] L. Suo, D. Oh, Y. Lin, Z. Zhuo, O. Borodin, T. Gao, F. Wang, A. Kushima, Z. Wang, H.-C. Kim, Y. Qi, W. Yang, F. Pan, J. Li, K. Xu, C. Wang. *J. Am. Chem. Soc.* **2017,** *139*, 18670-18680.

[7] S.-B. Son, T. Gao, S. P. Harvey, K. X. Steirer, A. Stokes, A. Norman, C. Wang, A. Cresce, K. Xu, C. Ban. *Nat. Chem.* **2018,** *10*, 532-539.

[8] C. Yan, C. Lv, L. Wang, W. Cui, L. Zhang, K. N. Dinh, H. Tan, C. Wu, T. Wu, Y. Ren, J. Chen, Z. Liu, S. Madhavi, X. Rui, Q. Yan, G. Yu. *J. Am. Chem. Soc.* **2020**.

[9] J. Joseph, J. Nerkar, C. Tang, A. Du, A. P. O'Mullane, K. Ostrikov. *ChemSusChem.* **2019,** *12*, 3753-3760.

[10] C. Wu, S. Gu, Q. Zhang, Y. Bai, M. Li, Y. Yuan, H. Wang, X. Liu, Y. Yuan, N. Zhu, F. Wu, H. Li, L. Gu, J. Lu. *Nat. Commun.* **2019,** *10*, 1-10.

[11] S. He, J. Wang, X. Zhang, J. Chen, Z. Wang, T. Yang, Z. Liu, Y. Liang, B. Wang, S. Liu, L. Zhang, J. Huang, J. Huang, L. A. O'Dell, H. Yu. *Adv. Funct. Mater.* **2019,** *0*, 1905228.

List of Publications

[1] **S. Kumar**, V. Verma, H. Arora, W. Manalastas, M. Srinivasan. *ACS Applied Energy Materials.* **2020,** *3*, 8627-8635.

[2] **S. Kumar**, R. Satish, V. Verma, H. Ren, P. Kidkhunthod, W. Manalastas, M. Srinivasan. *J. Power Sources.* **2019,** *426*, 151-161.

[3] **S. Kumar***, V. Verma*, R. Chua, H. Ren, P. Kidkhunthod, C. Rojviriya, S. Sattayaporn, F. M. F. de Groot, W. Manalastas Jr, M. Srinivasan. *Batteries & Supercaps.* **2020,** *3*, 619-630.

[4] Y. Cai*, **S. Kumar***, R. Chua, V. Verma, D. Yuan, Z. Kou, H. Ren, H. Arora, M. Srinivasan. *J. Mater. Chem. A.* **2020,** *8*, 12716-12722.

[5] V. Verma*, **S. Kumar***, W. Manalastas Jr, R. Satish, M. Srinivasan. *Adv. Sustainable Syst.* **2019,** *3*, 1800111.

[6] W. Manalastas Jr, **S. Kumar**, V. Verma, L. Zhang, D. Yuan, M. Srinivasan. *ChemSusChem.* **2019,** *12*, 379-396.

[7] V. Verma, R. M. Chan, L. Jia Yang, **S. Kumar**, S. Sattayaporn, R. Chua, Y. Cai, P. Kidkhunthod, W. Manalastas, M. Srinivasan. *Chem. Mater.* **2021**.

[8] D. Yuan, J. Zhao, W. Manalastas, **S. Kumar**, M. Srinivasan. *Nano Materials Science.* **2020,** *2*, 248-263.

[9] H. Ren, X. Sun, C. Du, J. Zhao, D. Liu, W. Fang, **S. Kumar**, R. Chua, S. Meng, P. Kidkhunthod, L. Song, S. Li, S. Madhavi, Q. Yan. *ACS Nano.* **2019,** *13*, 12969-12979.

[10] V. Verma, **S. Kumar**, W. Manalastas, J. Zhao, R. Chua, S. Meng, P. Kidkhunthod, M. Srinivasan. *ACS Applied Energy Materials.* **2019,** *2*, 8667-8674.

[11] R. Chua, Y. Cai, P. Q. Lim, **S. Kumar**, R. Satish, W. Manalastas, H. Ren, V. Verma, S. Meng, S. A. Morris, P. Kidkhunthod, J. Bai, M. Srinivasan. *ACS Appl. Mater. Interfaces.* **2020,** *12*, 22862-22872.

[12] Y. Cai, R. Chua, Z. Kou, H. Ren, D. Yuan, S. Huang, **S. Kumar**, V. Verma, P. Amonpattaratkit, M. Srinivasan. *ACS Appl. Mater. Interfaces.* **2020,** *12*, 36110-36118.

[13] V. Verma, R. M. Chan, L. Jia Yang, **S. Kumar**, S. Sattayaporn, R. Chua, Y. Cai, P. Kidkhunthod, W. Manalastas, M. Srinivasan. *Chem. Mater.* **2021,** *33*, 1330-1340.

[14] V. Verma, **S. Kumar**, W. Manalastas, M. Srinivasan. *ACS Energy Letters.* **2021,** *6*, 1773-1785.